Microstructure of epitaxial thin films of the ferromagnetic shape memory alloy Ni_2MnGa

Dissertation zur Erlangung des Grades

Doktor der Naturwissenschaften

am Fachbereich Physik
der Johannes Gutenberg-Universität Mainz

Tobias Eichhorn
geb. in Mainz

JOHANNES GUTENBERG UNIVERSITÄT MAINZ

Mainz, 2011

1. Berichterstatter:
2. Berichterstatter:
Tag der mündlichen Prüfung: 9. Dezember 2011

Abstract

This work is concerned with the preparation and detailed characterization of epitaxial thin films of the Heusler compound Ni_2MnGa. This multiferroic compound is of both technological and scientific interest due to the outstanding magnetic shape memory (MSM) behavior. Huge magnetic-field-induced strains up to 10 % have been observed for single crystals close to a Ni_2MnGa composition. The effect is based on a redistribution of crystallographic twin variants of tetragonal or orthorhombic symmetry. Under the driving force of the external magnetic field twin boundaries can move through the crystal, which largely affects the macroscopic shape. The unique combination of large reversible strain, high switching frequency and high work output makes the alloy a promising actuator material. Since the MSM effect results from an intrinsic mechanism, MSM devices possess great potential for implementation in microsystems, e.g. microfluidics.

So far significant strains, in response to an external magnetic field, have been observed for bulk single crystals and foams solely. In order to take advantage of the effect in applications concepts for miniaturization are needed. The rather direct approach, based on epitaxial thin films, is explored in the course of this work. This involves sample preparation under optimized deposition parameters and fabrication of freestanding single-crystalline films. Different methods to achieve freestanding microstructures such as bridges and cantilevers are presented. The complex crystal structure is extensively studied by means of X-ray diffraction. Thus, the different crystallographic twin variants, that are of great importance for the MSM effect, are identified. In combination with microscopy the twinning architecture for films of different crystallographic orientation is clarified. Intrinsic blocking effects in samples of (100) orientation are explained on basis of the variant configuration. In contrast, a promising twinning microstructure in (110) oriented films is detected stimulating further research.

Taking advantage of the thin film geometry spectroscopic methods are applied to the samples. The measurements provide the first experimental test for changes in the electronic structure of the involved $3d$ metals during a martensitic transition. Exploiting the X-ray magnetic circular dichroism quantitative information on the element-specific spin and orbital magnetic moments are accessed. In addition, angular-dependent experiments allow to trace the microscopic origin of the magnetic anisotropy in Ni_2MnGa improving the fundamental understanding of this material.

Kurzfassung

Gegenstand dieser Arbeit ist die Präparation und die ausführliche Charakterisierung epitaktischer Dünnschicht-Proben der Heusler Verbindung Ni_2MnGa. Diese intermetallische Verbindung zeigt einen magnetischen Formgedächtnis-Effekt (MFG), der sowohl im Bezug auf mögliche Anwendungen, als auch im Kontext der Grundlagenforschung äußerst interessant ist. In Einkristallen nahe der Stöchiometrie Ni_2MnGa wurden riesige magnetfeldinduzierte Dehnungen von bis zu 10 % nachgewiesen. Der zugrundeliegende Mechanismus basiert auf einer Umverteilung von kristallographischen Zwillings-Varianten, die eine tetragonale oder orthorhombische Symmetrie besitzen. Unter dem Einfluss des Magnetfeldes bewegen sich die Zwillingsgrenzen durch den Kristall, was eine makroskopische Formänderung mit sich bringt. Die somit erzeugten reversiblen Längenänderungen können mit hoher Frequenz geschaltet werden, was Ni_2MnGa zu einem vielversprechenden Aktuatorwerkstoff macht. Da der Effekt auf einem intrinsischen Prozess beruht, eignen sich Bauteile aus MFG Legierungen zur Integration in Mikrosystemen (z.B. im Bereich der Mikrofluidik).

Bislang konnten große magnetfeldinduzierte Dehnungen nur für Einkristalle und Polykristalle mit hoher Porosität ("*foams*") nachgewiesen werden. Um den Effekt für Anwendungen nutzbar zu machen, werden allerdings Konzepte zur Miniaturisierung benötigt. Eine Möglichkeit bieten epitaktische dünne Filme, die im Rahmen dieser Arbeit hergestellt und untersucht werden sollen. Im Fokus steht dabei die Optimierung der Herstellungsparameter, sowie die Präparation von freitragenden Schichten. Zudem werden verschiedene Konzepte zur Herstellung freistehender Mikrostrukturen erprobt. Mittels Röntgendiffraktometrie konnte die komplizierte Kristallstruktur für verschiedene Wachstumsrichtungen verstanden und die genaue Verteilung der Zwillingsvarianten aufgedeckt werden. In Verbindung mit Mikroskopie-Methoden konnte so die Zwillingsstruktur auf verschiedenen Längenskalen geklärt werden. Die Ergebnisse erklären das Ausbleiben des MFG Effekts in den Proben mit (100) Orientierung. Andererseits wurde für Schichten mit (110) Wachstum eine vielversprechende Mikrostruktur entdeckt, die einen guten Ausgangspunkt für weitere Untersuchungen bietet. Durch die spezielle Geometrie der Proben war es möglich, Spektroskopie-Experimente in Transmission durchzuführen. Die Ergebnisse stellen den ersten experimentellen Nachweis der Änderungen in der elektronischen Struktur einer metallischen Verbindung während des martensitischen Phasenübergangs dar. Durch Messen des magnetischen Zirkulardichroismus in der Röntgenabsorption konnten quantitative Aussagen über die magnetischen Momente von Ni und Mn getroffen werden. Die Methode erlaubt überdies die Beiträge von Spin- und Bahn-Moment separat zu bestimmen. Durch winkelabhängige Messungen gelang es, die mikroskopische Ursache der magnetischen Anisotropie aufzuklären. Diese Ergebnisse tragen wesentlich zum Verständnis der komplexen magnetischen und strukturellen Eigenschaften von Ni_2MnGa bei.

Contents

1 Introduction **1**

2 Background **5**
2.1 Heusler compounds 5
2.2 Shape memory effect 7
2.2.1 Phase transformation 8
2.2.2 Twinning 13
2.2.3 Thermal shape memory effect 15
2.2.4 Ferromagnetic shape memory effect 16
2.3 Properties of the system Ni-Mn-Ga 22
2.3.1 Crystal structure 22
2.3.2 Magnetism 25
2.3.3 Phase transition and compositional dependence 27

3 Experimental details **31**
3.1 Thin film sample preparation 31
3.1.1 Sputter deposition 32
3.1.2 Targets 35
3.1.3 Substrates 36
3.1.4 Optimized preparation parameters 37
3.2 Freestanding films 39
3.2.1 Sacrificial substrate method 40
3.2.2 Sacrificial buffer layer technique 41
3.2.3 Focused ion beam etching 46
3.3 Standard characterization methods 48
3.3.1 X-ray diffraction 48
3.3.2 Reflectometry 52
3.3.3 Magnetometry 53
3.3.4 Surface investigation 55

4 Crystal Structure **57**
4.1 Structural properties of the austenite 58
4.2 Structural phase transformation 68

4.3 Martensite crystal structure 71
4.3.1 Films on $Al_2O_3(11\bar{2}0)$ substrates 71
4.3.2 Samples on MgO(100) substrates 76
4.3.3 NaCl(100) substrates 83
4.4 Magnetic field assisted XRD 86
4.5 Key results 87

5 Surface morphology and twinning microstructure 89
5.1 $(110)_A$ oriented films 91
5.2 $(100)_A$ oriented films 91
5.3 Magnetically induced reorientation of variants 100
5.3.1 Model for variant alignment 100
5.3.2 Manipulation of twinning microstructure 104
5.4 Key results 112

6 Magnetic properties 113
6.1 Bulk magnetometry 113
6.1.1 Phase transformation 113
6.1.2 Saturation magnetization 119
6.1.3 Indication of MIR in hysteresis loops 121
6.2 XAS and XMCD 125
6.2.1 Phase transformation 128
6.2.2 Magnetic anisotropy 133
6.2.3 Surface properties 140
6.3 Key results 142

7 Conclusions 143

Bibliography 159

List of publications 161

Acknowledgments 163

List of Figures

2.1 Representation of the $L2_1$ structure 6
2.2 Temperature-dependence of the martensitic transformation 9
2.3 Gibbs free energy of austenite and martensite 10
2.4 Mechanism of lattice deformation during a displacive transformation 12
2.5 Twin plane alignment 14
2.6 Representation of orthorhombic twin variants 15
2.7 Thermal shape memory effect 17
2.8 Two-variant model 20
2.9 Model for twin boundary movement 20
2.10 Illustration of reversible magnetostrain in MSM alloys 21
2.11 Schematic of the 7M/14M structure 23
2.12 Structure-composition correlation 24
2.13 $Ni_{2+x}Mn_{1-x}Ga$ phase diagram 27
2.14 $Ni_2Mn_{1+x}Ga_{1-x}$ phase diagram 28

3.1 Deposition chamber and illustration of the sputter process 33
3.2 Influence of substrate temperature on saturation magnetization . 39
3.3 Composition dependence on the sputter pressure 40
3.4 Images of films prepared on NaCl substrates 42
3.5 Illustration of the patterning process 43
3.6 Optical microscopy image of a partly freestanding film 44
3.7 Images of a patterned and partially released sample 45
3.8 Redeposition of material during FIB etching 46
3.9 SEM image of a FIB etched cantilever 47
3.10 Side view of the mircostructure 47
3.11 Front view on a FIB cut cantilever 48
3.12 Ni_2MnGa powder diffraction pattern simulation 50
3.13 $\{hkl\}$ reflection list for a Ni_2MnGa powder sample 51
3.14 Operating angles of the four circle diffractometer 52
3.15 Determination of film thickness by XRR 53
3.16 XRR scan on a Al-Fe multilayer 54

4.1 XRD fullscan on MgO 59

4.2 XRD rocking curve on MgO 59
4.3 XRD fullscan on Al_2O_3 60
4.4 XRD rocking curve on Al_2O_3 60
4.5 Reciprocal space maps for different film growth modes 62
4.6 Sketch of the in-plane orientation on MgO and Al_2O_3 substrates. . 63
4.7 Representation of chemical order of substrate and film 64
4.8 Illustration of the chemical order at the film substrate interface . 64
4.9 Unconventional growth on MgO(100) 65
4.10 Phi-scans of the {220} and {400} film peaks. 67
4.11 Illustration of the multi-variant growth on MgO 67
4.12 Reciprocal space maps of the martensite {400} peaks 70
4.13 Temperature evolution of the $(400)_A$ peak 70
4.14 Temperature evolution of the $(202)_A$ peak 71
4.15 Model for twin plane alignment on Al_2O_3 substrates. 72
4.16 Variant configuration and XRD peak splitting 74
4.17 Twin variant alignment and modulation in $(110)_A$ oriented films . 75
4.18 7M structure probed by XRD line scans 76
4.19 XRD fullscan on MgO(100) + Cr buffer 77
4.20 Reciprocal space map of martensite peaks 78
4.21 Variant distribution probed by XRD 79
4.22 Variant configuration before and after releasing the film 81
4.23 Modulation for different variants 82
4.24 Modulated superstructure in a freestanding film 83
4.25 XRD fullscan on a film released from NaCl 84
4.26 Rocking curve of a freestanding film released from NaCl 85
4.27 Phi-scan of the freestanding film 85
4.28 Model for variant redistribution 86

5.1 Light microscopy images of surface reliefs 92
5.2 Changes in the surface pattern upon thermal cycling 94
5.3 SEM image of different twinning patterns 95
5.4 AFM image showing the tweed-like twinning pattern 96
5.5 SEM image of the FIB cut cross section 97
5.6 SEM image of etched film surface 98
5.7 AFM image of aged film surface 99
5.8 Illustration of surface relief induced by twinning 99
5.9 Twinning pattern on freestanding microbridges 101
5.10 Model for twin variant alignment 102
5.11 Illustration of surface pattern induced by twin bands 103
5.12 Sketch of twin band intersections 104
5.13 Indication of MIR in micro-cantilever 106
5.14 Model for MIR of variants 107
5.15 Manipulation of twinning pattern 109

5.16 Magnetically induced variant redistribution 110
5.17 Indication of MFIS 111

6.1 Temperature evolution of in-plane magnetization 114
6.2 T-Sweeps in high and low field 116
6.3 Shift of phase transformation due to crystallographic orientation . 116
6.4 T-Sweep for films with $T_C < T_{As}$ 117
6.5 Assignation of the phase transformation temperatures 118
6.6 Hysteresis loops for austenite and martensite phase 119
6.7 Difference in coercive field 120
6.8 In-plane $M(H)$ curves for a film on $Al_2O_3(11\bar{2}0)$ 122
6.9 Magnetization jumps 122
6.10 In-plane $M(H)$ curves for a sample on MgO(100) 124
6.11 Step-like increases in magnetization 124
6.12 XAS function principle 126
6.13 $2p \rightarrow 3d$ transition rules 127
6.14 XAS and XMCD for $T > T_M$ and $T < T_M$ 129
6.15 XAS comparison of theory and experiment 131
6.16 Temperature evolution of Ni and Mn moments 132
6.17 Hard-axis magnetization loops 134
6.18 Representation of the variant configuration in $(101)_A$ oriented films 135
6.19 Angular-dependent XAS and XMCD spectra 137
6.20 Angular dependence of Ni spin and orbital magnetic moments . . 138
6.21 Illustration of the changes in Ni d states 139

Chapter 1

Introduction

What image comes to your mind when you think of a chemistry lab? A room equipped with work benches, extractor hoods and shelves packed with chemicals of all sorts? Do you see a huge variety of glass vessels and lab equipment? So how about a lab that fits in your pocket, a lab on a chip? What sounds like a piece of equipment from a science fiction movie is actually the vision of a promising, interdisciplinary research field called microfluidics [1]. At the intersection of science and technology this growing research field deals with systems that process or manipulate small amounts of fluids, typically below 10^{-9} liters. The processing is done in a network of channels with dimensions of 10 to 100 μm. By adding functions like pumps, valves, sensors or electronics to the microchannel network, a complex microsystem called lab-on-a-chip can be realized. The possible applications range from chemical synthesis to biological analysis, like portable medical diagnostics. Besides the very small quantities of samples and reagents needed, the unique fluid dynamics in microchannels enable completely new applications. A challenging task in these microsystems is the implementation of the functional groups. To achieve a compact design, new functional materials are needed, one of which is investigated within this work.

The development of new technological concepts is closely connected with research on new functional materials. These so-called smart materials are characterized by distinct properties such as mechanical, electrical or magnetical properties, that can be significantly changed in a controlled way by an external field. The control mechanism may be a change in temperature, applying a mechanical stress or an electric or magnetic field. Coupling between different physical properties can lead to an increased functionality. Such a multi-functional material is the Heusler compound Ni_2MnGa that exhibits coupling between magnetic and structural order. In response to a magnetic field mechanical strains up to 10 % can be induced in single-crystals of this multiferroic compound. As the macroscopic shape of the sample is altered by the reversible magnetic field-induced strains, the effect is also referred to as "magnetic shape memory effect" (MSM effect). The fascinating phenomenon was first observed by Ullakko and co-workers in 1996.

They reported 0.2 % magnetic-field-induced strain (MFIS) in a sample close to stoichiometric Ni_2MnGa [2]. In the following years, the magnetically induced strains have been increased considerably. In 1999 a field-induced strain of more than 5 % was observed in the nearly tetragonal martensite phase of $Ni_{48}Mn_{31}Ga_{21}$ [3]. The record value of almost 10 % was measured for a $Ni_{49}Mn_{30}Ga_{21}$ single-crystal in 2002 [4]. These huge strains are generated by a redistribution of crystallographic variants in the material. Through the magnetocrystalline anisotropy the external field produces an internal stress on the twin boundaries that separate the different variants. Moderate magnetic fields (< 1 T) can induce twin boundary motion, which changes the variant distribution. The microscopic process leads to a macroscopic strain, that can reach the aforementioned values for single-crystalline samples. In contrast to conventional shape memory alloys like NiTi, no phase transformation is involved in the magnetic field-controlled process. As a consequence the slow heating and cooling process can be omitted. Thus, the response time of MSM materials can be below a millisecond, while the achievable strains exceed those of other active materials like Terfenol-D, Galfenol, and piezoelectrics by more than an order of magnitude. The combination of high switching frequency (up to the kHz range), large strains and high work output makes Ni_2MnGa a promising material for actuator applications [5]. Since the magnetically induced strains are based on an intrinsic mechanism, devices exploiting the MSM effect possess great potential for miniaturization. Due to their compactness and lightness, MSM components can be easily included in mechanical devices of small dimensions. Among the possible applications are valves or pumps for microfluidics systems. Using concepts of microelectronics one approach in microfluidics deals with silicon-based devices that are by principle compatible with MSM thin films. Other potential applications include positioning devices, e.g. optical mirrors in a microscanner [6], switches, active vibrational dampers and sensors that make use of the inverse effect. In principle, the inverse effect can be used for harvesting waste mechanical energy utilizing the Villari effect [7]. In addition to the magneto-elastic properties, another feature of the Ni-Mn-Ga system is of technological interest: the magnetocaloric effect [8]. In general, materials experiencing a structural phase transition in the ferromagnetic state are promising operating agents in refrigerators. For some compositions in the Ni-Mn-Ga system the structural and magnetic phase transitions appear at the same temperature. This gives rise to a large magnetocaloric effect comparable to the so-called giant magnetocaloric materials [9].

Currently, a number of potential magnetic shape memory compounds like Fe-Pd, Fe-Pt, Ni-Mn-Z (Z=In, Sn, Sb) or Co-Ni-Al are investigated both experimentally and theoretically [10]. To date the most promising candidate for applications is the extensively studied Ni-Mn-Ga system. Decisive parameters that limit the operation temperature, i.e. the Curie temperature and the phase transformation temperature, can be tailored by changing the composition. The Ni:Mn:Ga ratio has also a huge impact on the crystal structure of the active martensite phase in

Ni-Mn-Ga. Large magnetic-field-induced strains have been observed solely in single crystals with a modulated structure. In the non-modulated phase the twinning stress is too high to allow MFIS. While large MFIS can be achieved for monocrystals, polycrystalline bulk samples show almost no magnetostrain because of the grain boundaries that effectively suppress the motion of twin boundaries.

In order to take advantage of the MSM effect in microactuator applications, concepts for miniaturization are needed. Recently, several approaches including Ni-Mn-Ga powders, fibers, ribbons and films have been explored. These elements with one or more small dimension can be included in constructs such as composites, laminates or foams. A nice overview of different concepts was provided recently by Dunand and Müllner [11]. Although encouraging results have been achieved for fibers [12], foams [13] and compounds [14], the most promising and straight-forward approach is based on thin epitaxial films. The first successful attempt in growing epitaxial films was conducted by Dong and co-workers [15]. Using molecular beam epitaxy (MBE) they prepared epitaxial Ni_2MnGa films on lattice-matched GaAs(001) substrates with a $Sc_{0.3}Er_{0.7}As$ interlayer. On the basis of these samples the authors fabricated freestanding bridges and cantilevers using a complex etching procedure and reported indication of the MSM effect at T=135 K [16]. However, neither the used substrate materials nor the applied techniques of this work are suitable for commercial applications. This is not the case for sputter deposition, a preparation technique extensively used in semiconductor industry. In general, films deposited by sputtering will be polycrystalline or textured only [17].

The direct preparation of epitaxial Ni_2MnGa films using sputter deposition was pioneered in the preceding work [18]. Following these results the present thesis explores different concepts to obtain freestanding Ni-Mn-Ga films that can be used in microactuator application. The key focus of this work is not on the technical implementation, but on the physical properties of the thin film samples. In this context, effort is put into film preparation and detailed characterization. The decisive structural and magnetic properties of substrate-constrained and freestanding films are investigated by means of X-ray diffraction, surface imaging, magnetometry and X-ray absorption spectroscopy. Taking advantage of the unique properties of thin film samples, e.g. the fixed reference system provided by the substrate and the option to measure in transmission mode, elaborate investigation methods are applied to tackle fundamental questions. Among them are the influence of the film-substrate orientation relation on the microstructure of the martensite phase and the microscopic origin of the magnetocrystalline anisotropy. The first chapter provides an overview of the properties of Heusler compounds in general and the Ni-Mn-Ga system in particular. The relevant preparation techniques and characterization methods are reviewed in chapter 3. The studies on the crystal structure of the austenite and the complex martensite are elaborated in chapter 4. The variant configuration and associated twin plane alignment dictate not only the microstructure of the martensitic samples

but are also reflected in the surface morphology of the films. Hence, microscopy techniques can be applied to investigate the effect of twinning on different length scales, which is discussed in chapter 5. The important magnetic properties of the films are treated in chapter 6. This section presents the results obtained with magnetometry measurements and X-ray absorption spectroscopy. The last chapter provides an overview of the basic reults of this work that contribute to an increased comprehension of the interesting Ni-Mn-Ga system.

Chapter 2

Background

2.1 Heusler compounds

The prototype of the class of Heusler compounds, Cu_2MnAl, was discovered in 1903 by the chemist Friedrich Heusler [19, 20]. Surprisingly, the alloy shows ferromagnetic order, though none of the constituents does in the elemental form. Even at room temperature Cu_2MnAl is ferromagnetic. To date a large number of these ternary intermetallic compounds has been discovered and extensively studied, both experimentally and theoretically. The material class can be divided in full- and half-Heusler compounds, described by the sum formulas X_2YZ and XYZ, respectively, where X and Y are transition metals while Z is a main group element (group III.-V.). In contrast to conventional alloys, where the different elements are statistically distributed, the different atomic species in a Heusler "alloy" occupy defined lattice sites. The three constituents X, Y and Z are arranged on four interpenetrating fcc sub-lattices as shown in Fig. 2.1. For the fully ordered structure, referred to as $L2_1$ structure, this results in a cubic unit cell containing 16 atoms. In case of the half-Heusler compounds one of the X sub-lattices remains unoccupied and the crystal structure is designated $C1_b$. For both, half-Heusler and full-Heusler compounds, the structural order is accompanied by magnetic order in many cases. Diverse magnetic phenomena like itinerant and localized magnetism, antiferromagnetism or Pauli paramagnetism can be studied when varying the constituents. In spite of similar chemical and physical properties, the different members of the material class show a wide range of properties including superconductivity [21] and semiconducting behavior [22].

A prominent feature of many Heusler compounds is a high spin polarization of the electrons near the Fermi level. This makes the material class highly interesting for applications that make use of the intrinsic electron spin and the associated magnetic moment to establish an additional information channel. This new field of electronics based on the spin degree of freedom of electrons is called spintronics [23]. After the discovery of the giant magnetoresistance (GMR) effect

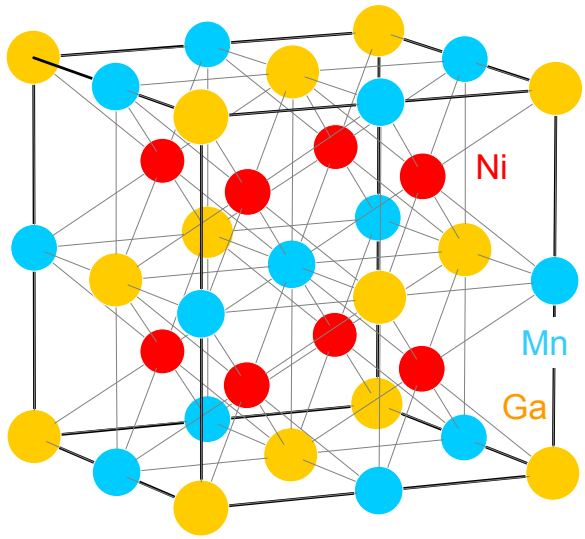

Figure 2.1: Representation of the $L2_1$ ordered Heusler structure X_2YZ. The unit cell is built from four interpenetrating fcc sub-lattices, two of which are occupied by the atomic species X while Y and Z sit on the remaining sub-lattices.

in 1988 [24, 25] this new research field has been attracting massive attention. In the experiment two ferromagnetic electrodes are separated by a non-magnetic metal layer. The resistance along the layer stack reveals a strong dependence on the relative alignment of magnetization direction of the magnetic layers. In the parallel configuration the resistance is considerably lower than in the antiparallel one. The GMR effect is based on the asymmetry of the majority and the minority charge carriers at the Fermi level which is reflected by the spin polarization P. The maximum effect can be achieved for P=100 %, which means a half-metallic ferromagnet [26]. These materials feature an energy gap in the minority-spin band-structure, which then is semiconducting, while the majority-spin band-structure is metallic. Though theoretical calculations predict a half-metallic behavior for many Heusler compounds [27], experimental proof of the high spin polarization remains a challenging task. A focus of scientific interest lies on the Co_2XY system that is well characterized by theory [28]. These Co-based compounds are interesting for applications because of their high Curie temperature, large magnetic moment and the predicted half-metalicity. A high spin polarization has been experimentally confirmed, for example, in the quaternary compound $Co_2Cr_{0.6}Fe_{0.4}Al$ [29].

In general, the magnetic properties of Heusler compounds are determined by the electronic structure of their valence bands. In particular the Co-based alloys obey a generalized Slater-Pauling rule, which states that the spontaneous magnetization can be derived from the accumulated number of valence electrons N_h according to $M = (N_v - 24)\mu_B$/formula unit (f.u.) [30]. This rule of thumb holds

for example for Co_2FeSi, that possesses 30 valence electrons and accordingly a saturation magnetization of $6\mu_B$/f.u. [28]. In spite of the identical number of valence electrons, the compound Ni_2MnGa shows only a saturation magnetization of 4.2 μ_B/f.u. Likewise other members of the X_2MnZ system, here the magnetization is essentially confined to the Mn sublattice [31]. Additional magnetization contributions appear at the X sites for X being Ni or Co. While Co_2MnGa shows a saturation magnetization following the generalized Slater-Pauling rule a strong deviation from the rule is observed in the case of Ni_2MnGa. In 1984 Webster et al. reported on neutron diffraction studies of the magnetic order in Ni_2MnGa that revealed a moment of 4.17 μ_B/f.u. largely confined to the Mn sites [32]. By means of temperature-dependent magnetization measurements the authors were the first to detect the anomalous magnetization behavior due to the structural phase transformation. According to this discovery, Ni_2MnGa is one of the rare magnetic materials undergoing a martensite transition.

The structural and magnetic properties that give rise to the exceptional magneto-elastic characteristics of martensitic Ni_2MnGa are reviewed in the following.

2.2 Shape memory effect

Conventional materials, such as steel or aluminum, can be deformed plastically at room temperature. When heated the macroscopic shape resulting from the deformation remains unchanged until melting starts. In contrast, some metallic compounds possess the ability to recover a limited plastic deformation upon heating and thus can regain their original macroscopic shape. This behavior, described as shape memory effect, was first discovered by Chang and Read on a gold-cadmium alloy in 1951 [33]. Though, in the following years, a few more shape memory alloys (SMA) were found, research interest in both the metallurgy and potential practical uses remained reserved. This was changed, when Buehler and co-workers observed the shape memory effect in equiatomic Ni-Ti in 1963 [34]. First commercial applications exploiting the shape memory effect followed soon.

The fascinating effect is based on a structural phase transformation between a high-temperature phase (austenite) and a low temperature modification (martensite). In particular, the complex microstructure in the low-temperature phase is responsible for the unique plastic deformation behavior. In the thermally or conventional shape memory alloys the plastic deformation is reset by heating upon the phase transformation temperature. Moreover, some materials allow magnetic control of the shape in the martensite. This means no heating is required here, which makes the process considerably faster. The direct manipulation of the shape by an external magnetic field is referred to as magnetic shape memory effect, or more precisely magnetically induced strain. Before reviewing the ba-

sic function principle of the effect for both materials, magnetic and conventional shape memory alloys, the characteristics of the phase transformation and the martensitic crystal structure will be discussed.

2.2.1 Phase transformation

Thermally activated structure changes in solids, such as alloys or compounds, usually result from diffusion of atoms. This is not the case for the structural phase transformation observed in Ni_2MnGa, which shows all characteristics of a martensitic transformation. Here the high-temperature phase called austenite transforms to the low-temperature martensite phase that features a reduced symmetry. The phase change is displacive and diffusionless, which means many atoms move in a cooperative, homogeneous way, but travel small distances only, i.e. less than the interatomic distances. Thus, the atoms maintain their relative relationships in the low-temperature phase. The most prominent alloy system that undergoes an austenite-martensite transformation is steel (FeC). In the Fe-rich austenite the crystal structure is cubic (bcc), while the martensite has a body-centered tetragonal lattice symmetry (bct). The martensitic phase emerges from the high-temperature modification by an athermal, cooperative shear process. The tetragonal distortion in the martensite is caused by the interstitial carbon atoms that amount to 0.2 - 2.0 % by weight depending on the steel type [35]. The phase transformation is of technological importance because martensitic steel features an increased hardness due to the characteristic microstructure. The heat treatment used to harden the steel involves heating above the austenite finish temperature (T_{Af}) and, subsequently, rapid cooling below the martensite start temperature (T_{Ms}). At elevated temperatures ($T > T_{Af}$) the carbon atoms can homogeneously distribute in the bcc Fe lattice by diffusion. The rapid cooling (quenching) is necessary to inhibit formation of the thermodynamically stable bcc ferrite (α-Fe) and Fe_3C precipitates. As the martensitic transition requires very little thermal activation, fast cooling below the transformation temperature leads to suppression of carbon diffusion. The C atoms are then trapped in the Fe bcc cell, when the a rapid rearrangement of atomic positions takes place, which slightly deforms the lattice to tetragonal. The increased hardness does not result directly from the crystal structure, but is a consequence of the microstructure. The martensitic steel is built up from platelets of lenticular shape that spread across the width of the individual crystallites. Adjacent platelets tend to grow perpendicularly to the existing ones, which leads to a nested structure generating the macroscopic hardness.

The complex microstructure clearly shows that the martensitic transformation is a phase transition of first order proceeding by nucleation and growth. When cooling below the martensite start temperature the collective shear process leads to formation of martensitic regions in the austenite lattice. As the temperature is further decreased, the martensite fraction increases. In the ideal case, like

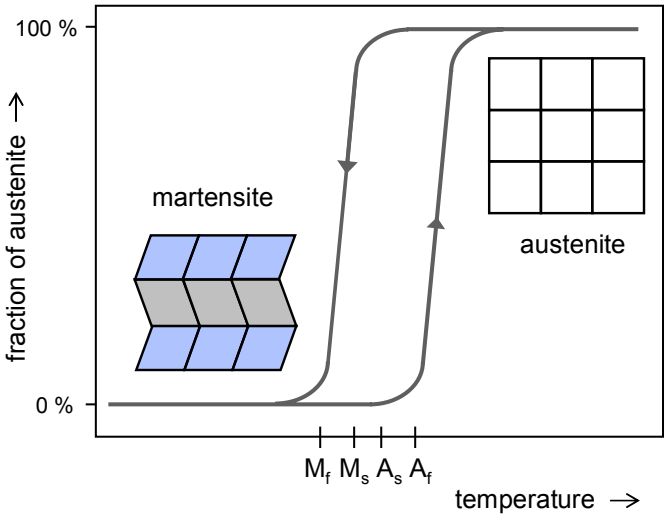

Figure 2.2: Illustration of the hysteretic behavior of the austenite-martensite transformation. On cooling the nucleation of martensite starts at T_{Ms} (martensite start temperature). The fraction of martensite increases until the complete sample is martensitic when reaching T_{Mf} (martensite finish temperature). On heating the transition to the high-temperature phase is characterized by the respective austenite start and finish temperatures T_{As} and T_{Af}.

illustrated in Fig. 2.2, the transformation stops at T_{Mf} (martensite finish temperature), as the complete volume features the martensitic lattice symmetry. On heating austenite nuclei begin to form at T_{As} and the re-transformation proceeds until at T_{Af} the high-symmetry phase is totally recovered. The observed discrepancy in start and finish temperature can be explained by internal friction of the phase boundaries that move through the crystal. At these phase boundaries the lattice mismatch of austenite and martensite causes an elastic deformation and hence a strain energy. This energy term can be reduced by forming an invariant lattice plane, a so called habit plane, at the phase boundary. The atoms of the habit plane do not move during the phase transition, meaning that this plane shows no distortion or rotation. The formation of such an invariant plane during the shear process requires either slip or twinning of the adjacent lattice planes. In particular, twinning is an effective mechanism to preserve the macroscopic shape of the crystallites or even a bulk single crystal, as will be discussed in the next section. Besides the occurrence of habit planes a characteristic feature of a displacive transformation is the (approximate) conservation of the unit cell volume upon phase change. The martensitic transition typically generates a symmetric lattice deformation that does not change the austenite cell volume significantly.

Furthermore, the transformation process shows a characteristic hysteresis that can be motivated by the thermodynamical description of the phase transition.

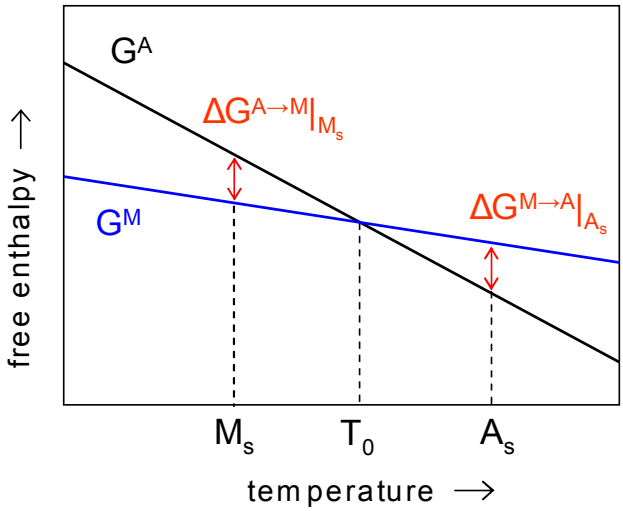

Figure 2.3: Free enthalpy of austenite (G^A) and martensite (G^M) as a function of temperature. At T_{Ms} (T_{As}, respectively) the difference in Gibbs free energy is the driving force of the phase transition. The two curves intersect at T_0 indicating the phase equilibrium $\Delta G = 0$.

To explain the occurrence of the phase transformation one has to consider the changes in free enthalpy. Fig. 2.3 shows schematically the free enthalpy as a function of temperature for austenite (G^A) and martensite (G^M). The different slopes of G^A and G^M result in two distinct regions of phase stability for $T < T_{Mf}$ and $T > T_{Af}$, respectively, where a single phase is observed (in the ideal material). Within the temperature interval $T_{Mf} < T < T_{Af}$ both phases coexist. When cooling a completely austenitic specimen, nucleation of martensite starts at T_{Ms} under the driving force of the difference in free enthalpy $\Delta G^{A\rightarrow M}|_{Ms} = G^M - G^A$. Similarly, on heating the difference in G drives the transformation from martensite to austenite starting at T_{As}. At T_0 where the curves intersect, the thermodynamical equilibrium between the two phases is reached ($\Delta G = 0$). The equilibrium temperature can be estimated by $T_0 \approx \frac{1}{2}(T_{Ms} + T_{As})$ [36]. T_0 is a suitable parameter to characterize the phase transformation and is referred to as the "phase transformation temperature" in the following. Because of the observed narrow hysteresis of typically 6 K for our samples (s. chapter 6.1.1), the difference between T_0 and T_{Ms} is small. Hence, the martensite start temperature can be used to generally characterize the transformation. In contrast to thermally driven phase transitions, the martensitic transformation requires only little thermal activation. Nevertheless, cooling below T_0 is necessary to provide the energy for the nucleation of martensite in the austenite matrix. The nucleation energy involves contributions of the interface energy and the energy needed to deform the surrounding lattice. In general, the change in free enthalpy during the phase

transition can be divided in two contributions [36, 37]:

$$\Delta G = \Delta G_c + \Delta G_{nc} \tag{2.1}$$

ΔG_c is the chemical Gibbs free energy, whereas the non-chemical part ΔG_{nc} comprises all energy contributions associated with the nucleation. At temperatures below T_{Ms}, where both phases coexist, and thus are in equilibrium ($\Delta G = 0$), ΔG_c is then exactly equal, but opposite in sign to ΔG_{nc}. Above T_{Ms} the chemical Gibbs free energy is too small to compensate ΔG_{nc}. Hence, undercooling ($\Delta T = T_0 - T_{Ms}$) is necessary to start the transformation. Likewise, the nucleation of austenite in the martensitic lattice requires superheating ($\Delta T = T_{As} - T_0$), which finally results in the observed hysteretic transformation behavior. In a real material lattice imperfections will cause an additional broadening of the hysteresis. So far, only the temperature induced phase transition has been discussed. For temperatures slightly above T_{Ms} it is also possible to induce the transformation from austenite to martensite by applying stress. The external stress field effectively shifts the martensite start temperature to higher values. This can be explained by the Gibbs free energy that takes the form:

$$\Delta G = \Delta G_c + \Delta G_{nc} - U \tag{2.2}$$

where U is the additional energy contribution caused by the external stress field. This contribution reduces the total energy, which means the transition can take place at a lower value of ΔG, meaning at a higher temperature (s. Fig. 2.3). The stress induced austenite-martensite transition is limited to a temperature interval $T_{Ms} < T < T_\sigma$, where T_σ defines the maximum temperature, for which a stress-induced transformation is observed. A direct relation between uniaxial stress σ and temperature is provided by the Clausius-Clapeyron equation [38]:

$$\frac{d\sigma}{dT} = \rho \frac{\Delta h}{\epsilon T} \tag{2.3}$$

Here Δh is the latent heat per atom, ρ the density and ϵ the strain during transformation. Furthermore, in the vicinity of T_{Ms} the martensitic transition can be induced by an external magnetic field. Due to the increased magnetic moment of the martensite, T_{Ms} can be shifted to higher values by applying a magnetic field [39]. The effect can be treated similar as the discussed case of applied external stress.

A theoretical description of the phase transformation from the crystallographic point of view was developed by Wechsler et al. [40] and, independently, by Bowles and McKenzie [41] in the 1950s. On basis of the lattice parameters and symmetry of austenite and martensite this theory describes the structural transition as a matrix product of rotation, shear and stretch operators. Assuming minimization of strain energy the macroscopic shape change $\mathbf{V}$ can be represented by a sequence of mathematical transformation applied to the parent phase lattice:

$$\mathbf{V} = \mathbf{B} \cdot \mathbf{R} \cdot \mathbf{P} \tag{2.4}$$

B describes the pure lattice deformation, that transforms the austenite to the martensite lattice parameters. To fulfill the orientation relation between the two phases, in addition, a rotation **R** and an inhomogeneous, lattice-invariant deformation **P** are required. The last factor involves either twinning or slip. As illustrated in Fig. 2.4, the homogeneous deformation (**B**) alone would result in a massive lattice mismatch of parent and product phase. This can be avoided by twinning or slip, which is described by **P**. The remaining operation, the rotation, is required to form a habit plane, which is relevant to match the two phases. If a lattice vector is increased in length by the pure deformation, it might be correspondingly decreased in length due to the application of **P** and **R**. A vector which remains invariant in length to these operations then defines a potential habit plane.

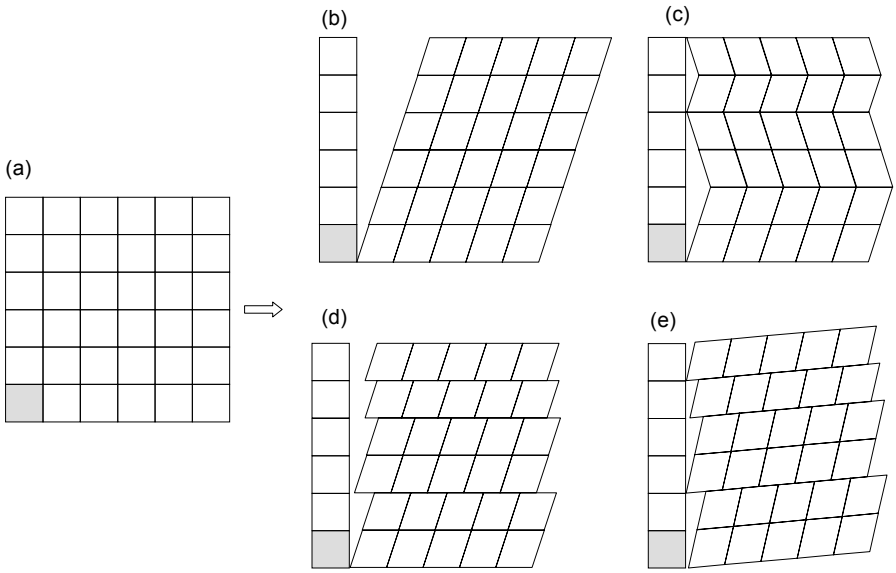

Figure 2.4: Schematic representation of a displacive transformation. The parent phase (a) can transform to the product phase by a homogeneous deformation (b), which results in large lattice mismatch. This can be avoided by either twinning (c) or slip (d). An increased matching of the two phases can be achieved by additional rotation of the product phase (e).

For shape memory materials the formation of habit planes that reduce strain energy between austenite and martensite is associated with twinning in the martensitic crystal. By forming different crystallographic variants separated by twin planes the product phase can adapt to the parent phase on both the microscopic and the macroscopic scale.

2.2.2 Twinning

Twinning occurs in a number of crystal systems and can lead to formation of macroscopic crystal areas showing a characteristic symmetry. Hence, in mineralogy the observation of twinning is a valuable diagnostics to identify the mineral type. The individual twins can be described as separate crystals that share some lattice points in a symmetrical manner. Because symmetry is added to the crystal by twinning, the process of twinning can be defined by the symmetry operations that are involved. If reflection across a mirror plane transforms the individual crystals into another, the added mirror plane is called a twin plane. The symmetry operation might also be rotation about a line in the lattice that then represents a twin axis. Furthermore inversion through a point, called twin center, can characterize crystal twins. In any case, the individual twins only differ in alignment, but feature identical lattice parameters and lattice symmetry. Hence, the different crystals separated by a twin boundary are referred to as orientational variants (also called crystallographic variants or briefly variants). In principle, three different types of twinning can be distinguished, i.e. primary twins and two basic types of secondary twins. Primary or growth twins form during crystal growth, whereas secondary twins are introduced either in response to mechanical stress (deformation twins) or result from a phase transformation. The latter type, called transformation twins, occurs when a crystal of high symmetry is cooled and converts to a lower symmetry structure, like during a martensitic transformation. The symmetry operation linking transformation twins is very frequently a rotation through π [42]. Depending on the symmetry of parent and product phase different twinning modes can occur. In NiTi, for example, the martensitic transition leads to a monoclinic structure that features several twinning modes, of which five are frequently observed [43]. However, in the case of Ni_2MnGa the martensitic transformation produces a crystal structure of tetragonal or (pseudo-)orthorhombic symmetry. In general, for a tetragonal or orthorhombic crystal the twin planes are considered to be commonly $\{110\}$ planes [42]. Indeed, the reported twin planes for martensitic Ni_2MnGa basically follow $\{110\}$ planes of the austenite [44, 45, 46]. These close-packed planes in the cubic parent phase can easily form an invariant plane that is simultaneously a twin plane separating two orientational variants [47]. Brown et al. argued that starting from the cubic parent phase the observed twin modes can be achieved by successive shear of $\{110\}$ planes along the respective directions (e.g. $[1\bar{1}0]$ for a (110) plane) [48]. The resulting modulated martensite structure can be described as tetragonal or (pseudo-)orthorhombic [49]. It is worth noting that a description of the twin planes in the reference system of the martensite lattice is possible but due to the reduced symmetry of this phase less comprehensible. Accordingly, in this work the cubic austenite lattice is used to describe the twin plane alignment and the associated variant configuration. Considering the symmetry of the austenitic unit cell, one can distinguish six equivalent $\{110\}$ planes as illustrated in Fig.

2.5. Each twin plane will link two martensite variants that both emerge from the parent phase, but differ in alignment of the crystal axes. The process of variant formation by twinning can be visualized by inspecting the lattice plane perpendicular to the twin plane (s. Fig. 2.6). For a $(110)_A$ twin plane the projection of the (hk)-plane contains two variants that differ in orientation of the short c-axis and the long a-axes. The third lattice vector, normal to the plane of projection, is identical for both variants. As can be seen from the illustration, the twinning process is accompanied by a lattice rotation needed to match the two variants at the twin boundary. In this simplified construction the third lattice vector can be considered as the rotation axis. Since each austenite $\{110\}$ plane can generate two martensite variants, in total 12 crystallographic variants result from this twinning mode. In addition, twin planes of lower symmetry might increase the total number of variants. In case of a true orthorhombic martensite structure ($c < b < a$) the occurrence of three principle twinning modes, a-b-, a-c- and b-c-twins, can extend the number of possible variants. However, for the (pseudo-) orthorhombic Ni_2MnGa martensite only a-c-twinning has been reported so far. In the following, only the discussed 12 variants resulting from $(110)_A$ type twinning will be considered, as they will represent the major portion of the martensite crystal for a cubic to tetragonal or (pseudo-)orthorhombic transformation.

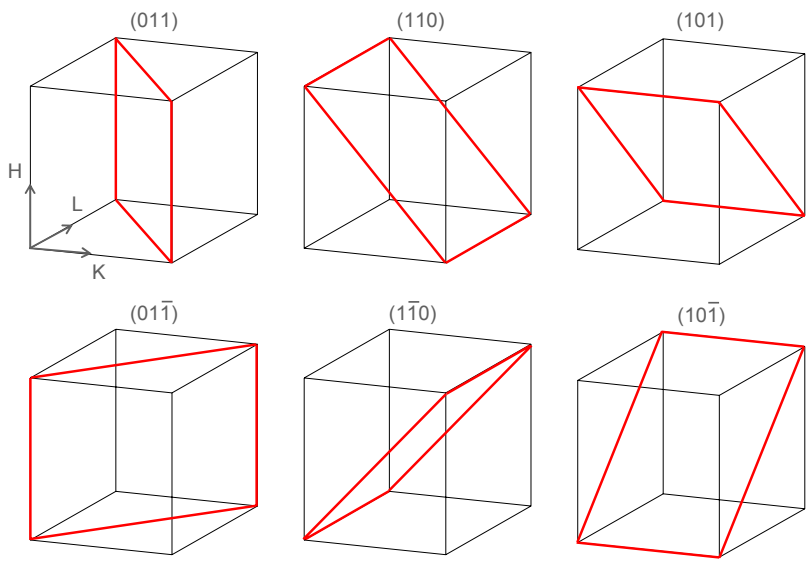

Figure 2.5: Illustration of the possible $(110)_A$ type twin planes that lead to a-c twinning in martensitic Ni-Mn-Ga. Each of the twin planes separates two variants that differ in alignment of a- and c-axis.

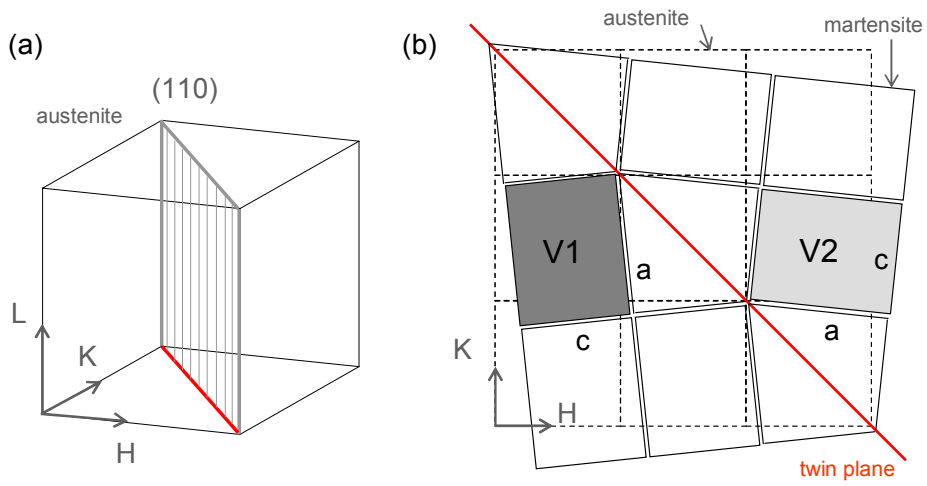

Figure 2.6: A twin plane derived from a (110) austenite plane (a) generates two martensite variants V1 and V2. The different orientation of the variants is illustrated in the (hk)-plane projection (b). The third lattice vector points out of the projection plane.

2.2.3 Thermal shape memory effect

As already mentioned, the thermal shape memory effect is based on the martensite-austenite phase transformation. The plastic deformation of the sample has to happen in the martensitic state, i.e. at temperatures below T_{Mf}. Subsequently, the shape recovery starts as the sample is heated to T_{As} and the restoration is finished at T_{Af}. A key role in the process plays the twinned microstructure of the martensite. The twin planes in a martensitic shape memory material are highly mobile and can move under the driving force of the applied stress. The macroscopic deformation of the SMA sample is in fact a redistribution of crystallographic variants via twin boundary motion. In the ideal case a single-variant state can be reached by detwinning. As the material is heated to T_{As}, the structural transformation affects all martensite variants and the twin planes vanish, as the lattice changes to cubic symmetry. An illustration of the shape memory effect is given in Fig. 2.7. The described process is the so-called "one-way memory effect". This means the shape restoration is achieved upon heating, whereas subsequent cooling below T_{Mf} leaves the shape unchanged. Under certain conditions a "two-way memory effect" can be achieved. Here the sample spontaneously deforms on cooling to temperatures below T_{Ms} into the shape that it had after the initial plastic deformation. This means the material remembers two different shapes (s. Fig. 2.7). Analog to the one-way effect, on heating the material remembers the shape of the parent phase. In addition, the shape of the martensite can be recovered, if a training procedure is applied to the sample.

The training involves successive heating-cooling cycles with (excessive) deformation in the martensitic state. During the deformation process dislocations in the martensite lattice are introduced, which stabilizes the actual martensite platelet configuration. These dislocations remain in the crystal lattice as the martensite disappears upon heating. On cooling re-nucleation of martensite plates proceeds in a similar way to accommodate the stress fields formed by the dislocations. Hence, the macroscopic shape in the low-temperature phase can be reproduced.

Another feature of many shape memory alloys is the superelastic or pseudoelastic behavior. This effect is based on the stress-induced transformation to martensite for temperatures $T_{Af} < T < T_\sigma$. While for temperatures above T_σ plastic deformation of the austenite is energetically favorable, below this temperature limit the stress is compensated by a partial transformation to martensite in combination with detwinning. Because the martensite fraction has been formed above T_{Ms}, the martensite reverts immediately to undeformed austenite as soon as the stress is removed. Thus, the sample shows a superelastic behavior. Similar to superelasticity, but not based on the stress-induced martensitic transformation is the so-called rubber-like behavior [50]. In this case, the restoring force for the deformation is not provided by the structural transformation, but by the short-range order configuration of lattice imperfections. The effect is observed for martensitic samples that have been aged in a stress-free state. During the aging atomic rearrangement within the same sublattice of the imperfectly ordered martensite takes place. If now stress is applied, the variant configuration is changed by moving twin boundaries. Similar to the martensitic transformation the variant redistribution is a diffusionless process. For the new variant configuration again atomic rearrangement in the sublattices would be required to reach equilibrium state. If the stress is removed in the distorted system restoration of the initial variant configuration appears, which explains the elastic behavior. The effect is not observed, when the loaded sample is aged, meaning atomic rearrangement is allowed to occur in the stressed sample.

2.2.4 Ferromagnetic shape memory effect

So far, only the thermally controlled shape memory alloys have been considered. Compounds that possess the ability of shape memory and, in addition, are ferromagnetic offer a further control mechanism, that is by a magnetic field. In principle, samples of this material class can be reversibly switched between two shapes without any heating or cooling required. In this actuation mode the shape manipulation completely takes place in the martensitic phase, which avoids the slow heating and cooling process that limits the operation frequency in a conventional shape memory alloy. In analogy to the described thermally driven process the shape change is based on a twin variant rearrangement associated with twin boundary motion. The difference is the driving force that is not an applied mechanical stress but the external magnetic field. To control the variant

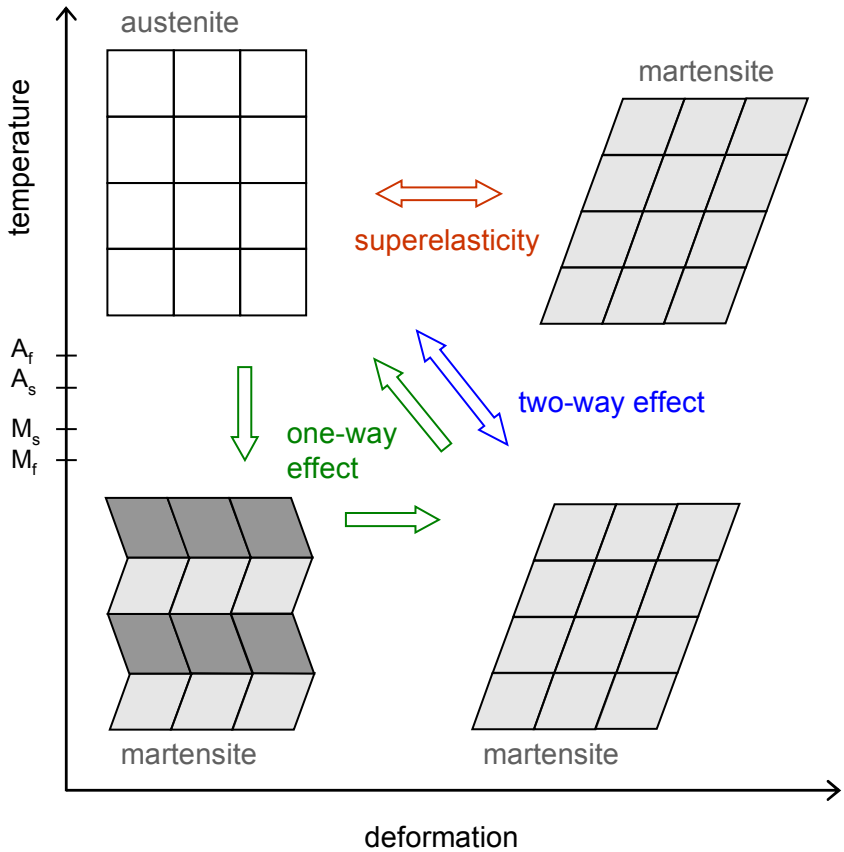

Figure 2.7: Sketch of the thermal shape memory effect. The one-way memory effect (green arrows) involves deformation of the martensitic sample by variant rearrangement. On heating the sample transforms to the parent phase and thus recovers the shape of the sample in the austenite. On subsequent cooling to the martensite no shape restoration is achieved. For a trained sample showing the two-way shape memory effect direct switching between two shapes, one in the austenite and one in the martensite is possible (blue arrows). At temperatures above T_{Af} a stress-induced martensitic transformation leads to an effect known as superelasticity or pseudo-elasticity. The deformation is based on variant rearrangement in the stress-induced martensite. As soon as the stress is removed the sample transforms back to austenite and hence recovers the original shape (red arrows).

configuration by an external field, a key requirement is a strong magneto-elastic coupling in the material. This means the compound has to have a considerable magnetocrystalline anisotropy that constrains the magnetization vector. In contrast to a conventional ferromagnet, for the MSM material it is more favorable to change the magnetization direction of a variant by twin boundary motion than by magnetization rotation. This, of course, requires that the energy to move a twin boundary is less than the magnetocrystalline anisotropy energy K_u of the martensite. Generally, a twin boundary motion can occur, if the energy difference between two adjacent twin variants ΔE exceeds the elastic energy needed to move the twin plane separating these variants:

$$\Delta E \geq \epsilon_0 \sigma_{TW} \tag{2.5}$$

where σ_{TW} is the twinning stress and $\epsilon_0 = 1 - c/a$ is the martensitic distortion. The excess energy can be an elastic energy due to an external stress, like in the deformation step for the conventional shape memory effect. Accordingly, a purely magnetic-field-induced twin boundary motion requires:

$$K_u \geq \epsilon_0 \sigma_{TW} \tag{2.6}$$

where the anisotropy energy K_u represents the maximum magnetic energy available. For many applications a combination of external stress σ_{ext} (e.g. from a bias spring) and magnetic field may be favorable. The condition for twin boundary motion then takes the form:

$$K_u \geq \epsilon_0 \sigma_{TW} + \epsilon_0 \sigma_{ext} \tag{2.7}$$

To illustrate and explain the process from a microscopic point of view a simplified two-variant model can be used (s. Fig. 2.8). The two variants emerge from the cubic parent phase by elongation of one lattice parameter and simultaneous compression of the second. The short c-axis is the magnetic easy axis in the system. Due to twinning the two variants, V1 and V2, are slightly rotated with respect to the lattice of the parent phase. The symmetry operation that transforms V1 into V2 is a rotation through $\phi = \pi \pm (\arctan(a/c) - \arctan(c/a))$ (depending on the rotation direction). Even for a strong tetragonal distortion of c/a=0.9 ϕ can be approximated by 90°, which simplifies considerations. In the case of strong magnetocrystalline anisotropy the magnetization vector for each variant will be aligned along the c-axis. For a system comprised of more than one variant the total magnetization will be composed of the magnetization contributions of the individual variants. In particular, the magnetization vector will change direction at a twin boundary, where different variants meet. The effect is indicated in Fig. 2.9 for the two-variant system with a single twin boundary. The state of lowest energy is the head to tail configuration that, in principle, allows flux closure. If now a magnetic field H_{ext} is applied parallel (or approximately

parallel) to the c-axis of variant 1, a Zeeman energy difference of $\Delta\mathbf{M} \cdot \mathbf{H}_{ext}$ arises. If rotation of M_2 is suppressed by the anisotropy energy, this difference in Zeeman energy represents a magnetic pressure on the twin plane. This pressure will induce boundary motion as soon as $\Delta M \cdot H_{ext} \geq \epsilon_0 \sigma_{TW}$ is valid. Similar to the process during the phase transformation a collective displacement of atoms mediates the twin boundary movement. As illustrated in Fig. 2.9 the twin plane moves through the crystal by sequential displacement of the atoms in the adjacent lattice plane. The propagation speed is in the order of the velocity of sound in the material, which makes the process much faster than the thermally induced shape change. In the ideal case, the magnetically induced redistribution of variants will result in a single-variant state. Moreover, the process is reversible, which allows to reset the magnetically induced variant rearrangement. Macroscopically the variant redistribution leads to an effective strain that can reach $\epsilon_0 = 1 - c/a$. In a real crystal, however, more than two variants and, accordingly, a number of twin planes will be involved. Nevertheless, considerable macroscopic strains can result, if the fraction of variants with c-axis aligned parallel to the external field can increase in response to the applied field. Fig. 2.10 depicts the effect of magnetically induced strain based on variant redistribution. It is worth pointing out that this type of shape control involves no phase transition. However, MSM alloys also show the conventional shape memory effect and thus can be used in applications using a combination of thermal and magnetic control. Moreover, another pure magnetically controlled process is possible for temperatures slightly above T_{Ms}. Here the shape change is triggered through the shift of the structural transition by the external magnetic field. When the field is applied, the sample transforms from austenite to martensite, which is reversed as soon as the field is removed. The process is called magnetic field-induced martensite (MIM) and has to be distinguished from magnetic field-induced reorientation of variants (MIR). Quite general, the macroscopically observed shape change in response to an external field is described as magnetic field-induced strain (MFIS). In the context of this work MFIS means the macroscopic strain that originates from the microscopic MIR process in the martensitic state.

A quantitative treatment of the described two-variant model was presented by O'Handley [51]. In addition to the Zeeman energy and uniaxial anisotropy energy, the model incorporates an elastic-energy density $E_{el} = C\epsilon_0^2$, where C is the effective stiffness of the material. This energy term accounts for the internal resistance to twin boundary motion. Despite the effective two-dimensional approach, the model is able to describe the observed nonlinearities for both $\epsilon(H)$ and $M(H)$. Moreover, three regimes of magnetocrystalline anisotropy strength are discussed. For $K_u > \Delta M \cdot H_{ext}$ the previously described variant rearrangement occurs. In the case of weak anisotropy the model predicts a rotation of the magnetization vector in those variants that are not oriented with their easy axis parallel to the field. The driving force on the twin boundary is then the magnetic anisotropy energy difference, which is to small to induce twin boundary motion.

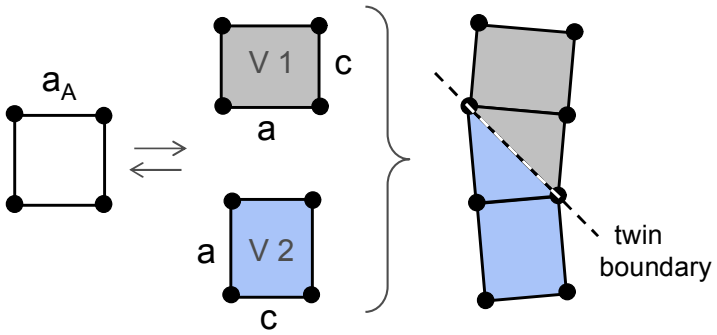

Figure 2.8: Two-variant model: Projection of the two martensite variants, V1 and V2, that arise from deformation of the cubic parent phase. To link the variants by a twin plane a slight rotation is required. For each variant the short c-axis is the magnetic easy axis.

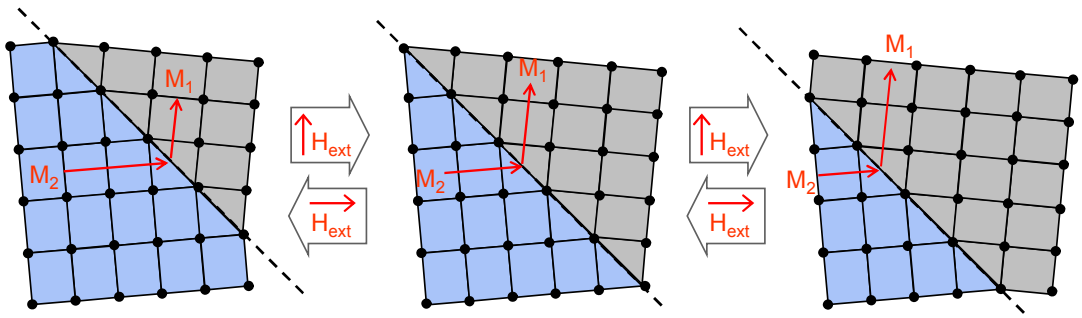

Figure 2.9: Illustration of the magnetically controlled variant redistribution in a MSM material. Under the driving force of the external field H_{ext} the twin boundary separating V1 and V2 moves through the crystal. The reversible process is based on collective displacement of atoms adjacent to the twin boundary.

Finally, an intermediate case with $K_u \approx \Delta M \cdot H_{ext}$ is considered. Here, the applied field produces both effects. In detail, the Zeeman pressure on the twin plane dominates for low field values, as the field strength is not sufficient to rotate the magnetization. At stronger fields a significant rotation of the magnetization vector can reduce the pressure on the twin plane, which in some cases may cause a reset of the variant reorientation. A model applicable to a MSM sample that is simultaneously exposed to mechanical stress and a magnetic field is provided by Murray et al. [52]. By calculating the balance between magnetic energy input and mechanical work output the model provides predictions of the materials response under both field and load. Besides the conventional axial actuation mode, also shear actuation is considered. A quantitative model for magnetostrain effects based on thermodynamic considerations was published by Likhachev and Ullakko [53].

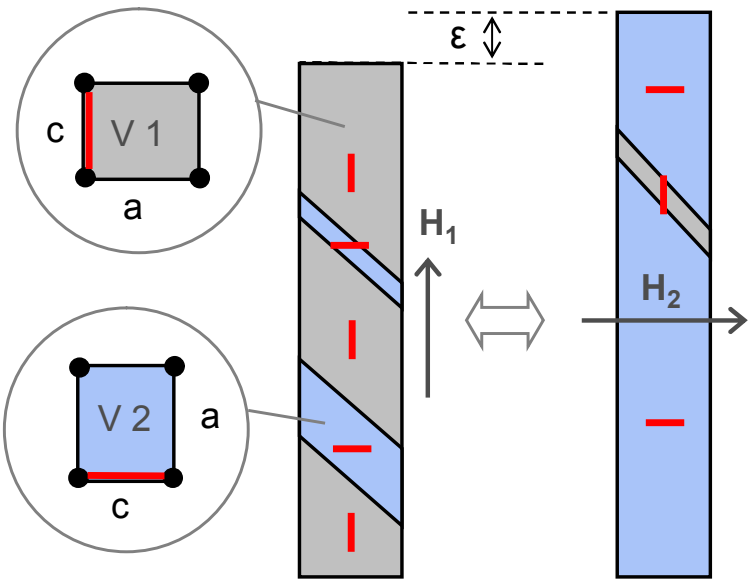

Figure 2.10: The variant redistribution associated with twin boundary motion results in a macroscopic strain ϵ. When exposed to a magnetic field, the fraction of variants with lower Zeeman energy increases in cost of the neighboring variants of higher magnetic energy. This produces an effective alignment of the magnetic easy axis that is the short crystallographic axis (c-axis) with the external field. Image adapted from [54].

Regardless of which model is used, the requirements for a MSM material to show magnetically induced strains can be summarized as follows:

- A high magnetocrystalline anisotropy to avoid rotation of the magnetization
- A large saturation magnetization to increase the difference in Zeeman energy across a twin boundary at a given value of H_{ext}
- A low twinning stress to promote twin boundary motion
- To achieve large strains a large martensitic distortion $\epsilon_0 = 1 - c/a$ is needed
- Concerning applications, a high martensite start temperature and a high Curie temperature are of importance

In case of Ni_2MnGa many of these characteristics can be manipulated by changing the composition, which makes the compound an interesting candidate for various applications.

2.3 Properties of the system Ni-Mn-Ga

The diverse structural and magnetic properties of Ni-Mn-Ga will be reviewed in this section. In particular, results obtained on bulk samples and the treatment by ab initio theory are discussed.

2.3.1 Crystal structure

In the high-temperature phase Ni_2MnGa has the characteristic Heusler structure, the cubic $L2_1$ structure (s. Fig. 2.11 (a)). The fully ordered structure can be obtained from the melt directly or via the partially disordered B2' phase [55]. For the stoichiometric compound the austenite structure is stable down to a temperature of ∼200 K, before the martensitic transformation sets in. For the low-temperature modification a modulated tetragonal phase is observed [32]. However, high-resolution neutron diffraction experiments indicate that the martensitic structure features an orthorhombic symmetry rather than a tetragonal one [56]. Hence, the crystal symmetry and space group of the martensite is still a subject of controversy. The situation becomes even more complex for off-stoichiometric Ni-Mn-Ga samples. Three martensitic crystal structures are frequently reported, i.e. the non-modulated tetragonal phase (NM), the modulated tetragonal phase (5M) and the modulated (pseudo-)orthorhombic structure (7M). As indicated by the acronyms the modulated phases possess a periodicity of 5 and 7 atomic layers, respectively. The construction of the 7M structure is illustrated in Fig. 2.11. The basal plane of the superstructure can be derived from the (110) plane of the parent phase. Then the modulation appears along the [110] martensite

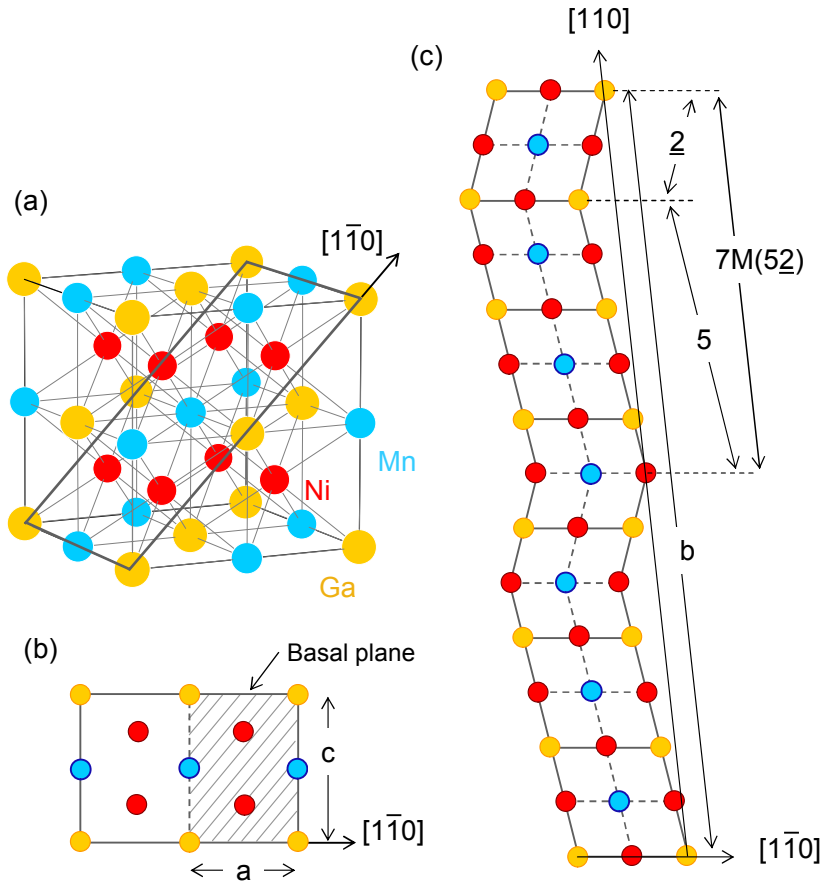

Figure 2.11: Representation of the modulated orthorhombic structure with a period of 14 layers. From the (110) plane of the cubic parent phase (a) the basal plane of the superstructure can be derived (b). Along [110] in the martensite lattice a periodic shuffling of the atomic layers occurs (c). The stacking sequence of (5$\underline{2}$) results in a periodicity of 14 layers. Though the full symmetry is included in the 14M cell only, the structure is referred to as 7M widely.

direction as symmetric shuffling of the atomic layers. As indicated the stacking sequence is usually (5$\underline{2}$). Since the first and the seventh atomic layer are not identical, the proper description is in fact 14M and not the widely used 7M. Similar to the 14M structure the 10M structure follows from the 5M structure by doubling the unit cell. The modulation plays an important role for the mobility of twin planes. According to that, the largest strains have been observed for bulk samples with 5M [3] or 7M/14M structure [4]. In the latter case the sample composition was determined to be $Ni_{48.8}Mn_{29.7}Ga_{21.5}$, whereas the 5M specimen was close to a $Ni_{48}Mn_{31}Ga_{21}$ composition. This demonstrates that the crystal structure of the martensite is extremely sensitive to composition. A sys-

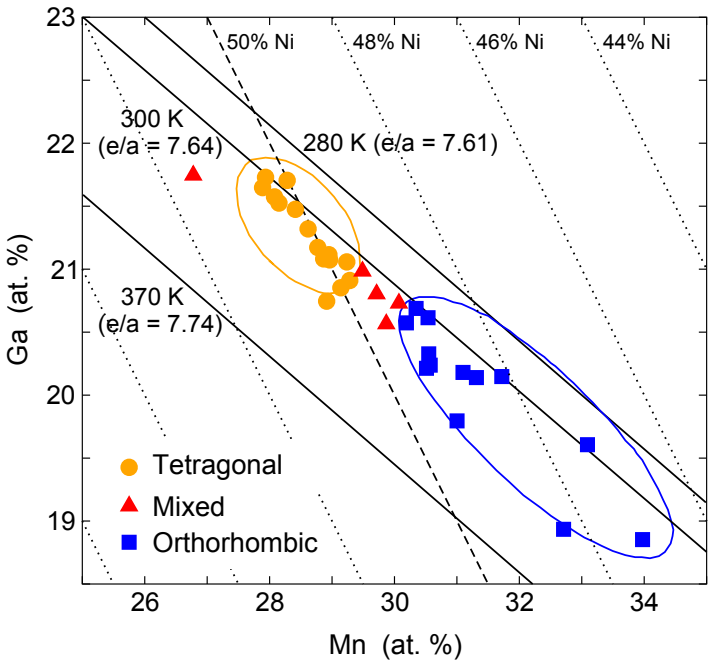

Figure 2.12: Phase diagram of the $Ni_{2\pm x\pm y}Mn_{1\mp x}Ga_{1\mp y}$ martensite system. In the (Mn, Ga)-composition plane the zones of tetragonal and orthorhombic lattice symmetry are clearly separated. At the intersection a region of mixed symmetry is observed. Solid lines indicate the martensite transformation temperatures, broken lines denote the Ni content. Image taken from [9].

tematic study of the composition-structure relationship in bulk samples has been conducted by Richard and co-workers [57]. The resulting phase diagram for the system $Ni_{2\pm x\pm y}Mn_{1\mp x}Ga_{1\mp y}$ is shown in Fig. 2.12. This slightly modified version was taken from the review article by Entel et al. [9]. The phase diagram reveals two distinct regions, one of tetragonal and one of orthorhombic symmetry, as a function of Mn excess and Ga deficiency. Where the two band-like regions meet, a small zone of mixed symmetry is observed. Based on first principles calculations a general trend for the structural stability as a function of e/a can be derived [58]. With respect to the stoichiometric compound with e/a=7.5 a reduction of the electron concentration stabilizes the modulated phases. In contrast, the non-modulated tetragonal martensite is favored in compositions with increased e/a. These trends are confirmed by experimental results from various samples (s. ref. [58]).

It is worth noting, that the designation of the martensitic crystal structures is not consistent in literature. In particular, the description of the tetragonal 5M structure does not follow the standard notation in crystallography. Commonly, the tetragonal unit cell is characterized by $a = b \neq c$ with c being the long axis.

In the case of Ni_2MnGa, however, the c-axis denotes the short axis, while a is the long lattice vector [59]. During the martensite transformation the cubic unit cell is contracted along one $\langle 100 \rangle$ axis and extended along the other two resulting in a tetragonal cell with $c < a = b$. In contrast, the common notation for the non-modulated tetragonal phase is $a < c$.

For some samples the martensite structure shows a further reduced symmetry that is described by a monoclinic unit cell. For example, compositions close to $Ni_{55}Mn_{20}Ga_{25}$ can exhibit a metastable tetragonal phase that transforms to a modulated monoclinic structure after one heating-cooling cycle [60]. A slight monoclinic distortion is occasionally observed for the orthorhombic structures as well, but can be neglected in most cases. Furthermore, recent observations on thin film samples of mixed NM and 7M/14M structure indicate that the modulated phase is a metastable, adaptive phase that can be constructed from the non-modulated tetragonal cell [61]. As a consequence, the 7M/14M structure has not a true orthorhombic but a pseudo-orthorhombic symmetry. Nevertheless, the (pseudo-)orthorhombic lattice that is derived from the cubic austenite is helpful in the evaluation of diffraction experiments.

In any case, tetragonal, orthorhombic or monoclinic lattice symmetry, the decisive prerequisite for large strains in response to a magnetic field seems to be the modulation. Because of the high twinning stress, no magnetically induced strains have been observed in the NM phase [59]. The large strains obtained for the modulated martensites can be motivated by the previously described two-variant model. For the (pseudo-)orthorhombic structure the 2D lattice in figures 2.8 and 2.9 represents a projection along the intermediate b-axis.

For the tetragonal martensite the situation is more complex, because of the two equivalent long crystal axes. As a consequence, an untreated sample will exhibit a variant ensemble that features two different $a - c$ twin modes. To align the short crystal axis a magneto-mechanical training may be required. As soon as the short c-axis is fully aligned by mechanical load or magnetic field, the effect can be treated by the model as indicated in Fig. 2.9.

2.3.2 Magnetism

The mechanical properties like the twinning stress σ_{TW} are essentially determined by the crystal structure and variant configuration. The second basic requirement for the MSM effect is the coupling of magnetization and crystal structure, in other words the magneto-crystalline anisotropy. In austenitic Ni-Mn-Ga this anisotropy is low, that means in the order of 10^3 J m^{-3}. This is changed by the transformation to the martensite phase that is accompanied by a magnetic anisotropy increase of two orders of magnitude [62, 63]. For the tetragonal crystal symmetry the anisotropy can be described by:

$$E_{aniso} = K_1 \sin^2\theta + K_2 \sin^4\theta + K_3 \sin^4\theta \cos\phi \tag{2.8}$$

with θ and ϕ denoting the polar and azimuthal angle of the magnetization vector with respect to the c-axis. In practice, the magnetic anisotropy of the 5M tetragonal martensite can be considered as uniaxial. Heczko and co-workers reported a ratio of $K_2/K_1 \approx 0.04$ [64]. Accordingly, the second anisotropy constant is negligible and the anisotropy can be approximated by

$$E_{aniso} = K_u \sin^2 \theta \tag{2.9}$$

with the uniaxial anisotropy constant K_u. Typical values for 5M bulk samples are (1.2-2.0)$\times 10^5$ J m^{-3} at ambient temperature [59]. In a similar way, the magnetization dependence in the orthorhombic phase can be characterized by two anisotropy constants K_b and K_c related to the b- and c-axis. Again, the magnetic easy axis is the short c-axis, while the long a-axis is hardest to magnetize. The b-axis is of intermediate character. When considering a single-variant state, the anisotropy energy takes the form:

$$E_{aniso} = K_c \cos^2 \theta + K_b \sin^2 \theta \sin^2 \phi \tag{2.10}$$

For bulk samples with 7M martensite structure the reported values are in the order of $K_c = -1.7 \times 10^5$ J m^{-3} and $K_b = -0.8 \times 10^5$ J m^{-3}, respectively [65] [1]. Likewise the 5M and 7M structure in the non-modulated martensite the longest crystal axis is the magnetic hard axis. In contrast to the modulated phases this is the c-axis in the NM phase. Thus, an easy plane of magnetization is present in this structure.

Besides the magnetocrystalline anisotropy, the saturation magnetization is a decisive parameter in the variant reorientation process. In the highly anisotropic MSM material the driving force for twin boundary motion is the difference in Zeeman energy across the twin plane. For a given value of the applied magnetic field the driving pressure on the twin plane scales with the saturation magnetization. Accordingly, a large saturation magnetization allows to reduce the external field. Neutron diffraction experiments show that the magnetic moment is mainly localized at the Mn sites [32, 66]. The total moment amounts to 4.2 μ_B per formula unit, while the contribution of the Ni atoms is in the range of 0.2 to 0.4 μ_B only. Although the magnetic moment of Ni is considerably smaller, the magnetic anisotropy is governed by the Ni atoms. According to ab initio calculations the magnetic coupling is mainly between atoms of the same species. While the Mn sublattice carries the spin moment, the anisotropy is largely attributed to Ni atoms [67]. The Ni sublattice also plays an important role in the structural stability of the $L2_1$ phase [58]. Accordingly, the changes in the electronic structure that manifest in the martensitic transition affect mainly Ni related states.

[1] In this publication the othorhombic structure is characterized by an anisotropy constant K_a assigned to the long a-axis, instead of K_c. Due to the crystal symmetry ($a \perp c$) this description is equivalent with $K_c = -K_a$ and a shift of the energy scale.

2.3.3 Phase transition and compositional dependence

Among the major objectives of theoretical studies are explaining the structural instability observed in Ni_2MnGa and modeling the phase diagram of the complex Ni-Mn-Ga system. There is interest in predicting the martensite structure and the phase transformation temperature. Besides T_{Ms}, also the compositional dependence of the Curie temperature is important. Two basic approaches can be found in literature, namely first principle methods like density functional theory [68] and phenomenological concepts using a Ginzburg-Landau expansion [69]. In particular, studies based on the latter approach are able to reproduce the experimentally observed phase diagrams. Figures 2.13 and 2.14 show two examples taken from a review article that collected data from various publications [9].

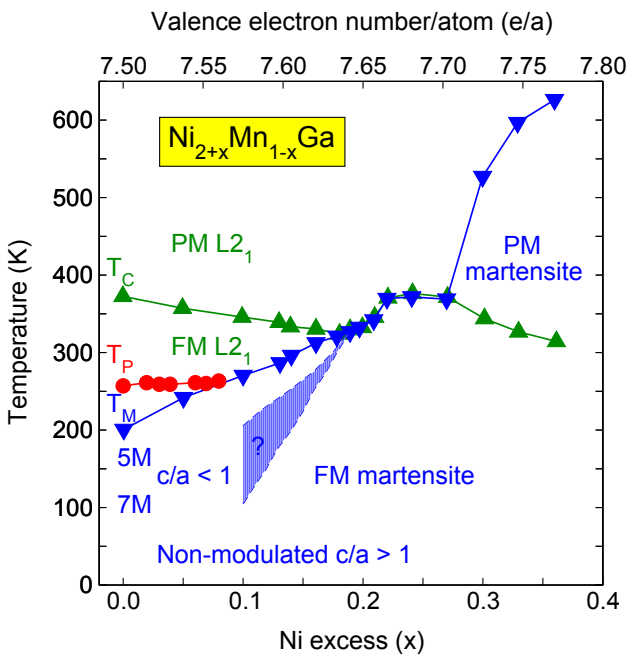

Figure 2.13: Phase diagram of $Ni_{2+x}Mn_{1-x}Ga$ in dependence of the Ni excess. The region of paramagnetic (PM) and ferromagnetic (FM) order are separated by the T_C curve (green line). A strong compositional dependence is observed for the martensite start temperature (T_M, blue line). For samples close to Ni_2MnGa composition, in addition, a pre-martensitic transition is observed at T_P. Image taken from [9].

Obviously, both T_C and T_{Ms} depend sensitively on the sample composition. However, the martensite transformation temperature shows a more pronounced composition-dependence. If Mn atoms are replaced by Ni, an increase in T_{Ms} is observed (s. Fig. 2.13). The effect is more severe for high Ni-excess ($x > 0.25$), but the resulting martensite is not ferromagnetic. Furthermore, the Ni-

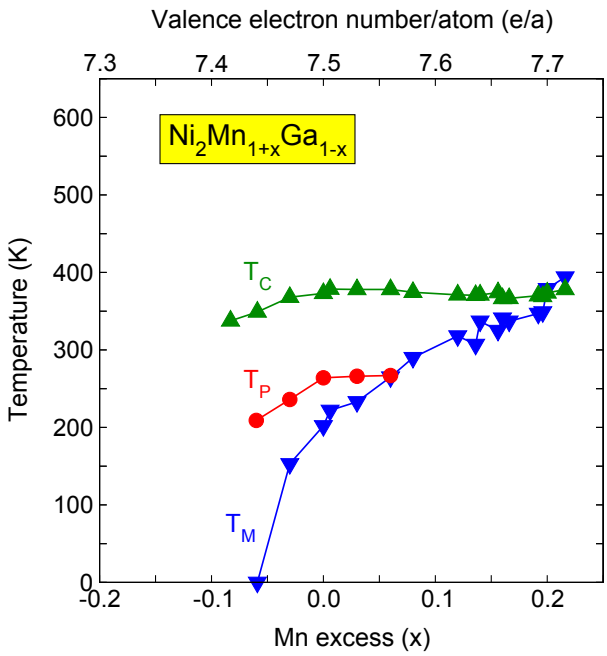

Figure 2.14: Phase diagram of $Ni_2Mn_{1+x}Ga_{1-x}$ as a function of the Mn excess. While T_C stays almost constant for $0 < x < 0.2$ the martensite start temperature considerably increases as a function of Mn excess. For small Mn deficiencies a strong decrease of T_M appears. Image taken from [9].

rich compositions possess a high valence electron concentration leading to the non-modulated martensite structure. Consequently, these alloys are not suitable for MSM applications. A high martensite start temperature can also be achieved by substituting Ga by Mn atoms (s. Fig. 2.14). Not included in the displayed phase diagrams is the case of replacing Ni by Mn while keeping the Ga content fixed. In general, a combination of all three cases will result in the complex system $Ni_{2\pm x\pm y}Mn_{1\mp x}Ga_{1\mp y}$. An empirical rule that describes the behavior of T_{Ms} as a function of e/a was established by Chernenko [70]. For $e/a < 7.7$ the transition temperature increases with valence electron concentration with a coefficient of roughly 900 $K(e/a)^{-1}$. For compositions with an electron concentration of $e/a \geq 7.7$ this coefficient is in the order of 500 $K(e/a)^{-1}$.

A first step in explaining the structural instability of the cubic parent phase is calculating the equilibrium lattice parameters of the martensite. The stability of the non-modulated phase is successfully explained by first principles atomistic calculations within the density functional theory. These studies identify the NM structure with $c/a > 1$ as the absolute energy minimum for low temperatures [71]. To reproduce the minima leading to the modulated phases with $c/a < 1$ the modulated "supercells" (s. Fig. 2.11) have to be taken into account [72]. However, there is disagreement between different theoretical studies about the

lattice constants of the martensitic phase.

In addition, ab initio calculations give valuable information on the source of the instability of the cubic $L2_1$ phase in Ni_2MnGa. In particular, the transition to the modulated phases with $c/a < 1$ is ascribed to a band Jahn-Teller mechanism [66]. The driving force for the phase transition is a redistribution of electrons around the Fermi level that lowers the free energy of the system. The electron redistribution is enabled by splitting of energy sub-bands, which are degenerate in the high temperature phase. Electronic structure calculation show distinct changes in the band structure arising from the reduced lattice symmetry [73]. In detail, the reduction of symmetry causes a peak splitting in the Ni related minority density of states. For $c = a$ the Fermi level lies just above a peak in the Ni minority-spin band. For $c/a < 1$ this peak splits up, which leads to a reallocation of states stabilizing the tetragonal distortion. A further approach to explain the microscopic origin of the phase transition is studying the phonon dispersion and lattice instabilities in the cubic parent phase. Inelastic neutron-scattering experiments on Ni_2MnGa found a significant softening in the TA_2 phonon branch along the [110] direction [74]. This softening is considered to give rise to the modulated crystal structure and precursor effects, i.e. pre-martensitic transitions. The origin of the phonon softening is discussed in the context of strong electron-phonon coupling and Fermi surface nesting [9, 75]. Since stable Heusler compounds do not show softening of the TA_2 shear mode, calculations of the phonon spectrum are useful to identify new potential MSM materials. Zayak and co-workers have studied chemical trends in the structural instability of the cubic structure for several Heusler compounds [76]. These results indicate that a number of Ni-based alloys feature an unstable $L2_1$ phase, such as Ni_2MnX (X = Al, Ga, In, Ge) or Ni_2CoX (X =Al, Ge, Sb), while for example Co_2MnGa is stable against a martensitic phase transformation.

Chapter 3

Experimental details

In this chapter the essential experimental details will be summarized. Especially, the preparation process of the thin film samples will be described. This includes a brief description of the deposition method in general, specifications of the preparation chamber and the used materials, i.e. targets, substrates, etc. A key issue in sample preparation is the feasibility of releasing the thin film from the substrate. The different approaches pursued in this work will be presented. This includes the fabrication process that gives access to partially freestanding structures like micro-bridges and -cantilevers. Furthermore the standard characterization methods to investigate the sample properties are introduced. The epitaxial growth of the Heusler compound is controlled by X-ray diffraction (XRD) in Bragg-Brentano geometry. Low angle x-ray reflectometry is used to determine the film thickness of selected samples. This allows to calculate the deposition rate with reasonable accuracy. The saturation magnetization and the phase transformation can easily be checked for a number of samples with magnetometry measurements. The complex crystal structure of the martensite is studied using XRD in 4-circle geometry. The techniques to image the film surface involve optical, atomic force, and scanning electron microscopy.

3.1 Thin film sample preparation

When speaking of thin films the layer thickness is typically in the range of several nm to few hundred nm. Films consisting only of a few monolayers are denoted as ultrathin layers. These can show interesting features like ferromagnetic frustration [77]. It is very likely that the structural phase transformation in Ni-Mn-Ga will be suppressed for films below a critical thickness due to the collective nature of the phenomenon. Especially, for applications rather thick films can be advantageous because of practical reasons. A film thickness of 0.5 to 2 μm makes handling of freestanding Ni-Mn-Ga films possible. The samples investigated in the course of this work have been prepared by sputter deposition onto heated single crys-

talline substrates as MgO, Al_2O_3, and NaCl. The deposition technique enables effective film preparation with high deposition rates and good reproducibility. The film thickness is typically between 50 and 100 nm. This allows for X-ray reflectometry measurements to determine the thickness precisely. Thus, saturation magnetization of the samples can be calculated from hysteresis loops. In addition, rather thin films make measurements in transmission possible. However, the high deposition rates of the sputtering process allow for effective preparation of thick films, too. These are suitable for experiments that require separation of the film from the rigid substrate. To enable magnetically induced reorientation of variants in the Ni-Mn-Ga film blocking effects of the rigid substrate have to be eliminated.

3.1.1 Sputter deposition

The term sputter deposition describes a physical vapor deposition technique where material is ejected from a target and condensed on a substrate surface. The evaporation process is driven by ion bombardment of the target surface. The target is mounted on a cathode that is electrically insulated against the vacuum chamber on the inner part. The outer part of the cathode, the shield, as well as the chamber walls are grounded. An applied dc voltage leads to formation of a plasma of the working gas that is introduced into the chamber. For metallic compounds this is usually Argon. The ionized Ar atoms are accelerated towards the cathode and finally hit the target surface. The result is a direct current (dc sputtering) between target and the cathode shield. The Ar ions that hit the target surface eject atoms and small clusters of the target material. The basic principle is sketched in Fig. 3.1 (c). A more detailed description is provided by [78, 79].

The energy distribution of the evaporated atoms has a wide range up to tens of eV. Due to collision with the atoms of the sputtering gas the target atoms move diffusively towards the substrate. Thus, impact of high energy atoms is suppressed. The working pressure is an important parameter that affects the deposition rate directly. A higher Argon pressure leads to a decreased deposition rate since the effective travel distance for target atoms undergoing a random walk is increased. For an alloy target the pressure of a given sputtering gas also influences the stoichiometry of the deposited film. Since different elements can have different diffusion rates the composition of the sample can be altered by the working pressure. Furthermore the evaporation rates for the different elements of the alloy target can differ. This is compensated by a period of pre-sputtering prior to deposition. Different evaporation rates will lead to different concentrations of the elements at the target surface. At some point a steady state is reached since a high evaporation rate produces a lower surface concentration. Thus, the rate is reduced for this element. For an electrically conducting target material, such as Ni-Mn-Ga, a dc power supply can be used to drive the process. In contrast,

a dielectric target will need a radio frequency power supply (rf sputtering). A charge build-up at the insulating target surface is avoided by the alternating bias voltage applied to the target. For high frequencies (MHz range) only the electrons can effectively move and follow the electric field. The Ar^+ ions can be considered stationary due to their low charge to mass ratio. This leads to an accumulation of electrons at the target that will consequently attract the Ar^+ ions. For both types of sputtering the deposition rate can be increased by introducing a set of permanent magnets at the target back side. Two ring magnets create a radial field at the target surface that forces the electrons on a helical path. This increases the ionization yield and thus the sputtering rate. The technique is referred to as magnetron sputtering. Typical deposition rates achieved with this method applied to Ni-Mn-Ga targets are 1.0-1.5 nm/s, which enables fast preparation of thick MSM layers.

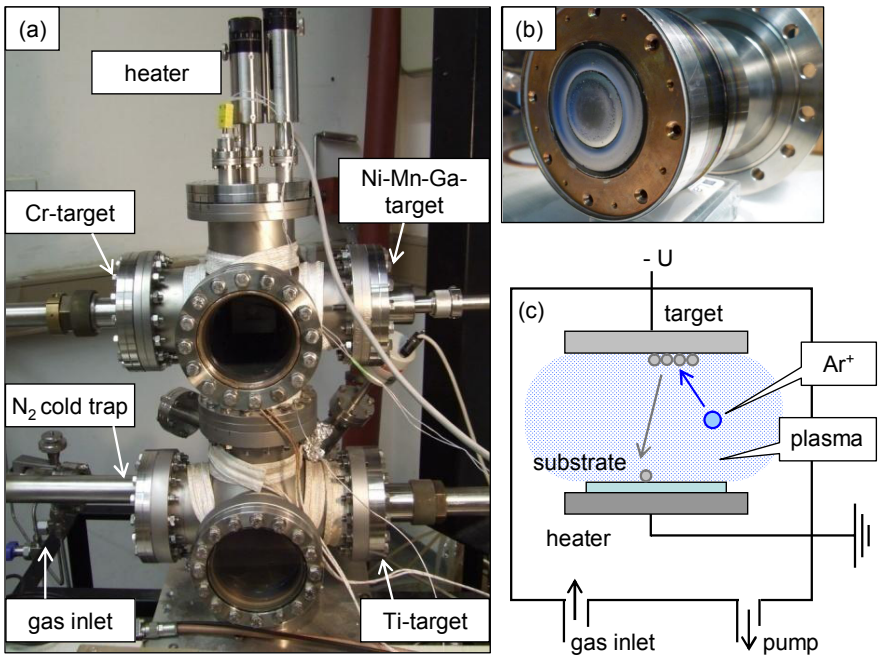

Figure 3.1: (a) Image of the deposition chamber equipped with different sputtering guns. (b) Image of a Ni-Mn-Ga target mounted on cathode. The ring-shaped erosion zone is produced by the magnets on the target back side (c) Sketch of the sputtering process.

To prevent oxidation of the evaporated metals during the deposition process low partial pressures of oxygen and water are necessary. For this reason sample preparation is done in a high vacuum chamber. Fig. 3.1 (a) shows an image of the used setup. The preparation chamber consists of two 6-way-crosses of tubes

with 4 inch outer diameter. Two of the twelve 6 inch CF flanges are connected forming the center of the chamber. At the bottom side a turbomolecular pump and a pre-pump are attached. The lower cross contains the pressure sensors, the Ar gas inlet, a liquid Nitrogen cold trap, a Titanium sputtering gun and a control window. Another window to monitor the sputtering plasma is mounted in the upper half, where the film preparation is done. Here three cathodes can be equipped with different targets. The rotatable resistive heater unit seals the chamber from the top. The base pressure of $10^{-7} - 10^{-8}$ mbar is measured with a penning gauge, while the Argon gas pressure during sample preparation is monitored with a capacitance vacuum gauge. After venting the chamber to load substrates a base pressure of $3 - 4 \cdot 10^{-7}$ mbar is reached within 24 hours. This proved to be sufficient for sample preparation. A lower base pressure of $\sim 5 \cdot 10^{-8}$ requires a bakeout procedure or an extended evacuation time. During deposition the cold surface of the liquid N_2 cold trap in the lower chamber half effectively decreases oxygen and water partial pressures. The gas molecules adsorb to the cold surface and the water freezes out. Additionally, the highly reactive Ti atoms evaporated from the sputtering gun facing the cold surface bind oxygen forming TiO_2. The surrounding chamber walls and the cooled surface act as a getter pump, because they are permanently coated with Ti. Furthermore, the gas inlet is designed such that the Ar gas passes the cold trap surface. Thus, residual water and oxygen in the high purity (6.0) Argon is removed effectively. The three cathodes in the upper cross are equipped with Ni-Mn-Ga targets of different composition and, if required, with a Chromium, iron or aluminum target. The Cr and Fe is used for depositing a buffer layer while Al serves as capping layer to prevent oxidation after removing the sample from the vacuum chamber. Samples prepared for surface sensitive measurements like X-ray absorption spectroscopy (s. Chapter 6) are protected by a 2-6 nm thick Al cap layer.

Preparation protocol:
The first step in the sample preparation process is filling the cold trap with liquid N_2. Subsequently, the substrates glued on the heater block with conducting silver are heated to typically 500 °C. During the heating-up the pressure rises, as gas molecules are desorbed from the heater and substrate surfaces. After a holding time of 40 minutes the pressure reaches again the base level and the substrate temperature is stable. Now the speed of the turbomolecular pump is decreased from 57000 rpm to 12000 rpm and Ar gas is introduced into the chamber. With a needle valve the Ar pressure is adjusted to typically 0.02 mbar and the Ti sputtering gun is started ($I = 50$ mA, $U \sim 250$ V). A second dc power supply drives the Ni_2MnGa plasma with a current of 100 mA and a bias voltage in the range of 300 V. After a pre-sputtering period of 10 minutes the heater unit holding the substrates is rotated towards the cathode and the deposition process starts. To stop deposition the power supply is switched off. The heater current is shut down immediately, the Ti plasma switched off, the gas flow is stopped and the

pump speed increased to 57000 rpm again. After a cooling time of 1.5 h the Al cap layer is applied. The sample temperature is then in the range of 100-120 °C. This cooling period is necessary to prevent interdiffusion of Al and Ni-Mn-Ga. X-ray absorption spectroscopy (XAS) revealed the formation of NiAl at the film surface when the Al layer is deposited at elevated temperature [80]. Further details on the XAS experiments are provided in chapter 6. To sputter the Al a rf power supply is used. For a sputtering power of 20 W (reflected power = 0) a deposition time of 40 s results in a 3 nm thick cap layer. In order to release the films from the rigid substrate a sacrificial Cr layer was introduced for a number of samples prepared on MgO(100). Here the Cr layer is deposited on the heated MgO first. As soon as the Cr plasma is switched off, the pre-sputtering and, subsequently, the deposition of the Ni-Mn-Ga is started. To avoid cross-contamination the Ni-Mn-Ga target is mounted opposite to the Cr cathode (180° configuration). Thereby the heater unit covers the cathode not in use. The third cathode is covered by a metal cap. A cathode configuration of only 90° would cause mixing of the evaporated elements. Typical preparation parameters for the Cr layer deposition are $T_{substrate}$ = 500 °C, I = 100 mA, U = 260 V at an Ar pressure of 0.015 mbar. The deposition time of 480 s results in a film thickness of 500 nm. The pre-sputtering process of the Ni-Mn-Ga cathode can be started while the Cr layer is deposited. This reduces the holding time until the second layer can be sputtered on top. Consequently reaction time of the hot Cr layer surface with residual oxygen is reduced. After the Ni-Mn-Ga layer is deposited the samples cool down to room temperature in high vacuum. To remove the films the chamber is vented with dry N_2 gas vaporized from liquid nitrogen.

3.1.2 Targets

The starting point for thin film preparation is the target material. For deposition of a metallic layer consisting only of one chemical element a disc of high purity can be used as sputter target. This is the case for the Chromium, the iron and the aluminum target that are commercially available 2 inch sputter targets in our setup. For deposition of a compound the situation is more complex. In the ideal case the composition of the target is transferred one by one to the substrate. The target is usually a polycrystalline disk made from melt cast. Key requirements are homogeneity and absence of impurity phases and pores in the material. Differences in the evaporation rates of the constituent elements will then level out while sputtering from the target. The element with lowest evaporation rate will accumulate at the target surface and, thus, the rate will increase by time. For Ni_2MnGa the production of bulk polycrystals for target material is not a trivial task. The ingot material Manganese is very sensitive to oxidation and shows a strong tendency to evaporate during the melt process. To cope with these problems one solution is sealing the ingots in a quartz glass tube. Since Ni_2MnGa polycrystals are hard and brittle the melt cast pieces are cut by spark erosion.

After polishing of the surface the stripes can be glued onto the target holder with conducting silver. Another possibility is centrifugal casting that results in a disk-shaped target outright. The material for the two stoichiometric targets used in this work was provided by Dr. S. Roth from IFW Dresden [81]. Target 1 is melt cast material cut by spark erosion, whereas target 2 is a disk produced by centrifugal casting. The targets 3-5 are off-stoichiometric with a Mn excess. Number 4 and 5 were purchased from Hauner company [82], whereas target 3 was prepared by arc melting by Dr. B. Balke from Mainz University [83]. A list of the targets used in this work is given in table 3.1. The actual composition of the targets was checked by energy dispersive X-ray spectroscopy (EDX). For target 5 the composition was probed by x-ray fluorescence spectroscopy. Both methods are considered to provide reliable results for bulk samples.

Target	**Composition** Ni:Mn:Ga in atomic %	
No.	nominal	EDX
1	50.0 : 25.0 : 25.0	50.8 : 23.4 : 25.9
2	50.0 : 25.0 : 25.0	48.5 : 24.6 : 26.9
3	49.0 : 30.5 : 20.5	44.5 : 30.6 : 24.9
4	49.0 : 30.5 : 20.5	49.0 : 30.5 : 20.5
5	48.1 : 30.1 : 21.8	52.1 : 28.3 : 19.5 [1]

Table 3.1: Composition of the used targets. [1]Probed by x-ray fluorescence spectroscopy.

3.1.3 Substrates

The choice of the substrate material is crucial for the structural properties of the deposited film. In general, a polycrystalline substrate will result in a polycrystalline or amorphous layer, since no preferential in-plane orientation direction is present. In contrast a single-crystalline substrate possesses a symmetrically ordered surface that acts as a constraint to the film on top. The first atoms that add to the surface will sit on the lattice sites of the substrate with attractive interaction of the involved elements. In case of repulsive interaction interstitial positions will be favored. The result in both cases is a duplication of the substrate crystal lattice. This requires of course matching lattice parameters and a compatible structure type. The lattice of the substrate is then a seed crystal for the layer growing on top. This process is called epitaxial growth [79]. If the substrate and the deposited material are chemically identical one speaks of homoepitaxy. In contrast heteroepitaxy denotes a monocrystalline layer grown on a seed crystal of different composition. Epitaxial growth of Heusler compounds is possible on several mono-crystalline substrates, including semiconductors like GaAs [15] and InAs [84], metal oxides as MgO and Al_2O_3 [85, 86] or $SrTiO_3$ [87]

and even halogenides like NaCl [88, 89]. The standard substrate materials used in this work are (100) oriented MgO and Al_2O_3(11-20) ("a-plane sapphire") in either 10 x 10 x 0.5 mm^3 or 10 x 5 x 0.5 mm^3 size. Sapphire is inert under ambient conditions and, thus, requires no special treatment. The Al_2O_3 surface is cleaned with acetone before glueing the substrates onto the heater unit. During the heat up process residual water on the substrate surface is evaporated. MgO, on the contrary, is hygroscopic and reacts with water when exposed to air. The formation of $Mg(OH)_2$ and $MgCO_3$ leads to degradation of the surface [90]. By annealing in an oxygen atmosphere the surface can be recovered [91]. Following previous works [18, 92] the annealing treatment was applied to MgO substrates in the early stages of this work. However, by using single-packed and sealed substrates stored in an exsiccator and limiting the time exposed to air the procedure could be omitted. To facilitate release of the Ni-Mn-Ga layer from the substrate two different water soluble substrate materials were tested. First sodium chloride and second barium fluoride. In spite of the large mismatch (s. table 3.2) it is possible to achieve epitaxial growth on BaF_2 and NaCl. Since particularly the latter is highly hygroscopic, these materials were exposed to air as short as possible. To obtain a fresh NaCl surface cleaving from bulk single crystal was tested, but did not prove to be a practicable method.

Substrate material	Crystal structure, lattice parameters	Orientation	Mismatch with respect to Ni_2MnGa in %
MgO	fcc, $a = 4.21$ Å	(100)	2.2
Al_2O_3	hex, $a = b = 4.76$ Å $c = 13.0$ Å	(11-20)	0.1*
NaCl	NaCl, $a = 5.64$ Å	(100)	3.2
BaF_2	CaF_2, $a = 6.20$ Å	(111)	6
Cr	bcc, $a = 2.91$ Å	(100)	0.1
Fe	bcc, $a = 2.87$ Å	(100)	1.5

Table 3.2: Overview of the structural properties of the used substrate and buffer layer materials. Lattice mismatch calculated with Ni_2MnGa a(Austenite) = 5.825 Å from [32]. * As calculated (s. chapter 4, Fig. 4.8)

3.1.4 Optimized preparation parameters

An important issue in sample preparation is the control of the film stoichiometry. For bulk Ni-Mn-Ga crystals a strong variation of the Curie temperature and the phase transformation temperature as function of the composition has been calculated and experimentally observed (s. chapter 2). In the sputter deposition process mainly two parameters will affect the film composition. On the one hand the working pressure and on the other the substrate temperature. The latter is

furthermore the decisive parameter for the structural and magnetic properties of the resulting film. At low substrate temperatures ($T < 300$ K) no epitaxial but polycrystalline growth is observed. High substrate temperatures, on the contrary, enable epitaxial growth but will result in an increased surface roughness as reported in [93] for Heusler films on Al_2O_3. To make use of the magneto-mechanical properties of the magnetic shape memory material rather thick films are advantageous. Thus, the surface properties play a minor role. This is not the case for samples used for surface sensitive experiments like X-ray absorption spectroscopy. To protect the film surface against oxidation by a thin Al cap layer the roughness has to be confined. To find the optimum preparation temperature besides structural properties the saturation magnetization of the samples was used as an indicator. Figure 3.2 displays the saturation magnetization determined by hysteresis loops at low temperature (i.e. 10 K for Al_2O_3 and 20 K for MgO substrates) for various samples prepared at different substrate temperatures. All other deposition parameters were fixed to allow direct comparison of the samples. While films grown at substrate temperatures up to 300 °C show a low saturation magnetization, the magnetization reaches values close to 4 μ_B per formula unit for samples prepared at 500 - 700 °C. This is in good agreement with values calculated by theory [94] and those reported for bulk samples [32, 66]. At a substrate temperature of 400 °C a distinct increase in saturation magnetization is observed. This coincides with structural properties of the samples probed by XRD. Epitaxial growth results for film deposition temperatures above 400 °C. As a good compromise between optimizing structural and magnetic ordering on the one hand and reducing surface roughness on the other hand a substrate temperature of 500 °C is chosen for the majority of samples prepared.

At a given substrate temperature the decisive parameter to control the film composition is the working pressure. A stable sputtering plasma with $I = 100$ mA, 250 V $< U <$ 300 V was achieved for an Argon pressure in the range of 0.01 to 0.1 mbar. In general a low working pressure is favorable, since implantation of Ar atoms is diminished. Furthermore a low Ar concentration in the chamber results in less scattering of the evaporated atoms and, thus, the deposition rate is higher. For Ar pressures below 0.01 mbar the plasma becomes unstable. Besides the deposition rate the Ar pressure influences the film composition markedly. This can be seen from the phase transformation temperature that is very sensitive on the sample stoichiometry. Figure 3.3 shows the martensite start temperature in dependence of the Ar pressure during film preparation. Other deposition parameters were kept constant for these samples. The phase transformation temperature, that was determined from magnetization measurements in low field (s. chapter 6.1.1), decreases linearly as function of the working pressure. This curve progression is attributed to changes in the film composition. However, an EDX analysis of these samples revealed no systematic variation of any of the three elements as can be gathered from table 3.3. As a consequence, the accuracy of EDX analysis applied to thin film sample seems to be not sufficient - at least for

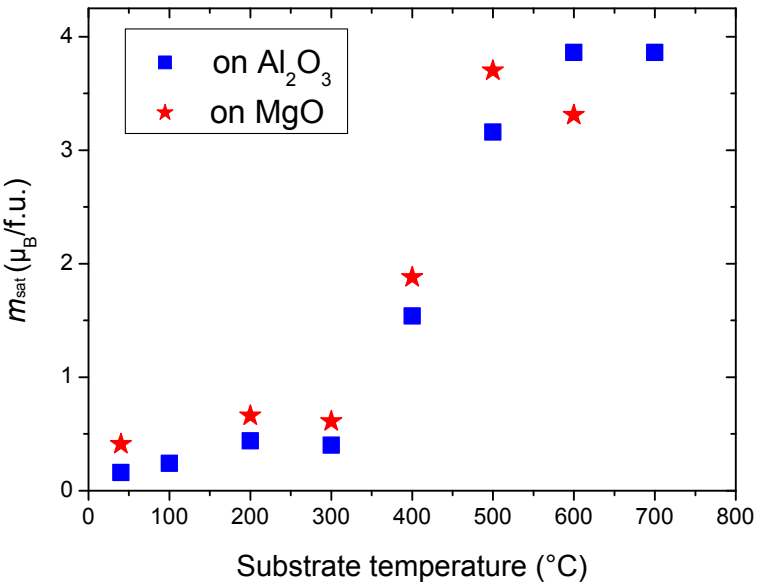

Figure 3.2: Saturation magnetization as a function of the substrate temperature during deposition. From hysteresis loops at 10 K (20 K for MgO substrates respectively) the saturation magnetization was calculated. The samples were prepared with identical conditions varying the substrate temperature only.

the available setup and used processing software. Hence, the composition of the samples was controlled only indirectly by comparing phase transformation and Curie temperature to theoretical calculations.

Sample	Ar pressure (mbar)	Ni	Mn	Ga
		(atomic %)		
A	0.02	51.1	22.4	26.5
B	0.03	51.2	22.5	26.3
C	0.04	50.3	22.0	27.7

Table 3.3: Compositional variation in samples prepared at different Ar working pressures. The sample stoichiometry was measured by EDX for the samples A, B and C displayed in Fig. 3.3.

3.2 Freestanding films

The simplest approach to release an epitaxial film from the substrate is peeling it off mechanically. Because of the relative low adhesion this is possible for several substrate materials. Though this seems to be a facile solution, problems arise from the significant stress on the film introduced by this procedure. First

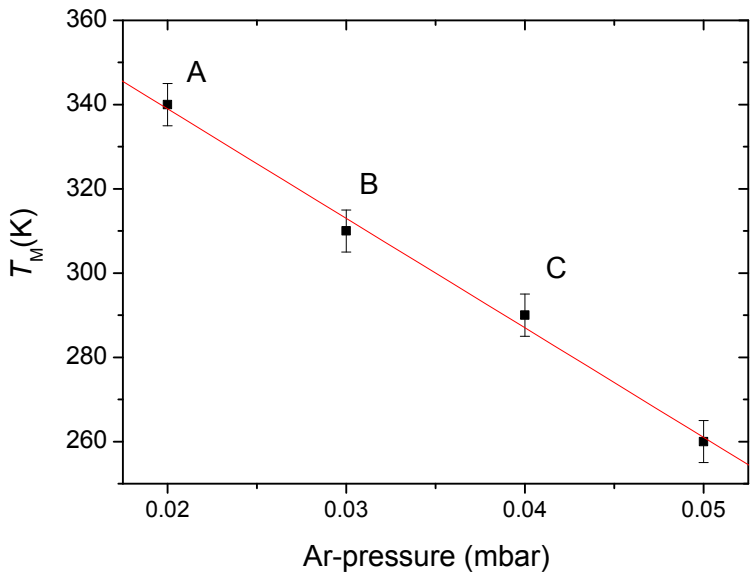

Figure 3.3: Dependence of the phase transformation temperature on the working pressure during film deposition. The displayed phase transformation temperature is the martensite start temperature determined by magnetization measurements in low field (s. chapter 6.1.1). Besides the Ar pressure for this set of samples all preparation parameters were identical.

difficulties arise from finding a point to apply the forceps. By breaking the substrate there is a bare chance to get delamination of the Ni_2MnGa layer at the edge. Pulling at the loose end of the film will then result in bending of the released part of the layer. Thus, a curled or even coiled film forms during the peel off process. In our experiments the flat geometry could not be recovered by simply unrolling these films. Since the introduced stress can not be controlled the method did not prove to be practicable. Another route to release the MSM layer is removing the substrate completely by a chemical reaction instead of mechanical treatment. If the substrate is soluble in any solvent that does not attack the Ni_2MnGa film, it is possible to eliminate the substrate. This is referred to as sacrificial substrate technique. The same concept can also be applied to a buffer layer that can be etched selectively. A third approach was a partial release of the films by cutting with an focused ion beam (FIB) under various angles.

3.2.1 Sacrificial substrate method

Materials suitable as a sacrificial substrate for preparation of freestanding epitaxial Ni-Mn-Ga films have to fulfill basically three requirements. First of all the lattice mismatch between substrate and film has to be low enough to allow epitaxial growth. Second chemical reactions at the interface and interdiffusion

of substrate elements into the layer should be restricted. Finally, a good solubility in a solvent that does ideally not react with the Ni-Mn-Ga layer is of importance. This last requirement is met by the first substrate material tested: sodium chloride. The (100) oriented NaCl single crystals can easily be dissolved in demineralized water without damaging the MSM layer. The mismatch of the Ni_2MnGa and the NaCl lattice parameter is with 3.3 % reasonably low. Problematic is the reactivity of the halogenide at high deposition temperatures. When heating the NaCl substrates above 480 °C the deposited layer looks flat and gray instead of metallic. This is a sure indication of a chemical reaction of the Heusler compound with the substrate material. Since NaCl is highly hygroscopic a careful bake-out process is necessary to evaporate the adherent water. Another drawback of this material is the severe difference of thermal expansion coefficients of NaCl and Ni-Mn-Ga. The films deposited at temperatures between 450 and 480 °C show a distinct buckling when cooling to room temperature. Figure 3.4 (left) shows an optical microscopy image of the Heusler layer on the NaCl substrate. A wavy film surface and a partial delamination can be observed. Furthermore, the surface of the film shows a line pattern that is induced by the substrate surface. The scratches produced by the polishing process are visible on the NaCl surface prior to deposition and transfer to the film surface during preparation. This is evident from Fig. 3.4 (right) that displays the released Ni-Mn-Ga film. The lines running under various angles clearly descend from the scratches of the substrate surface. The major disadvantage of NaCl(100) crystals as sacrificial substrates is the poor crystalline quality of the deposited films. The prepared samples show a textured crystal structure only. Single-crystalline growth on the used substrates could not be achieved, which is very likely a consequence of the degraded surface. Results of the crystal structure analysis of these samples are presented in chapter 4. The second soluble substrate material tested within this work was barium fluoride. On the available (111) oriented crystals of this compound epitaxial growth was achieved (s. chapter 4). In the literature (and in the product data sheet of several distributors) different solubility values for BaF_2 can be found. However, the single-crystalline substrates did not prove to be soluble in water in the least. Even a constant flow of demineralized water for over four hours did not affect the BaF_2 substrate. In order to increase the solubility of the barium fluoride by chemical precipitation of $BaSO_4$, addition of sodium sulfate was tried in the following. Still the solubility remained to low to dissolve the substrate.

3.2.2 Sacrificial buffer layer technique

Instead of eliminating the substrate in total, a sacrificial buffer layer between film and substrate can be introduced. This layer has to grow epitaxially on the substrate and moreover enable mono-crystalline growth of the top layer. Furthermore a selective removal of the buffer material is required. An element that meets all these requirements is Chromium. It grows epitaxially on MgO(100)

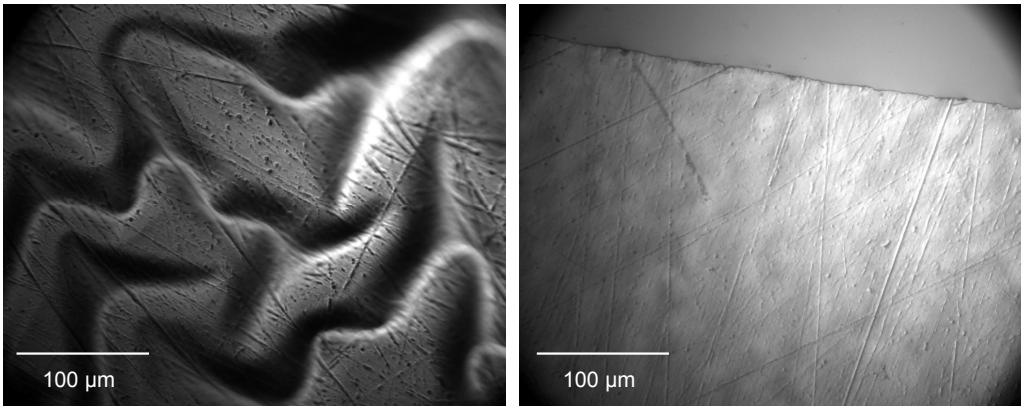

Figure 3.4: Optical microscopy images of Ni-Mn-Ga films deposited on NaCl(100) substrates. The different thermal expansion coefficients of substrate and film result in buckling of the layer after cooling to room temperature (left). After releasing the film surface shows a line pattern that originates from scratches on the NaCl surface due to polishing (right).

and facilitates epitaxial growth of Ni_2MnGa on top. The selective etchant used for the Cr layer is an acetic solution of cerium(IV) ammonium nitrate (20 g $(NH_4)_2Ce(NO_3)_6$, 3.5 ml acetic acid and 100 ml demineralized water) [95]. In contact to the reagent the Cr(0) is oxidized to Cr(+III) while Ce changes oxidation state from +IV to +III. The resulting reaction product $Cr(NO_3)_3$ is water soluble. The formation of a Cr metal complex makes the reaction highly selective. Nevertheless damages of the Ni-Mn-Ga layer like perforation was observed for some samples. This is an indication of either inhomogeneities in the film composition or diffusion of Cr into the Ni-Mn-Ga layer. By limiting the etching time this could be avoided. For an optimized Cr layer thickness of 100 nm an exposure time of 300 min was necessary to release a film of 10 mm length and 5 mm width. Surprisingly, thicker buffer layers (300 - 500 nm) required longer reaction time, although the contact area is larger for a rather thick Cr layer. Since the Cr etchant can attack the buffer layer on the side only, the process of completely releasing the film is slow. For an exposed Cr surface the reaction time to dissolve a 100 nm thick layer is just a few seconds. The relative slow process of etching the Cr underneath the MSM layer provides the opportunity of partial release. By limiting the exposure time to the Cr etchant only a small band along the film edges becomes freestanding. In combination with photolithography this method enables fabrication of freestanding microstructures. An illustration of the preparation process is provided in figure 3.5. In a first step, photolithography and wet chemical etching is applied to pattern the Ni-Mn-Ga layer. Subsequently, the Cr

buffer layer is etched until the designated regions are freestanding. Typical exposure times for releasing a 100 μm wide beam are 30 to 60 minutes. The progress of the etching process can be controlled by optical microscopy. Figures 3.6 and 3.7 show light microscopy images of patterned samples prepared by the sacrificial layer technique. The penetration depth of the Cr etchant is clearly visible, since the released film regions differ in reflectivity from the substrate-constrained area. The part of the film that is still fixed to the substrate via the Cr layer looks totally flat, whereas the freestanding regions appear to be strongly tilted. The surface tilt is in fact not as severe as suggested by the image, but caused by the normal incidence of the light. The released bands at the film edges are 75 μm wide. Besides the Cr layer also parts of the MgO substrate are removed by the etchant, as evident from the crater-like surface. Since substrate surface and the Ni-Mn-Ga film surface are in the focus of the microscope the removed MgO layer has to be less than 2 μm. The inclination of the released stripe is consequently in the range of 2 °considering the Cr layer thickness of 500 nm for this sample.

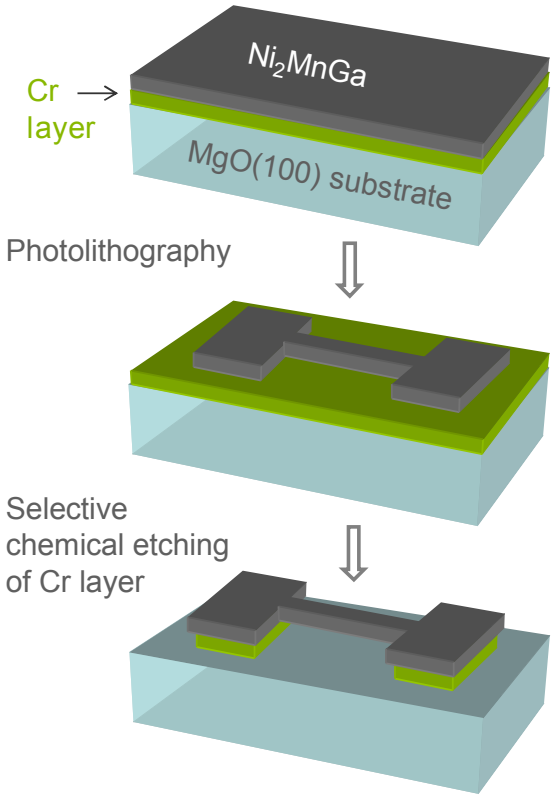

Figure 3.5: Illustration of the preparation process of a freestanding microstructure. In a first step the Ni-Mn-Ga layer is patterned using photolithography. Subsequently the Cr buffer is partially removed by selective chemical etching.

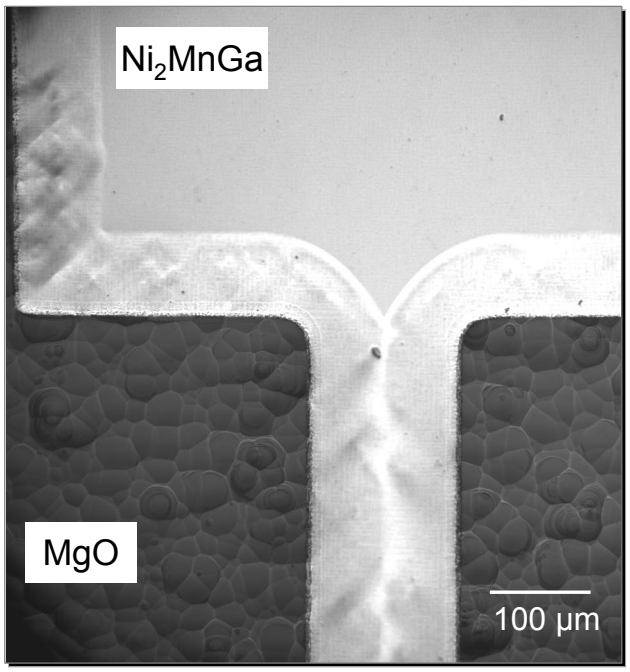

Figure 3.6: In light microscope images the freestanding regions of the film are clearly visible due to differences in reflectivity of the incident light. The Cr layer is retained underneath the flat part of the film (upper third). The damages on the MgO surface are caused by the Cr etchant.

Photolithography process:

- Spin-coating of the Ni-Mn-Ga film surface with positive photo resist (type: ma-p 1215). After application of the resist with a pipette spinning at 300 rpm for 10 s, then 30 s at 4000 rpm.
- Bake-out: 2 minutes on a hot-plate held at 120 °C
- Exposing: With shadow mask 40 s in UV light.
- Developing: 90 - 120 s in ma-D 331 (until pattern is faintly visible). Stop process by rinsing in demineralized water.
- Etching: 40 - 90 s in 12 % HNO_3 solution (visual control: the etched Ni-Mn-Ga becomes dark grey. When removed the metallic Cr gets visible). To stop etching rinse in demineralized water.
- Removal of residual photo resist with acetone.

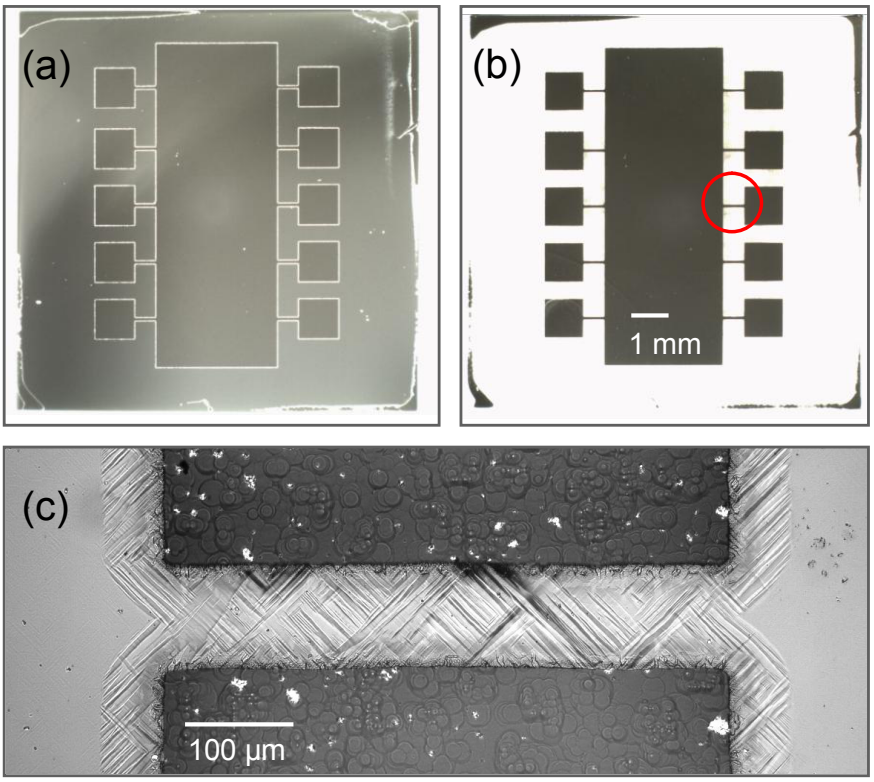

Figure 3.7: Light microscopy images of partly freestanding Ni-Mn-Ga film. The MSM layer is patterned by photolithography (a). In a second step the Cr layer is removed via selective chemical etching (b). By limiting the etch time the film is released partially (c), since the etchant attacks the Cr layer at the side only.

3.2.3 Focused ion beam etching

Freestanding microstructures such as cantilevers or bridges can also be fabricated by etching an epitaxial film with a focused ion beam (FIB). The patterning by FIB etching was done in cooperation with Professor M. Huth of Frankfurt University [96]. By cutting under an angle from both sides a freestanding triangular beam was prepared. With a third, perpendicular cut one side of the structure is released. Scanning electron microscopy (SEM) images are used to monitor the progress of the etch process (s. Fig. 3.8). Once the beam is released on the sides and one end completely, it is free to move. For a rather thin and long cantilever bending up was observed (s. Fig. 3.9). This proofs that the 25 μm long and 2 μm wide beam is in fact mobile. Since no mechanical or magnetic force has been applied yet, the curvature indicates that the substrate-constrained film was in a stressed state. However, another cantilever on this sample with a lower aspect ratio showed no curvature after releasing (s. Fig. 3.11). Problems associated with the preparation technique are potential damages in the crystal lattice of the regions around the FIB cut. Since gallium ions are used for the etching, changes in the Ga content of the film are possible. An EDX analysis before and after patterning revealed minor changes of the composition. Before treatment with the gallium ion beam the film composition was determined to be $Ni_{51.1}Mn_{23.3}Ga_{25.6}$. After the etch process a composition of $Ni_{49.7}Mn_{22.8}Ga_{27.6}$ was measured on the cantilever and $Ni_{50.9}Mn_{22.4}Ga_{26.6}$ far from this cantilever. These changes are attributed to the limited accuracy of the method applied to thin film samples rather than to changes in the stoichiometry associated with the FIB preparation. Nevertheless, a higher gallium concentration at the surface of the cantilever as well as defects in the lattice cannot be excluded. Further information on the preparation procedure are provided in references [97] and [98].

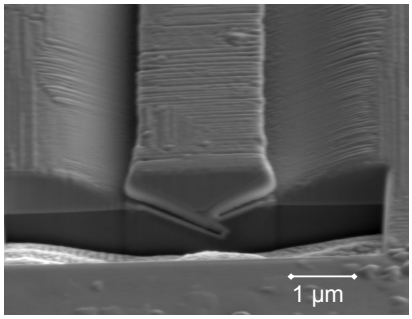

Figure 3.8: SEM image of a cantilever prepared by focused ion beam etching. The first angular cut was done from the right side in the image. Subsequently, the second cut under an angle is performed from the left. During the etch process redeposition of material can occur, which is visible at the intersection of the two cuts.

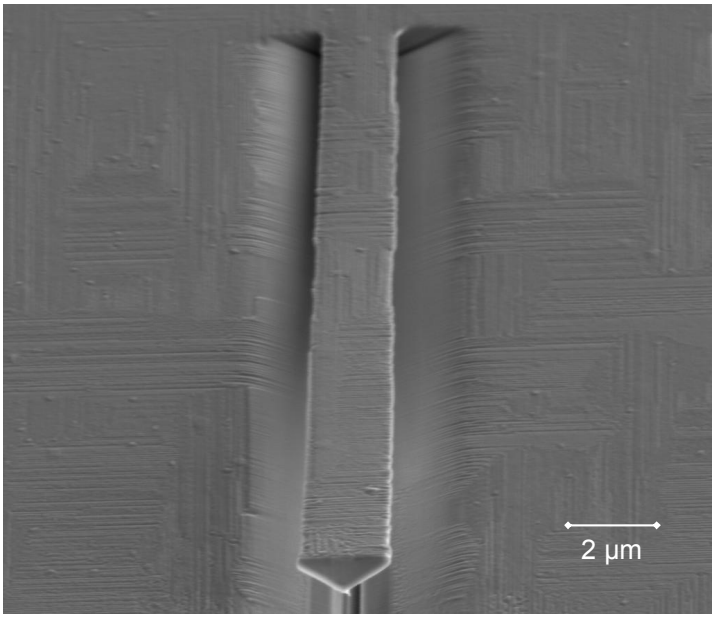

Figure 3.9: SEM image of a freestanding cantilever prepared by focused ion beam etching. The dimensions of the beam are 25 μm x 2 μm. The curvature indicates that the substrate-constrained film is in a stressed state. It is also possible that the stress is induced by the preparation process. On the film surface a distinct twinning pattern can be observed.

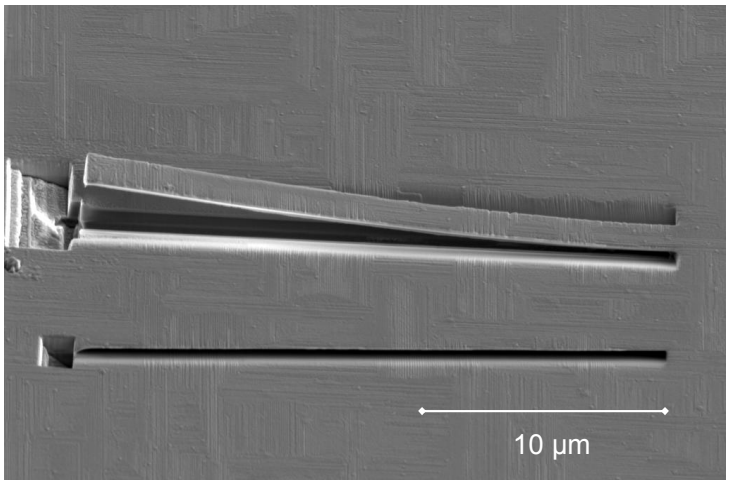

Figure 3.10: In the side view the curvature of the released cantilever is clearly visible. The structure was prepared by focused ion beam etching of a thick Ni-Mn-Ga film on a MgO(100) substrate.

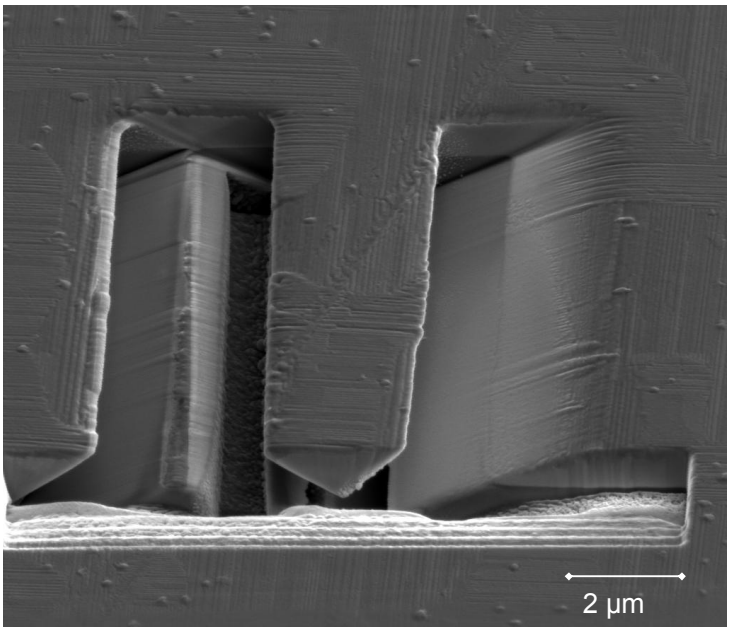

Figure 3.11: SEM image of a FIB cut cantilever of lower aspect ratio. On the surface of the 6 μm long and 2 μm wide beam a distinct twinning pattern is visible

3.3 Standard characterization methods

3.3.1 X-ray diffraction

The crystalline quality of the samples is controlled by X-ray diffraction (XRD) in Bragg-Brentano geometry. The used set-up is a commercial diffractometer (*Philips Xpert*) that utilizes Cu $K_{\alpha 1}$ radiation with a wave length of $\lambda = 1.5406$ Å. In addition, contributions of Cu $K_{\alpha 2}$, Cu K_{β} and lines of W and Mo impurities are visible in the diffraction pattern. The epitaxial growth of the film is checked by a θ-2θ-scan. Here the angle between incident X-ray beam and sample surface (ω) is varied in steps of typically 0.1° between 10 and 50°. At the same time the detector and the sample surface enclose an angle of $\theta = \omega$, which means the angle between source and detector is 2θ for each step. In the experiment the X-ray source is fixed, while sample stage and detector can be rotated independently (s. sketch of the 4-circle diffractometer in Fig. 3.14). The sample sits in the center of the turning circle of the detector. When the angle of incidence θ meets the Bragg condition:

$$2d\ \sin(\theta) = n\lambda \tag{3.1}$$

constructive interference can be detected under the emergent angle θ and, thus,

a peak occurs in the diffraction pattern. The peak position depends on the used X-ray wavelength and the distance d of the lattice planes parallel to the crystal surface. By this method only the out-of-plane lattice parameter d is probed. This yields information about the lattice spacing along the film normal. For orthogonal lattice systems with the lattice parameters a, b, c the following equation relates lattice plane distance d_{hkl} and lattice parameters:

$$\frac{1}{(d_{hkl})^2} = \left(\frac{h}{a}\right)^2 + \left(\frac{k}{b}\right)^2 + \left(\frac{l}{c}\right)^2 \tag{3.2}$$

To interpret the peaks, observed in the experiment, a comparison to a simulated diffraction pattern is necessary. The program *PowderCell* [99] provides calculated powder diffraction patterns for many elements and compounds. The database of the software contains the atomic form factors f_j of the individual elements. These are basically the Fourier transforms of the electronic density of the ion [100]:

$$f_j(\mathbf{K}) = -\frac{1}{e}\int d\mathbf{r}\ e^{i\mathbf{K}\cdot\mathbf{r}}\rho_j(\mathbf{r}) \tag{3.3}$$

Besides the electron density ρ of the considered atom j the form factor depends also on the difference $\mathbf{K}$ between incident and scattered wave vector. According to the Laue theory of diffraction [100] elastic scattering of the incident plane waves on the individual atoms located at $\mathbf{d}_j$ in the lattice occurs. Constructive interference results only, if the change of the wave vectors $\mathbf{K} = \mathbf{k}_i - \mathbf{k}_f$ is a vector of the reciprocal lattice. The observed intensity $I_{\mathbf{K}}$ is then:

$$I_{\mathbf{K}} \propto \sum_{j=1}^{n} f_j(\mathbf{K})\ e^{i\mathbf{K}\cdot\mathbf{d}_j} \tag{3.4}$$

If the form factors of all constituent atoms and their lattice positions, as well as the lattice parameters and the symmetry are known, all observable reflections can be calculated. Figure 3.12 displays such a calculated diffraction pattern for Ni_2MnGa. Since the software is designed for powder samples, crystallites of all possible orientations will contribute in the simulated scattering process. Thus, all possible orientations - (100), (110) and (111) - will be observed simultaneously. For a bulk single crystal or an epitaxial film this is not possible. When comparing the simulated diffraction pattern 3.12 with the list of all calculated reflections 3.13 it strikes that some peaks have very low or even zero intensity. This is a consequence of the different atomic form factors that can cause distinction of particular reflections (e.g. (200), (222), etc.). For a film grown on a MgO(100) substrate the incidence of the Ni_2MnGa (400) reflection is used to verify epitaxial growth. For non-stoichiometric samples the introduced chemical disorder leads to occurrence of the (200) peak in addition. When preparing films on Al_2O_3(11-20)

the epitaxial growth is confirmed, if the (220) peak appears while the (200) and (400) reflections are absent.

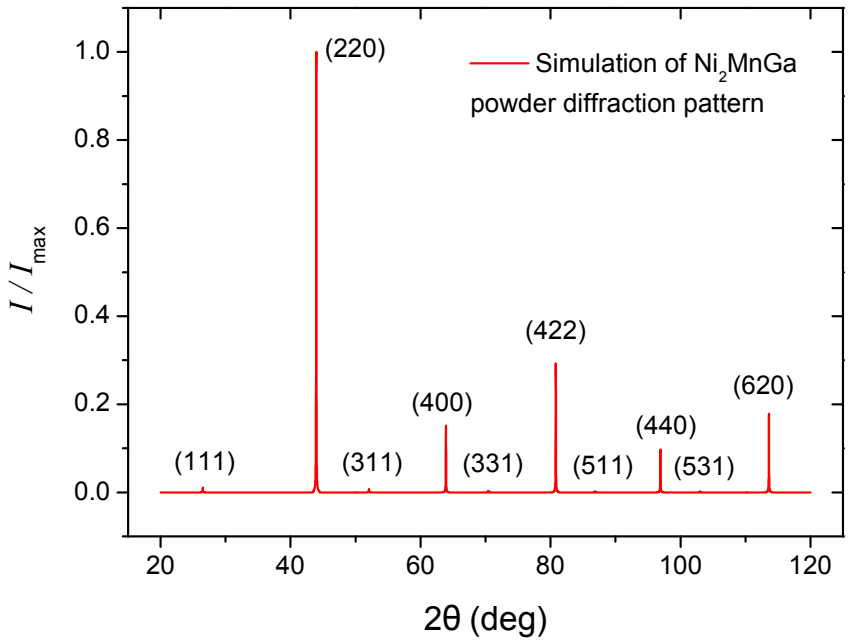

Figure 3.12: Simulation of a Ni_2MnGa powder diffraction pattern using the program *PowderCell 2.4*. The peak intensities are normalized to the strongest reflection.

Besides the peak position further information on the structural properties of the sample can be gained from the line broadening $\Delta(2\theta)$ at half maximum intensity. The size of the crystallites is related to the line width observed for a peak at θ as follows:

$$L = \frac{K\lambda}{\Delta(2\theta) \cdot \cos(\theta)} \tag{3.5}$$

where K is the dimensionless shape factor and λ the wavelength of the used X-ray light. Depending on the actual shape of the crystallites K is typically close to 1. The equation known as Scherrer formula [101] is limited to grain sizes $< 100\ \mu m$.

The second scan type used is the so-called "rocking curve" also referred to as ω-scan. Here the detector is fixed in 2θ at a lattice reflection, while ω is varied in the range of a view degrees around the value θ. For a perfect crystal this scan would result in a single line at $\omega = \theta$, whereas a fine-grained polycrystalline sample will show a Gaussian broadening of the intensity distribution around the peak maximum. The individual crystallites will meet the Bragg condition for different ω-values, which causes the peak broadening. This scan mode is only

H	K	L	2θ/deg	d/Å	I_{rel}/%
1	1	1	26.496	3.36133	1.07
2	0	0	30.688	2.91100	0.00
2	2	0	43.953	2.05839	100.00
3	1	1	52.057	175540	0.66
2	2	2	54.559	1.68067	0.00
4	0	0	63.907	1.45550	15.17
3	3	1	70.440	1.33566	0.30
4	2	0	72.556	1.30184	0.00
4	2	2	80.808	1.18841	29.26
5	1	1	86.864	1.12044	0.18
3	3	3	86.864	1.12044	0.06
4	4	0	96.912	1.02919	9.86
5	3	1	103.025	0.98410	0.28
6	0	0	105.094	0.97033	0.00
4	4	2	105.094	0.97033	0.00
6	2	0	113.606	0.92054	17.91

Figure 3.13: *h k l* reflection list for a Ni_2MnGa powder sample simulated with *PowderCell 2.4* The peaks routinely used to confirm epitaxial growth on MgO(100) and Al_2O_3(11-20) substrates are highlighted.

sensitive to the tilt of the crystallites with respect to the film normal. To get insight on the in-plane orientation of the lattice unit cells probing with a 4-circle diffractometer is required. In contrast to the 2-circle setup, here the sample can be rotated orthogonally to the scattering plane (χ-angle) and around the sample normal (φ-angle). The operating circles, as illustrated in Fig. 3.14, allow scanning of arbitrary lattice planes. In principle the set-up enables scanning of the entire reciprocal space. The control software (*STADI 4*) provides different scan types in reciprocal space coordinates as well as variation of the angles in real space. Thus, the precise orientation of the film lattice with respect to the substrate lattice, that acts as a reference frame, can be determined. For mapping the reciprocal space the software uses an orientation matrix of the crystal lattice based on a structural model. After adjusting the sample surface with the aid of a telescope and a reflected laser beam two geometrically independent reflection are needed as input for the orientation matrix. Subsequently, iterative scanning of a list of calculated reflections is performed. The measured peak positions are

used to refine the matrix. A second matrix containing the parameter set of the substrate lattice can be used as a reference system for specific scans.

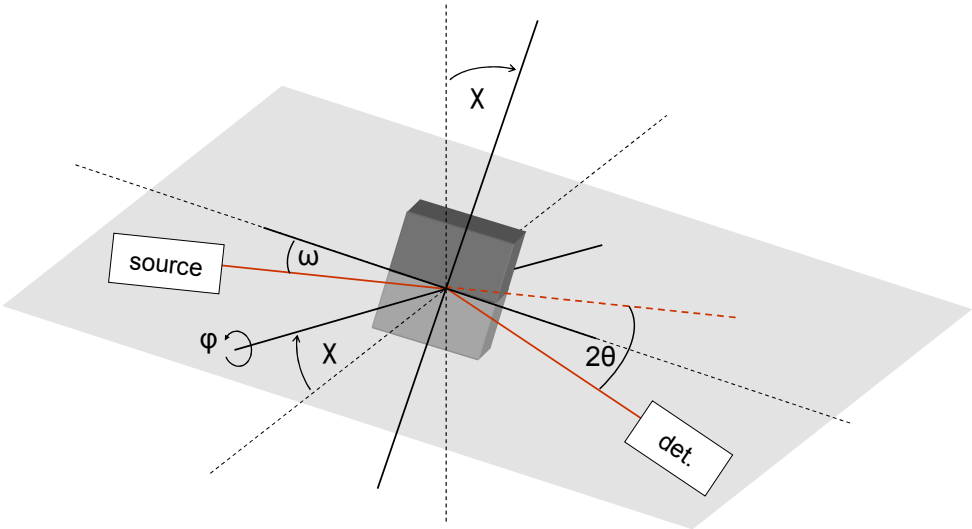

Figure 3.14: Schematic of the operating circles of the 4 circle diffractometer. For a fixed φ-value and $\chi = 0$ the geometry corresponds to that of the 2-circle diffractometer.

3.3.2 Reflectometry

Besides investigation of the structural properties the 2-circle diffractometer offers also an effective method to determine the layer thickness of the sample by monitoring the intensity of the X-ray beam reflected by the film at grazing angles. This measuring technique, called X-ray reflectometry (XRR), is fast, non destructive and provides high precision for single and multi-layer thin films up to 200 nm thickness [102]. In the experiment the sample surface is aligned parallel to the X-ray beam for $\theta = 0°$ blocking half of the maximum intensity observed without sample in the beam. Then a $\theta - 2\theta$ scan for $0.2° \leq \theta \leq 4°$ is performed. Below the critical angle θ_C of the topmost layer total reflection of the incident X-ray beam occurs. For $\theta > \theta_C$ the incident light partly penetrates the layer and is reflected at the interface to the substrate, or next layer respectively. Interference of the different partial beams results in oscillating intensity observed under the reflection angle θ ("Laue oscillation"). The position of the intensity maxima is sensitively depending on the layer thickness. To evaluate the experimental data a fit routine is provided by the program *PARRATT32* [103]. The database contains basically the refraction indices of the different elements and numerous compounds. The reflectivity can be calculated as a function of layer thickness

and surface and interface roughness for a single layer on a substrate. Figure 3.15 shows XRR data collected on a Ni_2MnGa film on MgO substrate in combination with the calculated reflectivity using *PARRATT32* software.

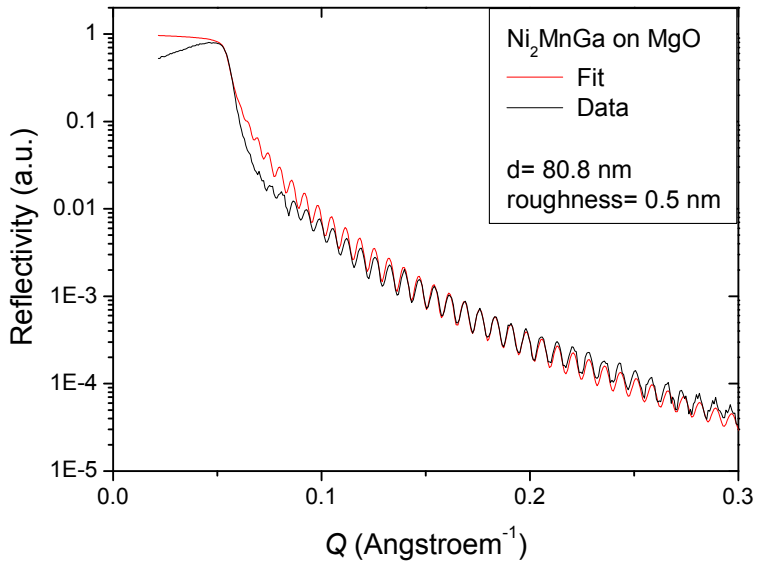

Figure 3.15: XRR scan measured on a thin Ni_2MnGa film on MgO. The calculated reflectivity fits the data best for a layer thickness of 80.8 nm and a surface roughness of 0.5 nm.

The software is also applicable to multilayer systems. This was of great benefit, when determining the deposition rate of the aluminum target that is used to cap the films. Due to the small difference of the refractive index of Al with respect to MgO or Al_2O_3, an Al layer deposited on these standard substrates gives no XRR signal. A better contrast is achieved, if the Al layer is enclosed by two layers of an element of higher atomic number. A suitable element is iron, that was available as target material for buffer layer deposition. The prepared multilayer shows a distinct reflectivity characteristics that allows calculating the thickness of the individual layers 3.16.

3.3.3 Magnetometry

Two different measurement techniques were applied to investigate the magnetic properties of the samples. The first machine in use is a Vibrating Sample Magnetometer (VSM) [104] of the type *Oxford Maglab*. The sample is attached to an oscillating sample holder and placed between two pick-up coils in the applied magnetic field. The motion of the magnetized thin film sample causes an electromagnetic induction in the sensing coil. The induced voltage in the pickup coil is

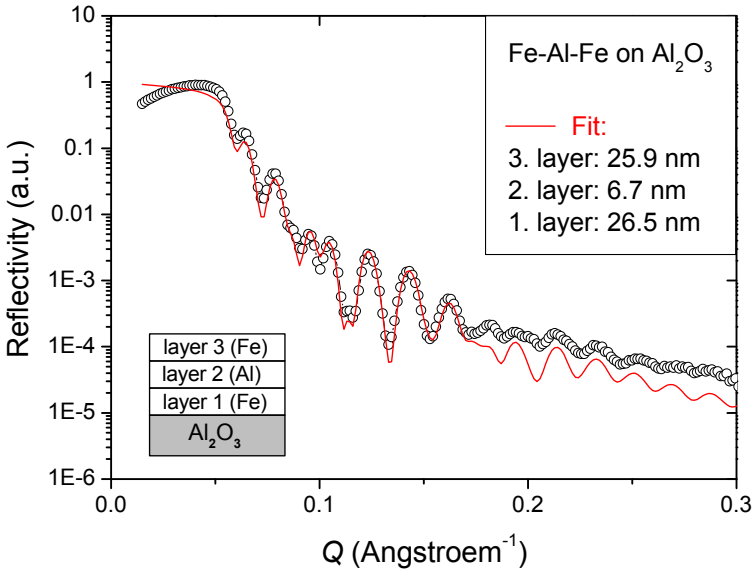

Figure 3.16: A multilayer system of Fe-Al-Fe on a Al_2O_3 substrate is used to determine the Al layer thickness. The XRR signal (black circles) was fitted with the program *PARRATT32* (red line).

proportional to the sample's magnetic moment. Since the signal has the same frequency as the driver it can be extracted with a lock-in amplifier. In the standard geometry the magnetic field is applied in the film plane along the long substrate edge (for 10 mm x 5 mm substrates). To record a hysteresis loop the magnetic field is varied between -4 and 4 Tesla and data is collected for each 10 mT step. From such a hysteresis loop the in-plane saturation magnetization can be calculated if the film thickness and thereby the sample volume is known. A second sample holder enables also probing the out-of-plane magnetization in the VSM. In combination with hysteresis loops measured for different in-plane orientation the magneto-crystalline anisotropy can be estimated. During the measurement the temperature of sample and surrounding is controlled by a variable temperature inset in the helium cryostat. The temperature control allows for scanning at a constant value as well as sweeping the temperature in the range of 2 - 300 K. The second instrument available is a *Quantum Design MPMS II* SQUID (*Superconducting Quantum Interference Device*) magnetometer [105, 106]. Similar to the VSM function principle the sample is moved linearly between a set of pick-up coils. Exploiting the Josephson effect [107] in a superconducting loop the induced current is converted to a voltage signal that is detected. Besides the increased sensitivity of the measuring principle, the variable temperature inset of the instrument offers a larger operating range compared to the VSM. Accordingly, the SQUID was mainly used to determine the Curie and the phase transformation temperatures. For that purpose, a field of 10 mT is applied in-plane along the

long substrate edge and the temperature-dependent magnetization of the film is scanned for a temperature range of 150 to 400 K with a ramp rate of 2 K min^{-1}. For these low field measurements the contribution of the substrate to the signal can be neglected. This is not the case if higher magnetic fields are applied. The paramagnetic contribution of the MgO and the diamagnetism of the Al_2O_3 substrates are clearly visible for fields above 1 T. By fitting a line to this part of the hysteresis loop these contributions can be subtracted. For a quantitative evaluation of the saturation magnetization of the sample it is necessary to calibrate the instruments with a standard.

3.3.4 Surface investigation

Thin metallic layers grown epitaxially on a planar substrate are usually flat with a certain surface roughness. For adsorbates that do not wet the substrate surface completely the formation of islands during growth is likely. Furthermore, the surface morphology depends on the deposition conditions, especially the substrate temperature and the energy distribution of the evaporated material. When examining the film surface accurately defects like holes or on smaller scale lattice imperfections can be located. In the case of Ni-Mn-Ga the formation of twinned variants in the martensite leads to deviation of the surface from a flat geometry. The film grows at elevated temperature in the cubic austenite phase. Under cooling the crystal structure changes from cubic to orthorhombic (or tetragonal), when the sample transforms to the martensite. As the substrate-constrained film cannot change the macroscopic shape, different crystallographic variants, separated by twin planes, will form in the low temperature phase. The twinning process involves tilting of the variants with respect to the cubic lattice of the parent phase. This results in a buckling of the film surface, that can be observed by optical microscopy in some cases. From the millimeter scale down to some micrometer the light microscope provides easy access to the surface pattern induced by the martensitic microstructure. The observed "macroscopic" structure is a consequence of the variant distribution and the twin plane alignment and, thus, allows conclusions on the microstructure of the sample. The complex crystal structure of the Ni-Mn-Ga martensite also involves hierarchical twinning that means the formation of "twins within twins". Therefore a mesoscopic twin configuration can link the macroscopic structure and the atomically sharp twin boundaries. To probe this mesoscopic scale a scanning electron microscope (SEM) and an atomic force microscope (AFM) have been employed. The former operates with electrons that are accelerated to energies of several keV and focused on the sample surface in raster scan pattern. For imaging the secondary electrons generated by inelastic scattering processes of the electrons on atoms near the surface are detected. Since the emission characteristic is symmetric around the surface normal, intensity variations can be used to create a plastic image of the surface topography. It is also possible to use the back-scattered electrons, that stem from elastic scat-

tering of high energy beam electrons on the specimen atoms, as signal. Atomic force microscopy utilizes the forces between a probing tip attached to the end of a cantilever and the specimen atoms to image the sample surface. The available set-up can be used in contact or non-contact mode. In the first operation mode the static tip deflection is directly observed. In non-contact mode the cantilever is placed a few nm above the sample surface and is oscillated slightly above the resonance frequency. The van der Waals forces between sample atoms and the tip will cause a change of the resonance frequency, which allows determination of the distance. In general, the achievable resolution of AFM exceeds that of SEM and can in principle reach the atomic scale. Comparable resolution is also supplied by transmission electron microscopy. Here the wave character of electrons is exploited to image a thin specimen in transmission mode by a suitable electron optics. A disadvantage of the method is the complicated preparation process of the sample under investigation. To achieve a magnetic contrast in the surface image the AFM can be equipped with a magnetized tip that interacts with the stray field on the sample surface. This technique is referred to as magnetic force microscopy (MFM).

Chapter 4

Crystal Structure

A key requirement for considerable magnetic-field-induced strains, as reported for bulk Ni_2MnGa samples, is the single-crystalline nature of the MSM alloy. In polycrystalline samples, twin boundary motion is suppressed by the grain boundaries, or equivalently, neighboring grains have incompatible MFIS. To date, the highest strains have been observed for bulk samples with 7M/14M structure [4]. Besides the modulation, the variant configuration and in particular the alignment of the magnetic easy axis play a decisive role in the magnetically controlled variant redistribution process. Thus, the precise knowledge of the martensitic crystal structure is of utmost importance.

In this section the structural properties of the samples are reviewed. This involves the results of X-ray diffraction (XRD) in two- and four-circle geometry. The former is used as the standard technique to control the epitaxial growth of the samples. The 2-circle diffractometer facilitates fast access to the out-of-plane orientation of the films and furthermore provides valuable information on the "crystalline quality" of the samples. From the rocking curve width (FWHM) the misalignment of individual crystallites can be estimated, while the FWHM of the peaks in the θ-2θ-scan contains information on the size of the crystallites. The in-plane alignment of the austenitic unit cell in the Ni-Mn-Ga films is determined with a diffractometer that uses a 4-circle goniometer to adjust the sample in the X-ray beam. This set-up also allows for detection of different crystallographic variants in the martensite state and moreover determination of the quantitative variant distribution. With a helium cryostat attached to the 4-circle diffractometer the temperature evolution of selected Bragg peaks can be pursued. For samples showing the martensitic phase transformation below room temperature the changes in the crystal lattice associated with the phase transition can be studied with the cryostat setup. To access the austenitic phase for the off-stoichiometric Ni-Mn-Ga films a Peltier element was utilized to heat the samples. To distinguish between the two structural phases the associated Bragg peaks are indexed with A for the cubic austenite and M for the orthorhombic martensite in the following. Finally, two different set-ups for XRD measurements with applied

magnetic field were tested: a set of permanent magnets with suitable sample holder and secondly a solenoid capable of generating a field of 400 mT.

4.1 Structural properties of the austenite

The structural phase transformation occurs well below room temperature at about 202 K for stoichiometric Ni_2MnGa samples [32]. The standard XRD scans thus probe the austenite phase, if the film composition is in the vicinity of Ni-50 Mn-25 Ga-25. This is the case for our films prepared from the stoichiometric Ni_2MnGa targets. Epitaxial growth was achieved on different substrate materials including MgO(100) and $Al_2O_3(11\bar{2}0)$ single crystals. In the first case the lattice of the Heusler compound follows the (100) orientation of the substrate. This is evident from the XRD diffraction pattern in Bragg-Brentano geometry displayed in Fig. 4.1. Besides the intense (200) and (400) MgO peaks the respective Ni_2MnGa reflections are visible. The additional lines are not due to impurity phases, but are present in a reference scan on the blank substrate too. According to the calculated reflection list (s. Fig. 3.13) the Ni_2MnGa $(400)_A$ peak is detected at a 2θ-value of 63.9°. For a completely $L2_1$ ordered Ni_2MnGa sample the $(200)_A$ reflection would have zero intensity due to extinction. The appearance of the $(200)_A$ peak at $2\theta = 30.7°$ clearly indicates a deviation of the sample's crystal structure from the $L2_1$ order. The reason for the disorder lies in the chemical composition of the film that deviates from Ni-50 Mn-25 Ga-25.

The rocking curve measured at the intensity maximum of the $(400)_A$ Ni_2MnGa peak is shown in Fig. 4.2. A fit with a Lorentz profile yields a peak broadening of 0.53° (FWHM), which is a typical value for films grown on MgO substrates. The peak broadening is caused by deviation of the film lattice from being a perfect single crystal. The X-ray spot probes a specimen volume that consists of individual crystallites separated by grain boundaries. These crystallites can slightly vary in alignment. The associated tilting of the lattice planes results in the observed line broadening. As a reference value the rocking curve width of a substrate reflection can be used. Here the ω-scan of the (200) peak shows a width of $\Delta\omega = 0.08°$. This can be considered as the resolution of the diffractometer, since the X-ray beam is not divergence-free.

For the films prepared on $Al_2O_3(11\bar{2}0)$ substrates the θ-2θ-scan generates a diffraction pattern as pictured in Fig. 4.3. The Ni_2MnGa grows epitaxially on the substrate surface with a $(110)_A$ orientation along the surface normal, as evident from the observed $(220)_A$ and $(440)_A$ film peaks. The corresponding rocking curve at $2\theta = 44.25°$ shows a FWHM of $\Delta\omega = 0.22°$ only (s. Fig. 4.4). In combination with the high peak intensity, this demonstrates the highly monocrystalline character of the samples. Using equation 3.5 the observed peak width $\Delta(2\theta)= 0.19°$ of the $(220)_A$ reflection results in a crystallite size of 50 nm for films grown on Al_2O_3. The broadening of the $(400)_A$ peak for samples on MgO

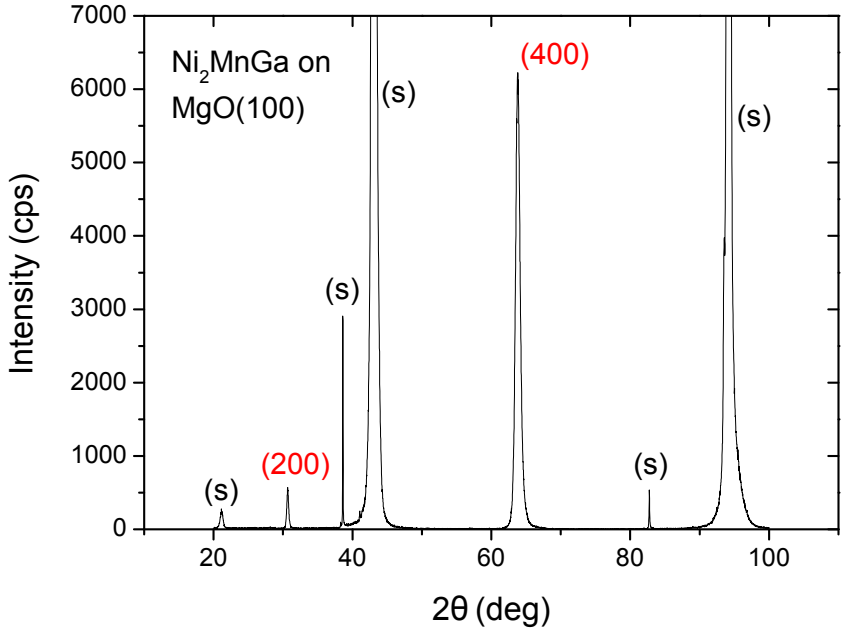

Figure 4.1: The XRD pattern (θ-2θ-scan) reveals the (100) out-of-plane orientation of the austenitic Ni_2MnGa film grown on MgO(100). Besides the substrate peaks (s) only the $(200)_A$ and $(400)_A$ Ni_2MnGa reflections are visible.

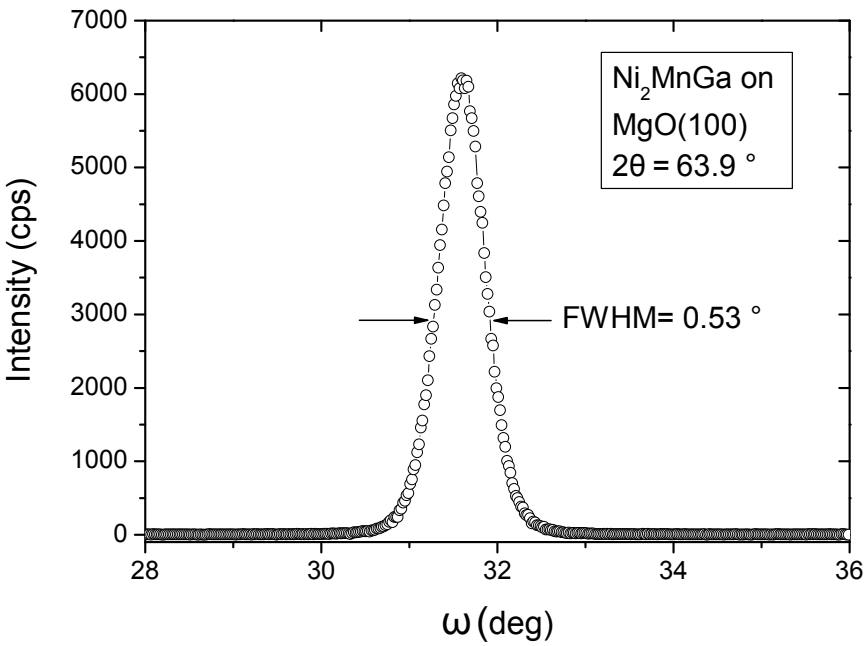

Figure 4.2: At $2\theta = 63.9$ degree the ω-scan of the $(400)_A$ peak shows a FWHM of 0.5°, which is a typical value for Ni_2MnGa films grown on MgO(100) substrates.

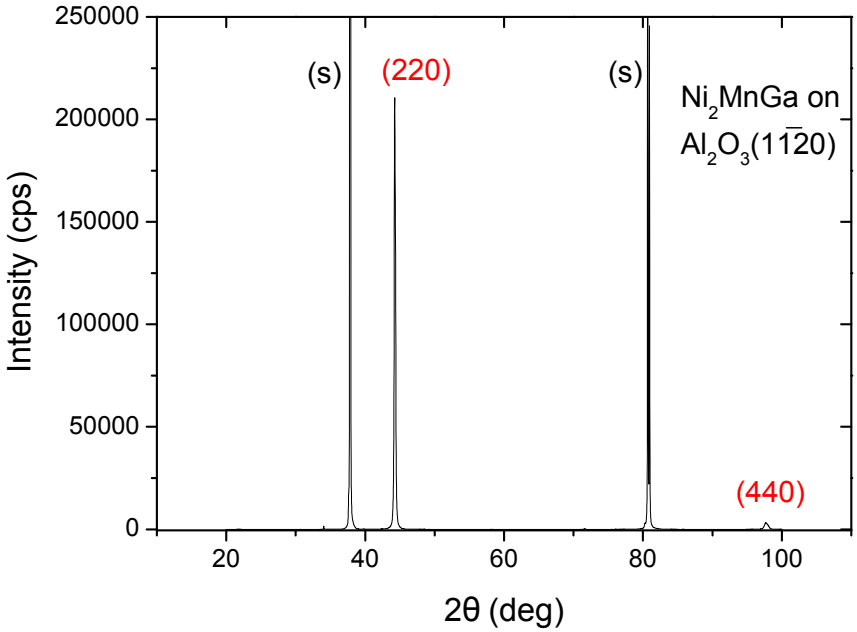

Figure 4.3: θ-2θ-scan of a Ni_2MnGa film grown on a $Al_2O_3(11\bar{2}0)$ substrate. Besides the substrate peaks (s) only the $(220)_A$ and $(440)_A$ Ni_2MnGa reflections are visible confirming epitaxial growth.

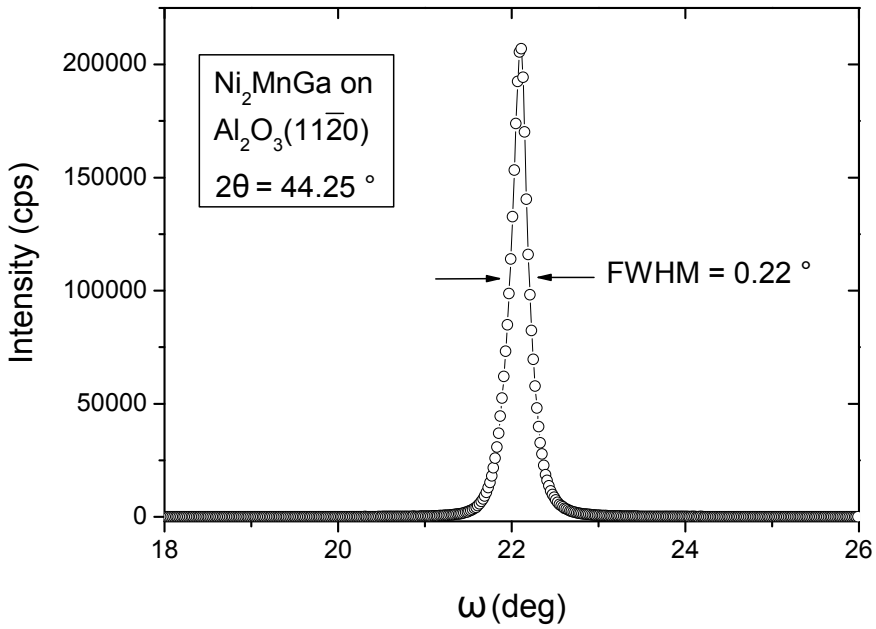

Figure 4.4: At $2\theta = 44.25°$ the ω-scan shows a FWHM of 0.22°, which is a typical value for the Ni_2MnGa $(220)_A$ peak for films grown on Al_2O_3 substrates.

leads to an estimated crystallite size of 15 nm only. In the calculation the shape factor K was assumed to be 1. In combination with the increased peak width of the rocking curve for samples on MgO(100), this leads to the conclusion that Al_2O_3(11-20) substrates facilitate better epitaxial growth of the Ni_2MnGa layer.

The in-plane orientation of the cubic Ni_2MnGa austenite unit cell is probed by scans in the reciprocal space with the 4-circle diffractometer. In case of films prepared on MgO(100) substrates the orientation of the in-plane lattice parameters is checked by scanning a (k,l)-plane at a constant h-value of 4. The contour plot of the measured intensity (s. Fig. 4.5 (a)) exhibits four peaks symmetrically arranged around the central $(400)_A$ peak. These $\{420\}_A$ peaks reflect the fourfold symmetry of the MgO substrate. When comparing to the positions of the MgO $\{220\}$ reflections (not shown) a difference in φ-angle of 45° is observed. Consequently the Heusler unit cell features an in-plane rotation of 45° with respect to the MgO lattice (s. illustration in Fig. 4.6). This is in agreement with results obtained for other Heusler compounds [108]. Fig. 4.5 (b) shows a (h,k,l) plane scan performed for a film on $Al_2O_3(11\bar{2}0)$. The plane is parallel to the film surface and maps the reciprocal space around the Ni_2MnGa $(220)_A$ peak. Following the naming convention of the peaks observed in the 2-circle XRD pattern the out-of-plane direction is (110) in reciprocal space coordinates. In order to scan a plane perpendicular to the $(220)_A$ vector h and k are varied such that the condition $h+k=4$ is satisfied. In the experiment for each l-value a line in the h,k-plane is scanned. The so-called reciprocal space map contains the $(220)_A$, the $(040)_A$ and $(004)_A$ Ni_2MnGa peaks. With lower intensity the $\{311\}_A$ and $\{222\}_A$ reflections are in evidence. Similar to the $(200)_A$ peak (observed for samples on MgO) the appearance of the $\{222\}_A$ peaks indicate structural order ($L2_1$), but chemical disorder. In contrast to the MgO(100) substrate surface the $Al_2O_3(11\bar{2}0)$ plane has a twofold symmetry only. The in-plane lattice parameters are defined by the long c-axis of the hexagonal lattice in one direction and a lattice spacing of $2\cos(30°)\cdot a = 8.245\mathring{A}$ in the perpendicular direction. This value is close to that of the long edge of the (110) plane in the Ni_2MnGa austenite unit cell that measures $8.238\mathring{A}$. According to the low mismatch of only 0.08 % one would expect that the $Ni_2MnGa[1\bar{1}0]_A$ direction aligns under 90° to the Al_2O_3 c-axis, which is equivalent with $Ni_2MnGa[001]||Al_2O_3[0001]$. When examining the $(2\bar{2}0)_A$ Ni_2MnGa peak and the (116) Al_2O_3 peak (that determines the *varphi*-angle of the c-axis) these reflections appear at the same φ-angle. Consequently the Ni_2MnGa $[1\bar{1}0]_A$ direction is in fact aligned along the c-axis contradicting the expectation. An illustration of the in-plane alignment of the Heusler unit cell is provided by Fig. 4.6 (b) and (c). An explanation for this crystallographic orientation can be gained by inspecting the atomic distribution at the film-substrate interface. The projection of the $(110)_A$ Ni_2MnGa plane and the $Al_2O_3(11\bar{2}0)$ surface is sketched in Fig. 4.7. When superimposing the two atomic planes a certain match of atomic positions can be achieved. For the $Ni_2MnGa[1\bar{1}0]||Al_2O_3[0001]$ orientation the degree of congruence is increased, compared to the $Ni_2MnGa[001]||Al_2O_3[0001]$

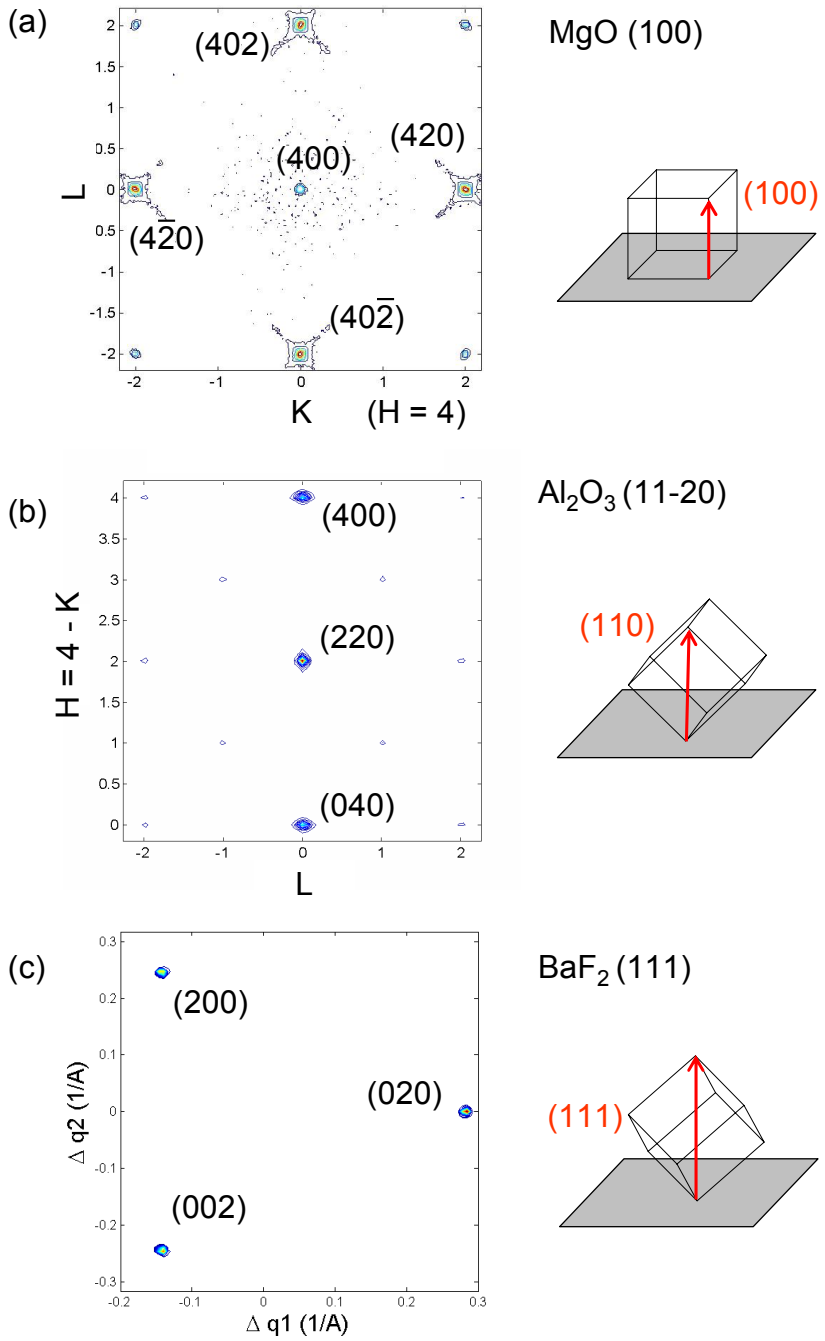

Figure 4.5: Plane scans in the reciprocal space for Ni_2MnGa films on (a) MgO(100), (b) $Al_2O_3(11\bar{2}0)$, and (c) $BaF_2(111)$ substrates. The detected peaks indicate the in-plane orientation of the austenitic unit cell of the Heusler compound as sketched on the right.

configuration (s. Fig. 4.8). The driving mechanism is very likely the chemical bonding between substrate and film elements. One scenario that would explain the observed layer orientation is a preferential arrangement of Mn atoms at oxygen sites of the Al_2O_3 surface. Manganese is known to be highly sensitive to oxidation [109]. Another mechanism that could lead to a lowered free energy at the interface is the coincidence of Ni and Al positions. The formation of NiAl was observed on the surface of samples that were capped by an Al layer at elevated temperature [80]. During film deposition the Ni atoms of the first layer possibly adjust to the Al sites and are preferably attached there. With progressing deposition the $L2_1$ Heusler structure forms on top of the interface. The absence of additional phases in the XRD pattern signifies that such "chemical reactions" are strictly limited to interface.

The third principle growth mode - the Ni_2MnGa (111) plane aligned parallel to the substrate surface - was realized on BaF_2(111) single-crystals. Here, the space map includes the three $\{200\}_A$ peaks that enclose an angle of 54.74° with the surface normal (s. Fig. 4.5 (c)). According to that, the crystallographic orientation of the shape memory film can be tailored by choosing the suitable substrate. All three possible growth modes can be prepared with good epitaxial quality.

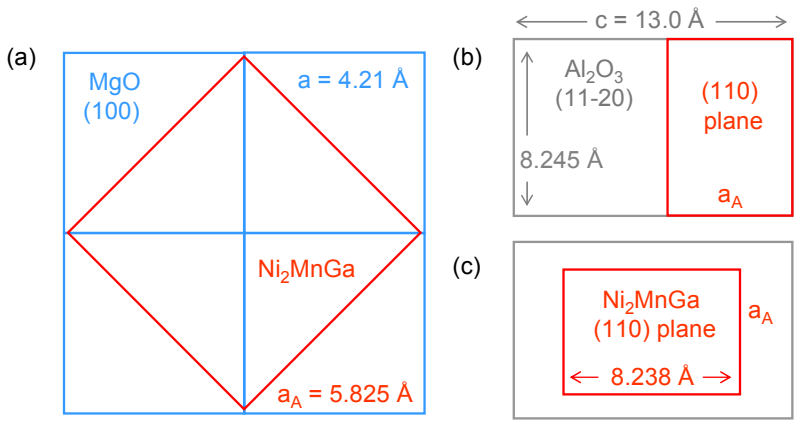

Figure 4.6: (a) Illustration of the in-plane orientation of the Ni_2MnGa austenite unit cell on MgO(100). (b) Expected alignment of the $(110)_A$ film plane on the $Al_2O_3(11\bar{2}0)$ surface. Experimentally observed orientation on sapphire A-plane substrates (c).

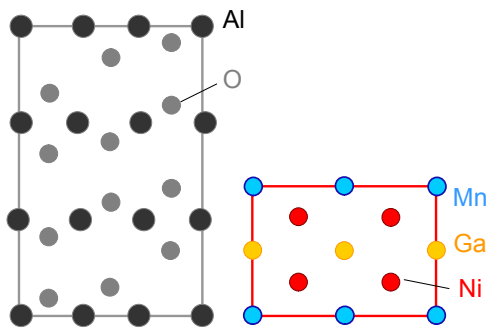

Figure 4.7: Representation of the distribution of Al and oxygen atoms on the $Al_2O_3(11\bar{2}0)$ surface (left) and chemical order of the Ni_2MnGa $(110)_A$ plane (right).

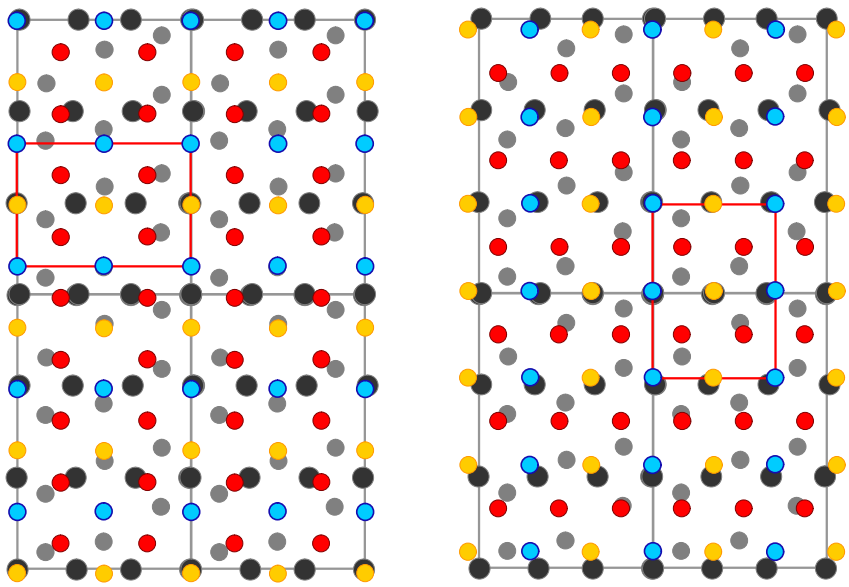

Figure 4.8: Projection of the $(110)_A$ Ni_2MnGa plane onto the $Al_2O_3(11\bar{2}0)$ surface. In a simple picture that considers the lattice parameters only an orientation of $Ni_2MnGa[001]_A||Al_2O_3[0001]$ is expected (left). Experimentally observed is the $Ni_2MnGa[1\bar{1}0]_A||Al_2O_3[0001]$ configuration (right) that increases atomic order at the interface.

For some films prepared on MgO(100) anomalous crystal growth was observed [18]. Instead of the $(400)_A$ peak the $(202)_A$ reflection appears in the 2-circle diffraction pattern as evident from the data presented in Fig. 4.9. This naming convention sets the $[0k0]$ direction parallel to the film surface and thus parallel to the b-axis of the martensite as will be motivated later on. In the austenite phase a disagreement with the conventionally observed orientation on MgO substrates is in evidence for these samples. The alignment of the Ni_2MnGa unit cell contradicts the expected "cube on cube" growth as observed for the vast majority of samples on this substrate material. To identify the orientation relation between film and substrate lattice phi-scans of the $\{220\}_A$ and $\{400\}_A$ Ni_2MnGa reflections and the $\{111\}$ MgO peaks have been carried out. The $\{220\}_A$ peaks enclose an angle of 30° with the substrate surface, the $\{400\}_A$ peaks are detected under 45° to the sample surface. For a single-crystalline film with the (101) plane perpendicular to the φ-axis (= film normal) a single $(400)_A$ peak and under a rotation of $\Delta\varphi = 180°$ a single $(004)_A$ peak will appear. Instead of these two reflections the phi-scan reveals 8 peaks that can be assigned to four different crystallographic variants (s. Fig. 4.10). The additional lines, present in the scan between two $\{400\}_A$ peaks, are tails of the strong MgO $\{220\}$ reflections. These appear at similar values of 2θ, θ and χ at this φ -position, as can be deduced from the phi-scan of the MgO $\{111\}$ reflections. The presence of four austenitic variants is confirmed by

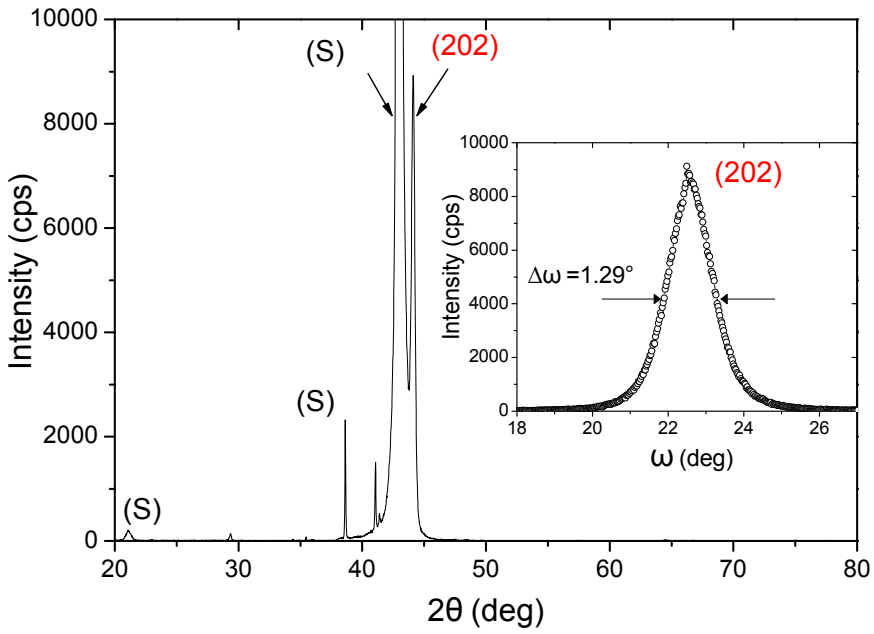

Figure 4.9: For some samples unconventional growth of Ni_2MnGa on MgO(100) is observed by XRD. Besides the substrate peaks (s) the $(202)_A$ instead of the $(400)_A$ film peak appears in the θ-2θ-scan. The inset displays the rocking curve of the $(202)_A$ peak.

the peaks emerging in the phi-scan probing the $\{220\}_A$ reflections. In total the four variants generate 16 peaks, instead of the four that would characterize a mono-crystalline sample. In agreement with the positions of the $\{400\}_A$ peaks the observed intensity maxima can be assigned to the four different variants as indicated by the symbols in Fig. 4.10. Following the symmetry of the substrate surface the variant configuration possesses a fourfold symmetry. Each variant features a tilt of $\pm$ 8° with respect to the MgO in-plane crystal axes. Similar to the in-plane alignment of the austenitic unit cell on $Al_2O_3(11\bar{2}0)$ substrates this can be motivated by inspection of the atomic distribution at the film-substrate interface. The $Ni_2MnGa(101)$ plane has a rectangular symmetry with a diagonal running under $\arctan(2/\sqrt{2}) = 54.74°$ to the [010] edge. Along this direction the density of atoms on the surface is increased. Likewise, the interatomic distance on the substrate surface is shortest for the [011] direction. Dense lines of oxygen atoms run under $\pm$ 45° to the MgO unit cell edges. Assuming that these directions of increased atomic density align parallel one expects four Ni_2MnGa variants with an in-plane rotation of $\pm$ 9.74° to the MgO [010] and [001] direction, respectively. This is in good agreement with the experimentally observed variant alignment. However, the fact that this growth mode was observed only for substrates exposed to air prior to deposition, implies that surface degradation processes play an important role. For MgO(100) single-crystals stored in vacuum or inert atmosphere at all times we found (100) oriented film growth exclusively. Thus, the formation of magnesium hydroxide and carbonate seems to promote the multi-variant growth.

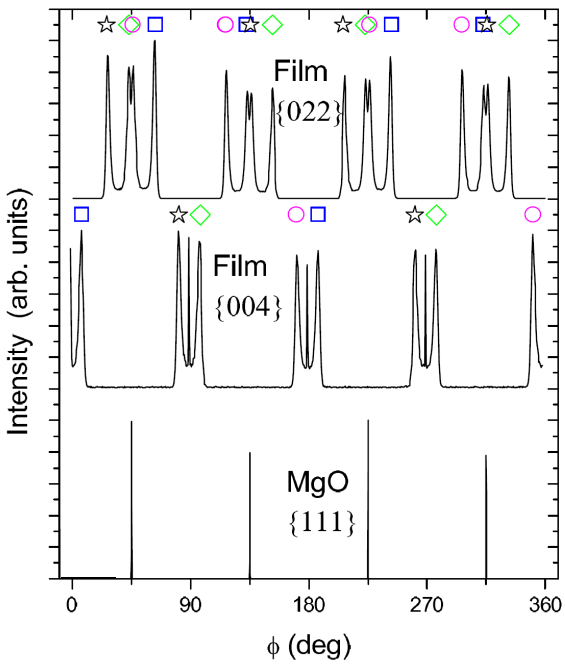

Figure 4.10: Phi-scans of the $\{220\}_A$ and $\{400\}_A$ reflections reveal the multi-variant growth of Ni_2MnGa on MgO(100) substrates observed for some films. The peaks originate from four cubic variants as indicated by different symbols. The lower line displays the phi-scan of the MgO {111} reflections.

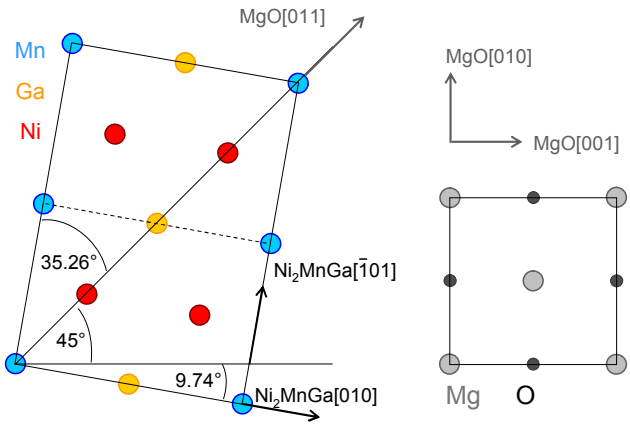

Figure 4.11: Model for the alignment of one Ni_2MnGa variant on the MgO(100) surface in the case of multi-variant growth. The diagonal of the sketched (101) plane points along the MgO[110] direction. This results in an angle of 9.74° between the Ni_2MnGa and the MgO cell edges.

4.2 Structural phase transformation

The samples prepared with the stoichiometric Ni_2MnGa target allow studying of the structural changes associated with the phase transition by cooling in the 4-circle diffractometer. At room temperature, in the austenite, all three lattice parameters of the investigated samples are close to the reference value for bulk samples, i.e. 5.825 $\mathring{A}$ [32]. Consequently, no indication of epitaxial stress is observed. When the sample is cooled below the phase transformation temperature the crystal structure changes from cubic to (pseudo-)orthorhombic or tetragonal. Instead of the uniform austenite lattice parameter (a_A) a short c-axis, a long lattice parameter a and an intermediate b-axis arise. Due to volume conservation the mean value of a-, b- and c-axis is approximately equal to a_A. To preserve the macroscopic volume twin variants will form, which leads to a tilt of the lattice of the different martensitic variants with respect to the lattice of the cubic parent phase. The macroscopic shape of the film cannot change considerably, since the film is fixed to the substrate at the interface. The combination of contraction (elongation, respectively) and tilting of the crystal axes leads to significant changes in the position of diffraction peaks. In general all three reciprocal space coordinates will be altered. In the experiment the sample is mounted onto a copper thread bar that is cooled by the helium gas cryostat, which is attached to the goniometer. To prevent condensation of water the sample is shielded by an evacuated beryllium cylinder. The attenuation factor of the Be cylinder for the used X-ray light is in the range of a few percent only. With the helium cryostat mounted the operation range of the χ-circle is limited to $\pm$ 35°. As a consequence not all reflections are accessible without remounting the sample. By mounting the film under an angle of 22.5° the specular reflection as well as peaks under 45° to the normal can be explored. To study the structural modifications in the low temperature phase a film on MgO(100) is convenient. Changes in the position of the $(400)_A$ peak can be monitored by plane scans in reciprocal space at different h-values using the cubic coordinate system as a reference. Thereby different variants with a common out-of-plane lattice parameter can be detected. At room temperature the sample is in the austenitic phase and consequently a single $(400)_A$ peak is observed. At 180 K the intensity of this reflection is reduced, but the peak does not vanish (s. Fig. 4.12). Besides this reflection no further intensity maxima can be spotted in the plane at h=4.00. In contrast, new peaks arise at h=3.85 and h=4.20, as can be seen in the contour plots of the scattered intensity in the respective reciprocal space planes (Fig. 4.12). These peaks are aligned symmetrically around the k=l=0 position and can be assigned to eight different orthorhombic variants. At h=3.85 the four different variants with a-axis along the h-direction contribute. These variants have the b- and c-axis aligned along the MgO[011] and $[1\bar{1}0]$ directions, respectively. The fourfold symmetry of the substrate is thus reproduced by the variant distribution. Similarly, four variants with a- and b-axis aligned in-plane form. These share the c-axis direction and

contribute to the intensity detected at h=4.20. The lattice constants deduced from the peak positions are $a = 6.05$ Å and $c = 5.54$ Å, resulting in $c/a = 0.92$. The observed variants can be classified as four pairs, where each pair is connected via a twin plane. Two adjoining variants feature a tilt of 4.7° and cause opposing reflections in the planes at h=3.85 and h=4.20. Due to the twinning the a- and c-axis of each individual variant show a tilt of 2.4° with respect to the surface normal. The twin planes, separating two twin variants, form along $(110)_A$ planes. In total six different twin planes will arise, but only the ones running under 45° to the surface normal result in a tilt of the $(400)_M$ reflections. These are the four twin planes that connect the observed eight variants. The residual intensity at h=4.00 could be attributed to remaining austenite as well to the four variants with twin planes running along the film normal. In principle, another set of four orthorhombic variants with b-axis pointing out-of-plane can form. Since the length of the martensite b-axis is close to the lattice parameter of the austenite, these variants will contribute to the peak detected at h=4.00. Therefore it is impossible to distinguish between residual austenite and martensitic variants with $b \approx a_A$ aligned out-of-plane from the scan at h=4.00. To identify these variants scans of the reflections with $k \neq 0$ or $l \neq 0$ like $\{220\}$ are needed. A comprehensive investigation of all possible variants was performed for a sample that is in the martensite phase at room temperature (s. Chapter 4.3).

Temperature-dependent XRD is furthermore a suitable tool to determine the phase transformation temperature of the sample under investigation. For that purpose θ-2θ-scans of a cubic reflection are measured while slowly cooling down the sample. The individual scans are performed at an almost constant temperature. From the evolution of the XRD peak the transition temperature can be ascertained directly. Fig. 4.13 shows the evolution of the Ni_2MnGa $(400)_A$ peak upon cooling from 300 to 200 K for a film on $Al_2O_3(11\bar{2}0)$. At about 270 K the intensity decreases significantly as the sample transforms to martensite. This transformation temperature is in agreement with magnetometry data that indicates a martensite start temperature of 270 K for this sample. When the film transforms to the orthorhombic phase most reflections observed for the cubic parent phase vanish, since the lattice plane distances are changed. This is not the case for peaks that contain contributions from a- and c-axis like the (202). In contrast to the $(400)_A$ the intensity of the specular $(220)_A$ peak does not decrease considerably (s. Fig. 4.14). This means the distance between the atomic layers along the film normal does not change significantly during the phase transition. Thus, the arising martensite peak contains contributions of the short c- as well as the long a-axis. Accordingly, the preferred naming convention is $(202)_M$, which sets (abc) parallel to (hkl). For a comparable film on MgO the lattice constants are known to be $a_M = 1.038a_A$ and $c_M = 0.952a_A$ leading to nearly identical lattice plane distances $d_{202,M}/d_{220,A} = 0.992$ in both phases. To achieve a consistent description in reciprocal space for both phases it is useful to chose a right-handed coordinate system with k-axis in the film plane. The specular reflection is then

labeled (202) for austenite and martensite.

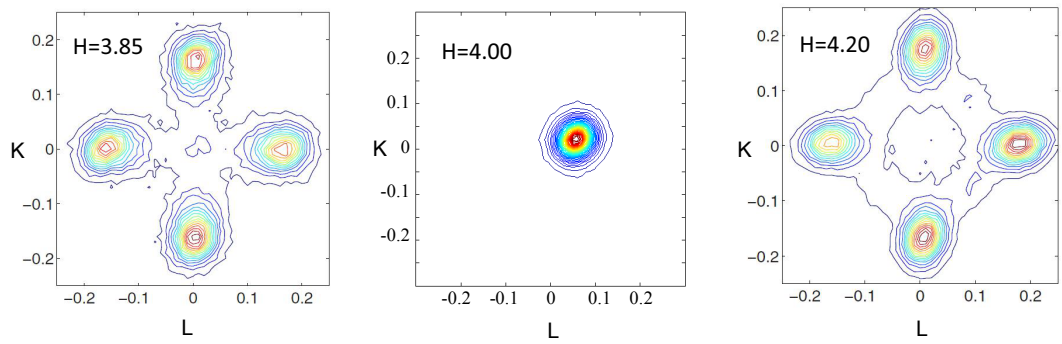

Figure 4.12: Contour plot of the scattered intensity in a (k, l)-plane at h=3.85 (left), h=4.00 (center) and h=4.20 (right). The sample was cooled well below the martensite start temperature. The intensity of the single (400) austenite peak at h=4.00 is decreased in the low temperature phase. The arising martensitic peaks can be assigned to eight different orthorhombic variants.

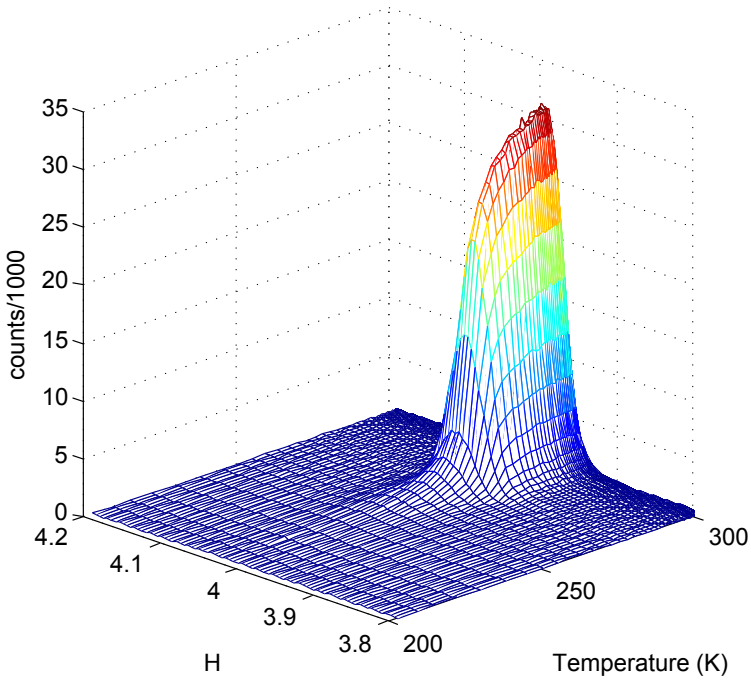

Figure 4.13: Temperature evolution of the cubic $(400)_A$ reflection of a Ni_2MnGa film on $Al_2O_3(11\bar{2}0)$. Around 270 K the transformation to martensite starts, which causes a clear drop in scattered intensity.

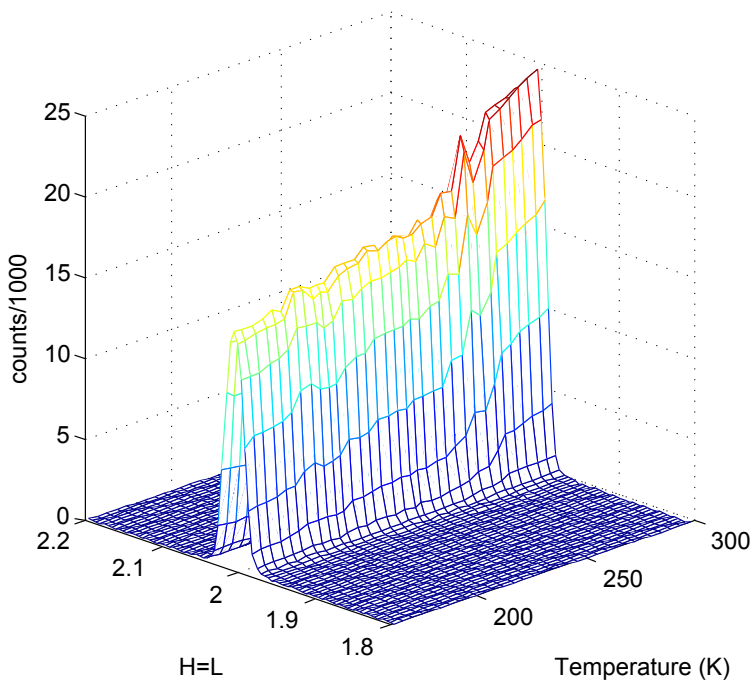

Figure 4.14: In contrast to the $(400)_A$ reflection the temperature evolution of the specular Ni_2MnGa $(202)_A$ peak features only a slight intensity decrease. This means the lattice plane distance along the film thickness is similar for both phases.

4.3 Martensite crystal structure

4.3.1 Films on $Al_2O_3(11\bar{2}0)$ substrates

A detailed study of all different crystallographic variants in the martensite is possible for samples that transform to the cubic phase above room temperature. This is the case for films prepared with the off-stoichiometric targets 3-5 and suitable deposition parameters. Without the limitations in the operating circles, when the He-gas cryostat is attached, a comprehensive mapping of the reciprocal space is feasible. For films grown on $Al_2O_3(11\bar{2}0)$ substrates the XRD pattern taken with the 2-circle diffractometer looks identical for all samples. In the θ-2θ-scans the (202) peak appears around 2θ=44° for all films. This is only a true $(202)_A$ reflection for the samples that are in the cubic phase at room temperature. For the films that are martensitic at 300 K it is a pseudo $(202)_A$ peak as described in the previous section. The formation of twin boundaries along the cubic $[10\bar{1}]$ direction allows for conservation of the out-of-plane lattice plane distance (s. Fig 4.15). The a- and c-axis of the two arising orthorhombic variants point roughly under 45 °to the surface normal, while the twin planes are aligned parallel to the film plane. Accordingly, the specular reflection for the martensitic films is

labeled as $(202)_M$, which sets (hkl) parallel to (abc). The b-axis of the martensite is then aligned in-plane and $\perp$ $Al_2O_3[0001]$. Along this $[010]_M$ direction the lattice parameter is not expected to change significantly. The conservation of the layer distance along the film normal requires lateral sliding of the atomic planes as illustrated in the model displayed in Fig. 4.15. Depending on the c/a ratio the $[100]_M$ and $[001]_M$ directions show a tilt of a few degrees with respect to the cubic lattice. The macroscopic volume of the film can be preserved by the formation of alternating twin variants with opposite direction of tilt. Starting from the substrate-film interface a first orthorhombic variant (= variant 1) can emerge by either sliding the atomic layers towards $[\bar{1}01]_A$ or $[10\bar{1}]_A$. The martensite unit cell is then tilted with respect to $[101]_A$ depending on the sliding direction. After some lattice planes a twin boundary is introduced that transforms variant 1 into

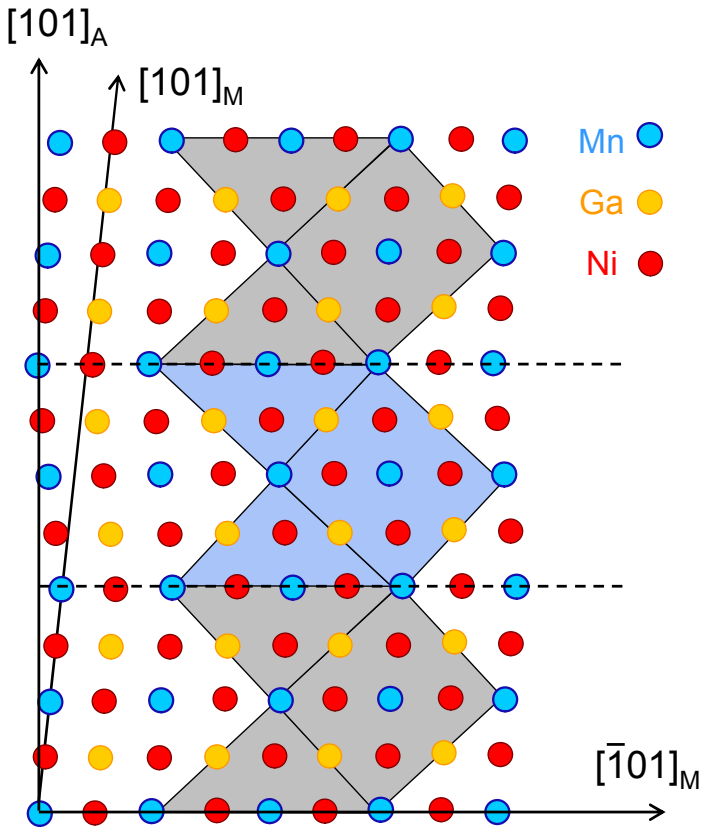

Figure 4.15: Model for twin plane alignment in Ni-Mn-Ga films on Al_2O_3 substrates. The b-axis points into the plane of projection for both variants. The twin planes, separating variant 1 (gray) and variant 2 (blue) are aligned parallel to the film surface. Thus, a habit plane can form at the film-substrate interface.

variant 2. A second twin plane recovers variant 1. Depending on the stacking sequence some of the twin planes will act as habit planes. In this plane the atomic positions are not changed during the phase transformation. This is of importance for the film-substrate interface, where the atoms cannot move easily. The variant configuration proposed by the model in Fig. 4.15 approves a habit plane at the interface. When looking at the $[101]_M$ direction it strikes that this vector is no longer orthogonal to the (101) lattice planes. This contradicts intuition, since all angles of the reciprocal lattice are preserved for an orthorhombic system. Consequently the reciprocal lattice vectors with one index only are orthogonal to the respective lattice planes. This is not the case for direction with more than one index different from zero.

The proposed twin plane configuration is validated in the XRD experiment. When scanning the plane around the $(202)_M$ peak (parallel to the film surface) no further reflections are detected. If there is a fraction of variants with twin boundaries running vertically (along $[101]_A$), these variants will cause a splitting of the $(202)_M$ peak. This is not in evidence in the XRD scan that shows a single peak at $h = l = 2$ and $k = 0$. This means that vertically aligned twin planes play only a minor role in the martensite structure of the investigated samples on $Al_2O_3(11\bar{2}0)$ substrates. The absence of further reflections in this reciprocal space plane is, in addition, an argument against twin planes running along $[110]_A$, $[1\bar{1}0]_A$, $[011]_A$, and $[01\bar{1}]_A$ directions. In agreement with twinning parallel to the film plane a peak splitting is observed for the $(220)_A$, $(2\bar{2}0)_A$, $(022)_A$, and $(0\bar{2}2)_A$ reflections, since no compensation of a- and c-axis is present here. These peaks appear two-fold split and can be assigned to two orthorhombic variants with $a_1 = 6.14$ Å, $b_1 = 5.76$ Å, $c_1 = 5.44$ Å and $a_2 = 6.12$ Å, $b_2 = 5.75$ Å, $c_2 = 5.44$ Å. The observed $c/a = 0.89$ leads to a rotation of the martensite unit cells of $\pm$ 3.35° due to the twinning. For both variants the rotation axis is the shared b-axis that is aligned in-plane, as illustrated in Fig. 4.16. In the side view, i.e. along the k-axis, variant 1 (red) is tilted to the left, while variant 2 (green) is rotated clockwise. To assign the measured XRD peaks to the two orthorhombic variants, two right-handed coordinate systems in reciprocal space are used (s. Fig. 4.17). A rotation of 180° around the film normal transforms one coordinate system into the other. A description that uses the mirror symmetry across the twin boundary would result in a left-handed coordinate system for one of the variants. A to scale model of the detected XRD peaks in reciprocal space is provided by Fig. 4.17. In the experiment the contributions of the two variants can be distinguished clearly. Furthermore superstructure peaks are detected along $[\bar{1}10]_M$ and $[\bar{1}\bar{1}0]_M$ reciprocal space directions for both variants. These superstructure reflections fit to a 7-layered modulated structure (7M/14M), that was previously reported for bulk samples [49, 110]. The scattered intensity that is detected when scanning along $[\bar{1}10]_M$ in reciprocal space is plotted in Fig. 4.18. The line scan includes the $(202)_M$ and $(022)_M$ reflections of variant 1. Between these strong peaks six satellite peaks appear with a spacing of 1/7 of the total distance. The

slight deviation in the peak position indicates that the structure is not fully commensurate. This agrees with crystallographic studies on polycrystalline samples, that revealed an incommensurately modulated phase [111]. In the vicinity of the $(202)_M$ and $(022)_M$ peaks additional intensity maxima are visible. These peaks can be attributed to the second variant or some residual austenite. As illustrated in Fig. 4.17 the density of superstructure peaks is high around the shared $(202)_M$ peak. Close to the $(022)_M$ reflection of variant 1 (red) the additional intensity in the line scan (Fig. 4.18) is probably a tail of the $(0\bar{2}2)_M$ peak of variant 2 (green). The respective line scan in the coordinate system of the second variant leads a similar diffraction pattern. As depicted in the model no satellite peaks appear along $[01\bar{1}]_M$ and $[0\bar{1}\bar{1}]_M$, which is a consequence of the reduced symmetry in the martensite. In contrast to the cubic parent phase these directions are not equivalent for the modulated orthorhombic phase, since different lattice planes are involved here.

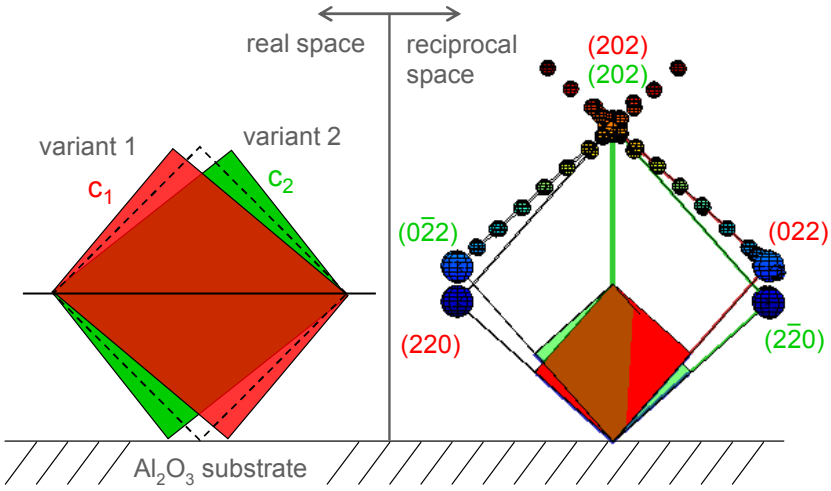

Figure 4.16: Illustration of the observed variant configuration in samples on $Al_2O_3(11\bar{2}0)$ substrates (left). The formation of two orthorhombic variants with twin planes parallel to the film plane leads to a peak splitting of the $\{220\}_A$ reflections as illustrated in the right half. The specular $(202)_M$ peak contains contributions of both variants. The superstructure peaks observed in XRD line scans are included in the reciprocal space model.

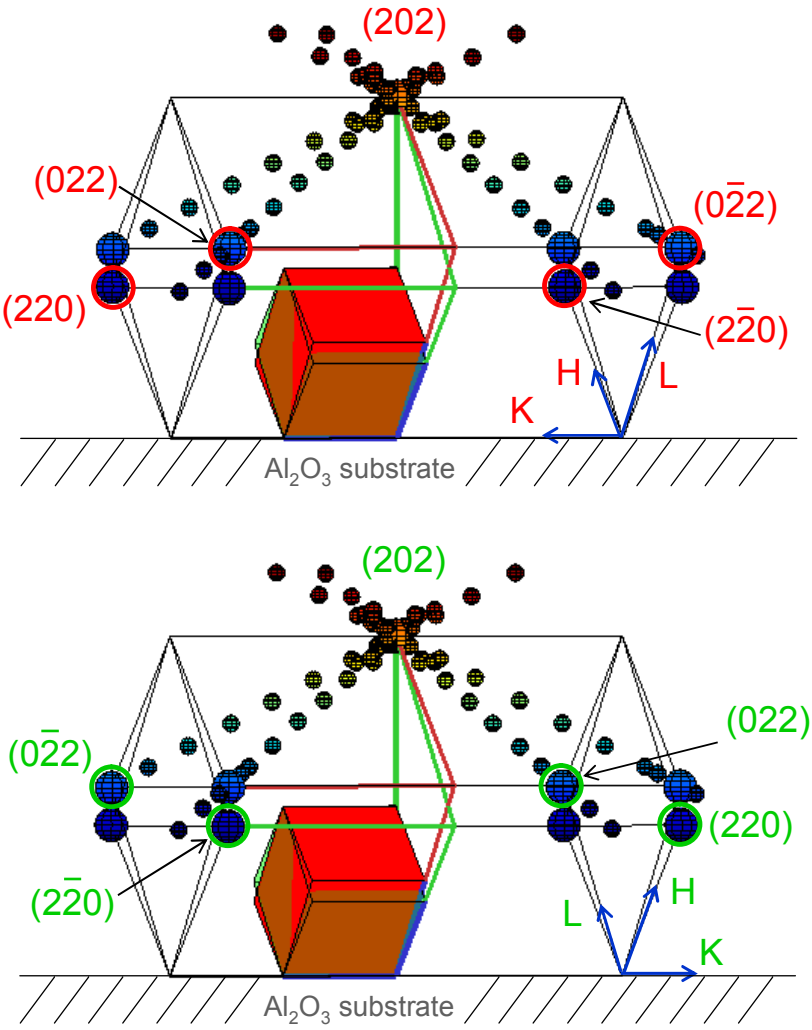

Figure 4.17: The observed XRD peaks can be assigned to two orthorhombic variants that share the b-axis, which is aligned in-plane. Each variant is described by a right-handed coordinate system in reciprocal space. The model contains the $\{220\}_M$ reflections and the observed superstructure peaks along $[\bar{1}10]_M$ and $[\bar{1}\bar{1}0]_M$ directions.

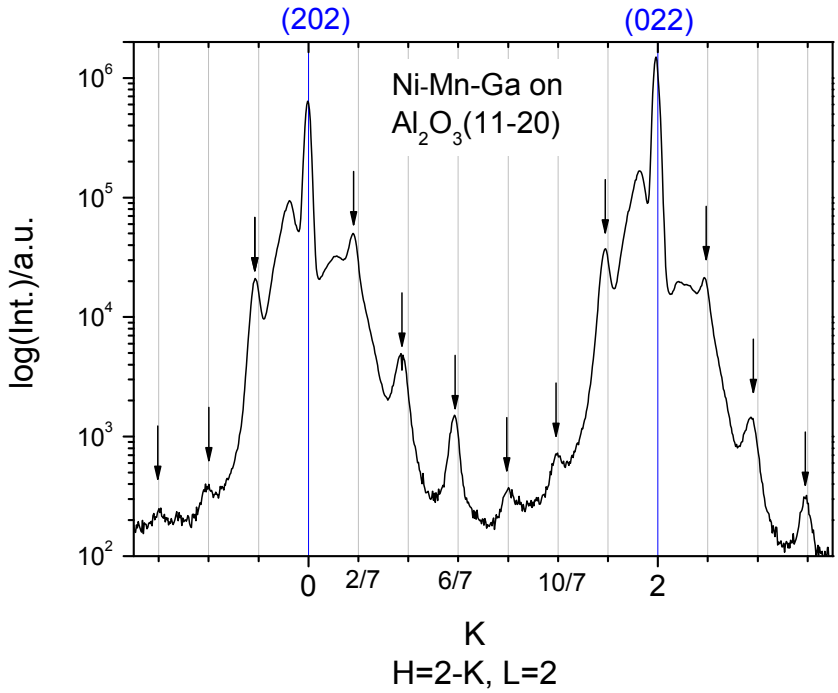

Figure 4.18: The 7-layered orthorhombic superstructure can be detected directly in a line scan along $[1\bar{1}0]_M$ in reciprocal space. This line includes the (202) and (022) peaks of one martensitic variant. The slight deviations of the superstructure peaks from the calculated positions (grid lines) indicate that the structure is not completely commensurable.

4.3.2 Samples on MgO(100) substrates

The crystalline quality of the Ni-Mn-Ga films prepared on MgO substrates can be improved by introducing a Chromium buffer layer. The films deposited on this sacrificial buffer layer show a reduced rocking curve width of typically 0.4°. Analog to the Heusler compound the Cr grows epitaxially on MgO with a 45° in-plane rotation of the unit cell with respect to the MgO lattice. In the θ-2θ-scan the sharp Cr (200) peak appears at $2\theta = 64.58°$ (s. Fig. 4.19). The associated ω-scan of the Cr (200) Bragg peak has a FWHM of 0.28° only, which proves the good epitaxial growth. Close to the Cr (200) peak a second reflection in the diffraction pattern (Fig. 4.19) is visible at $2\theta = 63.58°$. The peak position is not far from the expected 2θ-value of the Ni_2MnGa austenite (400) peak. In fact, the investigated sample is in the martensitic phase at room temperature. This is revealed by a detailed study of the variant configuration with the help of the 4-circle diffractometer. It turns out that the peak observed in the θ-2θ-scan is caused by the predominant variants that have the b-axis aligned along the film normal. To stick to the naming convention the peak has to be designated as $(040)_M$. That the film is indeed in the martensite phase is proved by the reciprocal space scan that maps

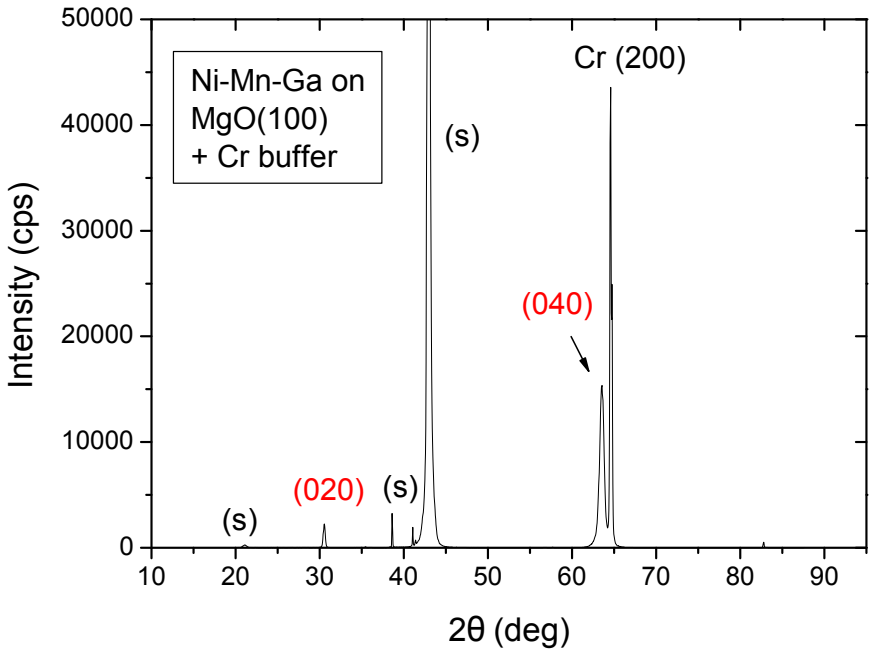

Figure 4.19: θ-2θ-scan of a Ni-Mn-Ga film grown on MgO(100) with a Chromium buffer layer. Besides the substrate peaks (s) the $(020)_M$ and $(040)_M$ Ni-Mn-Ga reflections (red) and the Cr (200) peak are visible.

the (h, l)-plane at k=2 (s. Fig. 4.20). The contour plot of the scattered intensity clearly shows a peak-splitting of the cubic $\{220\}_A$ reflection group. Around the central peaks that can be attributed to the Cr or austenitic Ni_2MnGa four peaks appear at position that are shifted in h and k by $\pm$ 0.1. These reflections can be assigned to four orthorhombic variants with a- and c-axis aligned in-plane. Figure 4.20 contains an illustration of the four variants that consist of two sets of twins. The related twin boundaries run along $[101]_A$ and $[10\bar{1}]_A$ directions respectively. Each of the variants features a tilt of $\pm$ 3° with respect to the austenite lattice. In detail, the rotation direction is opposite for the two variants forming a twin pair (in the model: variant I/II and III/IV respectively). Accordingly, the c-axes of the adjoining variants enclose an angle of 51°. The lattice parameters calculated from the peak positions are a = 6.10 $\AA$, b = 5.85 $\AA$, c = 5.51 $\AA$. Since a description of the four variants with four independent coordinate systems would be confusing, we use the cubic system as a basis here. To check for further variants (h, l)-plane scans at k=3.8, 4.0 and 4.2 were performed. At k=4.0 the described variants with a- and c-axis aligned in-plane can be observed, while variants with c-axis pointing out-of-plane contribute at a higher k-value ($\approx$ 4.2). If the long a-axis is aligned along the film normal the related $(400)_M$ peak is observed at a decreased k-value. As a consequence of the twinning the lattice of the martensite variants is rotated with respect to that of the cubic parent phase.

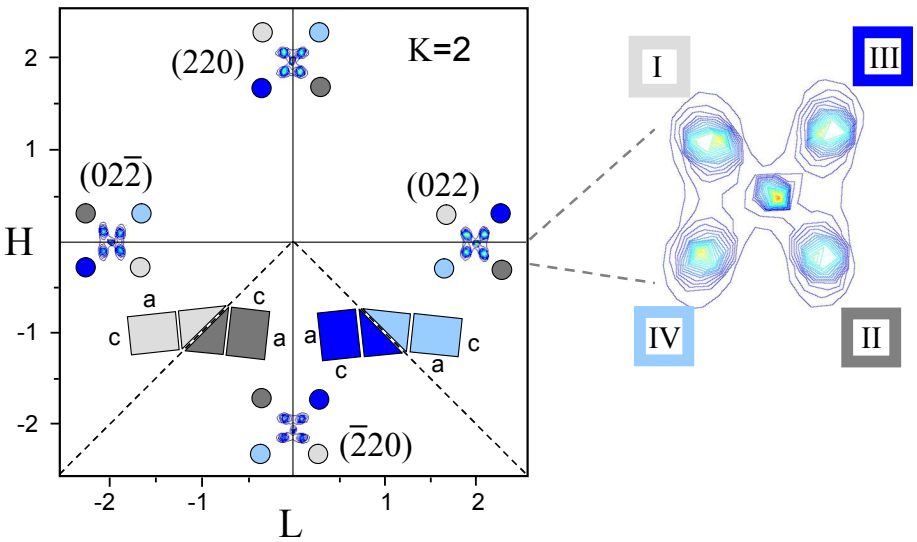

Figure 4.20: $(h2l)$ scans of the $\{220\}_M$ reflections of a Ni-Mn-Ga film on MgO(100) with a Cr buffer layer. On the right a close-up of the martensitic (022) reflections is provided. The central peak is the Cr (011) reflection. The surrounding intensity maxima can be assigned to four orthorhombic variants (I-IV) as illustrated in the lower half. The twin planes separating these variants run along $[101]_A$ and $[10\bar{1}]_A$, so that a- and c-axis are in the film plane.

Thus, the martensitic {400} reflections are not observable in the Bragg-Brentano scan (Fig. 4.19), as they differ not only in 2θ, but in χ too. Figure 4.21 shows plots of the measured intensity at k=4.0 and k=4.2. The single peak at h=l=0, k=4.0 contains intensity contributions of the four observed variants that feature a normally aligned b-axis. The twin planes separating these variants run perpendicular to the film plane and the rotation axis of the orthorhombic unit cells is the b-axis. If the b-axis is aligned in the film plane, the twinning leads to a tilt of the out-of-plane crystal axis. This is observed in the plane scan at k=4.2, where four peaks are detected. In agreement with the lattice parameters, calculated on basis of the $\{220\}_M$ peak positions, the reflections are shifted by $\pm$ 0.2 in h and l. Consequently these peaks originate from four variants with a- and b-axis in-plane and c-axis aligned along the film normal. The twin planes that intersect these variants run under 45° with respect to the film surface. This is also the case for the variants that have the a-axis perpendicular to the surface. The plane scan at k=3.8 that probes these four variants looks similar to that at k=4.2. In total, all twelve possible orthorhombic variants have been identified in this sample. By comparing the integrated peak intensities the quantitative variant distribution can be estimated. The evaluation of the $\{220\}_M$ peaks indicates that the four variants with b-axis normal are uniformly distributed. Same is true for the four variants with a-axis normal and the remaining four with c-axis normal. When

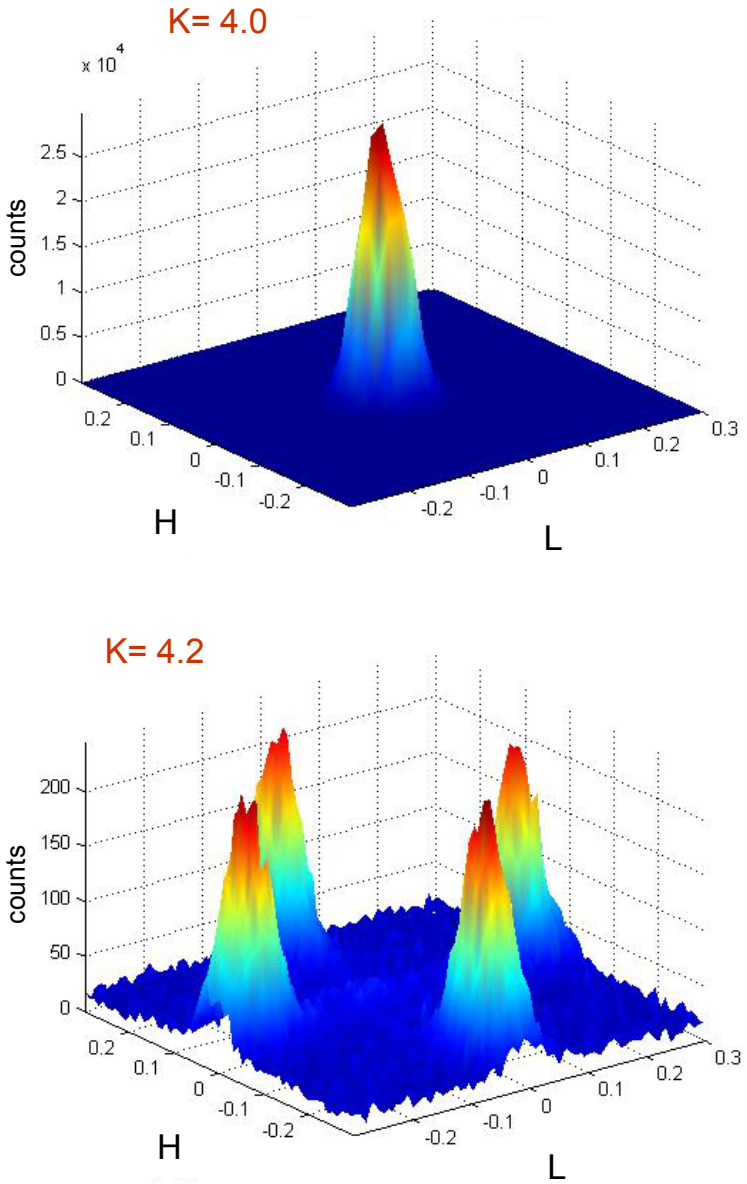

Figure 4.21: The 3D contour plots of the intensity detected by (h, l)-scans at k=4.0 (upper) and k=4.2 (lower) reveal the multi-variant character of the martensite. Likewise the scan at k=4.2 in the plane scan at k=3.8 (not shown) four variants with b-axis aligned in-plane are detected. The four variants with b-axis normal contribute to the single peak at k=4.0.

comparing the intensities of the $\{400\}_M$ peaks one notices a strong asymmetry. The fraction of variants with b-axis normal amounts to 86 %, while these with a- or c-axis normal add up to 7 % each. This is in contrast to observations

on comparable samples prepared on MgO(100) substrates by other groups that feature mainly variants with a- and c-axis aligned out-of-plane [112, 113]. The b-axis that fits the MgO lattice best is then arranged on the substrate surface. However, our samples prepared from off-stoichiometric targets exhibit only a minor fraction of variants with b-axis aligned in-plane. The mechanism that drives this variant configuration presumably involves minimization of the magnetostatic energy of the film. If the magnetic easy axis, which is the short crystallographic axis, is aligned in the film plane the magnetic stray field energy is reduced. The formation of domains with magnetization vector in-plane allows for flux closure and thus low magnetic stray field energy. To fulfill the geometrical constraints at the film-substrate interface the long a-axis is arranged parallel to the surface too. Since $(a+c)/2 = 5.81\mathring{A} \approx a_A$, the stress at the interface is considerably lower for variants with that combination of lattice parameters. The resulting mismatch of the atomic positions associated with the rotation of the orthorhombic unit cell is compensated by the formation of fine-twinned structure as described in chapter 5.2. The picture of a variant configuration that is controlled by magnetostatic energy minimization is supported by observations of Thomas et al. on a free-standing film [88]. After releasing the film from the NaCl substrate the variant distribution was found to be changed. In contrast to the substrate-constrained film the majority of variants in the released sample has the c-axis aligned in the film plane. Before dissolution of the NaCl substrate only a small fraction of these variants was observed. A change in the crystal structure is also reported for Ni-Mn-Ga released from the MgO(100) substrates by the sacrificial buffer layer technique [112]. Due to the low intensities in the XRD scans performed on the released film a quantitative analysis of the variant distribution was not possible in that case. In contrast, our sample under investigation shows distinct Bragg peaks after releasing it from the substrate. Fig. 4.22 presents scans of the $(220)_M$ reflection group before and after removing the Cr buffer layer by selective chemical etching. The central peak before releasing the film is the Cr (110). At this position the $(220)_A$ peak caused by a residual austenite fraction would also be observable. Thus, the scattered intensity can contain contribution of both Cr layer and Ni-Mn-Ga austenite phase. When repeating the measurement on the released film, the intensity of this peak is decreased significantly. Assuming a complete removal of the Cr the remaining austenite phase can be estimated to be below 4 %. It is also possible that the Cr etch process is not complete and the remaining intensity is the Cr (110) peak. Regarding the intensity maxima of the $(220)_M$ reflections no changes due to the release process are observed. Still the four predominant variants are uniformly distributed. The count rates at the peak maxima are just affected marginally. This is also the case for the $\{400\}_M$ peaks. Hence, the variant distribution in the freestanding film is the same as in the substrate-constrained state.

In agreement with the results obtained for off-stoichiometric films prepared on $Al_2O_3(11\bar{2}0)$ substrates the comparable samples on MgO(100) exhibit a modu-

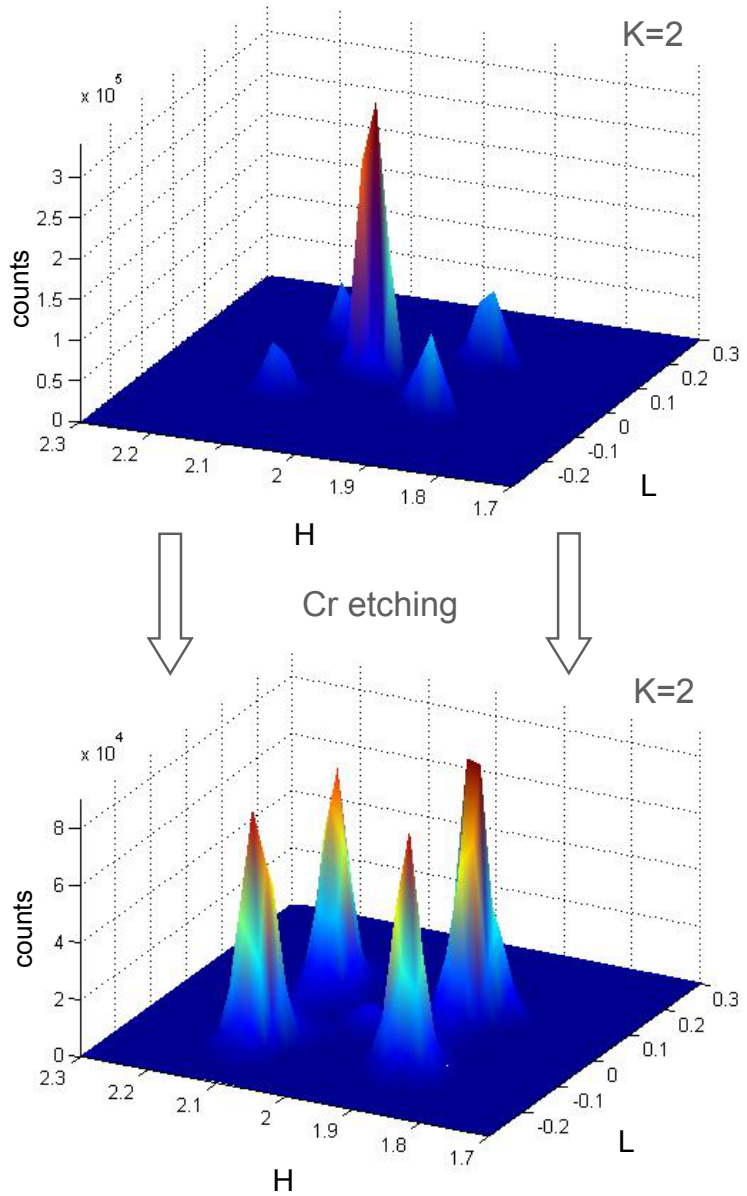

Figure 4.22: Comparison of the $(220)_M$ reflection set before and after releasing the film from the substrate. The central peak in the measurement on the substrate-constrained film (upper) is the Cr(110) reflection. In addition, an intensity contribution of residual austenite at this position is possible. After etching the Cr layer this peak has almost vanished (lower). The remaining intensity can be attributed to residual Cr or a small fraction of austenite. The intensity of the $(220)_M$ peaks is not affected significantly by the release process.

lated structure with a period of seven (or 14) layers. The 7M/14M superstructure is evident in the four line scans in reciprocal space taken for the individual variants with b-axis perpendicular. These scans connect the intensity maxima of the $(022)_M$ reflection group with the specular $(040)_M$ peak (s. Fig. 4.23). In the reference system of the individual variants this represents a $[\bar{1}10]_M$ direction for variants I and IV, but a $[01\bar{1}]_M$ direction for variants II and III (compare to the variant model in Fig. 4.20). Likewise the previous results the modulation is only present along directions that contain a contribution of the a- and b-axis, which is the case for variants I and IV. Analog to the variant distribution the superstructure is not altered by the release process. Both, substrate-bound and freestanding film, exhibit the 7M/14M structure (s. Fig. 4.24). The line scans along $[\bar{1}10]$ reciprocal space direction for variant I look almost identical. This means the crystal structure and variant distribution do not change during the release process. In particular, there is no indication of relaxation of epitaxial stress or variant redistribution due to magnetostatic energy reduction.

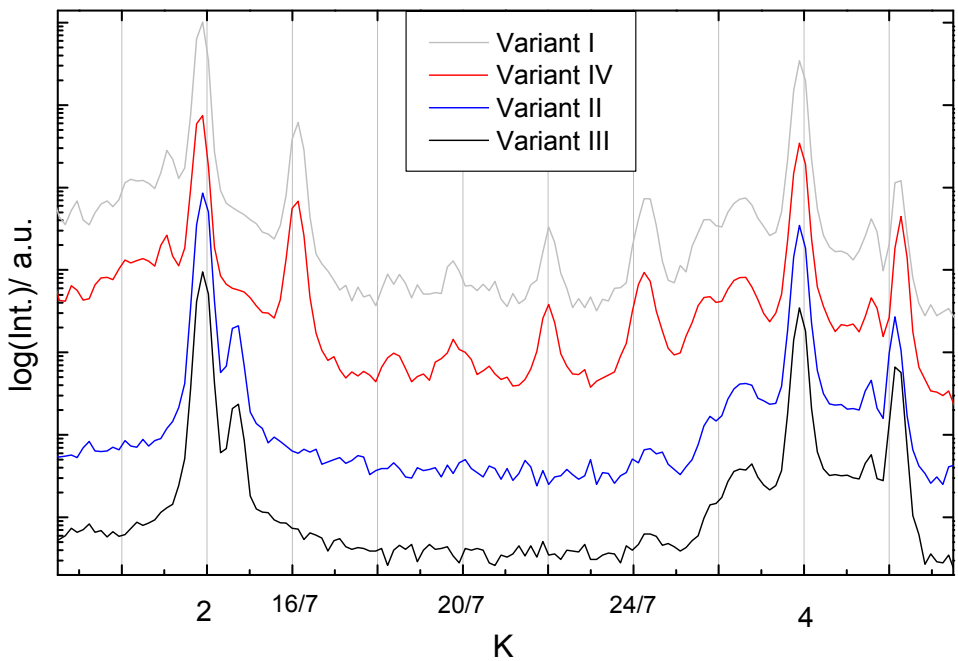

Figure 4.23: The 7M/14M modulation is observed for scans along $[\bar{1}10]_M$ directions (variants I and IV), while no superstructure appears along $[01\bar{1}]_M$ (variants II and III). The line scans connect the specular $(040)_M$ peak and the four martensitic (220) reflections.

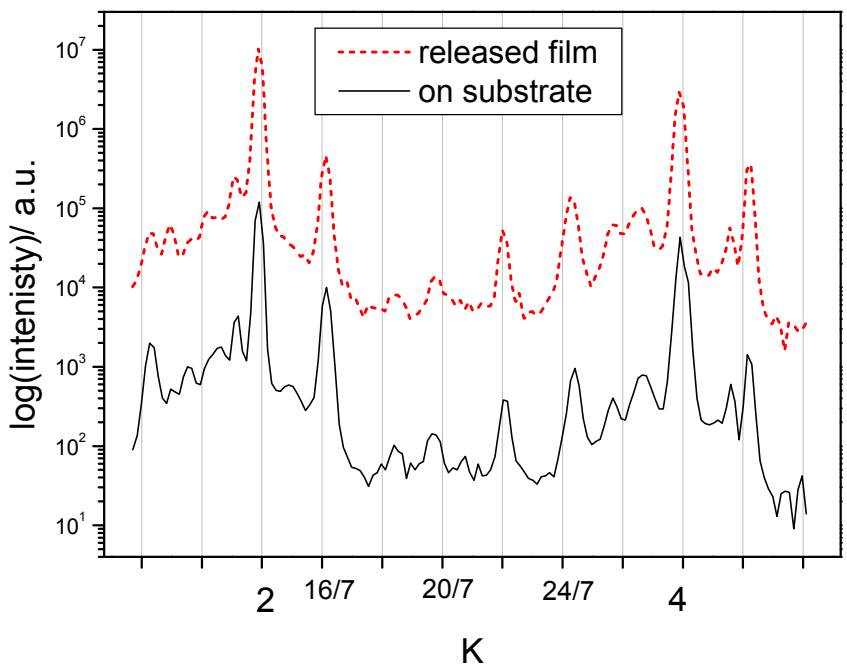

Figure 4.24: The observed modulation is not altered by the release process that involves chemical etching of the Cr layer. Both substrate-constrained (black line) and freestanding (red broken line) film exhibit the 7M/14M structure along $[\bar{1}10]_M$ in reciprocal space coordinates.

4.3.3 NaCl(100) substrates

A crystallographic study of the films prepared on NaCl(100) substrates is problematic, because of the strong buckling of the Ni-Mn-Ga layer on the substrate. The wavy surface decreases the intensity of the scattered X-ray light significantly. The effect is less severe for the released film that is carried by a silicon substrate. For such a sample the θ-2θ-scan reveals a (110) orientation, which disagrees with the (100) orientation of the substrate (s. Fig. 4.25). Instead of the expected Ni-Mn-Ga (400) peak the prominent (220) reflection appears in the diffraction pattern. Fig. 4.25 also provides a calculated XRD pattern for a polycrystalline Ni_2MnGa powder sample. The comparison to the simulated powder pattern shows that the film does not grow epitaxially, but features a (110) texture. This is also confirmed by the profile of the ω-scan of the (220) peak that shows a width of 4.5° (s. Fig. 4.26). The FWHM value clearly exceeds the ones typically measured for films on Al_2O_3 and MgO substrates and indicates a certain mosaic spread of the crystallites. To detect a preferential in-plane orientation of the crystallites a phi-scan of the $\{400\}_A$ peaks was performed (s. Fig. 4.27). In agreement with the observed out-of-plane texture two sets of $\{400\}_A$ peaks appear in the scan. The peaks can be assigned to two variants that differ by 90° in phi (= film

normal). The number of variants is in analogy to the samples on $Al_2O_3(11\bar{2}0)$ a consequence of the two-fold symmetry of the austenitic (110) plane. In summary, the desired single-crystalline character of the MSM layer was not achieved for the films deposited on NaCl substrates. Besides the problems in the preparation process (s. chapter 3.2), the poor crystalline quality of the films released from NaCl is a major drawback for this sacrificial substrate material.

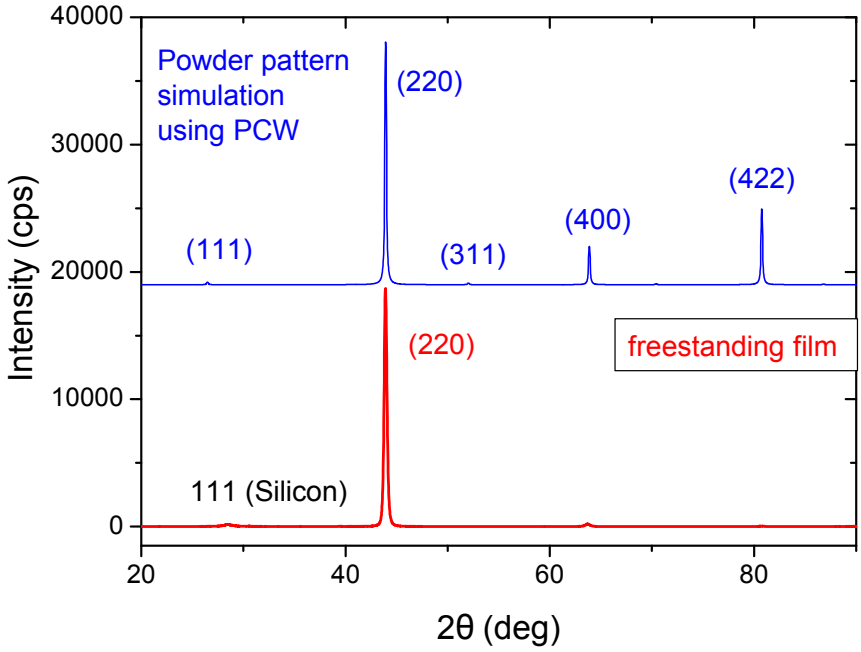

Figure 4.25: The θ-2θ-scan indicates a strong (110) texture in freestanding films that have been released from NaCl(100) (red curve). For comparison the calculated XRD pattern for a polycrystalline powder sample is displayed (blue). Besides a weak $(400)_A$ peak only the strong $(220)_A$ reflection is present. Hence, the Ni_2MnGa film features a (110) texture, though the substrate is (100) oriented.

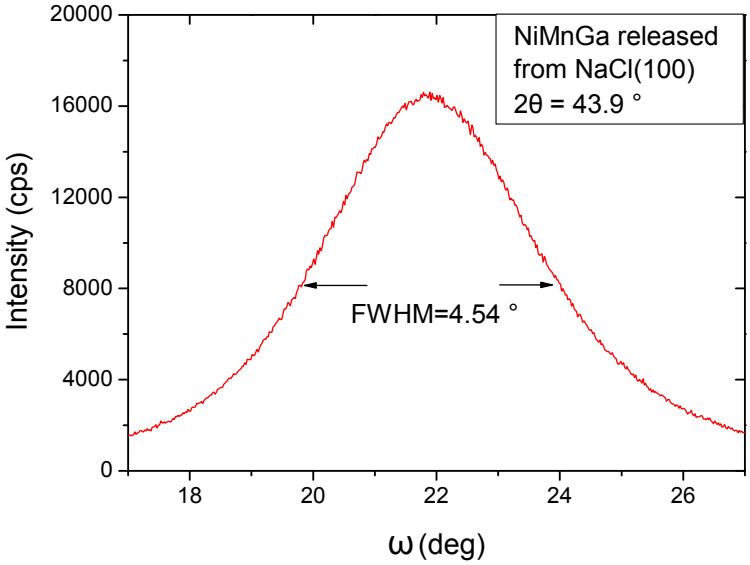

Figure 4.26: The ω-scan of the specular $(220)_A$ peak shows a Gaussian broadening with a FWHM value of 4.5°. Accordingly, the sample is not single-crystalline, but textured only.

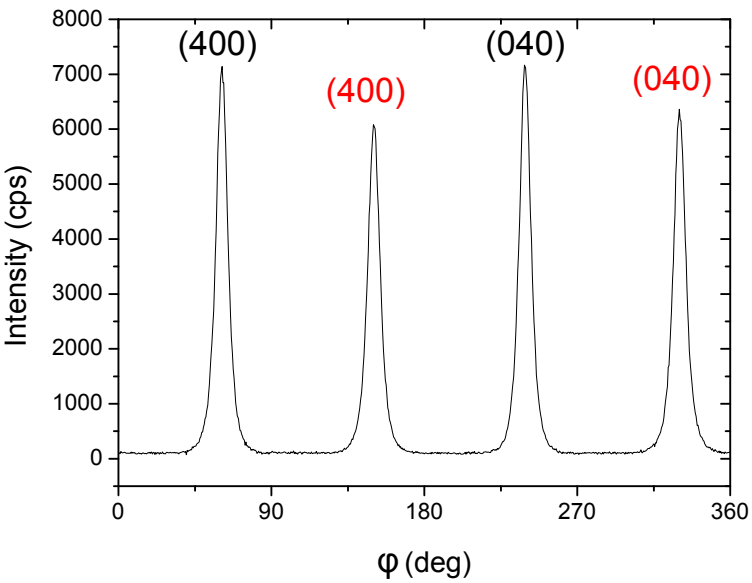

Figure 4.27: The four peaks in the phi-scan of the {400} austenite reflections can be assigned to two variants that differ by 90° in phi. The observed symmetry is a consequence of the two-fold symmetry of the (110) plane.

4.4 Magnetic field assisted XRD

Any magnetic field induced strains (MFIS) in shape memory alloys involve a reorientation - or more precisely redistribution - of variants. Such a magnetically induced reorientation (MIR) of variants can be directly monitored by XRD on a sample exposed to a magnetic field. The variants with magnetic easy axis (= c-axis in the orthorhombic system) parallel to the external field will grow in cost of those that have the c-axis approximately perpendicular to the field. The transformation between the variants is moderated by twin boundary motion. To study the variant redistribution under the driving force of a magnetic field the 4-circle diffractometer was upgraded with a solenoid and a set of permanent magnets within the scope of a diploma thesis [114]. Due to geometrical restrictions associated with the beamline the setup allows only application of the magnetic field parallel to the film plane. This is sufficient to manipulate the variant distribution in the previously described sample on MgO. By applying the field along $[100]_A$ or $[001]_A$ directions, respectively, a clear energy difference for two adjoining variants is provoked. If a redistribution of the four predominant variants occurs, the

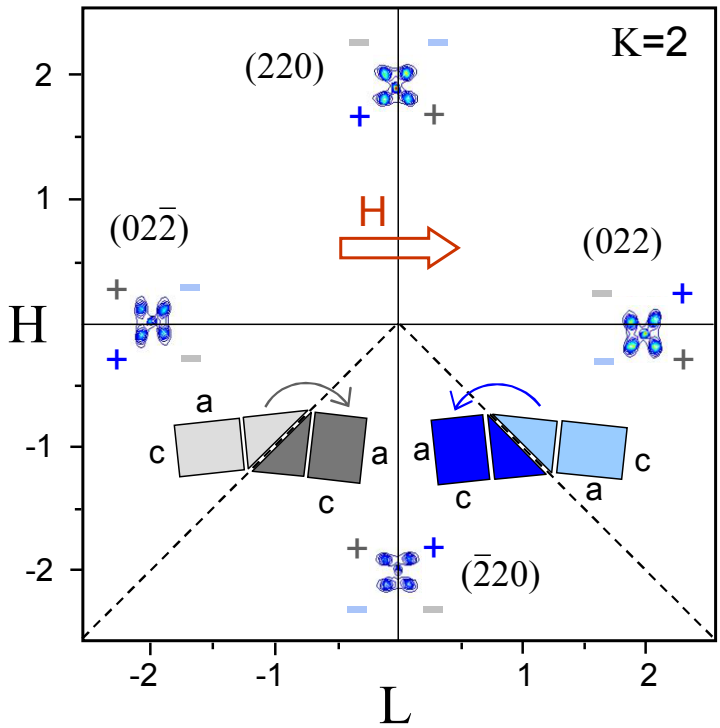

Figure 4.28: Expected changes in the $\{220\}_M$ peak intensities for application of an magnetic field along $[001]_A$. The peaks related to variant II (dark gray) and variant III (dark blue) are expected to increase, while the peaks assigned to variants I (light gray) and IV (light blue) should decrease in intensity.

relative intensities of the $\{220\}_M$ reflections will change. The expected changes are illustrated in Fig. 4.28. In the experiment the magnetic field was applied along the $[001]_A$ direction, which should lead to an increase of variants II and III and a respective decrease of variants I and IV. The observed changes in the related $\{220\}_M$ were not consistent with the expected intensity variations. While the small changes observed for the $(220)_M$ reflection group seemed to confirm the proposed variant redistribution, the modifications in the $(022)_M$ peak set contradicted the model. Here the intensity changes indicated an increase of variant I and II and a reduction of variants III and IV, which cannot be explained by twin boundary motion. All in all the produced changes were low and within the level of fluctuation of the peak maxima. Moreover, heating effects complicated the evaluation of the data. More details on the experimental approaches and results are provided in [114]. To answer the question, why there is no MIR observable in the studied samples, a more comprehensive picture of the twinning microstructure of the films is needed. The combination of the presented XRD analysis with an investigation of the morphology of the surface and the cross section provides further insight on the mechanism that blocks MIR. The investigation of the twinning microstructure is content of chapter 5.

4.5 Key results

Epitaxial growth has been achieved for different substrate materials, including MgO(100), $Al_2O_3(11\bar{2}0)$ and $BaF_2(111)$ single crystals, enabling a tailored crystallographic orientation of the Ni-Mn-Ga films. The in-plane alignment of the Heusler unit cell is dictated by the chemical order of the substrate surface, which leads to unexpected orientation relations in the case of $Al_2O_3(11\bar{2}0)$ monocrystals and MgO(100) substrates that have been exposed to air. Using temperature-dependent XRD the structural changes during the phase transformation have been observed. In the martensitic state films of $(110)_A$ orientation are composed of two orthorhombic variants that are separated by twin planes parallel to the film surface. In contrast, the predominant twin plane configuration in samples on MgO(100) is perpendicular to the film plane. In these films twelve different orthorhombic variants have been identified, of which four are strongly favored. For both, $(100)_A$ and $(110)_A$ orientation the 7M/14M modulation was confirmed by direct observation of the superstructure peaks. Freestanding films that have been released from NaCl(100) substrates show a textured structure only. In contrast, films prepared on MgO with a sacrificial Cr layer prove to be epitaxial. Moreover, the crystal structure, i.e. the variant configuration is not altered by the release process. This includes the modulation that is detected in a freestanding thin film sample for the first time. In spite of these promising results, magnetically induced variant redistribution could not be confirmed for these samples by means of XRD with applied magnetic field so far.

Chapter 5

Surface morphology and twinning microstructure

The collective, diffusionless displacement of atoms in magnetic shape memory materials is not only the basis for the large strains that arise in response to an external magnetic field, but also leads to a complex microstructure of twin variants in the martensite. In a bulk single crystal the twin microstructure is dictated by the elastic and the magneto-static energy. The formation of different crystallographic variants separated by twin planes can be explained in a simplified picture considering only the elastic energy balance. The transformation from the cubic phase to a single martensite variant would result in a huge elastic energy increase due to the lattice misfit at the austenite-martensite phase boundary. This energy can be decreased by the formation of different variants that are connected via twin planes. Of course, introducing a twin boundary is associated with an energy increase for the atoms in the vicinity of the boundary and hence for the system in total. If the twin boundary energy is low compared to the elastic energy due to the lattice misfit at the phase boundary the overall energy can be minimized by decreasing the variant width. The result is a fine-twinned microstructure with a regular twinning pattern. Considering also the magnetic energy in the highly anisotropic Ni_2MnGa system the situation becomes more complex. In a compromise between the different energy contributions and external constraints a complex martensitic microstructure will form. This usually involves different length scales starting from the atomic level and reaching the millimeter range. The twin microstructure on different scales can form a hierarchy involving branching or "twins within twins" [115]. As a result of the twin architecture the sample surface will show a characteristic relief. The local slope of the surface is a function of the present twinning type and the variant sequence. For example, the a-c twinning mode features $(101)_A$ twin planes that run parallel to the b-axis in the orthorhombic system. Across the twin boundary the a- and c-axis of the adjoining variants are interchanged. Depending on the actual variant alignment the associated tilt angle $\alpha = \arctan(a/c) - \arctan(c/a)$ can be

detected on the sample surface. Likewise, *a*-*b* and *b*-*c* twinning produces distinct tilt angles that can contribute to the surface relief. A nice overview of different relief types on a $(100)_A$ surface produced by different twin sequences is given in ref. [116]. The calculated surface tilt is compared to AFM and MFM studies on a bulk single crystal. The observed twinning mode strongly depends on the thermomechanical treatment in that case.

However, in the case of thin films additional constraints arise, since the atomic positions are fixed at the film-substrate interface. Hence, a strong tendency to form a habit plane at the interface can be expected. Furthermore the symmetry of the substrate surface determines the symmetry of the Ni-Mn-Ga film. Typically the film grows at elevated temperature in the austenite and then transforms to the martensite, when cooling down to T_M. Thus, the symmetry of the martensitic crystal structure is influenced by the substrate constraints, too. Based on the observed variant configuration probed by XRD, the arising twin planes essentially form along $(110)_A$ and equivalent planes. In the orthorhombic system the lattice plane distance is then preserved along the intermediate *b*-axis, since $b \approx a_A$. The twin planes run along *b* and connect variants that differ in alignment of *a*- and *c*-axis. Such a twin plane configuration directly allows for conservation of the macroscopic shape, if $(a + c)/2 \approx a_A$ is satisfied, which is the case for the films investigated within this work. The deformation of the cubic unit cell due to the martensitic transformation is reflected by the c/a ratio that reaches values of 0.89 to 0.92 for our samples. This large lattice deformation is compensated most efficiently by *a*-*c* twinning, which explains the preference for that twinning mode. Considering only *a*-*c* twinning the transformation from cubic to orthorhombic will generate six equivalent twin planes as discussed in chapter 2.2.2. Each of these twin boundaries will connect two crystallographic variants that differ in alignment of two lattice parameters, i.e. *a* and *c*. In an unconstrained monocrystal all twelve martensite variants should appear uniformly distributed. In case of the substrate-fixed film the different twin planes are not equivalent any more, since they feature different orientation relations to the substrate. Indeed, all possible orthorhombic *a*-*c* twin variants have been detected for $(100)_A$ oriented films, but as a consequence of the film-substrate interaction these variants are not uniformly distributed. A strong preference for twin plane alignment perpendicular to the substrate surface is observed. However, a small fraction of variants separated by twin planes running under 45° to the surface normal is present, too. On the contrary, films of $(110)_A$ orientation feature twin planes aligned parallel to the film plane. The different twin plane configurations, on the other hand, dictate the surface relief that can be observed by means of microscopy, as will be explained in the following.

5.1 $(110)_A$ oriented films

The crystallographic studies on films with $(110)_A$ orientation clearly indicate that the twin planes run primarily parallel to the film surface in these samples. On $Al_2O_3(11\bar{2}0)$ substrates two predominant variants with b-axis aligned in-plane are observed. For both variants the a-axis encloses an angle of 48.35° with the surface normal, while the c-axis points under 41.65° to the film normal. This symmetric rotation around the shared b-axis allows for compensation of the different lattice parameters a and c and hence leads to a conservation of the layer distance along the thickness of the film. Parallel to the b-axis the interatomic distance remains almost unaltered since $b \approx a_A$ is valid. Along the third dimension, i.e. in-plane and perpendicular to the b-axis, the compensation of a- and c-axis works similar to that along the film normal (compare Fig. 4.15 and 4.16 in chapter 4.3). A direct consequence of this variant configuration is the preservation of the macroscopic shape of the sample. As expected from the XRD results the surface of the samples on Al_2O_3 shows no characteristic structure, when examined in the light microscope. The surface appears basically flat without systematic corrugation. This is confirmed by SEM and AFM scans that indicate a flat film surface with a typical roughness of some nm (s. also [18]). In case of the (110) textured films prepared on NaCl substrates the severe buckling of the surface is due to the huge difference in the thermal expansion coefficients of Ni_2MnGa and NaCl. In order to prove this assumption the stoichiometric target was used to prepare a film on NaCl that is in the austenitic phase for $T > 280$ K. During the cooling from deposition temperature (480 °C) to ambient temperature the buckling started around 200 °C, while the sample was still in the austenite.

5.2 $(100)_A$ oriented films

In contrast to the (110) oriented samples, the films deposited on MgO(100) single-crystals show distinct surface patterns that can be examined in the light microscope. On a length scale of some μm up to 0.3 mm rectangular line patterns are observed for several samples. Depending on the precise preparation conditions the films prepared with the off-stoichiometric targets 3-5 show different surface morphologies (s. Fig. 5.1). Besides small variations in the film composition, the different deposition rates as a function of the working pressure are expected to be responsible for the variations in the surface pattern. Many samples exhibit rectangular lines that are aligned under 45° to the edges of the MgO unit cell, which means parallel to $[100]_A$ and $[001]_A$ (Fig. 5.1, left). In addition to these lines, scar-like trenches appear at some spots of the surface. These trenches have a triangular profile with slightly curved edges. As described in chapter 3.3, the incline of the trailing edges appears stronger than it actually is. In fact, the tilt angle is in the range of a few degrees only. Some samples, prepared at a slightly different

sputtering gas pressure, reveal a rectangular pattern consisting of fine lines that span along MgO [010] and [001] (s. Fig. 5.1, right). The dimension of these lines, that run along $[101]_A$ and $[\bar{1}01]_A$, varies between a few and several hundred μm. In both cases the observed twinning pattern has to be described as "mesoscopic" or even "macroscopic", since it originates from twinned variants that form the microstructure. If an intermediate level of variant arrangement exists, the observed pattern has to be classified as macroscopic. To link the martensitic surface pattern to the crystal structure a comparison to crystallographic studies is required. A detailed characterization of the variant distribution and associated twin plane alignment was carried out for films showing the line pattern parallel to MgO [011] and $[0\bar{1}1]$. As described in chapter 4.3 and [117] these samples feature an asymmetric variant distribution with a majority of variants with a- and c-axis aligned in-plane. Hence, the prevalent twin plane alignment is perpendicular to the film surface. Considering the 45° rotation of the Ni_2MnGa unit cell with respect to the MgO lattice the observed lines run under 45° to the twin boundaries. Against all expectations, the samples with the second type of surface pattern (lines along MgO [010] and [001]) have a similar variant distribution with a predominant vertical twin plane configuration. Consequently, the line pattern is parallel to the traces of the twin planes on the film surface in that case. This leads to the conclusion that both surface patterns are of macroscopic character,

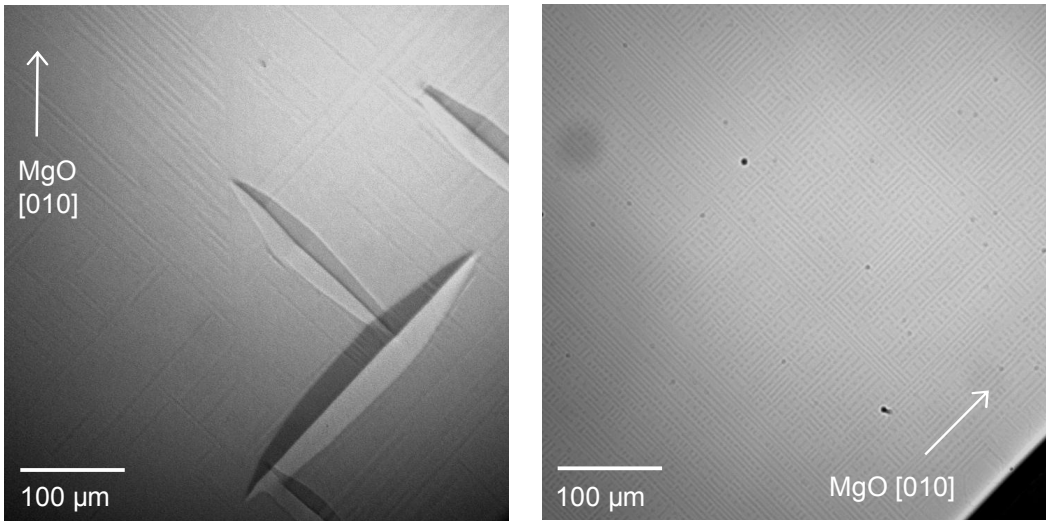

Figure 5.1: Light Microscopy images of Ni-Mn-Ga films on MgO(100). Sample A (left) shows long lines that run along MgO [011] and $[0\bar{1}1]$ and scar-like corrugations that extend up to 300 μm. In contrast, the line pattern of Sample B (right) follows MgO [010] and [001] directions. In this case some of the fine lines expand over hundreds of μm, while others are only a few μm long.

since they are generated by a very similar microstructure. The difference lies in the variant arrangement on a mesoscopic scale, that links the microstructure to the observed pattern. This assumption is supported by results obtained for a sample that was patterned and partially released from the MgO substrate. In the as-prepared state the film surface shows the pattern type that runs along $[101]_A$ and $[\bar{1}01]_A$. The short thin lines are visible on the whole surface, the substrate-constrained and the freestanding parts of the patterned film (s. Fig. 5.2 (a)). In order to determine the transformation temperature the sample was heated in the light microscope in the following. When entering the austenite state the twinning pattern on the surface vanishes, which is monitored with the microscope. Upon cooling the pattern is recovered as the film transforms back to martensite. Figure 5.2 (b) shows the investigated microbridge after such a heating-cooling cycle. At the right endpoint of the beam, where the bridge is clamped, the line pattern has changed. Instead of short lines parallel to MgO [010] the scar-like features along MgO [011] appear. Subsequently a second and a third martensite-austenite-martensite transformation cycle was performed. The further cycling resulted in a slight broadening of the region of modified surface pattern (s. Fig. 5.2 (c) and (d)). After this observation the variant configuration in this sample was examined with the 4-circle diffractometer. Likewise the results reported in chapter 4.3, the observed peak splitting and intensity distribution indicate that the majority of variants have the b-axis aligned parallel to the film normal. Consequently, both surface patterns originate from a twin microstructure that connects basically four orthorhombic variants with a- and c-axis oriented in the film plane.

The alternative twin variant configuration with a- and c-axis pointing approximately perpendicular to the film plane produces another surface pattern, which can be imaged with the enhanced resolution of the AFM or SEM. A few samples possess a tweed-like surface pattern that consists of wavy lines parallel to the diagonal of the MgO unit cell. Figure 5.3 displays a SEM image taken on a Ni-Mn-Ga film on MgO. Here the slightly curved lines forming a rectangular pattern are clearly visible. As evident in the image, this type of structure can coexist with the previously described straight lines along MgO [010] and [001]. In the upper right corner of the examined sample area this line pattern can be spotted. Most of the sample surface under investigation is covered by wavy lines that run vertically, but some areas show horizontal lines. At the boundary, where the lines change in direction, a narrowing of the lines can be observed. This is an indication of branching as described and sketched in [115] and [118]. In the context of the applied continuum model a branching of twin boundaries connecting two variants of different orientation is expected when approaching a habit plane. By the branching the elastic energy, that results from different crystallographic alignment of long and short axis, can be decreased on cost of an increased twin boundary energy. If the latter is low compared to the elastic energy a fine-twinned microstructure will result. In the present case the line pattern reflects the twin plane orientation, which is 45° away from the film normal.

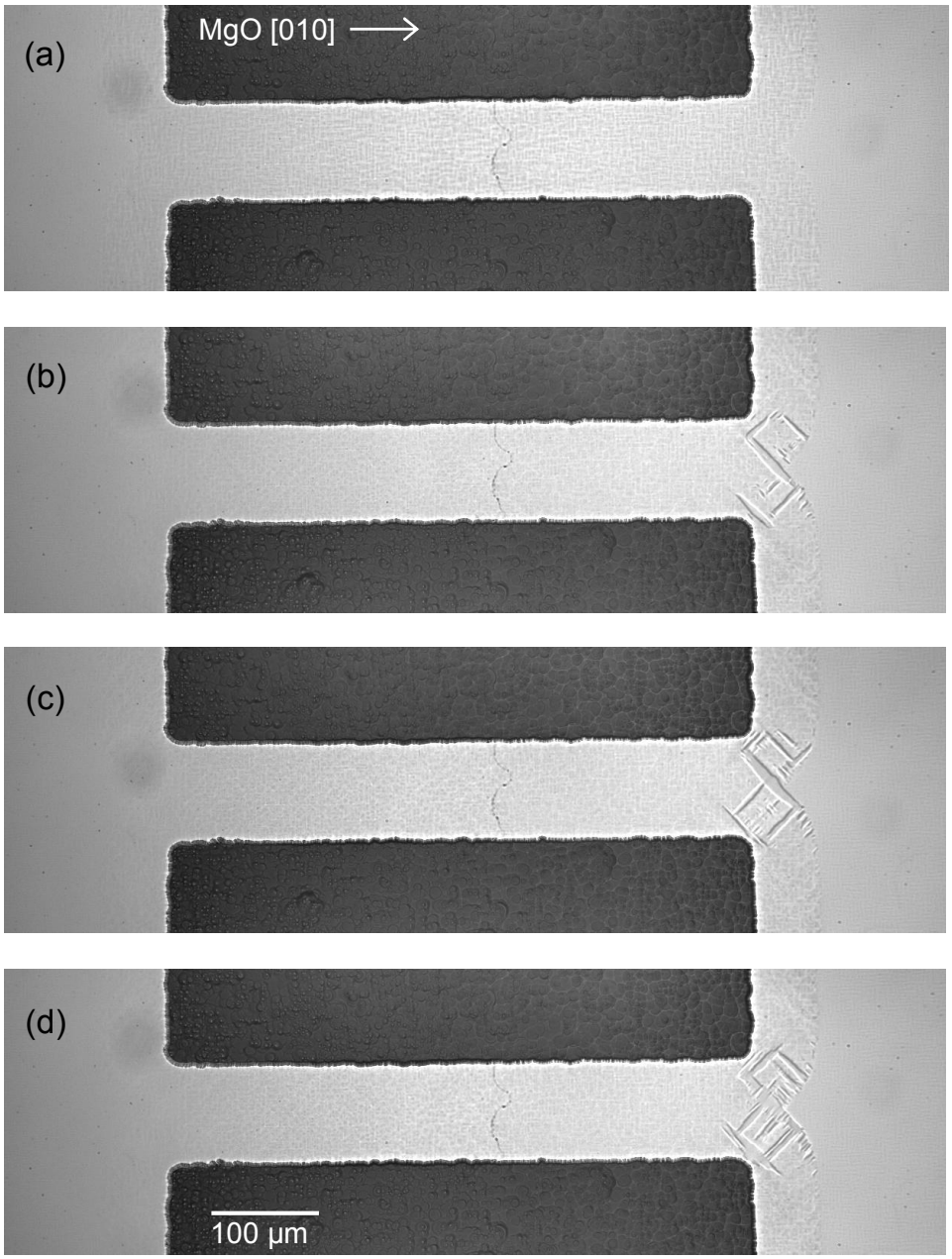

Figure 5.2: Optical microscopy images of a freestanding microbridge. In the as-prepared state (a) a fine twinning pattern with short lines along MgO [100] is visible. After heating the sample above the transformation temperature and cooling back to room temperature the martensitic surface pattern has changed at the right end of the bridge (b). Subsequently, a second (c) and a third (d) martensite-austenite-martensite cycle was performed, which results in further small variations of the pattern.

Where the twin planes intersect the film surface a contrast between the adjacent variants arises, which is visible in the SEM and AFM images (s. Fig. 5.3 and 5.4). This picture is supported by the structure of the film's cross section. Figure 5.5 displays a SEM image of a vertical cut through the Ni-Mn-Ga layer, prepared with FIB etching. In the right half of the profile the twin lamellae separated by twin planes under 45° to the surface are clearly visible. On the contrary, the surface line pattern parallel to MgO [010] is related to variants that are separated by twin planes running perpendicularly to the surface (s. left half of the cross

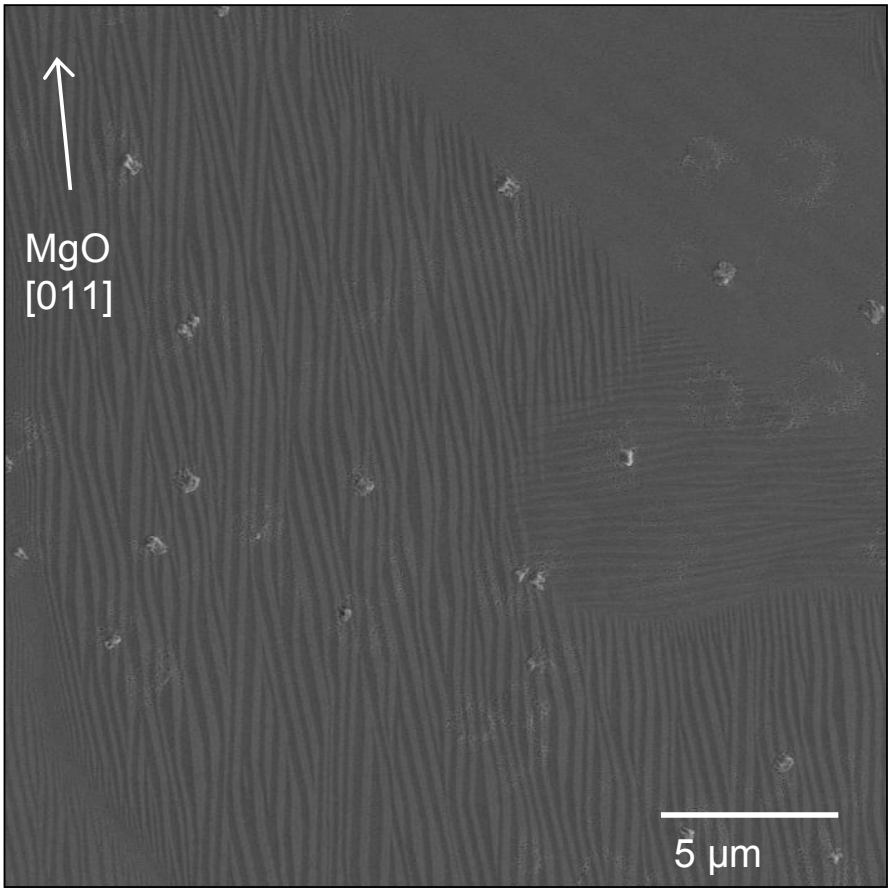

Figure 5.3: A few samples feature different, coexisting twinning patterns. The SEM image shows the tweed-like pattern, which covers most of the surface, but in the upper right part also straight lines along MgO [010] are visible. In the lower right, where the direction of the wavy lines changes, branching of twin boundaries can be spotted. When approaching the transition region the variant width decreases as the density of twin boundaries increases.

section). For both twin plane configurations the strong contrast between the crystallographic variants is very likely produced by differences in the etch rates for the respective crystallographic orientation of the variant. This effect was also observed for samples with AlO_x cap layer. The surface pattern is hardly visible through the 4 nm thick AlO_x layer (s. Fig. 5.6). After removing the Al cap the structure becomes visible, when etching approximately 8 nm deep into the Ni-Mn-Ga layer. A further etch of 10 nm leads to an accumulation of particles along the twin boundaries. Hence, the etch rate is lower in the vicinity of the twin plane, which results in an increased contrast. After removing the cap layer and the topmost layers of the MSM film the twinning pattern is clearly observable in the AFM, too (s. Fig. 5.7). While the majority of samples prepared within the scope of this work reveal a surface pattern consisting of straight lines, the wavy twinning pattern is commonly reported for comparable Ni-Mn-Ga films grown on MgO(100) [119, 120, 121, 122]. The related 45° twin plane configuration allows for in-plane alignment of the b-axis. Along this direction the interatomic distance can be preserved during the phase transition. Along the film normal a sequence of variants with either a- or c-axis pointing out-of-plane minimizes the

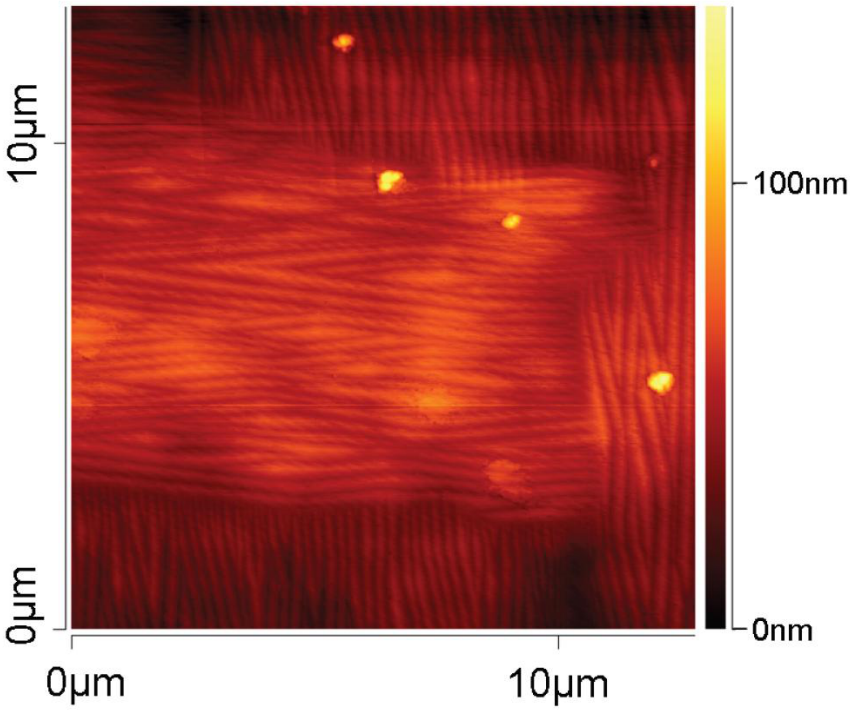

Figure 5.4: The tweed-like surface pattern consisting of wavy lines along MgO [011] can be imaged with the AFM. The variant width is well below a μm for the investigated sample.

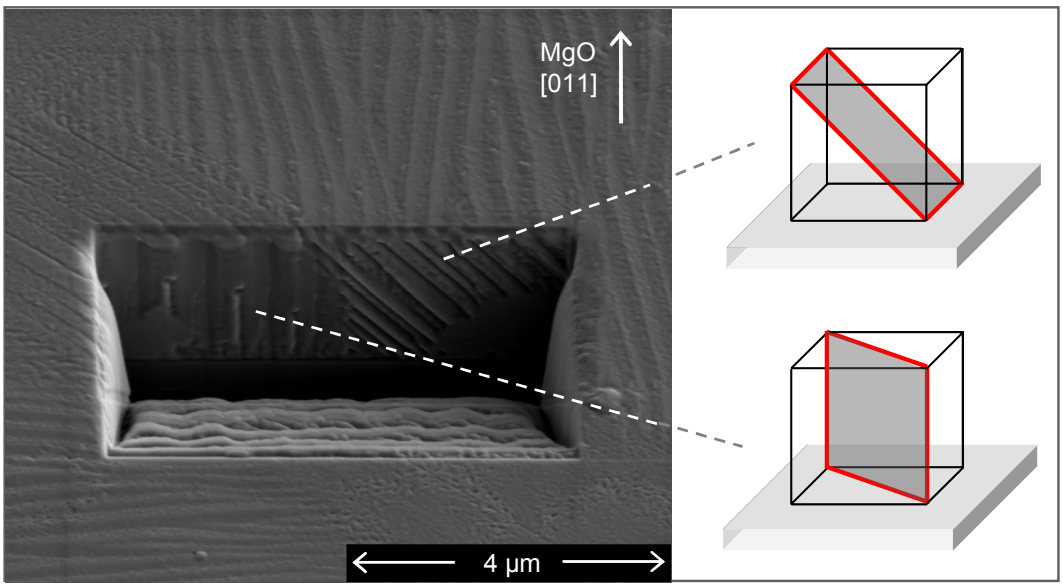

Figure 5.5: The FIB cut cross section reveals two different twin plane alignments coexisting in a film on MgO(100). The straight lines in the left part of the film surface originate from twin planes that are aligned perpendicularly to the film plane (as illustrated on the right). In contrast the wavy surface pattern results from twin planes that run under 45° to the film normal.

elastic energy. To connect these variants the twin planes have to run under 45° to the film surface. Likewise the out-of-plane direction, a compensation of a- and c-axis can be achieved in the film plane perpendicular to b. As a consequence of this twin plane arrangement the film surface will differ from being flat. In agreement with a simple geometrical model as illustrated in Figure 5.8), the surface was found to be bent in a regular fashion. Height profiles measured by AFM revealed a characteristic waveform, when scanning a line perpendicular to the observed line pattern on the film surface [112, 120]. The wave profile is approximately triangular with a periodicity of 110 nm in that case. The observed tilt angles are in good agreement with the calculation using the geometrical model $\alpha = 45° - \arctan(c/a)$ and the martensite lattice parameters as determined by XRD analysis. As illustrated by the model (s. Fig. 5.8) a completely martensitic film would tend to delaminate from the substrate surface. Indeed, a low adhesion of the Ni-Mn-Ga layer on MgO was observed (s. chapter 3.2). The weak bonding to the substrate can be used to prepare freestanding films by peeling of the MSM layer mechanically (s. also [123]). The major drawback of this method is the severe mechanical stress imposed on the film during the process, which likely results in plastic deformation.

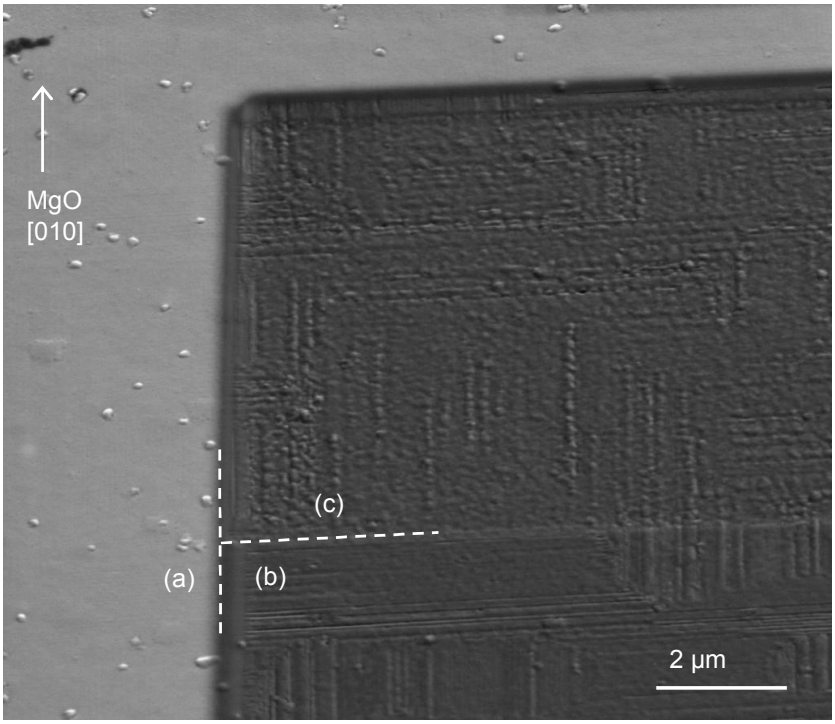

Figure 5.6: The FIB etch process clearly affects the visibility of the martensite twinning pattern. Region (a) shows the untreated surface, that is capped by a 4 nm thick AlO_x layer. Here the surface pattern is only faintly visible. This is changed by removing a 8 nm thick layer (b). A further etch of 10 nm reduces the contrast that is due to differences in the etch rates for the different crystallographic variants (c).

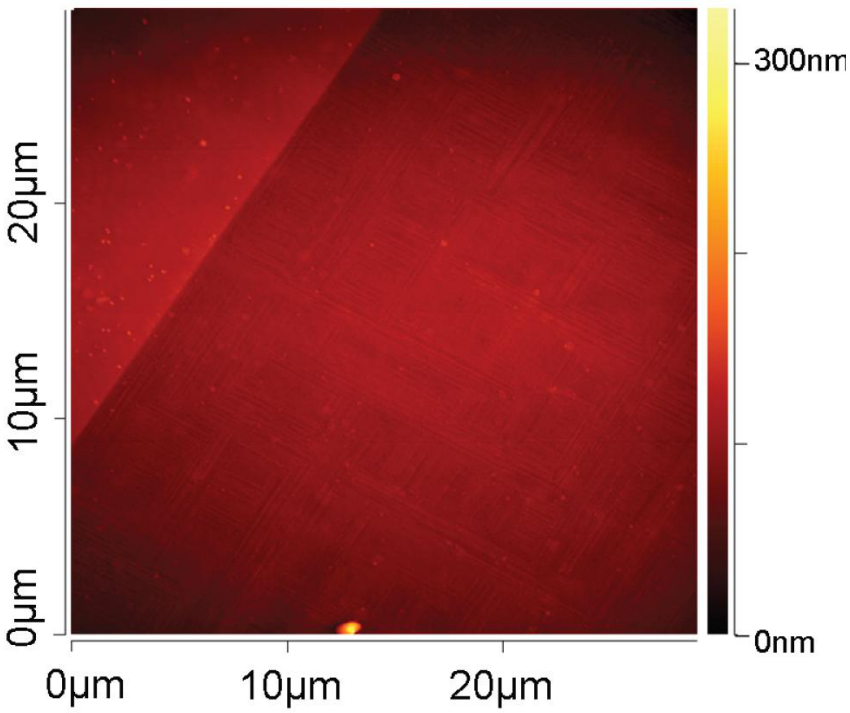

Figure 5.7: Once the surface pattern is uncovered by the FIB treatment, it can be imaged ex-situ by atomic force microscopy, too. Though the sample was exposed to air, the twinning pattern is not altered significantly.

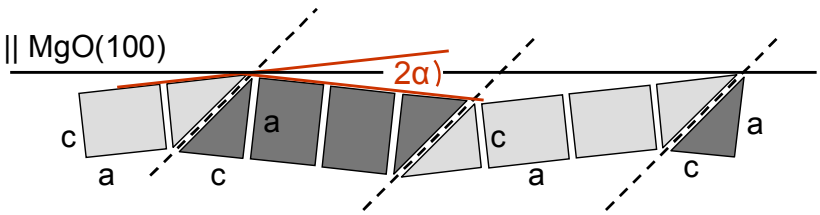

Figure 5.8: Model for variant alignment in the case of a 45° twin plane configuration. The *b*-axis points into the plane of projection. Along the film normal and the remaining in-plane direction *a*-*c*-twinning leads to low elastic energy. Consequently, the film features a wavy surface with a triangular profile. (Model adapted from [120]).

5.3 Magnetically induced reorientation of variants

The most promising approach to achieve freestanding films, that show magnetically induced strains, is the sacrificial buffer layer technique. In the course of this work, all samples prepared on MgO(100) with a Chromium interlayer feature a prevalent twin plane alignment perpendicular to the film plane. The related macroscopic twinning pattern that can be examined in the light microscope consists of straight lines parallel to MgO [010] and [001], or [011] and [0$\bar{1}$1] respectively. Likewise the curved lines of the tweed-like surface morphology in the case of 45° twin planes, the fine lines parallel to MgO [010] and [001] can be directly attributed to different variants connected by twin boundaries. The fine lines run along $[101]_A$ and $[10\bar{1}]_A$ directions (k= out-of-plane direction) and can be interpreted as traces of the twin planes on the film surface. This agrees with the variant alignment, as probed by XRD. The detected sets of orthorhombic variants are separated by twin boundaries along MgO [010] and [001] respectively. However, this simple picture does not hold for the second type of line pattern that runs along the diagonal of the MgO unit cell. These lines point along the Ni-Mn-Ga $[100]_A$ and $[001]_A$ directions, which means under 45° to the intersections of the twin planes with the film surface. In this case, a very similar microstructure of predominantly $(101)_A$ and $(10\bar{1})_A$ oriented twin planes leads to a completely different twinning pattern on the macroscopic scale. A possible correlation of the crystallographic studies and the observed macroscopic pattern is provided by a simple model for the variant alignment, described in the following.

5.3.1 Model for variant alignment

As mentioned before, the majority of samples prepared on MgO substrates with a Cr buffer layer show a surface pattern as imaged in figure 5.9. For the substrate-constrained films the line pattern is only faintly visible in most cases, while a distinct structure is apparent on the freestanding parts of the patterned samples. Once the Cr layer is removed underneath the beam structure the microbridge is completely freestanding between the endpoints and can move to some extent via bending and tilting. To exclude changes in the variant distribution caused by the release process a detailed crystallographic study was carried out for a reference sample (s. chapter 4.3). The crystal structure and variant distribution of this film was found to be nearly identical in both cases, i.e. the substrate-constrained and the completely freestanding state. Though the surface pattern is more prominent for the released film, no qualitative modification of the variant distribution was observed. According to that, the enhanced contrast of the twinning pattern on the freestanding parts of the film is likely caused by a slight buckling of the surface. The optical effect is increased by the normal incidence of the light that leads to

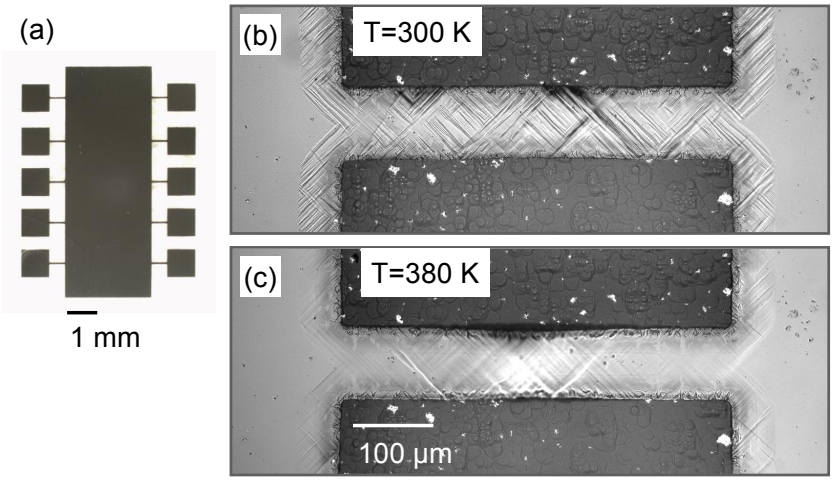

Figure 5.9: Light microscopy images of a patterned Ni-Mn-Ga film on MgO(100) with Cr buffer layer. The overall view of the sample (a) shows the released microbridges that are 550 μm long and 100 μm wide. In the martensite the freestanding bridges and the released film edges exhibit a distinct twinning pattern (b). When heated above the transformation temperature the lines along MgO [011] and [0$\bar{1}$1] vanish, as the film transforms to the cubic parent phase (c).

a huge reduction in reflectivity for a slightly tilted sample surface. To determine the phase transformation temperature the sample can be heated while observing the twinning pattern in the light microscope. When the lattice transforms to the cubic austenite modification, the surface structure nearly vanishes, as the twin boundaries disappear (s. Fig. 5.9). The martensite start temperature for the displayed sample lies around 365 K, while on cooling the twinning pattern starts to recover at 357 K. The observed hysteresis is in agreement with the one present in magnetization data (s. chapter 6.1.1).

To explain the origin of the martensitic surface pattern a simplified model, that takes into account the predominant variants only, is useful. When considering only the four crystallographic variants with b-axis aligned along the film normal, the possible variant configurations will look like illustrated in Fig. 5.10. As calculated on basis of the XRD peak intensities the neglected 8 variants form a minor fraction of 14 % in total. According to the model, the four different variants that feature in-plane alignment of a- and c-axis constitute the entire film volume. The layer surface is covered by the two sets of twin variants as sketched in Fig. 5.10. All possible configuration exhibit twin planes along Ni-Mn-Ga $[101]_A$ and $[10\bar{1}]_A$ directions connecting the variants I and II, and III and IV respectively. This leads to a lattice mismatch along $[100]_A$ and $[001]_A$, where variants II and III or I and IV meet. Due to the different rotation directions the a- and c-axes of the respective variants do not fit here. To compensate this mismatch a forma-

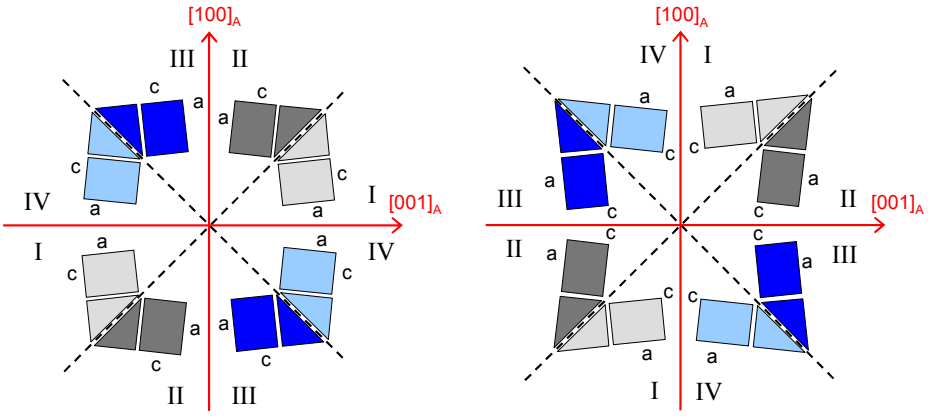

Figure 5.10: Schematic top view on the prevalent crystallographic variants observed for films on MgO(100). The two sets of twin variants are separated by twin planes running normal to the film surface and parallel to Ni-Mn-Ga $[101]_A$ and $[10\bar{1}]_A$ directions, respectively. All possible variant configurations lead to lattice mismatch along $[100]_A$ and $[001]_A$ due to the opposing rotation direction of the individual twin variants.

tion of fine-twinned bands consisting of $[101]_A$ microtwins (variants I and II) and alternating $[10\bar{1}]_A$ twin bands (built up from variants III and IV) is beneficial (s. Fig 5.11). Within the bands no lattice mismatch arises due to twinning. At the band edges, parallel to $[100]_A$ and $[001]_A$, the mismatch can be reduced by a low width of the individual twin variants. Figure 5.12 illustrates the mechanism of minimized lattice distortion for fine-twinned bands. With each twin boundary the misalignment switches from diverging to converging lattice parameters and vice versa. As sketched in Fig. 5.12 a symmetric twinning in adjacent bands effectively reduces the misfit in the transition region. Such a symmetric "herringbone" pattern will furthermore provide a strong coherence of the individual martensite variants. This would explain the intense and narrow XRD peaks caused by the four prevalent variants, although the volume of the individual twins is small. Since the 7M/14M superstructure was detected in these samples, the lower limit of the variant width is 7 unit cells. Probably, the actual variant size involves much more unit cells. It is worth mentioning that there is no blank space in the region of the twin band egdes as implied by the sketch (s. Fig. 5.12). At the band intersections an increased level of lattice defects and stress will emerge as a result of the lattice mismatch. For the suggested highly symmetric case the lines separating the twin bands represent mirror planes, that means the twin bands are connected via "twin boundaries" themselves. These "mesoscopic twin boundaries" are not atomically sharp, but diffuse since they expand over several atomic planes. According to the concept of adaptive martensite [61, 115] even the twin

planes within the fine-twinned bands are not atomically sharp. The seven-layered modulation, observed for the individual crystallographic variants by XRD, leads to incompatibilities at the twin boundaries. As a result, these have a diffuse character and hence have to be described as mesoscopic twin boundaries [115, 117]. To prove the proposed symmetric twinnig of the [101] and [10$\bar{1}$] twin bands a local probe, like electron backscatter diffraction [124] or high-resolution TEM [46, 125] is required. Despite this lack of information on the mesoscopic scale, the model links the observed crystal structure to the macroscopic pattern that appears in the optical microscope. The described twin bands run along $[100]_A$ and $[001]_A$, which is precisely the orientation of the macroscopic line pattern. To explain the observed slight buckling of the surface a more complex model, including all variants, is needed. Any tilt of the film surface requires the presence of variants with b-axis in the film plane. These variants are observed in the crystallographic study and have to be taken into account for a comprehensive description. Nevertheless, the simplified model explains the observed symmetry of the surface pattern on basis of the variant alignment probed by XRD.

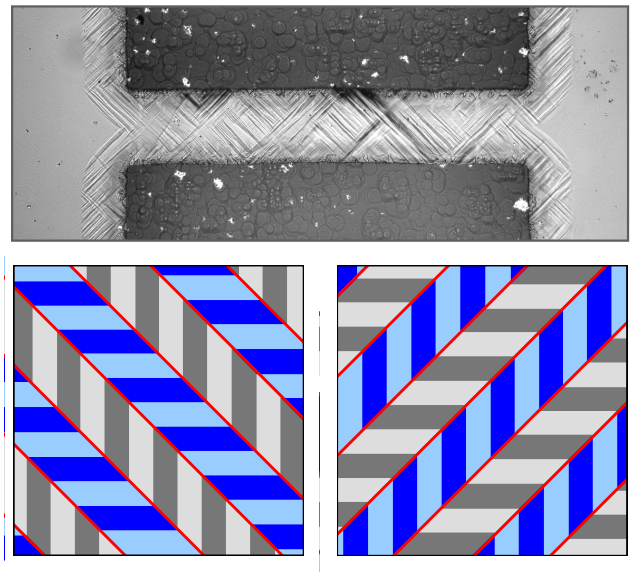

Figure 5.11: A reduced lattice mismatch can be achieved by forming a herringbone twinning pattern consisting of alternating $[101]_A$ and $[10\bar{1}]_A$ twin bands. Each band is composed of a twin variant pair (variants I/II and III/IV). Where the different bands meet (red lines) a lattice mismatch of the individual variants occurs. The observed macroscopic lines (s. image of the freestanding bridge) run parallel to the band edges and hence originate from the mesoscopic variant configuration.

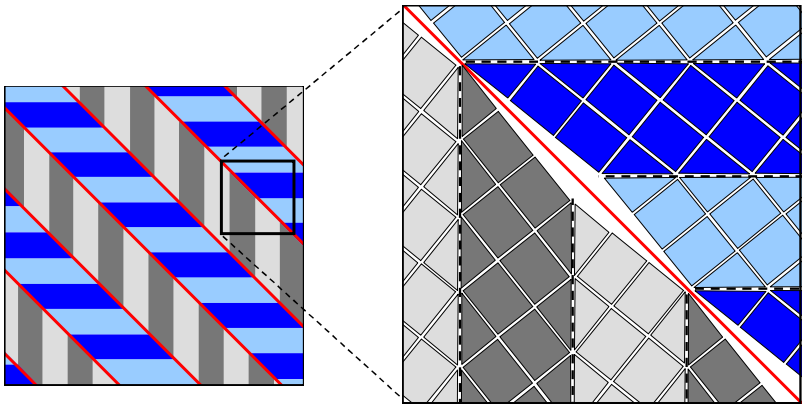

Figure 5.12: To provide a low lattice misfit at the twin band intersections a high density of twin boundaries is required. A symmetric twinning in adjacent bands leads to a low lattice mismatch that follows a zig-zag pattern. With each twin plane introduced the misalignment switches from diverging to converging lattice parameters and vice versa. The transition zone is of course not empty space, but a region of increased defect concentration and stress.

5.3.2 Manipulation of twinning microstructure

Besides the previously described attempts to directly observe a magnetically induced variant redistribution via X-ray diffraction the rather indirect probe by microscopy was applied to several samples. As the observable surface pattern is directly related to the variant configuration, a change in the latter should manifest in changes of the surface morphology. Since a rigid substrate will effectively block a variant rearrangement, the studies of magnetically induced changes in the twinning pattern was focused on the freestanding films. To enable in-situ observation with applied field in the light microscope a set of permanent magnets with a suitable sample holder was used. This setup provides a field strength of 0.2 T. To reach higher magnetic fields an electromagnet capable of 1.0 T was utilized. The image of the sample is then recorded in the remnant condition. In case of completely freestanding films handling is difficult, since the film needs to be fixed while exposed to the magnetic field. Problems arise from any mechanical strain due to handling. Thus, changes in the surface twinning pattern can be caused by the sample treatment. These problems can be avoided by employing partly freestanding structures as cantilevers or bridges. In the first approach such a microstructure was prepared by FIB etching. Figure 5.13 (a) shows a SEM image of the freestanding beam that was released at one side. The long side of the cantilever is parallel to Ni-Mn-Ga $[100]_A$ and measures 6 μm. The image was taken from an angle of 52° relative to the surface normal directly after the etch pro-

cess. On the cantilever surface the characteristic line pattern induced by a twin plane configuration as discussed in the previous section is in evidence. Hence, the magnetic easy axis runs approximately under 45° to the beam. Nevertheless, in the first step a magnetic field of 0.6 T was applied parallel to the long axis of the cantilever at room temperature. The surface pattern on the freestanding structure was then imaged by AFM (s. Fig. 5.13 (b)) in the remnant state. Subsequently, the sample was exposed to a second field parallel to the short edge of the cantilever. Figure 5.13 (c) displays the investigated part of the beam surface after this step. When comparing the two images the different angles between vertical and horizontal lines attract attention. After the field was applied along the length of the cantilever the lines enclose an angle of 86.8°, whereas the second field, applied perpendicular to the long axes of the beam, leads to a reduced angle of 83.5°. Obviously, the observed tilt angles in the line pattern directly reflect the rotation angles of the different martensite variants. The structural analysis yields lattice parameters of $a = 6.13$ Å, $b = 5.76$ Å and $c = 5.44$ Å for this sample. Hence, each variant features a rotation of $\alpha = 45° - \arctan(c/a) = 3.4°$ to the austenite crystal lattice. The c-axes of adjacent twin variants enclose an angle of $90° + 2\alpha$, while the a-axis of variant I runs under $90° - 2\alpha$ to the a-axis of variant II. According to the concept of fine-twinned bands of $[101]_A$ and $[10\bar{1}]_A$ microtwins, as described in the model for the variant alignment, the observed angles in the macroscopic pattern can be explained as follows. For the as-prepared samples the line pattern is rectangular. This reflects a symmetric twinning in the different twin bands, like illustrated in Fig 5.14 (a). Along $[100]_A$ and $[001]_A$ the lattice mismatch of the predominant variants induces the observable rectangular line pattern, when the adjacent bands are symmetric. If twin boundaries start moving under the driving force of an external magnetic field, annihilation of twin planes within the bands can occur. In the ideal case, this leads to a mono-variant state for neighboring bands, as visualized in Fig. 5.14 (b). The band intersection will then run under 3.4° to the $[100]_A$ direction that previously formed the interband boundary. If the twinning along $[001]_A$ is preserved, the lines separating the differently aligned bands enclose than an angle of 86.6°, which is close to the angle observed in the experiment. The twin boundary annihilation can also proceed along both directions, $[100]_A$ and $[001]_A$, which creates a pattern as illustrated in Fig. 5.14 (c) with a characteristic angle of 83.2°. This is again in good agreement with the experiment. It is worth pointing out, that a variant arrangement as suggested in Fig. 5.14 (c) will result in dislocation lines along $[100]_A$ and $[001]_A$, which is energetically unfavorable. Since the interband boundary is not a line, but rather an expanded region, the lattice mismatch can be compensated without forming a true dislocation line. As expected from the model, the induced changes are irreversible. Later experiments with a magnetic field applied under 0, 90 and ± 45° to the cantilever axis failed to induce any effects.

By developing the sacrificial buffer layer technique freestanding microstructures are available with reasonable effort using photolithography and wet chemical

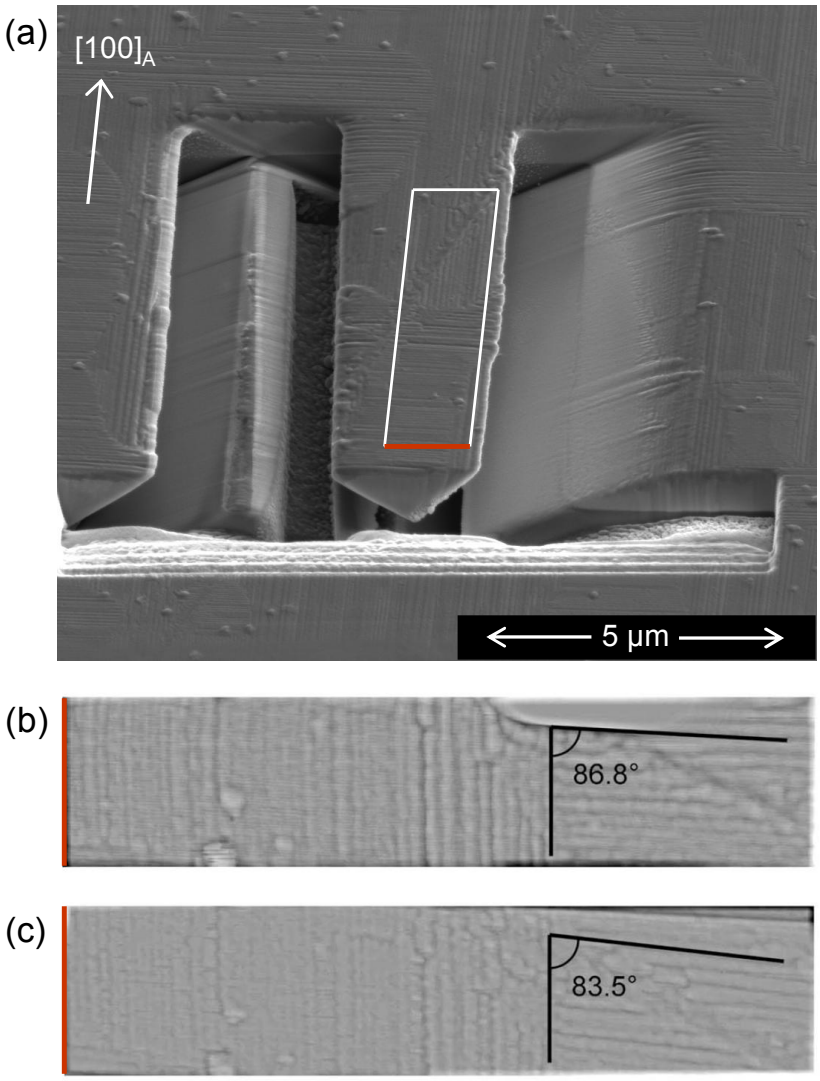

Figure 5.13: (a) SEM image of a freestanding cantilever in the as-prepared state. The beam structure was cut from a film on MgO(100) by FIB etching. The characteristic twinning pattern on the cantilever surface was affected by an external field of 0.6 T applied parallel to the long axis of the beam (b). The AFM image reveals lines running under an angle of 86.6° in the remnant state. Application of a second field perpendicular to the cantilever length results in a further reduction of the enclosed angle (c).

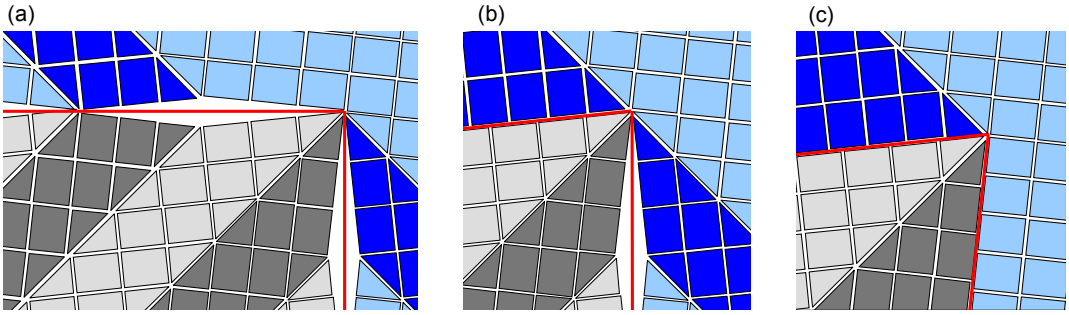

Figure 5.14: Following up the model for variant alignment the alternation in the macroscopic line pattern can be explained by symmetric twinning along $[100]_A$ and $[001]_A$ directions (a). This leads to a rectangular surface pattern indicated by the red lines. Magnetically induced twin boundary motion in adjacent bands can produce an annihilation of twin planes along one (b) or both (c) directions. This changes the relative orientation of the lines from rectangular to 86.6° (b) or 83.2° (c), respectively.

etching. The possibly damaging treatment of ion beam etching is avoided by this efficient preparation method that can be done in-house. Since most of the film is still fixed to the substrate handling is uncomplicated. The twinning pattern on the released parts of the film can be studied in the light microscope, while heating the whole sample, that is the substrate and the film. Thus, the phase transformation temperature can be determined easily, as the martensitic twinning pattern vanishes, when the film transforms to the austenite (s. Fig. 5.9). Upon cooling the surface pattern is recovered, when the MSM layer transforms back to martensite. To check for changes in the twinning pattern such a transformation cycle was repeated for several samples. After each heating-cooling cycle an image was recorded at room temperature in the martensite phase. Figure 5.15 shows one of the microbridges in the as-prepared state (a) and after three transformation cycles (b). Obviously, only minor changes in the surface pattern can be located. The macroscopic twinning pattern that originates from the microstructure is reproduced almost identically. Hence, the variant distribution and twin plane configuration is not altered significantly by the transformation process. Consequently, the austenite-martensite transformation proceeds in a very similar way for each heating-cooling cycle. This clearly indicates that the formation process that leads to the martensitic twin configuration involves pinning effects at lattice distortions. These lattice imperfections persist in the austenite phase and control the austenite-martensite transformation process. This conclusion is supported by observations on the surface of the freestanding microbridge. When heated clearly above the phase transformation temperature, the surface pattern does not vanish completely (s. Fig. 5.9 (c)). Some of the lines induced by the

twin variant configuration remain on the film surface. As discussed previously, these lines run along $[100]_A$ and $[001]_A$, where a lattice mismatch of the predominant martensite variants occurs. These distorted regions seem to persist, when the crystal transforms to the cubic parent phase, as evident from the remaining surface pattern on the austenitic sample.

As a consequence of the complex twin microstructure of the samples, no indication of magnetically induced variant rearrangement was detected on the surface of the released microstructures. Before establishing the model for the variant configuration, several attempts to manipulate the twinning pattern with magnetic fields of 0.2 to 1.0 T were conducted. At room temperature no changes of the martensitic surface pattern were observed, when applying a field of 0.2 T in the film plane under $\pm$ 45° to the long axis of the bridge. In this geometry the magnetic field is applied approximately parallel to the c-axes of two of the four predominant variants. Besides these in-situ experiments, the samples were exposed to a field strength of up to 1 T in the following. Again the field was pointing along $[100]_A$ and $[001]_A$ respectively, i.e. parallel to the c-axes of two prevalent variants. The sample surface appeared to be unaffected, when examined under the light microscope in the remnant condition. Further experiments with a magnetic field parallel and perpendicular to the microbridges failed in producing any changes in the twinning pattern. In contrast, cooling from austenite to martensite in a magnetic field induced a distinct modification of the line pattern (s. Fig. 5.15 (c)). The sample was heated to 380 K and subsequently cooled in a magnetic field of 0.5 T pointing under 45° to the length of the beam structure. When reaching room temperature, the sample was transferred from the electromagnet to the light microscope and an image was taken in the remnant state. The comparison to the initial state clearly shows that the line pattern in the center of the freestanding bridge has changed. The lines parallel to the applied field are more prominent now. This demonstrates that the nucleation of twin variants during the phase transition can be controlled by an external field. To test the reversibility of the effect the experiment was repeated with a magnetic field rotated by 90°. Figure 5.16 shows a series of images of the microbridge taken after subsequent heating-cooling cycles with alternating field direction. Close to the center of the beam, where clamping effects are low, the line pattern can be switched in part by the external field. The observations confirm that the modifications of the surface pattern are actually induced by the magnetic field. In order to reduce potential clamping effects, microbridges with a higher aspect ratio have been prepared. Instead of 550 μm long and 100 μm wide, these beams measure 2 mm x 25 μm (s. Fig. 5.17 (a)). On the freestanding parts of the investigated sample the small-scale line pattern parallel to $[101]_A$ and $[10\bar{1}]_A$ is visible. As a consequence of the high aspect ratio the long microbridges can twist along the long axis. After one heating-cooling cycle, to determine the transformation temperature of the patterned sample, some parts of the freestanding bridges feature a tilted surface. Due to the normal sample illumination in the microscope, these

tilted regions appear black (s. Fig. 5.17 (b)). In a first attempt the sample was examined in the light microscope, while exposed to a field strength of 0.2 T provided by the set of permanent magnets. This field strength failed in altering the twisted alignment of the microbridges. In response to a higher magnetic field of 1.0 T, provided by the electromagnet and applied parallel to the beam, the twist of the bridge was reduced, as evident from the optical microscopy image (s. Fig. 5.17 (c)). The magnetically induced changes of the macroscopic shape of the bridge involve no heating and hence no phase transformation like in the previous case. Whether this effect is based on local variant rearrangement or driven by the shape anisotropy of the structure remains questionable. Nevertheless, the combination of the sacrificial buffer layer preparation technique and the investigation by optical microscopy is a promising method to detect MIR in thin film samples.

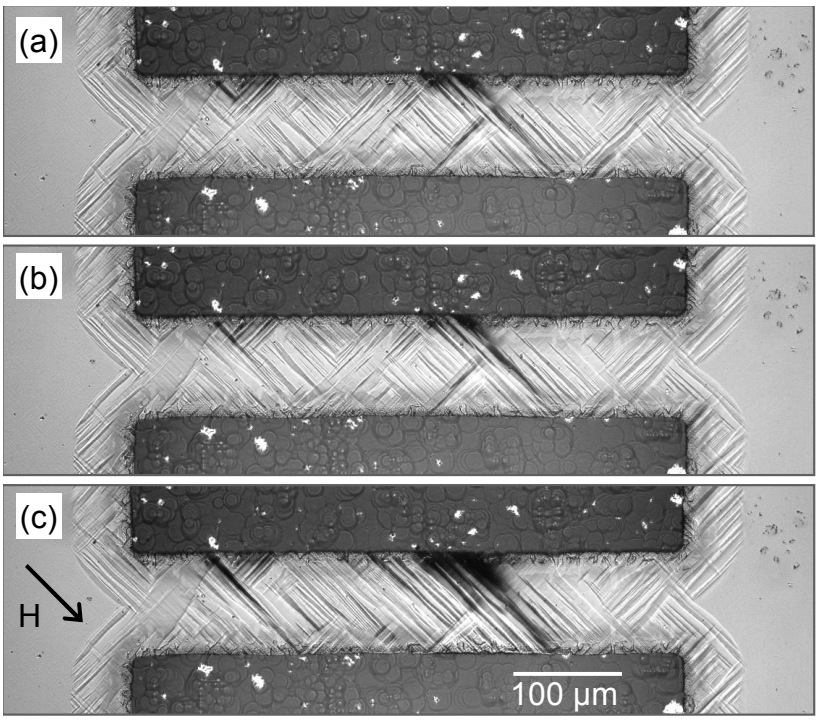

Figure 5.15: Light microscopy images of a freestanding microbridge in the as-prepared state (a), after 3 transformation cycles (b) and after cooling from austenite to martensite in a magnetic field of 0.5 T (c). While the heating-cooling cycles produce only marginal changes in the surface pattern, the application of an external field leads to clear modifications in the twinning pattern. The sample was cooled from 380 to 300 K with the magnetic field applied as indicated by the arrow. All images were taken at room temperature and in the remnant condition for (c).

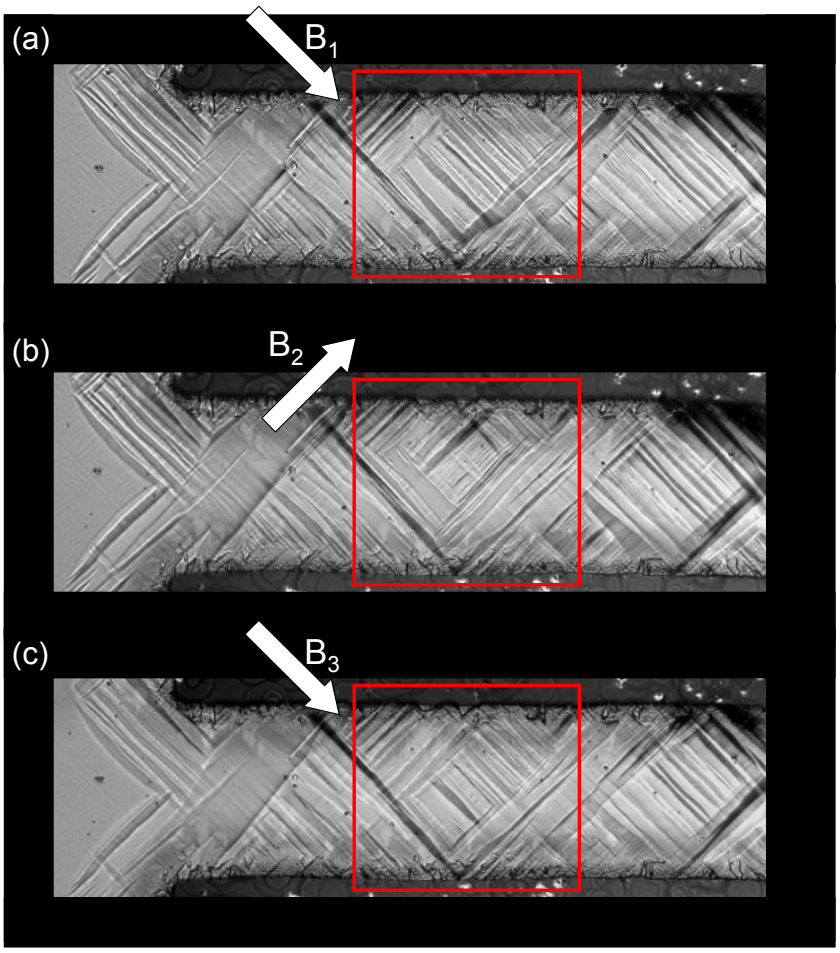

Figure 5.16: Optical microscopy images of the released microbridge after subsequent heating-cooling cycles. The beam was exposed to a magnetic field of 0.5 T during cooling from 380 to 300 K. As indicated by the arrows the field was applied under ± 45° to the length of the bridge. Close to the center of the beam the twinning pattern can be manipulated by the external field. Here the line pattern is changed depending of the field direction (a)-(c).

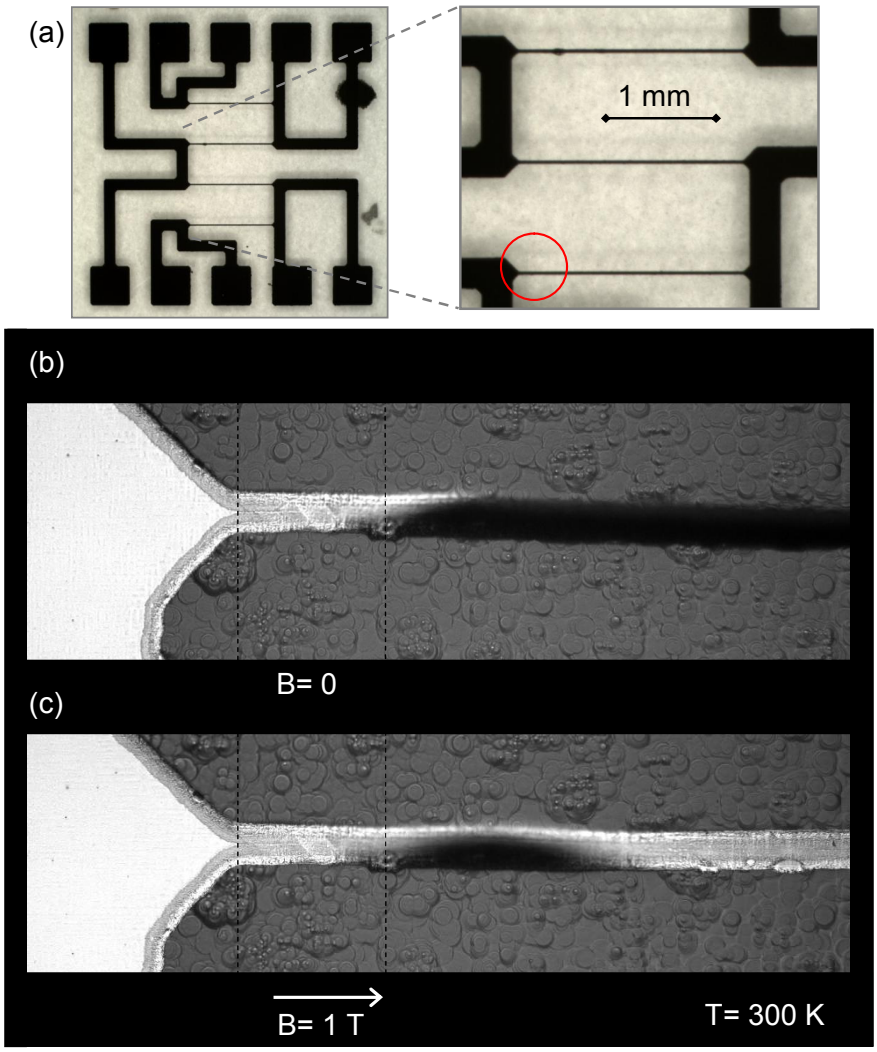

Figure 5.17: Microbridges with a high aspect ratio can be prepared using the pattern imaged in the overall view of the sample (a). The freestanding beams in the center are 2 mm long and 25 μm wide. After one transformation cycle the lower bridge is slightly twisted near the left endpoint (b). This twist is partly eliminated after a magnetic field of 1.0 T was applied parallel to the length of the bridge. This shape modification can originate from MIR of variants within the beam structure.

5.4 Key results

The surface morphology of films with different crystallographic orientation has been studied by optical microscopy in conjunction with AFM and SEM. For martensitic samples of $(100)_A$ orientation three different regular surface patterns generated by twinning are observed. In contrast, no twinning pattern is visible on the surface of $(110)_A$ oriented films, because different martensite variants are separated by twin planes running parallel to the surface in that case. Using a combination of FIB etching and SEM two basic twin plane configurations have been identified for films prepared on MgO(100). Twin planes can either be aligned under 45° or perpendicular to the film surface. The different microstructures manifest in distinct surface reliefs that can be distinguished in the light microscope. The observed macroscopic twinning patterns are explained on the basis of the variant configuration as probed by XRD. The majority of films with $(100)_A$ orientation are composed of four orthorhombic variants that are separated by $(101)_A$ type twin planes aligned along the film normal. A simple model to link the microscopic variant arrangement with the macroscopic surface pattern was derived. The absence of magnetically induced reorientation of variants in films released from MgO(100) substrates is explained in the context of this qualitative model. The failed attempts to directly observe magnetic-field-induced changes in the twinning pattern is motivated by the highly symmetric, fine-twinned martensite structure. In addition to optical microscopy with applied magnetic field, a custom heater stage was used to study the martensite-austenite transformation for samples with $T_{Ms} > 300$ K. The phase transformation can be directly followed, as the surface pattern starts to vanish at T_{As}. On cooling the twinning pattern is recovered at T_{Ms}. Accordingly, this methods provides fast identification of the structural transformation temperatures.

Chapter 6

Magnetic properties

The magnetic properties of the Ni_2MnGa system are of utmost importance for the appearance of the magnetic shape memory effect. A crucial prerequisite for magnetically induced strains is a high magneto-crystalline anisotropy that couples the magnetization to the crystal lattice. Furthermore a high saturation magnetization (M_S) is beneficial, since the introduced magnetic energy is directly proportional to M_S. The saturation magnetization of the thin film samples is deduced from hysteresis loops measured with a VSM and a SQUID magnetometer. Magnetometry is, moreover, a suitable tool to determine the phase transformation temperature of the samples. For that purpose the temperature evolution of the magnetization in low field is scanned.

To gain insight on the microscopic origin of the magneto-crystalline anisotropy some films were investigated with polarized X-ray light facilitated by a a synchrotron light source. The spectroscopy method exploits the magnetic circular dichroism and provides element-specific information on spin and orbital magnetic moments. The combination of two detection modes, the surface sensitive total electron yield signal and the measurement of the transmitted X-ray light intensity, allows comparing the moments at the film surface and in the sample volume. Moreover, X-ray absorption spectroscopy is a sensitive probe for the electronic structure of the involved $3d$ metals. The absorption spectra contain information about the unoccupied local density of states (LDOS) involving hybridized d states of Mn and Ni near the Fermi level. Hence, changes in the electronic structure of Ni_2MnGa during the phase transition can be detected by XAS.

6.1 Bulk magnetometry

6.1.1 Phase transformation

The structural phase transformation in Ni_2MnGa is accompanied by a drastic change in the magnetic properties. In the austenitic phase, below T_C the com-

pound is ferromagnetic and almost isotropic, since the crystal lattice is cubic. This does not hold for the martensite phase, where the lattice distortion leads to a considerable magneto-crystalline anisotropy. In the orthorhombic system the short c-axis is the magnetic easy axis, while in the non-modulated tetragonal phase the c-axis denotes the crystallographic long axis that is the hardest to magnetize. For the two modulated phases, i.e. 5M and 7M, the magnetic easy axis is the short c-axis, though 5M is described as a tetragonal structure [59]. Due to the change in anisotropy the phase transition can easily be detected in temperature-dependent magnetization measurements in low field. Fig. 6.1 shows the temperature evolution of the in-plane magnetization for a Ni-Mn-Ga film on a $Al_2O_3(11\bar{2}0)$ substrate. The sample is exposed to a magnetic field of 0.01 T applied parallel to the film plane. This field strength is not sufficient to saturate the sample. Starting from room temperature the magnetization increases to a peak-like maximum at 360 K. With increasing temperature a sharp drop in the magnetization occurs, as the Curie temperature of 370 K is approached. On cooling the magnetization is recovered until a distinct decrease sets in at T=340 K. This is the martensite start temperature. As the structure changes from cubic to orthorhombic the magnetization is dictated by the forming variant configu-

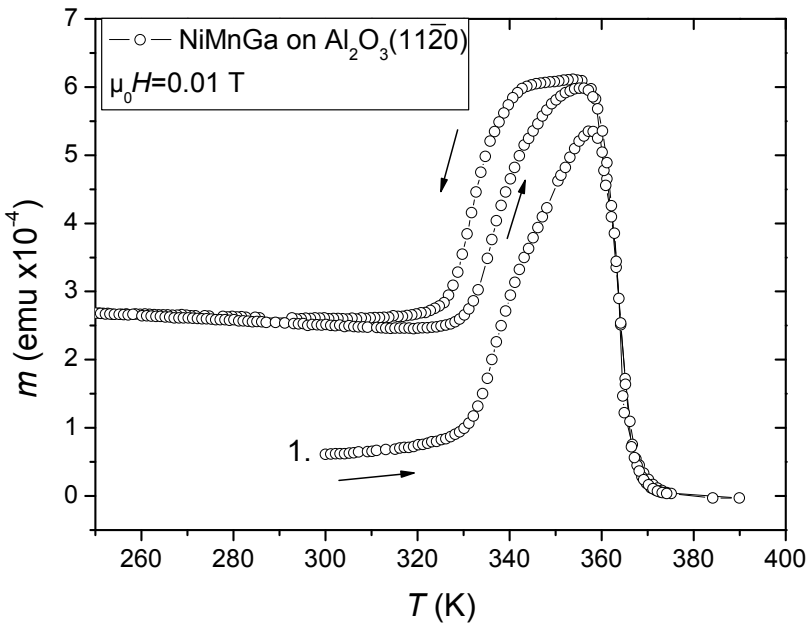

Figure 6.1: Temperature evolution of the in-plane magnetization in low field for a Ni-Mn-Ga film on $Al_2O_3(11\bar{2}0)$. Under cooling a clear drop in magnetization indicates the phase transition. In the martensitic phase, below T=330 K, a strong uniaxial anisotropy leads to the reduced in-plane magnetization. The phase transformation shows a characteristic hysteresis of 6 K.

ration. Qualitatively the magnetization vector is rotated from in-plane towards out-of-plane alignment. According to the XRD analysis of the martensite structure (s. chapter 4.3), $(110)_A$ oriented films essentially feature twin planes that run parallel to the film surface and separate two orthorhombic variants. The c-axes of these variants point roughly under 45° to the film surface. Considering a complete alignment of the local magnetization vector along the easy axis, a decrease of 50 % in the total magnetization is expected. This is in good agreement with the observation. In fact, the macroscopic in-plane magnetization in the martensite is even less than half that of the austenite. This can be motivated by looking at the martensite crystal structure in detail. As a consequence of the rotation of the martensite lattice the c-axes of both variants are aligned under $\alpha = \arctan(a/c) \approx 48.4°$ to the film surface. Hence, the in-plane projection of the magnetization vector of each variant is reduced by $|\mathbf{m}_{\parallel}| = \cos\alpha \cdot |\mathbf{m}|$, while the out-of-plane component is increased to $|\mathbf{m}_{\perp}| = \sin\alpha \cdot |\mathbf{m}|$. The result is an effective out-of-plane anisotropy that is reflected in the measured macroscopic magnetization of the martensitic sample.

On re-heating the in-plane magnetization jumps back to the original value, as the film transforms from martensite to austenite (s. Fig. 6.1). The curve progression of the austenite-martensite transition is reproduced with a slight shift in the transformation temperature. A thermal hysteresis of 6 K is observed, which is a typical value for the $(110)_A$ oriented films prepared within this work.

For stoichiometric Ni_2MnGa bulk samples an increase of the saturation magnetization at the austenite-martensite transformation was observed by Webster et al. [32]. If the external field strength is sufficient to saturate the sample this increase is observable when cooling below T_M. Fig. 6.2 displays the temperature evolution of in-plane and perpendicular magnetization for three different values of the applied magnetic field. The characteristic change of the easy axis direction is evident in the low field measurement (red curve). At T=270 K the sample enters the martensitic phase that features a strong uniaxial anisotropy, which causes the described drop in the in-plane magnetization. In contrast, measurements in high field reveal an increase of the total magnetic moment in the martensite. For both measurement geometries, with magnetic field applied in-plane (black line) and perpendicular to the film plane (blue line), the total magnetization increases at the austenite-martensite transition. This is in agreement with observations on bulk samples [32, 66] and theoretical calculations [73].

The phase transformation temperature in Ni-Mn-Ga depends sensitively on the composition (s. chapter 2.3.3). While for bulk Ni_2MnGa single crystals the phase transformation occurs at T=202 K [32], values up to 625 K have been calculated for Ni-rich compositions [126]. Our thin film samples prepared with the stoichiometric target show martensite start temperatures in the range of 220 to 280 K. Besides the strong influence of the actual film composition the crystallographic orientation significantly affects the transformation temperature. Fig. 6.3 shows magnetization vs. temperature curves for two films that were prepared

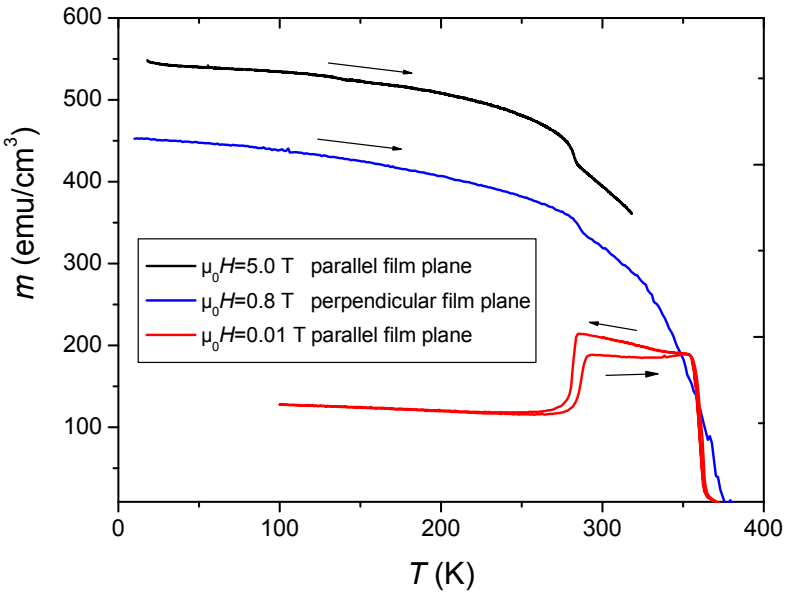

Figure 6.2: Magnetization vs. temperature for a thin Ni-Mn-Ga film on $Al_2O_3(11\bar{2}0)$ substrate. The high field data have been corrected with a constant diamagnetic contribution of the substrate.

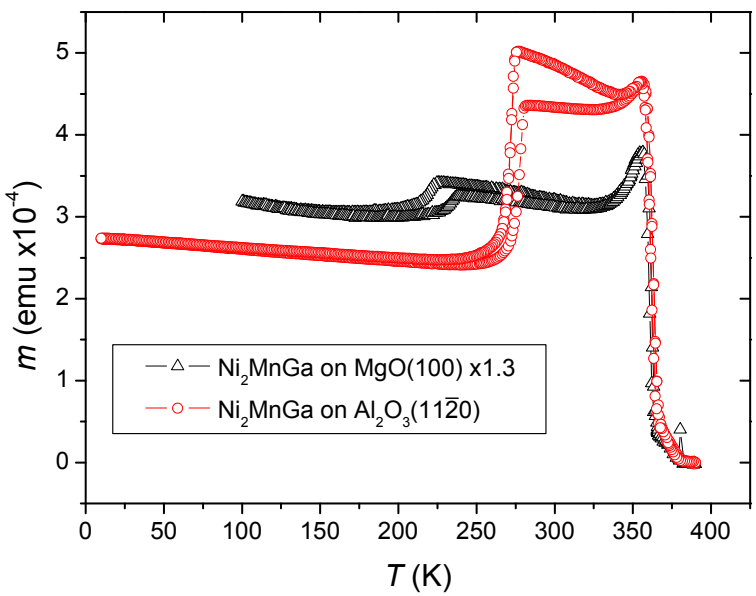

Figure 6.3: Temperature evolution of the in-plane magnetization in low field for Ni_2MnGa films on MgO(100) (black triangles) and $Al_2O_3(11\bar{2}0)$ (red circles) that have been prepared simultaneously. The phase transformation temperatures differ significantly for the two different crystallographic orientations.

simultaneously and hence have the same composition. The characteristic drop of the in-plane magnetization appears at 275 K for the film on $Al_2O_3(11\bar{2}0)$, while the $(100)_A$ oriented sample on the MgO(100) substrate has a martensite start temperature of 220 K. As described in chapter 4.3 the different crystallographic orientations result in different variant configurations. The $(110)_A$ oriented samples feature twin planes that are aligned parallel to the film surface, whereas films on MgO(100) possess twin planes running predominantly along the surface normal. This discrepancy in twin plane alignment yields a difference in interaction between twin boundaries and substrate. In the case of $Al_2O_3(11\bar{2}0)$ substrates the twin planes do not intersect with the substrate surface, which is not the case for the films on MgO(100). Furthermore the variant configuration observed for $(110)_A$ oriented samples facilitates a habit plane forming at the film-substrate interface. In combination with the favorable twin plane alignment with reduced substrate interaction this leads to a stabilization of the martensite for $(110)_A$ oriented films. The different variant configurations motivate not only the discrepancy in the austenite start temperature, but also the size of the magnetization drop. The change of the in-plane magnetization is comparably low for the films on MgO(100) substrates, where the phase transformation leads to martensitic variant configuration with an effective in-plane alignment of the c-axis. Consequently, the magnetization vector remains parallel to the film plane, as the anisotropic martensite forms.

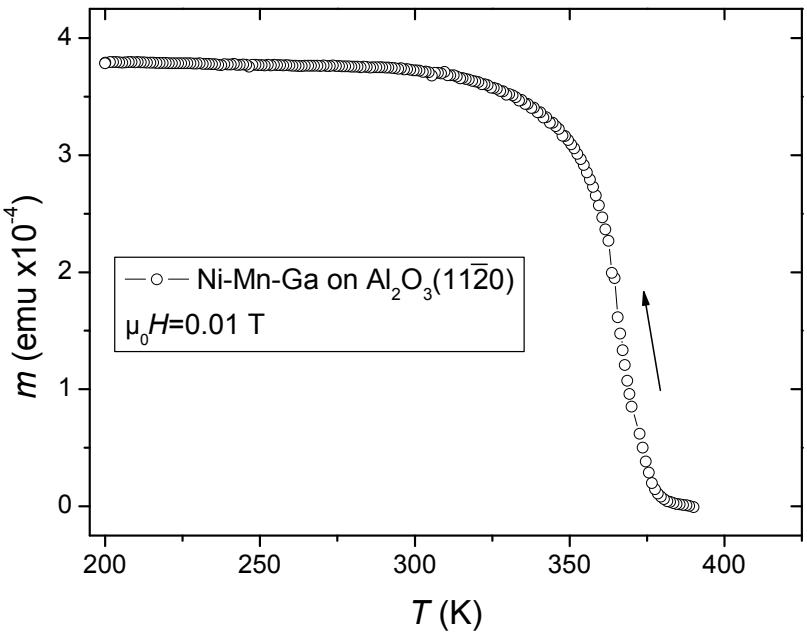

Figure 6.4: In the case of Ni-rich samples the structural phase transition cannot be detected in temperature-dependent magnetization measurements, since T_C is lower than the austenite start temperature.

It is worth mentioning that the structural phase transformation in Ni-Mn-Ga can occur above the Curie temperature. Theoretical calculations indicate that this is the case for $Ni_{2+x}Mn_{1-x}Ga$ with a Nickel excess of 0.2 and higher [58]. For samples prepared with the off-stoichiometric targets at low working pressure ($\leq$ 0.01 mbar) such a behavior is observed. The temperature evolution of the sample magnetization exhibits no step-like changes in the temperature interval of 100 to 400 K (s. Fig. 6.4). In accordance with the previously described samples of different composition (s. Fig. 6.1 to 6.3) T_C is approximately 375 K. High temperature XRD reveals a structural phase transition from martensite to austenite at T_{As}=410 K for this sample (s. also [18]). Hence, it is not possible to detect the structural phase transformation in temperature-dependent magnetization measurements, as the ferromagnetic-paramagnetic transition occurs below T_{Ms}.

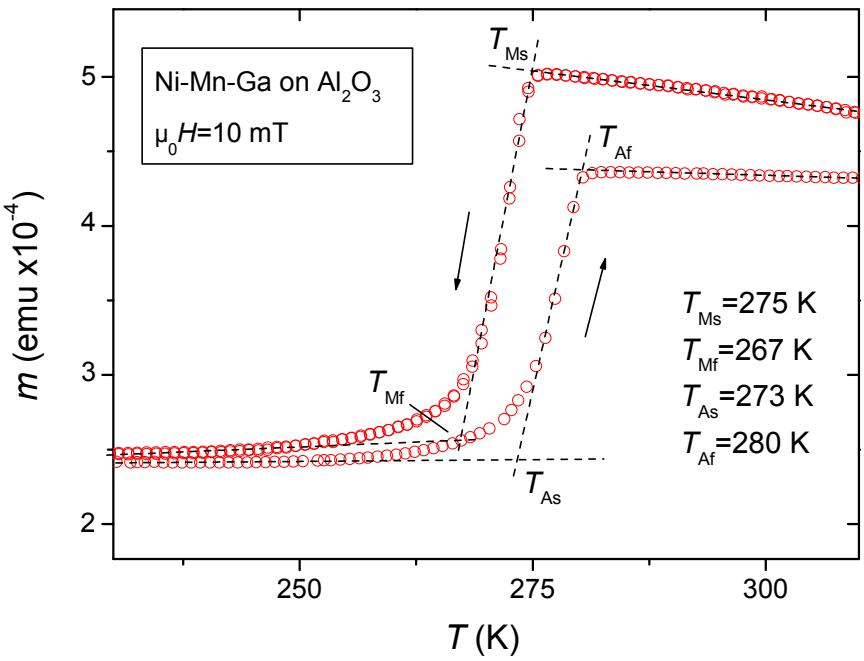

Figure 6.5: A linear extrapolation of the experimental data is used to determine the start and finish temperatures of the austenite and martensite, respectively.

As described in chapter 3.1 the film composition and thus the phase transformation temperature can be tuned by adjusting the Argon pressure during sputter deposition (s. Fig. 3.3 in chapter 3.1). For the samples with $T_{Ms} < T_C$ the evolution of the phase transformation can be studied by scanning the magnetization as a function of the sample temperature. To determine the start and finish temperature of the phase transformation upon heating and cooling an extrapolation of the linear parts of the magnetization curves can be used (s. Fig. 6.5). In particular, the martensite start temperature and the austenite finish temperature

can be deduced directly from the magnetization curve, since a sharp change of slope is visible here. This is not the case for the martensite finish and the austenite start temperature. On cooling the martensite start temperature shows as a defined drop in magnetization. This linear curve progression is followed by a temperature interval with rather continuous gradient of magnetization variation. On heating the described curve progression is reproduced.

6.1.2 Saturation magnetization

The observed increase of the saturation magnetization at the austenite to martensite transition can also be detected in hysteresis loops measured for different temperatures in the vicinity of T_M. The samples prepared with the stoichiometric target show a narrow hysteresis in the magnetic polarization in the austenite phase (s. Fig. 6.6). The saturation magnetization of the displayed sample is calculated to M_S=2.94 μ_B/formula unit (f.u.) in the austenite at T=282 K. The scan at T=255 K yields a value of 3.31 μ_B/f.u. for the martensitic film. The start and finish temperatures for austenite and martensite of this sample were determined by T-sweeps in low field (s. Fig. 6.5). At 10 K, which is the typical temperature to determine the saturation magnetization of our samples on $Al_2O_3(11\bar{2}0)$, M_S reaches a value of 3.43 μ_B/f.u. Hence, the considerable increase in M_S from T=282 K to T=255 K is basically caused by the phase transformation. When

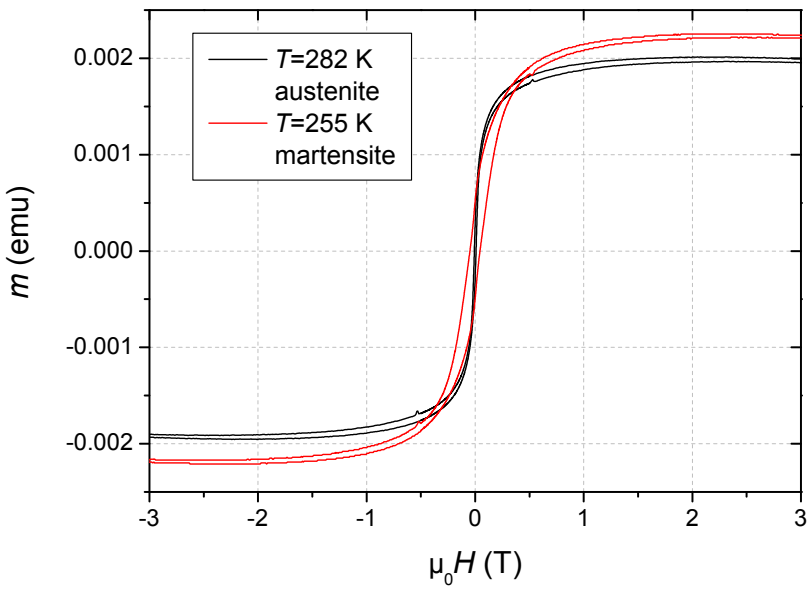

Figure 6.6: Hysteresis loops measured above (black line) and below the martensite start temperature (red line) for a sample on $Al_2O_3(11\bar{2}0)$. In the martensitic phase the saturation magnetization is considerably increased.

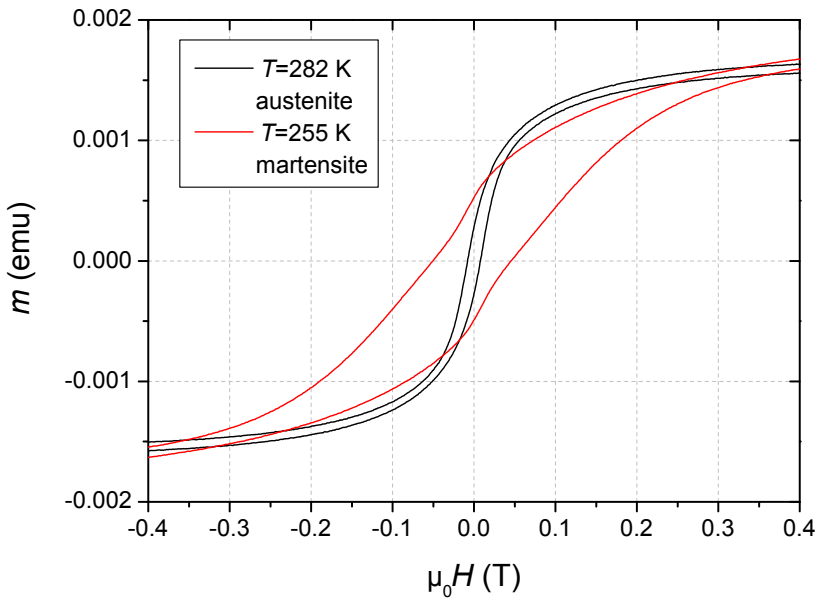

Figure 6.7: While the cubic parent phase exhibits a narrow hysteresis loop with a coercive field of 8 mT (black line), the martensitic phase shows an increased coercivity of 50 mT (red line).

comparing the low field region of the hysteresis loops (s. Fig. 6.7) the difference in coercive field strength for austenite and martensite stands out. While the cubic parent phase shows a coercivity of 8 mT, the martensitic phase exhibits an increased value of 50 mT for this sample. As discussed in chapter 3.1 the saturation magnetization is sensitive on the substrate temperature during film deposition. For the films with near-stoichiometric composition a maximum value of M_S=3.86 μ_B/f.u. was deduced from hysteresis loops. The deviation from the reported value of 4.2 μ_B/f.u. for bulk single crystals indicates atomic disorder in the thin film samples. In particular, disorder at Mn sites can lead to antiferromagnetic coupling of Mn atoms and thus to a reduction of the magnetic moment [94]. For the Mn-rich off-stoichiometric targets 3 and 4 with e/a ≈7.65 theoretical calculations predict a saturation magnetization of 3.5 μ_B/f.u. [71]. Experimental results on bulk material provided in ref. [71] vary between 3.2 and 3.4 μ_B/f.u., while our thin film samples typically possess a saturation magnetization of 3.0 μ_B per formula unit at low temperature. In case of target 5 X-ray fluorescence spectroscopy reveals a composition of $Ni_{2.1}Mn_{1.1}Ga_{0.8}$ (s. chapter 3.1), which means e/a ≈7.8. In accordance with theoretical calculations and observations for bulk samples [71] our films prepared from this target show saturation magnetization values slightly below 3 μ_B/f.u.

6.1.3 Indication of MIR in hysteresis loops

For some of the Mn-rich samples (sputtered from target 5) an anomalous shape of the hysteresis loops was observed. At room temperature, that means in the martensitic phase, a step-like increase appears, when applying the field parallel to Ni-Mn-Ga $[10\bar{1}]_A$ for films on $Al_2O_3(11\bar{2}0)$ (s. Figs. 6.8 and 6.9). Starting at zero field the sample magnetization increases linearly with increasing external field strength. When reaching $\mu_0 H_{ext}$=60 mT the slope of the polarization curve suddenly changes and becomes steeper. Above $\mu_0 H_{ext}$=100 mT the slope continuously decreases as the magnetization approaches saturation. The described sudden increase in sample magnetization was observed in bulk Ni-Mn-Ga single crystals and identified as signature of magnetically induced reorientation of variants [127]. As soon as the difference in magnetic energy of adjacent, but differently aligned variants exceeds the elastic energy needed to move a twin boundary, a change in the variant distribution occurs. The redistribution effectively increases the variant fraction with magnetic easy axis aligned parallel to the external field, which leads to a rise in magnetization. This scenario could explain the observed increase for the magnetization curve with H $||[10\bar{1}]_A$. Accordingly, the steps in the hysteresis loops are not present, if the magnetic field is applied parallel to $[010]_A$, i.e. along the b-axis of the martensite. In contrast to the magnetization curve with field applied along Ni-Mn-Ga $[10\bar{1}]$ this hysteresis loop reveals the "hard" axis character of the intermediate b-axis. As known from measurements on bulk material [4], the long a-axis of the 7M structure is the magnetic hard axis, while the short c-axis is the easy magnetization axis. The b-axis shows an intermediate magnetization behavior. When comparing directly the in-plane magnetization curves with H $||[10\bar{1}]_A$ to those with H $||[010]_A$, the second configuration reveals a hard axis behavior, as no contribution of the c-axis is included here.

A similar discrepancy in the magnetization curves for different in-plane directions of applied field is present for films on MgO(100) substrates (s. Figs. 6.10 and 6.11). While no indication of MIR of variants is detected for scans with H $||[001]_A$, the hysteresis loops with H $||[101]_A$ exhibit jump-like increases in the magnetization. Likewise the samples on $Al_2O_3(11\bar{2}0)$ the magnetization jumps appear, if the external field is applied parallel to the twin plane. According to the phenomenological model for strain and magnetization in MSM alloys suggested by O'Handley [51] this field configuration produces the highest pressure on the twin plane. Counter to what one would expect, the magnetic driving force is greatest for a field orientation parallel to the twin plane for a two-variant system with strong anisotropy. Nevertheless, similar steps in magnetization have been observed for the H $||[001]_A$ configuration by other groups [128, 129]. For these films on MgO(100) the hysteresis loops for both in-plane field configurations (H $||[001]_A$ and H $||[011]_A$) show sharp changes in slope that have been interpreted as indication of MIR. In contrast, our samples on MgO substrates show no signature

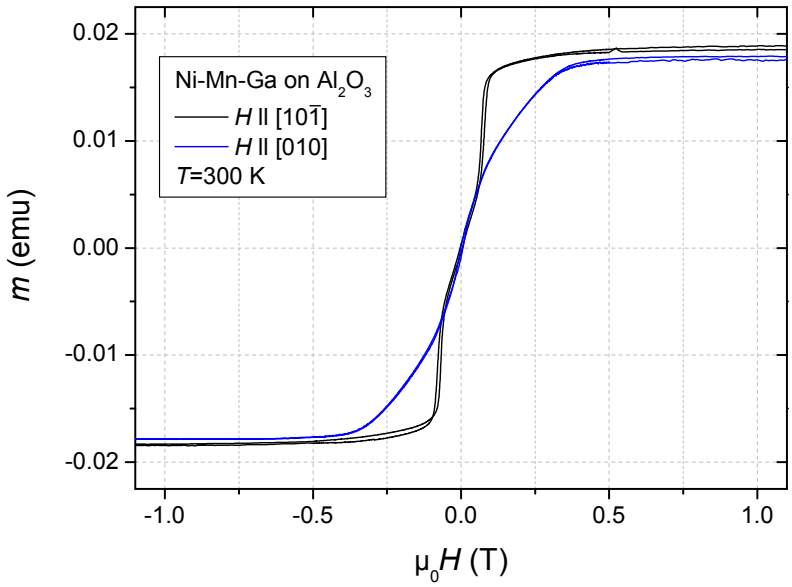

Figure 6.8: In-plane magnetization curves for a Ni-Mn-Ga film on $Al_2O_3(11\bar{2}0)$ substrate. The field orientation parallel to $[010]_A$ reveals the "hard-magnetic" character of the b-axis (blue line), while for $H \parallel [10\bar{1}]_A$ the a- and c-axis of the two prevalent variants contribute (black line). A zoomed view of the low-field region is provided by Fig. 6.9.

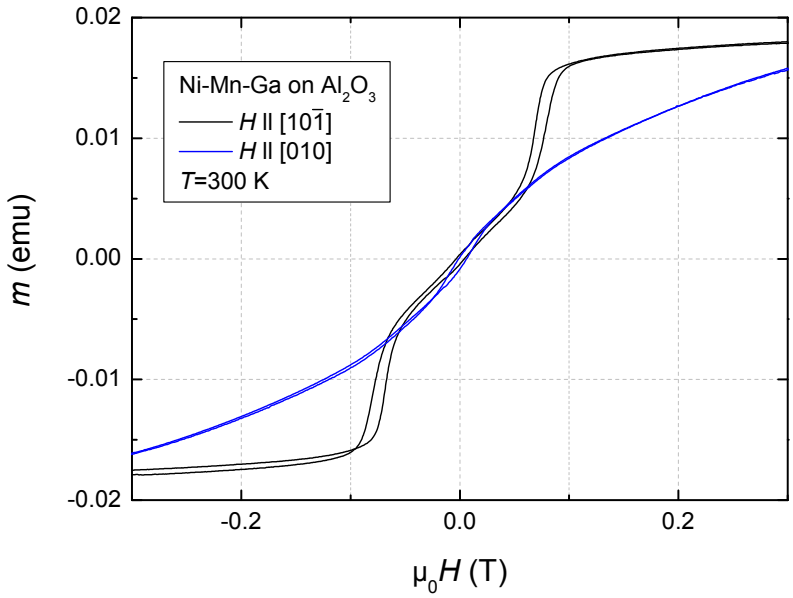

Figure 6.9: For an external field applied parallel to Ni-Mn-Ga $[10\bar{1}]_A$ a step-like increase in magnetization occurs around $\mu_0 H_{ext}$=60 mT. The sudden rise of sample magnetization can be explained by MIR of variants.

of MIR, if the magnetic field is applied parallel to $[100]_A$ or $[001]_A$. For this field configuration two different regions in the polarization curve can be distinguished. In the region of low external field strength a soft-magnetic contribution dominates the magnetization curve, while above $\mu_0 H_{ext}$=100 mT a hard-axis magnetization behavior appears. These two contributions can be assigned to differently aligned martensite variants. As identified by XRD the martensitic films on MgO(100) basically feature four different variants, two of which have the *c*-axis oriented almost parallel to $[001]_A$. This variant fraction (that constitutes roughly 40 % of all variants) causes the soft-magnetic contribution, if the field is applied along the $[001]_A$ direction. For the other two variants the magnetic field is then almost parallel to the *a*-axis, which is the magnetic hard axis. This explains the shape of the hysteresis loops for $\mu_0 H_{ext} \geq 100$ mT, where the external field strength is sufficient to rotate the local magnetization from *c*- towards *a*-axis direction for the respective fraction of variants ($\approx$ 40 %). However, this two-component model does not explain the shape of the magnetization curve for $H \,||[101]_A$. For both crystallographic orientations, i.e. films on $Al_2O_3(11\bar{2}0)$ and MgO(100), the steps in magnetization occur, if the external field is applied parallel to the twin planes. Such a magnetization curve was also observed for freestanding films that were released from MgO substrates. Though the observations are a strong indication for MIR of variants (compare refs. [128, 129]), the results of magnetic field assisted XRD contradict this interpretation. None of the investigated samples showed any change in the martensite variant distribution, when exposed to a field strength of 200 mT and higher. The variant configuration was directly probed by scans of the XRD peaks, that can be assigned to the different variants. Consequently, these results indicate that no field induced variant redistribution takes place. Since no structural changes in response to a magnetic field have been deteced, the interpretation of the magnetization data remains questionable. Probably the sudden increase in magnetization is caused by a complex saturation process of the multi-variant film that involves rotation of the local magnetization of microscopic domains. For the samples on MgO substrates (as well as films released from MgO) the proposed mesoscopic twinning pattern might affect the shape of the hysteresis loop. Further investigations with a technique capable of mapping the small-size domains are needed to identify the origin of the anomalous magnetization behaviour.

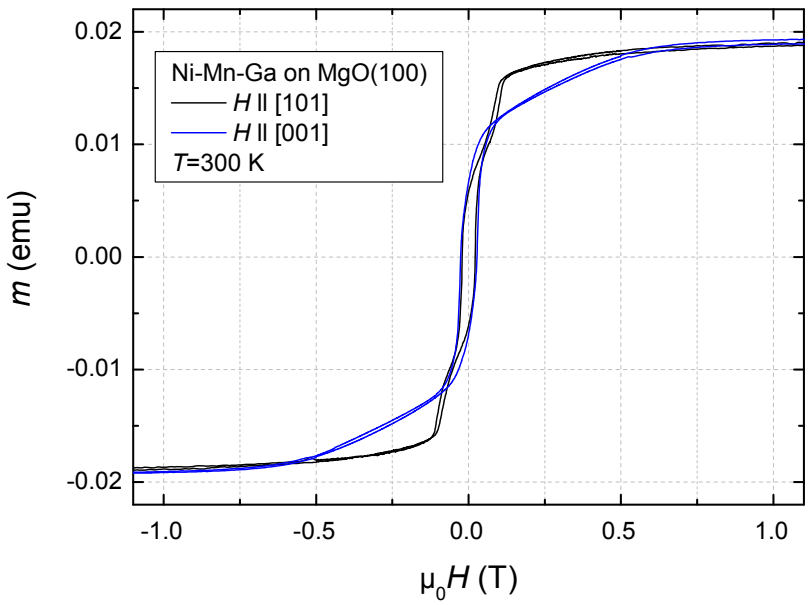

Figure 6.10: In-plane magnetization curves for a Ni-Mn-Ga film on MgO(100) substrate with magnetic field applied along $[101]_A$ (black line) and $[001]_A$ (blue line). For a zoomed view of the low-field region s. Fig. 6.11.

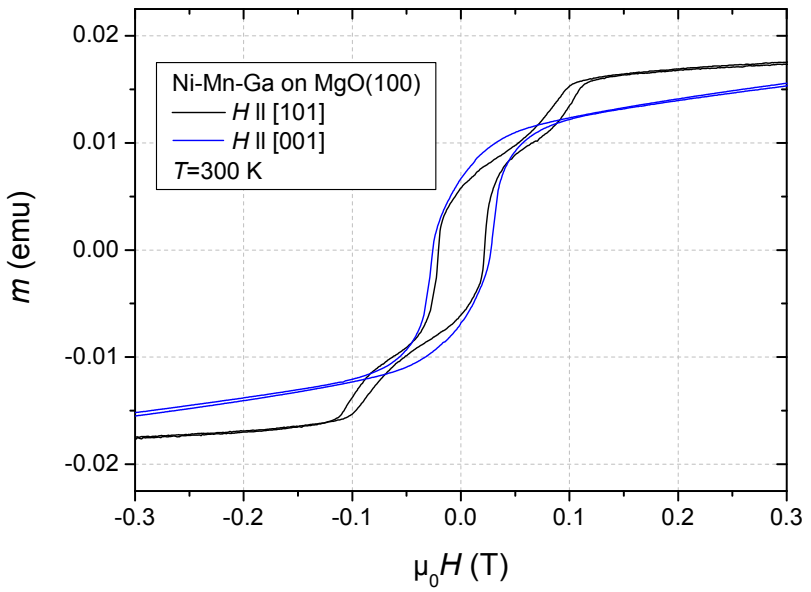

Figure 6.11: Likewise the samples on Al_2O_3 the films on MgO show jump-like increases in magnetization in response to an external field applied parallel to the twin planes of the predominant variants.

6.2 XAS and XMCD

Complementary to the magnetometry measurements some samples have been investigated with X-ray absorption spectroscopy (XAS). This rather new analytical method [130, 131] is based on resonant excitation of electrons from a defined ground state to vacant states close to the Fermi level. When using circularly polarized light, the X-ray magnetic circular dichroism (XMCD) effect can be used to obtain element-specific information on spin and orbital magnetic moments. In contrast to magnetometry measurements, these experiments allow to discriminate between surface and bulk properties, as both are determined separately. For surface sensitive measurements the so-called total electron yield (TEY) is detected. Here the Auger electrons and the secondary electron cascades, created by the absorbed X-ray light, are directly measured as electric current between sample and a conducting shield. The information depth of this signal is limited by the characteristic escape depth of the electrons, which is typically a few nm. In addition, the intensity of the transmitted light is detected via x-ray luminescence in the MgO or Al_2O_3 substrate. The transmission signal (TM) yields information on the magnetic properties integrated along the thickness of the thin film sample. The XAS experiments were performed in collaboration with the group of professor Elmers of Mainz University [132]. All spectra were measured at the UE56/1-SGM beamline of the BESSY II synchrotron light source. Experimental details can be found in refs. [133] and [134].

The function principle of XAS is illustrated in Fig. 6.12 (a). The absorbed X-ray light excites electrons of the $2p$ core level into vacant states above the Fermi level (E_F). For that purpose, the energy of the incident light is varied around the characteristic absorption edge of the investigated element in the compound (s. Fig. 6.12 (b)). For transition metals the resulting absorption spectrum features two peaks corresponding to the $2p_{3/2} \rightarrow 3d$ transitions (L_3 edge) and the $2p_{1/2} \rightarrow 3d$ transitions (L_2 edge). In fact, the absorption spectrum contains contribution from both $p \rightarrow d$ and $p \rightarrow s$ transitions. The latter can be removed by subtracting a step function. When exciting the $2p$ electrons with light of left or right circular polarization, an effective spin polarization of the photoelectrons occurs. The measured intensity then depends on the number of vacant d-states with the respective spin direction. Hence, the spin polarized photoelectrons act as a detector for the spin-resolved local density of states for electrons above E_F.

In general, dichroism denotes the effect of polarization-dependent differences in optical absorption. For a magnetic material the peak intensities in the absorption spectra will depend on the relative orientation of the light polarization vector $\mathbf{P}$ and sample magnetization $\mathbf{M}$, which is utilized in the XMCD technique. The observable intensity difference is strongest for parallel vs. antiparallel alignment of $\mathbf{P}$ and $\mathbf{M}$. For a fixed sample magnetization the spectrum recorded with right circularly polarized light (σ^+) is labeled μ^+, while μ^- denotes the spectrum taken with light of left circular polarization. The difference $\mu^+ - \mu^-$ is the XMCD sig-

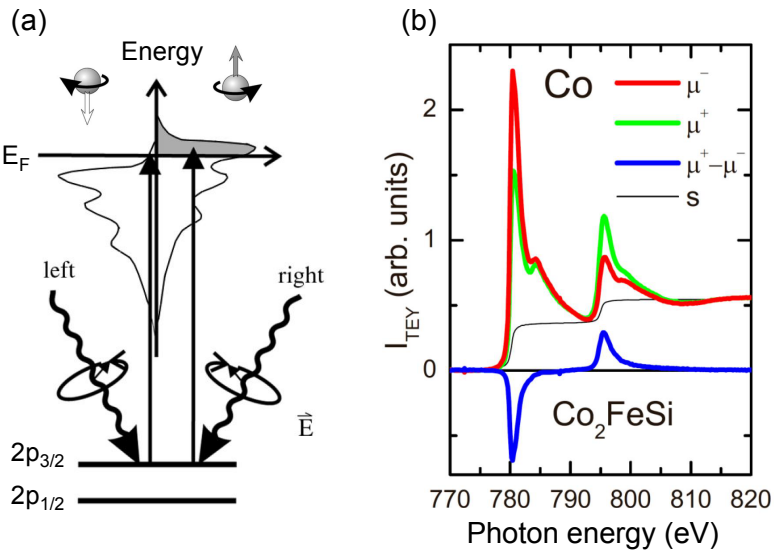

Figure 6.12: (a) Illustration of the XAS and XMCD function principle. X-ray light of circular polarization excites electrons from a spin-orbit split inner shell to vacant d states above the Fermi level. (b) Typical XAS spectrum recorded at the Co $L_{2,3}$ edges for parallel (μ^+) and antiparallel (μ^-) alignment of polarization and magnetization vector. After subtracting the $p \rightarrow s$ background (black line) the XMCD spectrum results from the difference $\mu^+ - \mu^-$. Taken from [134].

nal (s. Fig. 6.12 (b)). In the experiment X-ray light of fixed polarization is used and the sample magnetization is switched from parallel (μ^+) to antiparallel (μ^-) orientation by an external field.

To describe the process that creates the XMCD effect a simplified one-electron model can be used [136]. Neglecting the degeneracy of the fully occupied $2p$ states, the spin-orbit splitting of the core shell is described as an initial state here. The proper description makes use of the configuration picture that involves a ground state and an excited state of the atom [135]. The photon induced transition between initial (i) and final state (f) can be described by Fermi's golden rule:

$$I(\hbar\omega) \propto \sum_{i,f} \int_{BZ} d^3k \; M_{fi}^2 \; \delta(E_f(\mathbf{k}) - E_i(\mathbf{k}) - \hbar\omega) \; \mathcal{F}(E_i(\mathbf{k})) \; [1 - \mathcal{F}(E_f(\mathbf{k}))] \quad (6.1)$$

where M_{fi}^2 is the transition matrix element and $\mathcal{F}$ the Fermi function that describes the occupation of initial and final states. The Delta function (δ) ensures energy conservation, when summing over all initial and final states and integrating all $\mathbf{k}$-points of the Brillouin zone (BZ). This comprehensive description takes correlation effects into account and is able to describe multiplet structures observed in the XMCD spectra of oxides [137]. However, for $3d$ metals the one-

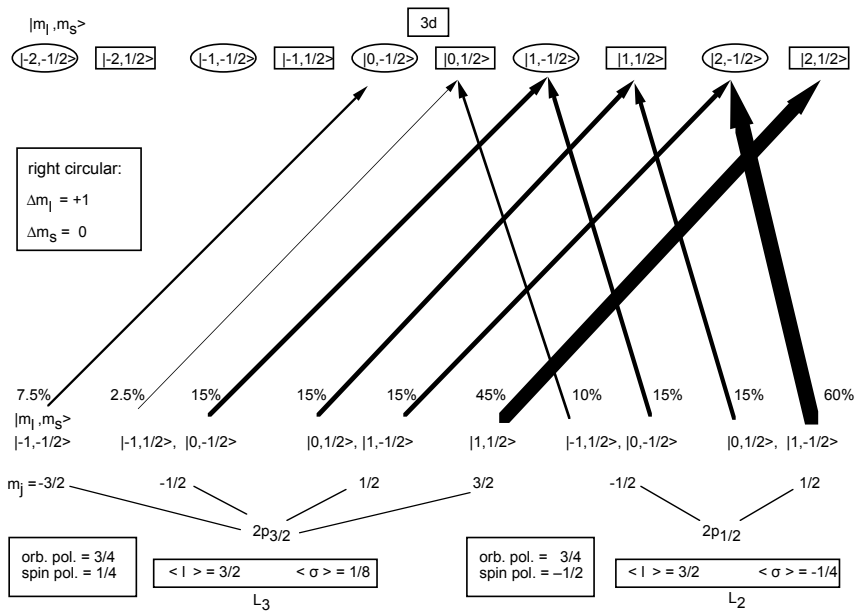

Figure 6.13: Possible $2p \rightarrow 3d$ transitions for excitation with right circularly polarized light. The transitions between states with respective quantum numbers $|m_l, m_s\rangle$ have to satisfy $\Delta m_s = 0$ and $\Delta m_l = +1$. Considering the different transition probabilities as calculated from the angular matrix elements an effective spin polarization of the photoelectrons occurs. The scheme is taken from ref. [135].

electron picture, described in the following, is sufficient to explain the process that leads to the observed spectra. When exciting the $2p$ electrons with circularly polarized light the possible transitions to $3d$ states are polarized concerning spin and orbital moment. Fig. 6.13 depicts the initial $2p$ states sorted by quantum number $m_j = m_l + m_s$. The spin-orbit coupling is $l - s$ for $2p_{1/2}$ states, while the opposite interaction $(l + s)$ is true for $2p_{3/2}$ states. All possible transition to $3d$ states have to obey the transition rules, that is $\Delta m_l = +1$ and $\Delta m_s = 0$ in the case of right circularly polarized light. The probabilities for the individual transitions can be derived from the respective angular matrix elements [138]. By looking at the possible final states and the transition probabilities, one obtains a spin polarization of -0.5 for the L_2 edge ($2p_{1/2} \rightarrow 3d$). The transitions from $2p_{3/2} \rightarrow 3d$ result in 62.5 % in final states with spin-up. Hence, the spin polarization is 0.25 at the L_3 absorption edge. For left circularly polarized light the effective spin polarization changes sign. For both transitions also an orbital polarization occurs, as 60 % of the final states feature a magnetic quantum number m_l=2. In the experiment some of the d-states of the transition metal are occupied, whereas the unoccupied, exchange split states at the Fermi energy act as a spin detector for the excited electrons. The opposing spin polarization at the L_2

and L_3 edges leads to the characteristic dichroism signal (s. Fig. 6.12 (b)). With the help of sum rules quantitative information of spin and orbital moment can be gained [139, 140]. Following the description in [135], for parallel/antiparallel alignment of **P** and **M** the spin and the orbital magnetic moments (μ_s and μ_l) can be derived from:

$$\mu_s = -\frac{(A-2B)}{\overline{I(L_2)+I(L_3)}}\ \mu_B\ N_h \tag{6.2}$$

$$\mu_l = -\frac{2}{3}\ \frac{(A+B)}{\overline{I(L_2)+I(L_3)}}\ \mu_B\ N_h \tag{6.3}$$

where A is the area under the L_3 difference peak, while B denotes the respective area of the L_2 difference peak (blue curve in Fig. 6.12 (b)). The area under the averaged spectrum, $\overline{I(L_2)+I(L_3)}$, is calculated from $(\mu^+ + \mu^-)/2$ after subtracting the step function (black line in Fig. 6.12 (b)). The only input parameter required is the number of d holes N_h that can be derived from theoretical calculations.

6.2.1 Phase transformation

As described in the previous section, temperature-dependent magnetization measurements present a convenient way to determine the phase transformation temperature for Ni-Mn-Ga samples. The observed changes of the in-plane magnetization appear in the same temperature interval where the structural phase transition is identified by XRD. This implies that the modified magnetic order is directly related to the reduced lattice symmetry of the martensitic phase. For the involved $3d$ metals the magnetic properties are mainly determined by their d valence electrons [141]. Consequently, the different magnetization behavior for martensite and austenite indicates that changes in the electronic structure of the Ni-Mn-Ga valence bands occur. Another method to determine the phase transformation temperature is studying the temperature evolution of the sample resistivity, as described in [142] and utilized in the previous work [18]. The observed jumps in magnetization and resistivity at the martensite start temperature are a clear indication of changes in the electronic structure during the phase transition.

The electronic structure, magnetic properties and equilibrium crystal structure of the Ni-Mn-Ga system is subject of several theoretical studies starting from the microscopic point of view. These ab initio calculations identify an electronic instability as the cause for the martensitic phase transformation [72, 73, 143]. The change in electronic structure mainly involves Ni related minority d states with $3d_{z^2}$ and $3d_{x^2-y^2}$ symmetry. These states are degenerated in the cubic parent phase, but split up in the tetragonal/orthorhombic martensite state. According to calculations of Ayuela et al. [73] the modifications in the band structure at

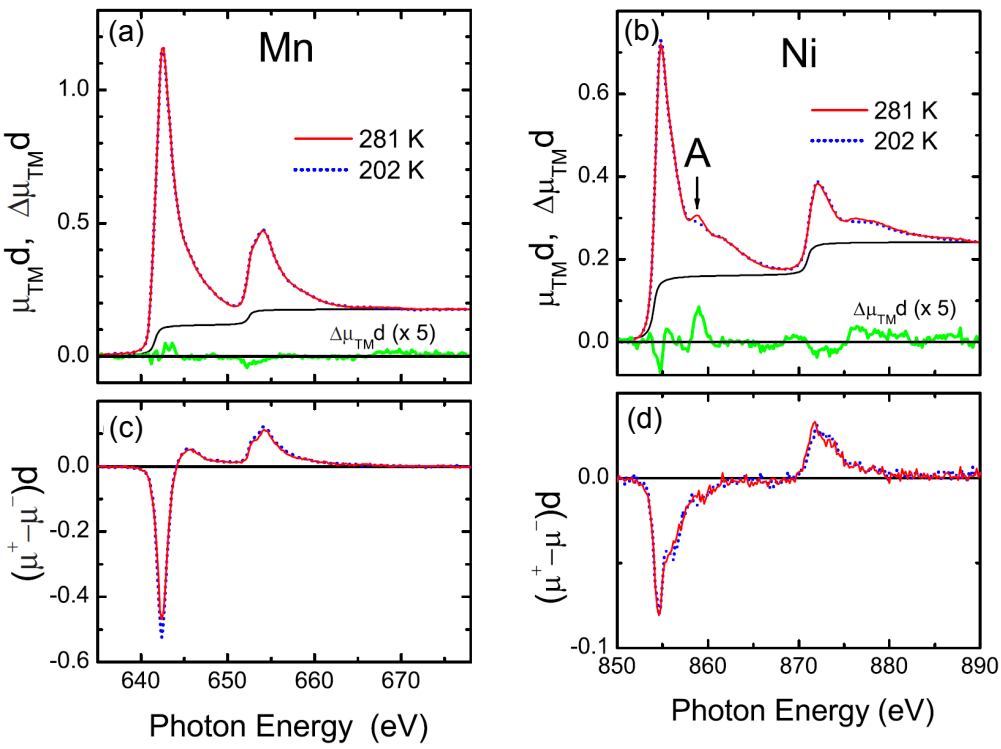

Figure 6.14: X-ray absorption coefficients measured at the Mn (a) and Ni (b) $L_{2,3}$ edges for $T < T_M$ (broken, blue line) and $T > T_M$ (red line). The difference of the spectra is plotted in green. The lower panel shows the XMCD signals derived from the Mn (c) and Ni (d) spectra for the respective temperatures. Originally published in [86].

the phase transition should be observable in experiments probing the density of Mn and Ni hybridized d states around the Fermi level. A suitable experiment to explore these states chemically resolved is energy-dependent X-ray absorption spectroscopy at the Ni and Mn $L_{2,3}$ edges. In the experiment we measure the intensity of the transmitted X-ray light via luminescence of the $Al_2O_3(11\bar{2}0)$ and MgO(100) substrates for various temperatures above and below T_M. The absorption coefficient for parallel (+) and antiparallel (−) alignment of **P** and **M** is given by $k^{\pm}(h\nu) = \mu^{\pm}(h\nu)d = -\ln[I^{\pm}(h\nu)/I_{ref}(h\nu)]$. The XAS and XMCD spectra measured on a 83 nm thick $Ni_2MnGa(110)$ film prepared on $Al_2O_3(11\bar{2}0)$ are presented in Fig. 6.14. When scanning the Mn $L_{2,3}$ edges for $T < T_M$ and $T > T_M$, the resulting spectra look almost identical. This is not the case for the Ni spectra, where a clear discrepancy can be spotted at a photon energy of 859 eV. Here a distinct satellite peak (A) is present in the cubic parent phase, while for the distorted martensite this feature is almost completely suppressed. The detailed temperature dependence of feature A is shown in Fig. 6.15 (c),

where the intensity increase $\Delta I_A = I_A(T) - I_A(202\text{ K})$ on heating is plotted. For comparison the temperature evolution of the XRD (400) austenite peak intensity is displayed. At low temperatures (T <270 K) the film is in the martensite phase, where the lattice symmetry leads to suppression of the $(400)_A$ reflection. On heating a sharp increase in the XRD peak intensity indicates the structural phase transition to the cubic parent phase. A similar temperature behavior is observed for the intensity variation of XAS peak A confirming the correlation to the structural phase transition. Moreover, the observed intensity change of peak A is in full agreement with theoretical predictions [73]. On basis of density functional theory calculations Ayuela et al. predict an observable spectral variation at the Ni $L_{2,3}$ edge for Ni_2MnGa austenite compared to martensite. A comparison between calculated and measured spectra is provided by Fig. 6.15 (b). When plotting the difference between the data measured at $T < T_M$ and $T > T_M$, the agreement with theory is striking (s. Fig. 6.15 (b)). Besides the mentioned variation of feature A (at $E_{ph} = 859$ eV), a second predicted change at lower energy (855 eV) is reproduced by the experiment. According to the ab initio calculations this spectral variation is caused by a Ni $3d$ state of d_{z^2} character in the minority LDOS just above the Fermi level. As the crystal structure changes from cubic to tetragonal or orthorhombic ($c/a < 1$) this peak is narrowed, which leads to the observed increase for $T < T_M$. The experimentally observed intensity change of peak A can be attributed to changes in hybridized Ni $3d$-Ga $2p$ states. These states are degenerated in the cubic austenite, whereas their degeneracy is lifted for the martensitic lattice symmetry. This results in a reduced density of states at the respective energy position for the martensite. In the calculated X-ray absorption spectrum (s. Fig. 6.15 (a)) these changes in the band structure lead to a considerably decreased intensity of peak A. Our experiment precisely reproduces the predicted intensity reduction. In contrast to the discussed Ni $L_{2,3}$ spectra, no significant changes are visible in the respective Mn spectra, which is in agreement with the theoretical calculations. For $c/a < 1$ only little changes in the Mn bands near the Fermi level are calculated. This is different for the case $c/a > 1$, where the reduced atomic distance in the ab-plane causes larger changes in the Mn related LDOS.

In addition to the described qualitative evaluation of the absorption spectra, a sum rule analysis of the XMCD spectra results in quantitative spin and orbital magnetic moments for Ni and Mn. Fig. 6.16 summarizes the temperature dependence of effective spin and orbital magnetic moments for both atomic species. In the whole temperature range the orbital to spin moment ratio of Mn stays close to zero indicating that the magneto-crystalline anisotropy is mainly caused by Ni states. In contrast, the Ni orbital moment is clearly altered by the phase transformation. In the martensite the Ni orbital to spin moment ratio amounts to 0.15, while in the austenite we calculate a value of 0.05. In the transition region a maximum of μ_{orb}/μ_{spin}=0.18 is observed. The increased orbital moment in the martensitic phase can be motivated by the reduced lattice symmetry compared

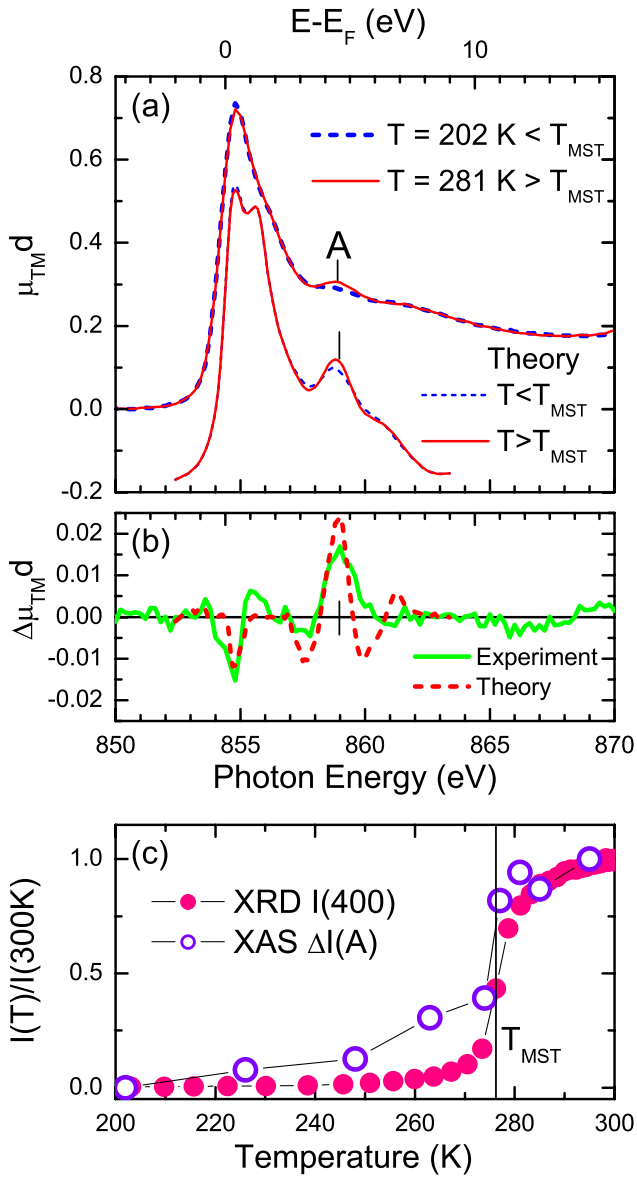

Figure 6.15: (a) Comparison of measured (upper curves) and calculated absorption coefficient for $T < T_M$ (blue dashed line) and $T > T_M$ (red line). (b) Difference of the spectra taken at the respective temperatures (green line) compared to the difference of the calculated spectra (red dashed line). (c) Temperature dependence of the intensity increase of feature A (open circles) and the XRD (400) peak intensity (full circles) indicating the structural phase transition. The values have been normalized to their respective room temperature values. Image taken from ref. [86].

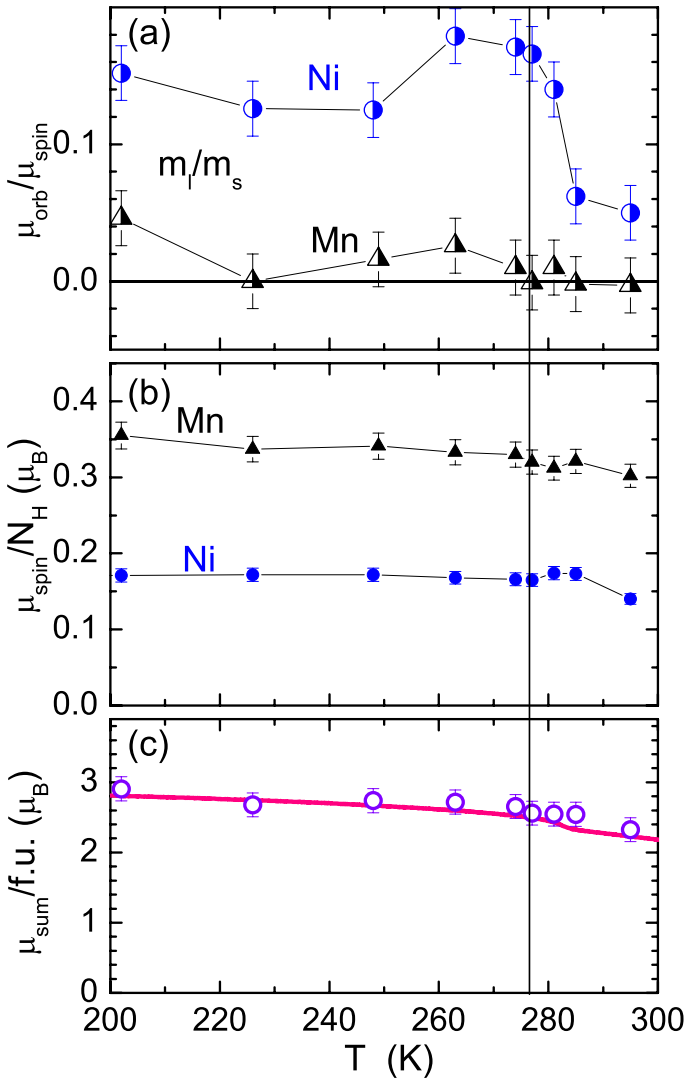

Figure 6.16: Temperature dependence of Ni (blue circles) and Mn (black triangles) spin and orbital magnetic moments. (a) The orbital to spin moment ratio for Ni shows a distinct maximum around T_M (vertical line), while the Mn orbital moment is constantly small in the whole temperature range. (b) The effective Mn spin moment per d hole, N_h, decreases slightly with increasing temperature, whereas the Ni spin moment stays almost constant. (c) Calculated sum moment per f.u. For comparison the magnetization data measured by magnetometry is shown (red line). Originally published in ref. [86].

to the cubic parent phase. In the transition region the maximum of μ_{orb}(Ni) indicates a strong variation in the interatomic distances and consequently a reduced symmetry of the local crystal field.

For the effective spin moment per open d-electron state (N_h) a contrary behavior is observed. The Ni spin moment stays constant, while the Mn spin moment slowly decreases, as the sample is heated from 200 to 300 K. In the transition region no significant variations are visible for both spin moments. In particular, we cannot confirm the predicted drop of the Ni moment at the phase transformation [143]. In fact, a slight increase of μ_{spin}(Ni) occurs around T=280 K. To calculate the sum magnetic moment per formula unit we consider the different numbers of d-holes, i.e. N_h(Ni)=1.3 and N_h(Mn)=4.3 and a correction factor of 1.5 for Mn because of the jj mixing. The total moment calculated from the XMCD results is in good agreement with respective magnetization data collected by magnetometry (s. Fig. 6.16 (c)). The analysis of the XMCD data indicates that the observed decrease in magnetization upon transformation to the austenite is essentially due to the Mn spin moment behavior. On the other hand, the crystal anisotropy is exclusively caused by Ni related electronic states.

6.2.2 Magnetic anisotropy

The ability to discriminate spin and orbital magnetic moments for Ni and Mn atoms separately makes XMCD spectroscopy an ideal tool to investigate the origin of the magnetic anisotropy in martensitic Ni_2MnGa. For that purpose we evaluate the angular dependence of the X-ray absorption spectra measured for an epitaxial Ni_2MnGa film of $(101)_A$ orientation. In the martensitic state we find a clear uniaxial anisotropy that originates from the crystal anisotropy. As a consequence of the variant configuration, the crystal anisotropy features an easy axis pointing out-of-plane, which is discussed in the following.

First, the out-of-plane magnetic anisotropy of the martensite is probed by using the magneto-optical contrast of XMCD at the Mn L_3 absorption edge that provides largest contrast. Fig. 6.17 displays the magnetization loops measured at constant circular polarization and an external magnetic field applied perpendicular to the film surface. The signal was normalized to the maximum value (for maximum applied field) after subtracting the value measured at zero external field. Neglecting interface effects the total uniaxial anisotropy is described by the anisotropy energy $f(\theta) = L\cos^2\theta$, where θ is the angle between magnetization vector and surface normal (s. inset in Fig. 6.17). The anisotropy constant L comprises two contributions: the shape anisotropy and the crystal anisotropy, i.e. $L = J_s^2/2\mu_0 + K_v$. From the extrapolated hysteresis curve one obtains the saturation field $\mu_0 H_s$ that is related to the out-of-plane anisotropy via $H_s J_s = \partial^2 f(\pi/2)/\partial\theta^2 = 2L$, where J_s is the saturation magnetization. In combination with the previous equation this results in $H_s = J_s/\mu_0 + 2K_v/J_s$. Hence, one can determine the bulk anisotropy constant K_v from the experimen-

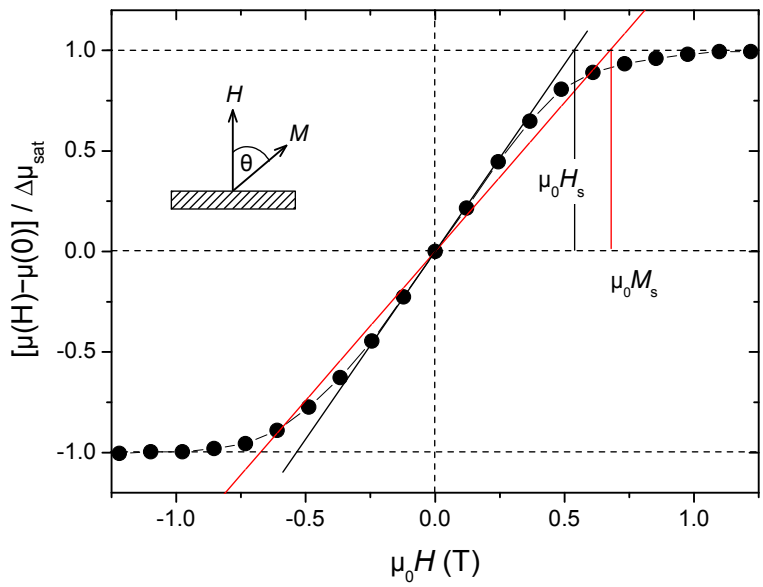

Figure 6.17: The X-ray absorption $\mu(H)$ is used to measure hysteresis loops with external field applied perpendicular to the film plane. By extrapolation of the small field susceptibility the saturation field is determined (black line). The saturation magnetization can be deduced from the respective fit for the in-plane magnetization curve (red line).

tal values $\mu_0 H_s = 0.537$ T and $J_s = 0.675$ T. The saturation magnetization of the sample was determined by in-plane hysteresis loops recorded with the VSM. The calculated value of $K_v = -3.7 \times 10^4$ J m^{-3} is in agreement with previously reported results for epitaxial Ni_2MnGa films [144, 145], but an order of magnitude smaller than values measured for bulk single crystals [63]. The negative sign of K_v indicates that the easy axis of the crystal anisotropy is directed perpendicular to the film surface.

This can be explained on basis of the variant distribution in the $(101)_A$ oriented sample. As described in chapter 4.3, films of that crystallographic orientation feature basically two orthorhombic variants with the b-axis aligned in-plane. In contrast to the $(100)_A$ oriented films, the twin planes are not aligned along the film normal, but parallel to the surface. Hence, the variant configuration does not promote an in-plane alignment of the magnetization, but generates an effective easy axis that points out-of-plane. Fig. 6.18 recapitulates the variant configuration model for films of $(101)_A$ orientation. For this twin configuration the c-axes of the two orthorhombic variants enclose an angle of $\beta = 2\arctan(a/c)$. For the observed martensitic deformation of $c/a \approx 0.9$ this results in β=96° which means an effective c-axis pointing out-of-plane. Consequently, one can expect a uniaxial anisotropy, as the magnetization in the individual variants tends to align parallel to the c-axis. Since the magnetic exchange length is much larger than the

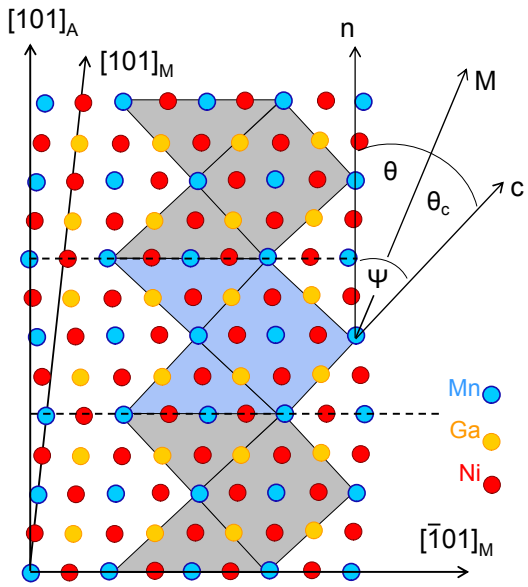

Figure 6.18: Representation of the variant configuration in $(101)_A$ oriented films. The intermediate b-axis points into the plane of projection, while a- and c-axis are aligned under roughly 45° to the film normal. The structure involves two orthorhombic variants that are separated by twin planes parallel to the film surface. For an individual variant the magnetization vector tends to align along the c-axis. Without external field the sample magnetization $\mathbf{M}$ is generated by the variant configuration, whereas in the experiment $\mathbf{M}$ is aligned by the external field applied under θ to the film normal.

length scale of the individual twins, a homogeneous magnetization within the film arises. The macroscopic magnetization is then dictated by the variant structure that results in an averaged magnetic anisotropy.

The investigated sample was prepared on MgO(100) and exhibits a multi-variant growth involving four austenite variants rotated azimuthally by ±8° with respect to the MgO lattice (s. Figs. 4.10 and 4.11 in chapter 4.1). Hence, eight variants have to be considered in the martensitic state. For an individual variant the anisotropy can be described by:

$$f_v(\theta_c, \phi) = K_c \cos^2 \theta_c + K_b \sin^2 \theta_c \sin^2 \phi \tag{6.4}$$

with θ_c and ϕ denoting the polar and azimuthal angle of the magnetization vector with respect to the c- and a-axis of the variant. The crystal anisotropy is characterized by the two anisotropy constants K_b and K_c related to the b- and c-axis. After averaging over all eight variants the anisotropy energy can be transformed into:

$$f_v(\theta, 0) = \left[K_c(\cos^2\psi - \frac{1}{2}\sin^2\psi) - \frac{1}{2}K_b\right]\cos^2\theta \tag{6.5}$$

The thorough description including the derivation of equation 6.5 is provided in this article: [146]. The polar angle θ_c has been substituted by $\theta_c = \theta \pm \psi$, where ψ is fully determined by the martensitic distortion c/a. For the investigated sample XRD reveals martensite lattice parameters of $a = 0.607$ nm and $c = 0.551$ nm leading to c/a=0.91. Hence, we obtain $f_v(\theta, 0) = (0.32K_c - 0.5K_b)\cos^2\theta$, which results in the relation $K_v = 0.32K_c - 0.5K_b$ between the experimentally determined anisotropy constant K_v and those related to the axes in the individual variant. Due to volume conservation the intermediate axis in the orthorhombic martensite satisfies $b \approx (a + c)/2$ in most cases and thus $K_b = 0.5K_c$ is a reasonable assumption. Furthermore, such a ratio of K_b and K_c was experimentally observed for comparable samples by Kaufmann et al. [61]. With this assumption the averaged crystal anisotropy constant is $K_v = 0.07K_c$, which explains the factor of ten between expected and experimentally observed value.

Information on the microscopic origin of the crystal anisotropy can be gained from XAS and XMCD measured for different angles θ between surface normal and incident X-ray beam. In the experiment the sample magnetization is aligned parallel (or antiparallel) with respect to the X-ray polarization vector by an external magnetic field, while the sample surface is tilted. Fig. 6.19 displays the absorption spectra and corresponding XMCD spectra measured at the Ni $L_{2,3}$ edges for different θ values. The presented absorption coefficients are calculated from the transmitted X-ray intensity. Thus, interface effects can be excluded. As expected, in the cubic parent phase no systematic variations are observed in the absorption spectra for different θ values. In particular, the characteristic satellite peak slightly above the Ni L_3 edge indicates the symmetry of the $L2_1$-ordered austenite [86]. The corresponding XMCD spectra do not vary as a function of θ. In contrast, distinct changes are visible in the respective spectra measured below T_M. Here the reduced symmetry of the martensite leads to changes in the electronic structure of the Ni related states that are observable as spectral variations. The corresponding measurements at the Mn $L_{2,3}$ edge (not shown) reveal no spectral variations for different θ values above and below T_M. Accordingly, the Mn effective spin and orbital magnetic moments, as derived by the sum rule analysis, show no dependence upon rotation of the magnetization vector with respect to the crystal lattice. Confirming previous results, this leads to the conclusion that the magnetic anisotropy is mainly caused by the Ni related electronic states (s. also chapter 6.2.1 and ref. [86]). The angular dependence of the Ni spin and orbital magnetic moments is presented in Fig. 6.20. For the austenitic sample no significant changes in both μ_{spin} and μ_{orb} are observed. In contrast, for $T < T_M$ the orbital moment decreases with increasing angle between magnetization vector and surface normal, according to $\mu_{orb} = \mu_{orb}(0) - \Delta\mu_{orb}\sin^2\theta$. At the same time, the spin moment stays almost constant indicating a minor effect from the

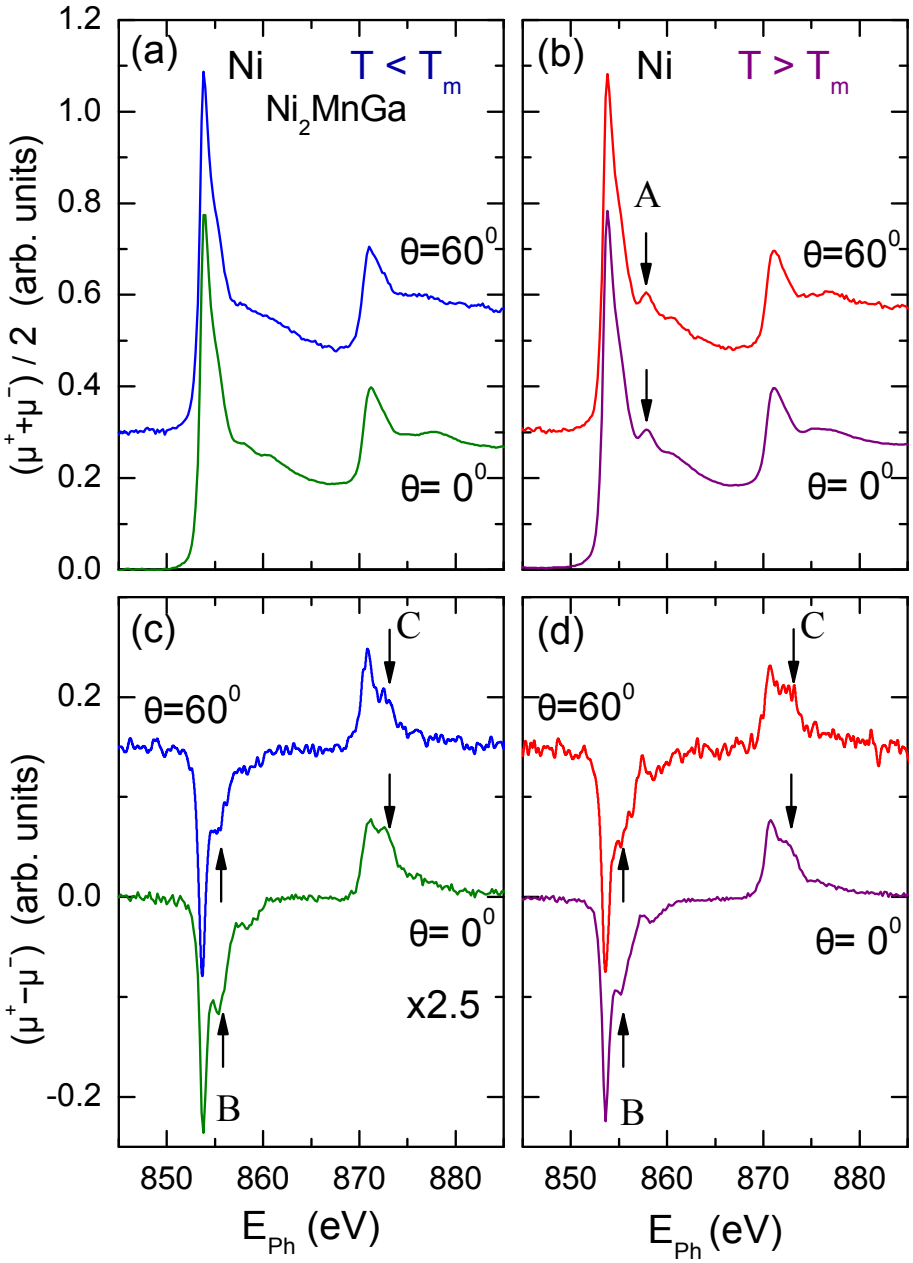

Figure 6.19: X-ray absorption spectra measured at the Ni $L_{2,3}$ edge for different angles of incidence θ in both phases. In the austenite the characteristic satellite peak A is visible (b), whereas the martensitic distortion leads to suppression of this feature (a). The corresponding XMCD reveals distinct changes in the spectra of the martensitic sample (c), as θ is varied. These changes are not observed for the austenitic film (d).

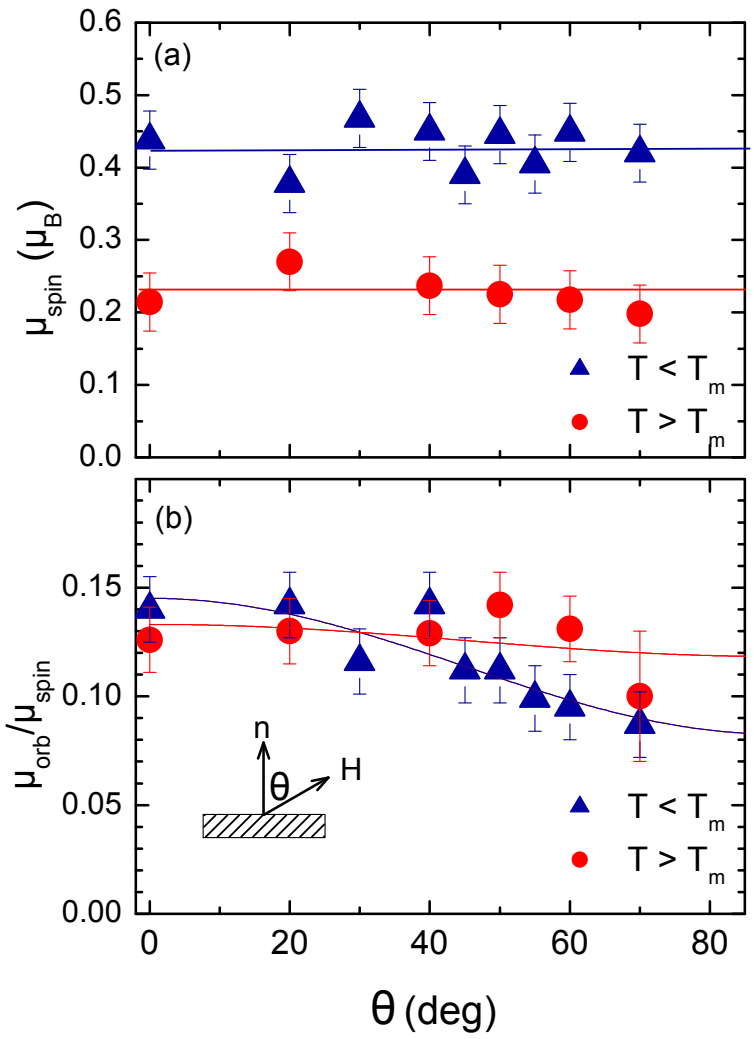

Figure 6.20: Angular dependence of the Ni spin moment (a) and the orbital to spin moment ratio (b) as calculated by sum rule analysis. In both phases the effective spin magnetic moment shows no systematic variation with θ. In contrast, the evolution of the orbital moment can be described by $\mu_{orb} = \mu_{orb}(0) - \Delta\mu_{orb} \sin^2\theta$ in case of $T < T_M$. Originally published in [146].

magnetic dipole anisotropy in the martensitic phase.

If the crystal anisotropy is exclusively caused by the Ni related states, the anisotropy energy per atom e_{Ni} is calculated to $e_{\mathrm{Ni}} = K_v a_A^3/8 = -5.7\mu\mathrm{eV}$. Here the volume of the martensitic unit cell is approximated by a_A^3 with the austenite lattice parameter a_A known from XRD. Considering the reduction factor ($K_v = 0.07K_c$) that results from averaging over the different variants, we obtain $K_{\mathrm{var}} = -5.3 \times 10^5$ J m^{-3} for a single variant corresponding to a single atom anisotropy of $e_{\mathrm{Ni,var}} = -81$ μeV. This value is in good agreement with results on other

Ni-Mn-Ga thin film samples [61].

An explanation for the observed uniaxial anisotropy can be achieved by comparing the spectral changes in XMCD to the density of states (DOS) at the Ni site as predicted by calculation [73]. In a simplified picture the experiment probes directly the changes in the DOS that arise upon magnetization rotation. The density functional theory calculations presented in ref. [73] predict two distinct peaks in the DOS close to E_F, that are related to Ni d_{z^2} and d_{xy} states, respectively. At the respective energy positions we observe a strong variation in the XMCD spectra for different angles of incidence that can be explained by a reallocation of the Ni d_{z^2} and d_{xy} states. For $\theta = 0°$ the magnetization is aligned parallel to the effective short crystallographic axis. In this case the long axis of the d_{z^2} state that aligns with the external field points out-of-plane (s. Fig. 6.21), which is parallel to the effective c-axis. Hence, the atomic distance is reduced along this direction and hybridization is large. This causes a small peak of large bandwidth in the DOS. If the magnetization is now rotated towards $\theta = 90°$ hybridization of the d_{z^2} states is reduced, which leads to a larger DOS peak with

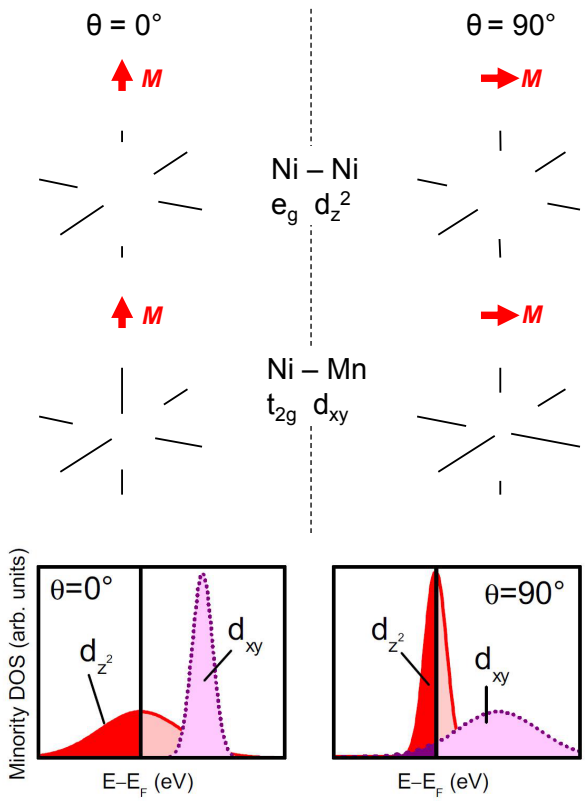

Figure 6.21: Illustration of the alignment of the d_{z^2} and d_{xy} orbitals for perpendicular (left) and in-plane (right) magnetization. The two cases result in changes in the DOS due to hybridization effects. Adopted from [146].

low bandwidth. As the d_{z^2} states are nearly half filled, the decreased bandwidth in the case of $\theta = 90°$ results in a reallocation of occupied states to higher kinetic energies (s. Fig. 6.21). Thus, a rotation of the magnetization towards in-plane alignment increases the total energy of the system, which explains the observed magnetic anisotropy that features an easy axis along the perpendicular direction. However, these changes in occupation does not explain the observed increase of μ_{orb}, because the magnetic quantum number of the d_{z^2} state is zero. This is not the case for the d_{xy} states. For these states the situation is opposite to the previously discussed states of d_{z^2} symmetry. Here the increased bandwidth for $\theta = 90°$ results in an increase of occupied states below E_F, which reduces the total energy. As the peak maximum is located at a higher energy this competing energy contribution is much smaller than that of the d_{z^2} states. The additional occupied states for $\theta = 90°$ generate an increase of minority orbital moment. As the spin-orbit interaction favors parallel spin and orbital moments this increase in the minority states presents a decrease in total orbital moment in agreement with the experiment. A detailed description of the considerations and results can be found in reference [146].

6.2.3 Surface properties

The results discussed in the previous sections are all based on X-ray absorption spectroscopy in transmission mode (TM) that probes the volume of our thin film samples. Commonly, XAS experiments exploit the surface sensitive total electron yield (TEY) signal. This method provides a moderate surface sensitivity because of the characteristic electron escape depth of 2-3 nm. Due to the much higher penetration depth of the X-ray light, also buried surfaces can be investigated. To prevent oxidation of the film surface the Ni_2MnGa layer is capped by a 4 nm thick Al protection layer in situ. During deposition the substrate temperature is typically 773 K, which is approximately the surface temperature, when deposition is finished. To minimize the reaction time of the hot film surface with residual oxygen, direct capping of the Heusler film is advantageous. On the other hand, interdiffusion and chemical reactions at the interface are promoted by elevated temperatures. To avoid these effects a first approach was depositing the Al layer after the sample is cooled down to 670 K. The combined investigation with XAS in transmission and TEY mode allows then to detect changes of the chemical state of the $3d$ metal constituents at the surface. When comparing the volume and surface sensitive signals, we find clear discrepancies in the spectra that indicate a solid state reaction at the film cap layer interface [80]. At the Ni $L_{2,3}$ edges characteristic shoulders are indicative for NiAl formation. These features are not present in the spectrum measured in transmission mode confirming that interdiffusion plays only a minor role. For samples that are capped at a lower temperature of 520 K the NiAl features are less pronounced, but still visible. In the following, the Al protection layer was deposited at a further decreased film

temperature of 370 K suppressing the surface reaction.

As mentioned the enhanced cooling time likely results in an increased oxidation of the topmost film layers. In particular, Mn is highly reactive and thus sensitive to oxide formation. Again XAS in TEY and TM mode is a suitable probe to detect changes in the chemical states of Mn and Ni, like oxidation, via spectral variations. The comparison of our experimental results to the fully oxidized state leads to the conclusion that approximately 10 % of the Mn atoms at the surface are oxidized. In addition, the TEY signal at the Mn $L_{2,3}$ edges shows a considerably lower intensity than the corresponding TM measurement, which is not the case for the respective Ni spectra. The large reduction of the Mn TEY signal cannot be explained by oxide formation alone, but indicates a reduced Mn concentration in the surface region [147]. A scenario that can explain these Mn deficiencies is a selective evaporation of Mn atoms directly after the deposition process. While the sample cools down the high vapor pressure of Mn could result in a considerable Mn loss due to evaporation. The decreased Mn concentration in the surface region also affects the magnetic moment. The surface spin moments calculated from the TEY data are smaller for both Mn and Ni, but the effect is more severe for the Mn atoms.

When comparing the Ni TEY and TM spectra a difference in the previously described satellite peak A is visible. This peak is well pronounced in the volume sensitive experiment, while hardly visible in the corresponding measurement limited to the surface. As described in section 6.2.1 this feature A is indicative for the cubic $L2_1$ symmetry and suppressed in the martensitic phase and thus can be used to detect the phase transition. On heating the satellite peak shows a sharp intensity increase as the sample enters the cubic austenite. Such a temperature evolution is only observed for the TM mode, while the characteristic increase is missing in the data derived from the TEY signal. Hence, we observe a suppression of the austenite-martensite phase transition in the surface region as a consequence of the reduced chemical order.

The surface sensitive XAS experiments provide a valuable feedback for the sample preparation. To avoid the observed chemical reactions between cap layer and Ni_2MnGa film an enhanced cooling period prior to aluminum deposition has been established. Furthermore the combination of TEY and TM measuring mode revealed a reduced Mn concentration in the surface region. This might be avoided by decreasing the sample cooling time, that means introducing active cooling. It is worth pointing out that concerning the MSM effect the surface properties play only a minor role. In the film volume we clearly see the phase transformation that manifests in significant changes in the electronic structure. In addition, the transmission XAS measurements on epitaxial films represent a true bulk measurement, because any interface related effects are suppressed. According to that, angular-dependent XAS in TM mode allows us to trace the microscopic origin of the bulk magnetic anisotropy in the material.

6.3 Key results

Key features such as the saturation magnetization and the phase transformation temperatures of the Ni-Mn-Ga samples can be determined by magnetometry measurements. The characteristic change in anisotropy is reflected in the temperature evolution of the magnetization in low field. These measurements reveal a strong influence of the crystallographic orientation and associated twin plane configuration. A shift in T_{Ms} of roughly 50 K is observed for samples of the same composition, but different orientation. In the case of $(110)_A$ oriented films, twin planes are predominantly aligned parallel to the film plane, which stabilizes the martensite phase. In contrast samples of $(100)_A$ orientation feature twin planes that run along the film normal or under 45° to the film plane. This configuration increases the interaction of twin boundaries with the substrate and complicates the formation of a habit plane. The hysteresis loops for substrate-constrained and freestanding films show characteristic steps in the magnetization that can be interpreted as MIR of variants. However, the results of XRD with applied magnetic field contradict a magnetic-field-induced variant redistribution process.

Quantitative information about the element-specific spin and orbital magnetic moments have been obtained from XMCD experiments. The spin moment is largely confined to the Mn sites, while the crystal anisotropy of the martensitic phase is almost exclusively caused by the orbital moment of the Ni atoms. At the martensitic phase transition we found a distinct change in the X-ray absorption spectra confirming theoretical predictions. According to ab initio calculations the reduced crystal symmetry of the martensite phase is associated with considerable changes in the Ni related minority DOS. These calculated band structure changes are detected in the XAS experiment representing the first experimental test for changes in the electronic structure during a martensitic transition. Moreover, angular-dependent XAS experiments provide informations on the microscopic origin of the magnetic anisotropy in Ni_2MnGa. The measurements show that the reallocation of electrons in the Ni related minority spin states is responsable for the increased bulk magnetocrystalline anistropy of the martensitic phase.

Chapter 7

Conclusions

This work was concerned with the preparation and detailed characterization of epitaxial Ni_2MnGa thin films. A focus was put on the investigation of structural and magnetic properties of the films with regard to the applicability in devices utilizing the magnetic shape memory effect. Exploiting the unique characteristics of thin film samples a second central objective was exploring the microscopic magnetism in the Ni-Mn-Ga system.

For sample preparation conventional dc sputter deposition proved as an effective and reliable technique. A systematic variation of the deposition parameters, i.e. working pressure, sputtering power and substrate temperature, revealed that the structural and magnetic order of the samples are largely determined by the substrate temperature. The working pressure, however, has a strong effect on the sample composition. By varying the Argon pressure for a given alloy target the film composition can be adjusted, which enables tuning the phase transformation temperature. For off-stoichiometric targets the martensite start temperature of our films lies well above room temperature, which is important for potential applications.

To eliminate blocking effects of the rigid substrates three different strategies have been pursued. A first approach was film deposition on a sacrificial substrate. The samples grown on NaCl(100) single crystals can easily be released by dissolving the substrate in water. Since the resulting crystal structure is not single-crystalline but textured only, these samples are not suitable for applications or further sophisticated investigations. The second, rather direct attempt was patterning epitaxial films by focused ion beam etching. By using that technique the fabrication of freestanding cantilevers has been demonstrated. The most promising results have been achieved by the sacrificial buffer layer technique developed within this work. The combination of photolithography and selective chemical etching allows the preparation of freestanding microstructures, such as bridges or cantilevers while maintaining the substrate as a carrier. Thus, the surface relief that is induced by the twinned microstructure can be studied in the light microscope. On heating the twinning pattern disappears as the film transforms to the

cubic parent phase and is recovered as soon as the sample is cooled below T_{Ms}. Hence, a fast access of the structural transformation temperatures is provided by optical microscopy.

A key requirement for a large MSM effect is the single-crystalline nature of the material. The crystal structure of the films prepared during this work has been extensively studied by X-ray diffraction in two- and four-circle geometry. Epitaxial film growth was confirmed for different substrate materials, including MgO, Al_2O_3, and BaF_2 demonstrating fully tunable crystallographic orientation of the Ni-Mn-Ga layer. For films of (100) and (110) orientation the structural changes during the phase transformation have been studied by temperature-dependent XRD. The structural investigation of the martensite phase revealed that the variant alignment and distribution is dictated by the film-substrate interaction. This results in different variant configurations and associated twin plane alignments for films on Al_2O_3 and MgO, respectively. However, in both cases a modulated superstructure (7M/14M) is present. The modulation that plays an important role in the MSM effect was also confirmed for freestanding films released from MgO substrates. Despite the promising crystal structure of the samples, no magnetic-field-induced variant redistribution was observed. The suppression of the MSM behavior in these films is explained by a model of the complex variant structure. On basis of the XRD studies in combination with microscopy the fine-twinned, symmetric martensite variant structure was recognized to be responsible for blocking of twin boundary movement.

While conventional magnetometry served as a valuable tool to analyse the magnetization behavior of the samples, more elaborate techniques are needed to study the microscopic magnetism in Ni_2MnGa. Taking advantage of the thin film geometry X-ray absorption spectroscopy (XAS) experiments in transmission mode have been accomplished in a joint cooperation. Exploiting the magnetic circular dichroism effect these measurements yield quantitative information on the spin and orbital magnetic moments of the constituent atoms. The results clearly show that the bulk spin moment is carried by the Mn atoms, while the magnetic anisotropy is caused by the Ni related electronic states. Using angular-dependent XAS the bulk magnetocrystalline anisotropy is traced back to changes in the minority Ni *d*-states explaining the macroscopic magnetization behavior. The applied method opens up new perspectives on true bulk measurements of the electronic and magnetic anisotropies in materials with itinerant electron states. Moreover, a remarkable change in the Ni absorption spectra during the martensite phase transition was observed. The detected spectral changes are in excellent agreement with predictions based on band structure calculations. The observations represent the first experimental test of changes in the electronic structure upon a martensitic transition, which is in the case of Ni_2MnGa a transition between two ferromagnetic phases.

Regarding the MSM effect a future work is recommended to focus on films of (110) orientation. The advantageous twin plane configuration observed for these

samples offers a great potential for direct observation of magnetic-field-induced variant redistribution. According to recent results, the complex twin microstructure of (100) oriented films effectively blocks magnetically induced twin boundary motion. The findings of this work clearly demonstrate that the martensitic microstructure in Ni_2MnGa films is largely dictated by the substrate symmetry. The presented concepts used for layers grown on MgO(100) substrates can, in principle, be applied to films prepared on $Al_2O_3(11\bar{2}0)$. In particular, with a suitable sacrificial buffer layer on sapphire substrates freestanding films with a beneficial variant microstructure could be realized, while avoiding blocking effects due to an entangled twinning structure.

In addition to the relevant results on the electronic structure and the microscopic magnetism in Ni_2MnGa, these findings improve the basic understanding of this interesting material and represent an important step towards potential applications based on MSM thin films.

Bibliography

[1] G. M. Whitesides, "The origins and the future of microfluidics," *Nature*, vol. 442, 2006.

[2] K. Ullakko, J. K. Huang, C. Kantner, R. C. O'Handley, and V. V. Kokorin, "Large magnetic-field-induced strains in Ni_2MnGa single crystals," *Appl. Phys. Lett.*, vol. 69, p. 1966, 1996.

[3] O. Heczko, A. Sozinov, and K. Ullakko, "Giant field-induced reversible strain in magnetic shape memory NiMnGa alloy," *IEEE Trans. Magn.*, vol. 36, p. 3266, 2000.

[4] A. Sozinov, A. A. Likhachev, N. Lanska, and K. Ullakko, "Giant magnetic-field-induced strain in NiMnGa seven-layered martensitic phase," *Appl. Phys. Lett.*, vol. 80, p. 1746, 2002.

[5] A. Nespoli, S. Besseghini, S. Pittaccio, E. Villa, and S. Viscuso, "The high potential of shape memory alloys in developing miniature mechanical devices: A review on shape memory alloy mini-actuators," *Sensors and Actuators A: Physical*, vol. 158, p. 149, 2010.

[6] M. Kohl, D. Brugger, M. Ohtsuka, and T. Takagi, "A novel actuation mechanism on the basis of ferromagnetic SMA thin films," *Sensors and Actuators A: Physical*, vol. 114, p. 445, 2004.

[7] I. Karaman, B. Basaran, H. E. Karaca, A. I. Karsilayan, and Y. I. Chumlyakov, "Energy harvesting using martensite variant reorientation mechanism in a NiMnGa magnetic shape memory alloy," *J. Appl. Phys.*, vol. 90, p. 172505, 2007.

[8] K. A. Gschneidner, V. K. Pecharsky, and A. O. Tsokol, "Recent developments in magnetocaloric materials," *Reports on Progress in Physics*, vol. 68, p. 1479, 2005.

[9] P. Entel, V. D. Buchelnikov, M. E. Gruner, A. Hucht, V. V. Khovailo, S. K. Nayak, and A. T. Zayak, "Shape Memory Alloys: A Summary of Recent Achievements," *Materials Science Forum*, vol. 583, p. 21, 2008.

[10] P. Brown, A. Gandy, K. Ishida, R. Kainuma, T. Kanomata, M. Matsumoto, H. Morito, K.-U. Neumann, K. Oikawa, B. Ouladdiaf, and K. Ziebeck, "Magnetic shape memory behaviour," *Journal of Magnetism and Magnetic Materials*, vol. 310, p. 2755, 2007.

[11] D. C. Dunand and P. Müllner, "Size effects on magnetic actuation in Ni-Mn-Ga shape-memory alloys," *Advanced Materials*, vol. 23, p. 216, 2011.

[12] N. Scheerbaum, O. Heczko, J. Liu, D. Hinz, L. Schultz, and O. Gutfleisch, "Magnetic field-induced twin boundary motion in polycrystalline NiMnGa fibres," *New Journal of Physics*, vol. 10, p. 073002, 2008.

[13] M. Chmielus, X. X. Zhang, C. Witherspoon, D. C. Dunand, and P. Müllner, "Giant magnetic-field-induced strains in polycrystalline Ni-Mn-Ga foams," *Nature Materials*, vol. 8, p. 863, 2009.

[14] N. Scheerbaum, D. Hinz, O. Gutfleisch, K.-H. Müller, and L. Schultz, "Textured polymer bonded composites with NiMnGa magnetic shape memory particles," *Acta Materialia*, vol. 55, p. 2707, 2007.

[15] J. W. Dong, L. C. Chen, J. Q. Xie, T. A. R. Muller, D. M. Carr, C. J. Palmstrom, S. McKernan, Q. Pan, and R. D. James, "Epitaxial growth of ferromagnetic Ni_2MnGa on GaAs(001) using NiGa interlayers," *J. Appl. Phys.*, vol. 88, p. 7357, 2000.

[16] J. W. Dong, J. Q. Xie, J. Lu, C. Adelmann, C. J. Palmstrom, J. Cui, Q. Pan, T. W. Shield, R. D. James, and S. McKernan, "Shape memory and ferromagnetic shape memory effects in single-crystal Ni_2MnGa thin films," *J. Appl. Phys.*, vol. 95, p. 2593, 2004.

[17] M. Ohtsuka, M. Sanada, M. Matsumoto, and K. Itagaki, "Magnetic-field induced shape memory effect in Ni_2MnGa sputtered films," *Materials Science and Engineering: A*, vol. 378, p. 377, 2004.

[18] T. Eichhorn, "Epitaktische dünne Schichten des ferromagnetischen Formgedächtnis-Materials Ni_2MnGa," Master's thesis, University of Mainz, 2007.

[19] F. Heusler, "Über magnetische Manganlegierungen," *Verhandlungen der Deutschen Physikalischen Gesellschaft*, vol. 5, p. 219, 1903.

[20] F. Heusler, W. Starck, and E. Haupt, "Magnetisch-chemische Studien," *Verhandlungen der Deutschen Physikalischen Gesellschaft*, vol. 5, p. 220, 1903.

[21] S. Waki, Y. Yamaguchi, and K. Mitsugi, "Superconductivity of Ni_2NbX (X=Al, Ga and Sn)," *Journal of the Physical Society of Japan*, vol. 54, p. 1673, 1985.

[22] P. J. Webster and K. R. A. Ziebeck, "The paramagnetic properties of heusler alloys containing iron," *Phys. Lett. A*, vol. 98, p. 51, 1983.

[23] S. A. Wolf, D. D. Awschalom, R. A. Buhrman, J. M. Daughton, S. von Molnr, M. L. Roukes, A. Y. Chtchelkanova, and D. M. Treger, "Spintronics: A Spin-Based Electronics Vision for the Future," *Science*, vol. 294, p. 1488, 2001.

[24] M. N. Baibich, J. M. Broto, A. Fert, F. N. Van Dau, F. Petroff, P. Etienne, G. Creuzet, A. Friederich, and J. Chazelas, "Giant Magnetoresistance of (001)Fe/(001)Cr Magnetic Superlattices," *Phys. Rev. Lett.*, vol. 61, p. 2472, 1988.

[25] G. Binasch, P. Grünberg, F. Saurenbach, and W. Zinn, "Enhanced magnetoresistance in layered magnetic structures with antiferromagnetic interlayer exchange," *Phys. Rev. B*, vol. 39, pp. 4828–4830, 1989.

[26] R. A. de Groot, F. M. Mueller, P. G. van Engen, and K. H. J. Buschow, "New Class of Materials: Half-Metallic Ferromagnets," *Phys. Rev. Lett.*, vol. 50, p. 2024, 1983.

[27] I. Galanakis and P. Mavropoulos, "Spin-polarization and electronic properties of half-metallic Heusler alloys calculated from first principles," *Journal of Physics: Condensed Matter*, vol. 19, p. 315213, 2007.

[28] G. H. Fecher, H. C. Kandpal, S. Wurmehl, C. Felser, and G. Schönhense, "Slater-Pauling rule and Curie temperature of Co_2-based Heusler compounds," *J. Appl. Phys.*, vol. 99, p. 08J106, 2006.

[29] C. Herbort, E. A. Jorge, and M. Jourdan, "Morphology induced magnetoresistance enhancement of tunneling junctions with the Heusler electrode $Co_2Cr_{0.6}Fe_{0.4}Al$," *Appl. Phys. Lett.*, vol. 94, p. 142504, 2009.

[30] I. Galanakis, P. Mavropoulos, and P. H. Dederichs, "Electronic structure and SlaterPauling behaviour in half-metallic Heusler alloys calculated from first principles," *Journal of Physics D: Applied Physics*, vol. 39, p. 765, 2006.

[31] J. Kübler, A. R. William, and C. B. Sommers, "Formation and coupling of magnetic moments in Heusler alloys," *Phys. Rev. B*, vol. 28, p. 1745, 1983.

[32] P. J. Webster, K. R. A. Ziebeck, S. L. Town, and M. S. Peak, "Magnetic order and phase transformation in Ni_2MnGa," *Philos. Mag. B*, vol. 49, 1984.

[33] L. Chang and T. Read, "Plastic deformation and diffusionless phase changes in metals the gold-cadmium beta phase," *Transactions of the American Institute of Mining and Metallurgical Engineers*, vol. 191, p. 47, 1951.

[34] W. J. Buehler, J. V. Gilfrich, and R. C. Wiley, "Effect of Low-Temperature Phase Changes on the Mechanical Properties of Alloys near Composition TiNi," *J. Appl. Phys.*, vol. 34, p. 1475, 1963.

[35] D. Askeland, P. Fulay, and W. Wright, *The Science and Engineering of Materials.* Stanford: Cengage Learning, 2010.

[36] L. Kaufman and M. Cohen, "Thermodynamics and kinetics of martensitic transformations," *Progress in Metal Physics*, vol. 7, p. 165, 1958.

[37] G. Kostorz, *Phase Transformations in Materials.* Weinheim: Wiley-VCH, 2001.

[38] L. Bergmann and C. Schaefer, *Lehrbuch der Experimentalphysik - Band 1.* Berlin: de Gruyter, 2008.

[39] A. Gonzàlez-Comas, E. Obradó, L. Mañosa, A. Planes, V. A. Chernenko, B. J. Hattink, and A. Labarta, "Premartensitic and martensitic phase transitions in ferromagnetic Ni_2MnGa," *Phys. Rev. B*, vol. 60, p. 7085, 1999.

[40] M. S. Wechsler, D. S. Lieberman, and T. A. Read, "On the Theory of the Formation of Martensite," *Transactions of the American Institute of Mining and Metallurgical Engineers*, vol. 197, 1953.

[41] J. S. Bowles and J. K. Mackenzie, "The crystallography of martensite transformations I," *Acta Metallurgica*, vol. 2, p. 129, 1954.

[42] C. Giacovazzo, H. L. Monaco, G. Artioli, D. Viterbo, G. Ferraris, G. Gilli, G. Zanotti, and M. Catti, *Fundamentals of Crystallography.* New York: Oxford University Press, 2011.

[43] K. Otsuka and X. Ren, "Physical metallurgy of TiNi-based shape memory alloys," *Progress in Materials Science*, vol. 50, p. 511, 2005.

[44] Q. Pan and R. D. James, "Micromagnetic study of Ni_2MnGa under applied field," *J. Appl. Phys.*, vol. 87, p. 4702, 2000.

[45] G. Liu, J. Chen, Y. Cui, Z. Liu, M. Zhang, G. Wu, E. Brück, F. de Boer, F. Meng, Y. Li, and J. Qu, "Characterization of preferential orientation of martensitic variants in a single crystal of NiMnGa," *Solid State Communications*, vol. 130, p. 687, 2004.

[46] J. Pons, R. Santamarta, V. A. Chernenko, and E. Cesari, "Long-period martensitic structures of Ni-Mn-Ga alloys studied by high-resolution transmission electron microscopy," *J. Appl. Phys.*, vol. 97, p. 083516, 2005.

[47] A. G. Khachaturyan, S. M. Shapiro, and S. Semenovskaya, "Adaptive phase formation in martensitic transformation," *Phys. Rev. B*, vol. 43, p. 10832, 1991.

[48] P. J. Brown, B. Dennis, J. Crangle, T. Kanomata, M. Matsumoto, K.-U. Neumann, L. M. Justham, and K. R. A. Ziebeck, "Stability of martensitic domains in the ferromagnetic alloy Ni_2MnGa: a mechanism for shape memory behaviour," *Journal of Physics: Condensed Matter*, vol. 16, p. 65, 2004.

[49] J. Pons, V. A. Chernenko, R. Santamarta, and E. Cesari, "Crystal structure of martensitic phases in NiMnGa shape memory alloys," *Acta Materialia*, vol. 48, p. 3027, 2000.

[50] X. Ren and K. Otsuka, "Origin of rubber-like behaviour in metal alloys," *Nature*, vol. 389, p. 579, 1997.

[51] R. C. O'Handley, "Model for strain and magnetization in magnetic shape-memory alloys," *J. Appl. Phys.*, vol. 83, p. 3263, 1998.

[52] S. J. Murray, R. C. O'Handley, and S. M. Allen, "Model for discontinuous actuation of ferromagnetic shape memory alloy under stress," *J. Appl. Phys.*, vol. 89, p. 1295, 2001.

[53] A. A. Likhachev and K. Ullakko, "Quantitative Model of Large Magnetostrain Effect in Ferromagnetic Shape Memory Alloys," *EPJ direct*, vol. 1, p. 1, 2000.

[54] AdaptaMat, "http://www.adaptamat.com/technology/msm/," 2011.

[55] R. W. Overholser, M. Wuttig, and D. A. Neumann, "Chemical ordering in Ni-Mn-Ga Heusler alloys," *Scripta Materialia*, vol. 40, p. 1095, 1999.

[56] P. J. Brown, J. Crangle, T. Kanomata, M. Matsumoto, K.-U. Neumann, B. Ouladdiaf, and K. R. A. Ziebeck, "The crystal structure and phase transitions of the magnetic shape memory compound Ni_2MnGa," *Journal of Physics: Condensed Matter*, vol. 14, p. 10159, 2002.

[57] M. Richard, J. Feuchtwanger, D. Schlagel, T. Lograsso, S. M. Allen, and R. C. O'Handley, "Crystal structure and transformation behavior of NiMnGa martensites," *Scripta Materialia*, vol. 54, p. 1797, 2006.

[58] P. Entel, V. D. Buchelnikov, V. V. Khovailo, A. T. Zayak, W. A. Adeagbo, M. E. Gruner, H. C. Herper, and E. F. Wassermann, "Modelling the phase diagram of magnetic shape memory Heusler alloys," *Journal of Physics D: Applied Physics*, vol. 39, p. 865, 2006.

[59] O. Söderberg, Y. Ge, A. Sozinov, S.-P. Hannula, and V. K. Lindroos, "Recent breakthrough development of the magnetic shape memory effect in Ni-Mn-Ga alloys," *Smart Materials and Structures*, vol. 14, p. S223, 2005.

[60] R. Ranjan, S. Singh, H. Boysen, D. Trots, S. Banik, A. M. Awasthi, P. K. Mukhopadhyay, and S. R. Barman, "Competing tetragonal and monoclinic phases in $Ni_{2.2}Mn_{0.80}Ga$," *J. Appl. Phys.*, vol. 106, p. 033510, 2009.

[61] S. Kaufmann, U. K. Rößler, O. Heczko, M. Wuttig, J. Buschbeck, L. Schultz, and S. Fähler, "Adaptive modulations of martensites," *Phys. Rev. Lett.*, vol. 104, p. 145702, 2010.

[62] R. Tickle and R. James, "Magnetic and magnetomechanical properties of Ni_2MnGa," *Journal of Magnetism and Magnetic Materials*, vol. 195, p. 627, 1999.

[63] L. Straka and O. Heczko, "Magnetic anisotropy in Ni-Mn-Ga martensites," *J. Appl. Phys.*, vol. 93, p. 8636, 2003.

[64] O. Heczko, L. Straka, N. Lanska, K. Ullakko, and J. Enkovaara, "Temperature dependence of magnetic anisotropy in Ni-Mn-Ga alloys exhibiting giant field-induced strain," *J. Appl. Phys.*, vol. 91, p. 8228, 2002.

[65] L. Straka, O. Heczko, and K. Ullakko, "Investigation of magnetic anisotropy of NiMnGa seven-layered orthorhombic martensite," *Journal of Magnetism and Magnetic Materials*, vol. 272-276, p. 2049, 2004.

[66] P. J. Brown, A. Y. Bargawi, J. Crangle, K.-U. Neumann, and K. R. A. Ziebeck, "Direct observation of a band Jahn-Teller effect in the martensitic phase transition of Ni_2MnGa," *Journal of Physics: Condensed Matter*, vol. 11, p. 4715, 1999.

[67] J. Enkovaara, A. Ayuela, L. Nordström, and R. M. Nieminen, "Magnetic anisotropy in Ni_2MnGa," *Phys. Rev. B*, vol. 65, p. 134422, 2002.

[68] J. Enkovaara, *Atomistic Simulations of Magnetic Shape Memory Alloys.* PhD thesis, Helsinki University of Technology, 2003.

[69] A. N. Vasil'ev, V. D. Buchelnikov, T. Takagi, V. V. Khovailo, and E. I. Estrin, "Shape memory ferromagnets," *Phys.-Uspekhi*, vol. 46, p. 559, 2003.

[70] V. A. Chernenko, "Compositional instability of β-phase in Ni-Mn-Ga alloys," *Scripta Materialia*, vol. 40, p. 523, 1999.

[71] J. Enkovaara, A. Ayuela, A. T. Zayak, P. Entel, L. Nordstrm, M. Dube, J. Jalkanen, J. Impola, and R. M. Nieminen, "Magnetically driven shape memory alloys," *Materials Science and Engineering A*, vol. 378, p. 52, 2004.

[72] A. T. Zayak, P. Entel, J. Enkovaara, A. Ayuela, and R. M. Nieminen, "First-principles investigations of homogeneous lattice-distortive strain and shuffles in Ni_2MnGa," *Journal of Physics: Condensed Matter*, vol. 15, p. 159, 2003.

[73] A. Ayuela, J. Enkovaara, and R. M. Nieminen, "Ab initio study of tetragonal variants in Ni_2MnGa alloy," *Journal of Physics: Condensed Matter*, vol. 14, p. 5325, 2002.

[74] A. Zheludev, S. M. Shapiro, P. Wochner, and L. E. Tanner, "Precursor effects and premartensitic transformation in Ni_2MnGa," *Phys. Rev. B*, vol. 54, p. 15045, 1996.

[75] C. Bungaro, K. M. Rabe, and A. D. Corso, "First-principles study of lattice instabilities in ferromagnetic Ni_2MnGa," *Phys. Rev. B*, vol. 68, p. 134104, 2003.

[76] A. T. Zayak, W. A. Adeagbo, P. Entel, and K. M. Rabe, "e/a dependence of the lattice instability of cubic Heusler alloys from first principles," *Appl. Phys. Lett.*, vol. 88, p. 111903, 2006.

[77] H. J. Elmers, J. Hauschild, H. Fritzsche, G. Liu, U. Gradmann, and U. Köhler, "Magnetic frustration in ultrathin Fe films," *Phys. Rev. Lett.*, vol. 75, p. 2031, 1995.

[78] A. Elshabini and F. D. Barlow, *Thin film technology handbook.* New York: McGraw-Hill, 1997.

[79] M. A. Hermann, W. Richter, and H. Sitter, *Epitaxy - Physical principles and technical implementations.* Berlin, Heidelberg: Springer-Verlag, 2004.

[80] M. Kallmayer, K. Hild, T. Eichhorn, H. Schneider, G. Jakob, A. Conca, M. Jourdan, H. J. Elmers, A. Gloskovskii, S. Schuppler, and P. Nagel, "Solid state reaction at the interface between Heusler alloys and Al cap accelerated by elevated temperature and rough surface," *J. Appl. Phys.*, vol. 91, p. 192501, 2007.

[81] S. Roth, "Leibniz-Institut für Festkörper- und Werkstoffforschung Dresden, http://www.ifw-dresden.de/institutes/imw/sections/25/members/roth," 2011.

[82] Hauner, "Metallische Werkstoffe, http://www.hmw-hauner.de/," 2011.

[83] C. Felser, "AG Felser, University of Mainz, http://www.superconductivity.de/," 2011.

[84] J. Q. Xie, J. W. Dong, J. Lu, C. J. P. m, and S. McKernan, "Epitaxial growth of ferromagnetic Ni_2MnIn on (001) InAs," *Appl. Phys. Lett.*, vol. 79, 2001.

[85] H. Schneider, G. Jakob, M. Kallmayer, H. J. Elmers, M. Cinchetti, B. Balke, S. Wurmehl, C. Felser, M. Aeschlimann, and H. Adrian, "Epitaxial film growth and magnetic properties of Co_2FeSi," *Phys. Rev. B*, vol. 74, p. 174426, 2006.

[86] G. Jakob, T. Eichhorn, M. Kallmayer, and H. J. Elmers, "Correlation of electronic structure and martensitic transition in epitaxial Ni_2MnGa films," *Phys. Rev. B*, vol. 76, p. 174407, 2007.

[87] O. Heczko, M. Thomas, J. Buschbeck, L. Schultz, and S. Fähler, "Epitaxial Ni-Mn-Ga films deposited on $SrTiO_3$ and evidence of magnetically induced reorientation of martensitic variants at room temperature," *Appl. Phys. Lett.*, vol. 92, p. 072502, 2008.

[88] M. Thomas, O. Heczko, J. Buschbeck, Y. W. Lai, J. McCord, S. Kaufmann, L. Schultz, and S. Fähler, "Stray-Field-Induced Actuation of Free-Standing Magnetic Shape-Memory Films," *Advanced Materials*, vol. 21, p. 3708, 2009.

[89] T. Eichhorn and G. Jakob, "Structural and Magnetic Properties of Epitaxial Ni_2MnGa Thin Films," *Materials Science Forum*, vol. 635, p. 155, 2010.

[90] D. K. Aswal, K. P. Muthe, S. Tawde, S. Chodhury, N. Bagkar, A. Singh, S. K. Gupta, and J. V. Yakhmi, "XPS and AFM investigations of annealing induced surface modifications of MgO single crystals," *Journal of Crystal Growth*, vol. 236, p. 661, 2002.

[91] M. Murugesan, H. Obara, Y. Nakagawa, S. Kosaka, and H. Yamasaki, "Influence of MgO substrate annealing on the microwave properties of laser ablated $YBa_2C_3O_z$ thin films," *Superconductor Science and Technology*, vol. 17, p. 113, 2004.

[92] A. Conca, *Magnetic tunneling junctions with the Heusler compound $Co_2Cr_{0.6}Fe_{0.4}Al$.* PhD thesis, University of Mainz, 2007.

[93] G. Jakob, F. Casper, V. Beaumont, S. Falk, N. Auth, H.-J. Elmers, C. Felser, and H. Adrian, "Thin epitaxial films of the Heusler compound $Co_2Cr_{0.6}Fe_{0.4}Al$," *Journal of Magnetism and Magnetic Materials*, vol. 290-291, p. 1104, 2005.

[94] J. Enkovaara, O. Heczko, A. Ayuela, and R. M. Nieminen, "Coexistence of ferromagnetic and antiferromagnetic order in Mn-doped Ni_2MnGa.," *Phys. Rev. B*, vol. 67, p. 212405, 2003.

[95] T. Hofmann, *Erprobung und Optimierung verschiedener Magnetfelddetektionsverfahren im Hinblick auf ihre Eignung als ultraschnelle Messtechnik.* PhD thesis, University of Frankfurt, 2003.

[96] M. Huth, "AG Huth - University of Frankfurt, http://www.pi.physik.uni-frankfurt.de/Wissenschaftliche_Arbeitsgruppen/thinfilm/index.html," 2011.

[97] C. A. Jenkins, *Thin film Heusler compounds $Mn_{3-x}Ni_xGa$.* PhD thesis, University of California, Berkeley, 2009.

[98] C. A. Jenkins, R. Ramesh, M. Huth, T. Eichhorn, P. Pörsch, H. J. Elmers, and G. Jakob, "Growth and magnetic control of twinning structure in thin films of Heusler shape memory compound Ni_2MnGa," *Appl. Phys. Lett.*, vol. 93, p. 234101, 2008.

[99] PowderCell, "Bundesanstalt für Materialforschung und -prüfung, http://www.bam.de/de/service/publikationen/powder_cell.htm," 2011.

[100] N. W. Ashcroft and N. D. Mermin, *Solid State Physics.* Philadelphia: Saunders College, 1976.

[101] A. Guinier, *X-ray diffraction in crystals, imperfect crystals, and amorphous bodies.* New York: Dover Publications, 1994.

[102] L. G. Parratt, "Surface Studies of Solids by Total Reflection of X-Rays," *Phys. Rev.*, vol. 95, p. 359, 1954.

[103] C. Braun, "Parratt32, Hahn-Meitner-Institut Berlin GmbH," 1997-2002.

[104] S. Foner, "Versatile and sensitive Vibrating-Sample Magnetometer," *Review of Scientific Instruments*, vol. 30, p. 548, 1959.

[105] R. C. Jaklevic, J. Lambe, A. H. Silver, and J. E. Mercereau, "Quantum Interference Effects in Josephson Tunneling," *Phys. Rev. Lett.*, vol. 12, p. 159, 1964.

[106] V. D. Kuznetsov, "Measurement of magnetic susceptibility with the aid of a quantum magnetometer," *Russian Physics Journal*, vol. 27, p. 118, 1984.

[107] B. D. Josephson, "Possible new effects in superconductive tunnelling," *Physics Letters*, vol. 1, p. 251, 1962.

[108] K. Matsuda, T. Kasahara, T. Marukame, T. Uemura, and M. Yamamoto, "Epitaxial growth of $Co_2Cr_{0.6}Fe_{0.4}Al$ Heusler alloy thin films on MgO(001) substrates by magnetron sputtering," *Journal of Crystal Growth*, vol. 286, p. 389, 2006.

[109] J. S. Foord, R. B. Jackman, and G. C. Allen, "An X-ray photoelectron spectroscopic investigation of the oxidation of manganese," *Philosophical Magazine A*, vol. 49, p. 657, 1984.

[110] J. Pons, R. Santamarta, V. Chernenko, and E. Cesari, "Structure of the layered martensitic phases of NiMnGa alloys," *Materials Science and Engineering: A*, vol. 438-440, p. 931, 2006.

[111] L. Righi, F. Albertini, E. Villa, A. Paoluzi, G. Calestani, V. Chernenko, S. Besseghini, C. Ritter, and F. Passaretti, "Crystal structure of 7M modulated Ni-Mn-Ga martensitic phase," *Acta Materialia*, vol. 56, p. 4529, 2008.

[112] A. Backen, S. R. Yeduru, M. Kohl, S. Baunack, A. Diestel, B. Holzapfel, L. Schultz, and S. Fähler, "Comparing properties of substrate-constrained and freestanding epitaxial NiMnGa films," *Acta Materialia*, vol. 58, p. 3415, 2010.

[113] Y. Ge, O. Heczko, S.-P. Hannula, and S. Fähler, "Probing structure and microstructure of epitaxial Ni-Mn-Ga films by reciprocal space mapping and pole figure measurements," *Acta Materialia*, vol. 58, p. 6665, 2010.

[114] R. Hausmanns, "Magnetfeld- und temperaturabhängige Röntgendiffraktometrie an magnetischen Formgedchtnismaterialien," Master's thesis, University of Mainz, 2011.

[115] S. Kaufmann, R. Niemann, T. Thersleff, U. K. R. ler, O. Heczko, J. Buschbeck, B. Holzapfel, L. Schultz, and S. Fähler, "Modulated martensite: why it forms and why it deforms easily," *New Journal of Physics*, vol. 13, p. 053029, 2011.

[116] M. Reinhold, C. Watson, W. B. Knowlton, and P. Müllner, "Transformation twinning of Ni-Mn-Ga characterized with temperature-controlled atomic force microscopy," *J. Appl. Phys.*, vol. 107, p. 113501, 2010.

[117] T. Eichhorn, R. Hausmanns, and G. Jakob, "Microstructure of freestanding single-crystalline Ni_2MnGa thin films," *Acta Materialia*, vol. 59, p. 5067, 2011.

[118] R. V. Kohn and S. Müller, "Branching of twins near an austenite/twinned-martensite interface," *Philosophical Magazine A*, vol. 66, p. 697, 1992.

[119] M. Thomas, O. Heczko, J. Buschbeck, L. Schultz, and S. Fähler, "Stress induced martensite in epitaxial Ni-Mn-Ga films deposited on MgO(001)," *Appl. Phys. Lett.*, vol. 92, p. 192515, 2008.

[120] J. Buschbeck, R. Niemann, O. Heczko, M. Thomas, L. Schultz, and S. Fähler, "In situ studies of the martensitic transformation in epitaxial Ni-Mn-Ga films," *Acta Materialia*, vol. 57, p. 2516, 2009.

[121] J. Tillier, D. Bourgault, S. Pairis, L. Ortega, N. Caillault, and L. Carbone, "Martensite structures and twinning in substrate-constrained epitaxial Ni-Mn-Ga films deposited by a magnetron co-sputtering," *Physics Procedia*, vol. 10, p. 168, 2010.

[122] Y. Luo, P. Leicht, A. Laptev, M. Fonin, U. Rüdiger, M. Laufenberg, and K. Samwer, "Effects of film thickness and composition on the structure and martensitic transition of epitaxial off-stoichiometric Ni-Mn-Ga magnetic shape memory films," *New Journal of Physics*, vol. 13, p. 013042, 2011.

[123] F. Khelfaoui, M. Kohl, J. Buschbeck, O. Heczko, S. Fähler, and L. Schultz, "A fabrication technology for epitaxial Ni-Mn-Ga microactuators," *The European Physical Journal - Special Topics*, vol. 158, p. 167, 2008.

[124] N. Scheerbaum, Y. Lai, T. Leisegang, M. Thomas, J. Liu, K. Khlopkov, J. McCord, S. Fähler, R. Träger, D. Meyer, L. Schultz, and O. Gutfleisch, "Constraint-dependent twin variant distribution in Ni_2MnGa single crystal, polycrystals and thin film: An EBSD study," *Acta Materialia*, vol. 58, p. 4629, 2010.

[125] C. Bechtold, J. Buschbeck, A. Lotnyk, B. Erkartal, S. Hamann, C. Zamponi, L. Schultz, A. Ludwig, L. Kienle, S. Fähler, and E. Quandt, "Artificial Single Variant Martensite in Freestanding $Fe_{70}Pd_{30}$ Films Obtained by Coherent Epitaxial Growth," *Advanced Materials*, vol. 22, p. 2668, 2010.

[126] A. N. Vasil'ev, A. D. Bozhko, V. V. Khovailo, I. E. Dikshtein, V. G. Shavrov, V. D. Buchelnikov, M. Matsumoto, S. Suzuki, T. Takagi, and J. Tani, "Structural and magnetic phase transitions in shape-memory alloys $Ni_{2+x}Mn_{1-x}Ga$.," *Phys. Rev. B*, vol. 59, p. 1113, 1999.

[127] O. Heczko, "Magnetic shape memory effect and magnetization reversal," *Journal of Magnetism and Magnetic Materials*, vol. 290-291, p. 787, 2005.

[128] M. Thomas, O. Heczko, J. Buschbeck, U. K. Röler, J. McCord, N. Scheerbaum, L. Schultz, and S. Fähler, "Magnetically induced reorientation of martensite variants in constrained epitaxial NiMnGa films grown on MgO(001)," *New Journal of Physics*, vol. 10, p. 023040, 2008.

[129] Y. Zhang, R. A. Hughes, J. F. Britten, J. S. Preston, G. A. Botton, and M. Niewczas, "Self-activated reversibility in the magnetically induced reorientation of martensitic variants in ferromagnetic Ni-Mn-Ga films," *Phys. Rev. B*, vol. 81, p. 054406, 2010.

[130] G. Schütz, W. Wagner, W. Wilhelm, P. Kienle, R. Zeller, R. Frahm, and G. Materlik, "Absorption of circularly polarized X-rays in iron," *Phys. Rev. Lett.*, vol. 58, p. 737, 1987.

[131] C. T. Chen, F. Sette, Y. Ma, and S. Modesti, "Soft-x-ray magnetic circular dichroism at the $L_{2,3}$ edges of nickel," *Phys. Rev. B*, vol. 42, p. 7262, 1990.

[132] H.-J. Elmers, "AG Magnetismus, Johannes Gutenberg-Universität Mainz, http://www.uni-mainz.de/FB/Physik/Magnetismus/," 2011.

[133] M. Kallmayer, H. Schneider, G. Jakob, H. J. Elmers, B. Balke, and S. Cramm, "Interface magnetization of ultrathin epitaxial $Co_2FeSi(110)/Al_2O_3$ films," *Journal of Physics D: Applied Physics*, vol. 40, p. 1552, 2007.

[134] M. Kallmayer, *Röntgenabsorptionsspektroskopie und magnetischer Röntgenzirkulardichroismus an dünnen Heusler-Filmen.* PhD thesis, University of Mainz, 2011.

[135] W. Kuch, *Abbildende magnetische Mikrospektroskopie.* Habilitation, Martin-Luther-Universität Halle-Wittenberg, 2002.

[136] J. Stöhr, "Exploring the microscopic origin of magnetic anisotropies with X-ray magnetic circular dichroism (XMCD) spectroscopy," *Journal of Magnetism and Magnetic Materials*, vol. 200, p. 470, 1999.

[137] G. van der Laan, R. V. Chopdekar, Y. Suzuki, and E. Arenholz, "Strain-Induced Changes in the Electronic Structure of $MnCr_2O_4$ Thin Films Probed by X-Ray Magnetic Circular Dichroism," *Phys. Rev. Lett.*, vol. 105, p. 067405, 2010.

[138] H. Ebert, "Magneto-optical effects in transition metal systems," *Reports on Progress in Physics*, vol. 59, p. 1665, 1996.

[139] B. T. Thole, P. Carra, F. Sette, and G. van der Laan, "X-ray circular dichroism as a probe of orbital magnetization," *Phys. Rev. Lett.*, vol. 68, p. 1943, 1992.

[140] P. Carra, B. T. Thole, M. Altarelli, and X. Wang, "X-ray circular dichroism and local magnetic fields," *Phys. Rev. Lett.*, vol. 70, p. 694, 1993.

[141] O. Eriksson, B. Johansson, R. C. Albers, A. M. Boring, and M. S. S. Brooks, "Orbital magnetism in Fe, Co, and Ni," *Phys. Rev. B*, vol. 42, p. 2707, 1990.

[142] F. Zuo, X. Su, P. Zhang, G. C. Alexandrakis, F. Yang, and K. H. Wu, "Magnetic and transport properties of the $Ni_{2-x}Mn_{1+x}Ga$ alloys," *Journal of Physics: Condensed Matter*, vol. 11, p. 2821, 1999.

[143] S. R. Barman, S. Banik, and A. Chakrabarti, "Structural and electronic properties of Ni_2MnGa," *Phys. Rev. B*, vol. 72, p. 184410, 2005.

[144] V. Golub, K. M. Reddy, V. Chernenko, P. Müllner, A. Punnoose, and M. Ohtsuka, "Ferromagnetic resonance properties and anisotropy of Ni-Mn-Ga thin films of different thicknesses deposited on Si substrate," *J. Appl. Phys.*, vol. 105, p. 07A942, 2009.

[145] V. A. Chernenko, V. Golub, J. M. Barandiarn, O. Y. Salyuk, F. Albertini, L. Righi, S. Fabbrici, and M. Ohtsuka, "Magnetic anisotropies in Ni-Mn-Ga films on MgO(001) substrates," *Appl. Phys. Lett.*, vol. 96, p. 042502, 2010.

[146] P. Klaer, T. Eichhorn, G. Jakob, and H. J. Elmers, "Microscopic origin of magnetic anisotropy in martensitic Ni_2MnGa," *Phys. Rev. B*, vol. 83, p. 214419, 2011.

[147] P. Pörsch, M. Kallmayer, T. Eichhorn, G. Jakob, H. J. Elmers, C. A. Jenkins, C. Felser, R. Ramesh, and M. Huth, "Suppression of martensitic phase transition at the Ni_2MnGa film surface," *Appl. Phys. Lett.*, vol. 93, p. 022501, 2008.

Publications related to this work

1. T. Eichhorn, R. Hausmanns, and G. Jakob
   "Microstructure of freestanding single-crystalline Ni_2MnGa thin films"
   Acta Materialia, vol. 59, p. 5067, 2011

2. P. Klaer, T. Eichhorn, G. Jakob, and H. J. Elmers
   "Microscopic origin of magnetic anisotropy in martensitic Ni_2MnGa"
   Phys. Rev. B, vol. 83, p. 214419, 2011

3. T. Eichhorn and G. Jakob
   "Structural and Magnetic Properties of Epitaxial Ni_2MnGa Thin Films"
   Materials Science Forum, vol. 635, p. 155, 2010

4. M. Kohl, Srinivasa Reddy Y., F. Khelfaoui, B. Krevet, A. Backen, S. Fähler, T. Eichhorn, G. Jakob, A. Mecklenburg
   "Recent Progress in FSMA Microactuator Developments"
   Materials Science Forum, vol. 635, p. 145, 2010

5. M. Kallmayer, P. Pörsch, T. Eichhorn, H. Schneider, C. A. Jenkins, G. Jakob, and H. J. Elmers
   "Compositional dependence of element-specific magnetic moments in Ni_2MnGa films"
   J. Phys. D: Appl. Phys., vol. 42, p. 084008, 2009

6. H. J. Elmers, A. Conca, T. Eichhorn, A. Gloskovskii, K. Hild, G. Jakob, M. Jourdan, M. Kallmayer
   "Magnetic and Electronic Properties of Heusler Alloy Films Investigated by X-Ray Magnetic Circular Dichroism"
   Adv. Sol. Stat. Phys., vol. 48, p. 171, 2009

7. T. Eichhorn, C. A. Jenkins, M. Kallmayer, H. J. Elmers, and G. Jakob
   "Growth and magnetic properties of epitaxial Ni_2MnGa based films"
   Proc. Actuator 2008, 11th Conf. on New Actuators, Bremen, Germany, p. 723, 2008

8. G. Jakob, T. Eichhorn, M. Kallmayer, H. J. Elmers
"Martensite Transition and Microscopic Magnetism of Epitaxial Ni_2MnGa Films"
Mater. Res. Soc. Symp. Proc., vol. 1050E, p. 1050-BB08-02, 2008

9. C. A. Jenkins, R. Ramesh, M. Huth, T. Eichhorn, P. Pörsch, H. J. Elmers, and G. Jakob
"Growth and magnetic control of twinning structure in thin films of Heusler shape memory compound Ni_2MnGa"
Appl. Phys. Lett., vol. 93, p. 234101, 2008

10. P. Pörsch, M. Kallmayer, T. Eichhorn, G. Jakob, H. J. Elmers, C. A. Jenkins, C. Felser, R. Ramesh, M. Huth
"Suppression of martensitic phase transition at the Ni_2MnGa film surface"
Appl. Phys. Lett., vol. 93, p. 022501, 2008

11. G. Jakob, T. Eichhorn, M. Kallmayer, H. J. Elmers
"Correlation of electronic structure and martensitic transition in epitaxial Ni_2MnGa films"
Phys. Rev. B, vol. 76, p. 174407, 2007

12. G. Jakob and H.J. Elmers
"Epitaxial films of the magnetic shape memory material Ni_2MnGa"
Journal of Magnetism and Magnetic Materials, vol. 310, p. 2779, 2007

Acknowledgments

At this point, I'd like to express my thanks to the people who have been very helpful to me during this work. The great working atmosphere created by my colleagues provided a solid basis to do the research presented in this thesis. I thank the heads of the group for giving me the opportunity to work in a well equipped environment. In particular, I would like to thank my tutor for the invaluable support. His brilliant ideas and infinite patience in answering my questions made this work possible. He was the one to introduce me to the secrets of film preparation and the various characterization methods.

I sincerely thank all members of the group, both past and present, I had the chance to work with. I am grateful for fruitful discussions, technical support and all the helpful hands during lab work.

I'd also like to thank the people of the external group I had the privilege to work with. Their expertise on magnetism in general and X-ray absorption spectroscopy in particular gave rise to interesting new results achieved in the joint cooperation.

Of course, I'd like to thank my family and friends for the support and advice.

Furthermore I'm grateful for financial support from the *Deutsche Forschungsgemeinschaft* through project C5 in SPP-1239.

http://www.magneticshape.de/